Investigation of centrosome-dependent signaling axis driving stemness and chromosomal instability of ALDH-positive cancer stem-like cells

Henry G. Yu

Division of Experimental Medicine

Faculty of Medicine, McGill University, Montreal December 2021

A thesis submitted to the Faculty of Graduate Studies and Research in partial fulfillment of requirements of the degree of Doctor of Philosophy

Investigation of centrosome-dependent signaling axis driving stemness and chromosomal instability of ALDH-positive cancer stem-like cells

THESIS FOR DOCTORAL DEGREE (Ph. D.)

By

Henry G. Yu

Principal supervisor:
Professor Moulay Alaoui-Jamali
McGill University
Department of Medicine - Division of Experimental Medicine

To my parents, friends, colleagues, my supervisor Dr. Jamali, and my loving wife Qianhui/Cherry: I am eternally grateful for your care, support, and companionship. Your illuminating glow endow me with the courage to venture boldly into the endless abyss of scientific discovery.

Abstract

Growing efforts to eradicate cancer are hamstrung by intratumoral heterogeneity. Genotypic heterogeneity arises from genomic instability and genetic mutations seen in most cancer, and its underlying mechanisms include chromosomal instability (CIN). Phenotypic heterogeneity is generally enhanced during cancer progression through acquisition of stem cell-like features (stemness). The degree of stemness and CIN often evolves in parallel as cancer advances, but interplays between these hallmarks is poorly understood. Mechanistic studies on this front can uncover critical insight on the emergence of intratumoral heterogeneity and aid ongoing efforts to overcome drug resistance and relapse.

Chapter 1 of this thesis is a literature review to examine the question: "can cancer stemness directly influence CIN? Acquisition of stemness is a widely observable in leukemia and solid tumors. This chapter identifies that, among the core functionalities of stem cells, programs which enhances their capacity to perform asymmetrical cell division is poorly understood in the context of cancer stemness. Asymmetrical cell division is accomplished, in part, via the asymmetrical behavior of centrosomes: organelles that function to organize parts of the cytoskeleton, including the mitotic spindle. In addition to playing a pivotal role in stem cell asymmetrically cell division, the centrosomes can also cause chromosomal/genomic instability through centrosome amplification. Consequently, the central hypothesis derived from chapter 1 is that regulation of cancer stemness and CIN could intersect at centrosome regulation pathways.

Chapter 2 consists of three manuscripts which explores the postulation that centrosome regulatory networks can be important co-regulators of stemness and CIN. Manuscript 1 identified anaplastic thyroid cancer (ATC) as a cancer model where stemness directly impacts CIN. Using flow cytometry-based sorting based on stem cell-like marker, we identified that ALDH+ stem-like cells are unusually tolerant to CIN compared to bulk tumor cells. Both stemness and CIN-tolerance were driven by ALDH-mediated transcriptional upregulation of the scaffolding protein NEDD9. Mechanistically, NEDD9 linked these hallmarks by uniquely regulating ALDH+ cell centrosomes. In ALDH+ cells with 2 centrosomes, NEDD9-knockdown restored centrosome asymmetry and hampered their ability to perform asymmetrical cell division. In those same cells with >2 centrosomes, NEDD9-knockdown activated an excess number of supernumerary centrosomes prior to mitosis, increasing the severity spindle multipolarity, consequently preventing the completion of CIN-prone mitosis. NEDD9-depletion therefore can lead to dual inhibition of

stemness/CIN. Manuscript 2 investigates the factors downstream of NEDD9 that regulates asymmetrical centrosome behavior. Through pharmacological/genetic perturbation of the NEDD9 interactome, we identified that the centrosome asymmetry observed above was due to an unexpected cytoplasmic NEDD9/STAT3 pathway existing in ALDH+ but not ALDH- ATC cells. Lastly, manuscript 3 is a translational study using the concepts and factor identified in manuscript 1 to identify a novel multikinase inhibitor "MEAP" that can recapitulate benefits of NEDD9-knockdown by activating supernumerary centrosomes, leading to inhibition of stemness/CIN in vitro and *in vivo*. These manuscripts collectively reveal critical insight into both pathogenesis and treatment of ATC, a disease for which the median survival is only six months and which urgently require effective forms of treatment. Additionally, they also highlight centrosome regulation in cancer stem-like cells as an important link between stemness and CIN in cancer, potentially informing novel approaches for limiting intratumoral heterogeneity.

Résumé

Malgré les avancées dans la découverte de nouvelles approches thérapeutiques pour le traitement des cancers, l'apparition de rechutes demeure un obstacle pour éradiquer ces maladies. Plusieurs facteurs sont impliqués dans cet échec, parmi lesquelles l'hétérogénéité intra tumorale demeure un problème majeur responsable de l'apparition de sous populations de cellules cancéreuses résistantes aux effets cytotoxiques des médicaments. Ces populations cellulaires peuvent manifester des caractéristiques similaires aux cellules souches normales, telles que l'expression de récepteurs membranaires qui caractérisent les cellules souches et la capacité d'auto-renouvellement/différenciation qui permet à ces cellules d'agir comme précurseurs à la diversité des cellules cancéreuses au sein d'une même masse tumorale.

Dans mon projet de thèse, j'ai établi la présence d'un mécanisme de régulation des centrosomes impliquant l'instabilité chromosomique dans des cellules souches isolées de carcinôme anaplasique de la thyroïde, un cancer agressif avec une survie moyenne de six mois. Mon travail est organisé en 2 chapitres: Le premier est une revue de la littérature abordant les liens entre cellules souches cancéreuses et l'instabilité génomique. L'acquisition par les cellules cancéreuses de caractéristiques semblables aux cellules souches normales est un phénomène mieux caractérisé dans les leucémies. Parmi les caractéristiques canoniques associées avec ces cellules, leur capacité à effectuer une division cellulaire asymétrique est un comportement unique à ces cellules mais l'impact sur la progression tumorale est peu élucidé. La division cellulaire asymétrique dans les cellules souches est accomplie, en partie, via le comportement des centrosomes qui fonctionnent comme le principal centre d'organisation des microtubules durant la division cellulaire asymétrique. En plus, les centrosomes peuvent favoriser l'instabilité chromosomique (IC) et génomique impliquant la formation erronée de pôles mitotiques. Par conséquent, l'hypothèse centrale dérivée du chapitre 1 est que l'acquisition des caractéristiques des cellules souches et de l'IC pourraient se croiser au niveau des voies de régulation des centrosomes.

Le deuxième chapitre explore l'hypothèse selon laquelle les mécanismes qui contrôlent les centrosomes ont un double impact sur l'acquisition de caractère de cellules souches tumorales et de l'instabilité génomique. Dans ce contexte, le manuscrit 1 révèle que dans les cellules souches cancéreuses de la thyroïde (ALDH+), une augmentation de l'expression de NEDD9 associée aux centrosomes est nécessaire pour maintenir à la fois les cellules souches et le statut d'IC. Nous avons démontré que NEDD9 régule ces deux caractéristiques (la caractère de cellule souche et

l'IC), en partie, en inactivant l'une des paires de centrosomes associée aux cellules souches. Notamment, cette asymétrie des centrosomes était particulièrement essentielle pour les cellules ALDH+ avec amplification des centrosomes. Nous avons découvert qu'un grand pourcentage de centrosomes excédentaires pouvait être inactivé pendant le début de la mitose pour faciliter la formation de fuseaux mitotiques pseudo-bipolaires, assurant ainsi un taux de réussite élevé de la mitose au dépend de l'IC. Le deuxième manuscrit approfondit les facteurs moléculaires qui agissent en aval de NEDD9 pour réguler les centrosomes. Grâce à une perturbation pharmacologique/génétique du NEDD9, nous avons identifié que l'asymétrie des centrosomes observée dans les cellules ALDH+ était due en partie à une activation de voie NEDD9/STAT3 cytoplasmique. Enfin, le manuscrit 3 a élargi nos données d'un point de vue clinique. À cette fin, nous avons développé un nouvel inhibiteur ciblant l'interaction de NEDD9 avec ses partenaires et capable d'induire (i) l'activation des centrosomes excédentaires entraînant ainsi la formation accrue de fuseaux multipolaires, et (ii) la réduction des cellules ALDH+ et de l'INC. En conclusion, ce travail établit une régulation et un comportement distincts des centrosomes au sein des cellules souches cancéreuses, ayant un impact sur la stabilité génomique. En plus, il a permis l'identification de cibles thérapeutiques pour prévenir l'hétérogénéité intra tumorale et donc la progression de la maladie.

Contents

List of Scientific Manuscripts/Publications

Manuscripts as first author

Yu H, Bijian K, Silva S, Su J, Morand G, Spatz A and Alaoui-Jamali MA Asymmetrical centrosome behavior and DNA sensing coregulation links stemness to chromosomal instability during thyroid cancer progression. Under revision for Oncogene.

Yu H, Bijian K**,** Alaoui-Jamali MA Differential STAT3 regulation by NEDD9-interactome contributes to centrosome asymmetry in thyroid cancer stem-like cells. In preparation.

Yu H, Bijian K, Silva S, Su J, Morand G, Wernic D, Spatz A and Alaoui-Jamali MA Targeting tumorigenic thyroid cancer stem cells through centrosome-activation-induced mitotic catastrophe. In preparation.

Other Publications

Bijian K, Lougheed C, Su J, Xu B, **Yu H**, Wu JH, Riccio K, Alaoui-Jamali MA. Targeting focal adhesion turnover in invasive breast cancer cells by the purine derivative reversine. British journal of cancer**.** 2013 Nov;109(11):2810-8.

Marques M, Jangal M, Wang LC, Kazanets A, da Silva SD, Zhao T, Lovato A, **Yu H**, Jie S, Del Rincon S, Mackey J. Damaraju S, Alaoui-Jamali M, Witcher M. Oncogenic activity of poly (ADP-ribose) glycohydrolase. Oncogene. 2019 Mar;38(12):2177-91.

Guo Q, Li VZ, Nichol JN, Huang F, Yang W, Preston SE, Talat Z, Lefrère H**, Yu H**, Zhang G, Basik M. M, Gonçalves C, Zhan Y, Plourde D, Su J, Torres J, Marques M, Habyan SA, Bijian K, Amant F, Witcher M, Behbod F, McCaffrey L, Alaoui-Jamali M, Giannakopoulos NV, Brackstone M, Postovit LM, Del Rincón SV, Miller WH Jr. MNK1/NODAL signaling promotes invasive progression of breast ductal carcinoma in situ. Cancer research. 2019 Apr 1;79(7):1646-57.

Chang CH, Bijian K, Wernic D, Su J, da Silva SD, **Yu H**, Qiu D, Asslan M, Alaoui-Jamali MA. A novel orally available seleno-purine molecule suppresses triple-negative breast cancer cell proliferation and progression to metastasis by inducing cytostatic autophagy. Autophagy. 2019 Aug 3;15(8):1376-90.

Acknowledgements

I'd like to foremost thank my supervisor Dr. Moulay Alaoui-Jamali for guiding me throughout my years as a graduate student. I am eternally grateful for the opportunity to work under your research team. Your guidance and encouragement gave me the confidence to pursue research that I can be interested in.

I would also like to thank Dr. Krikor Bijian for the hundreds/thousands of help he has offered me throughout my studies. From project design to reagent selection, you have guided me every step of the way. I will always be grateful to you.

Next, I would like to thank Jie Su for his experimental contributions, especially for the animal experiments in the manuscript and his companionship and banter.

I would also like to thank all the wonderful team members who offered technical guidance throughout the years, including many former lab members (Dr. Yingjie Xu, Dr. Xu Bin, Dr. Chia-Hao Chang, Dinghong Qiu) as well as Christian Young and Naciba Benlimame for technical assistance with flow cytometry/imaging and immunohistochemical staining respectively

A warm thank you to my academic committee members, Dr. Colin Crist, Dr. Nicoletta Eliopolous, and Dr. Lorraine Chalifour for their expert guidance.

We thank Dr. John Copland for providing the cell lines THJ-11T, THJ-16T, and THJ-29T, and Dr. Mark Trifiro for providing the cell lines 8505c, TPC, and BCPAP. We thank Dr. Michel Tremblay for providing the PTP-PEST and PTP1B antibody.

Lastly, to all the wonderful peers and staffs, including the custodial and maintenance team at the Lady Davis Institute for providing a clean, efficient and friendly/intellectually engaging environment to study.

Contribution to original knowledge

The three manuscripts presented in this thesis are, to our knowledge, the first to postulate and investigate centrosomes as a linkage between cancer stemness and chromosomal instability (CIN). Manuscript 1 identifies that overexpression of the scaffolding protein, NEDD9, simultaneously promotes asymmetrical centrosome behavior (a feature unique to stem cells) and tolerance to chromosomal instability. Manuscript 2 identifies a cytoplasmic NEDD9/STAT3 pathway which links NEDD9 expression to asymmetrical centrosomes. Manuscript 3 identifies a novel small molecule which can selectively eliminate CIN-driving cancer stem-like cells by exploiting their asymmetrical centrosome.

Contribution of authors

For manuscript 1, **Henry Yu** performed the cell-based experiments, including all western blot, immunofluorescence imaging, live cell imaging, flow cytometric analysis, microtubule regrowth assay, tumorsphere formation assay, reporter assay, chromatin-immunoprecipitation (ChIP), BrdU-pulse chase assay, and quantitative polymerase chain reaction. **Henry Yu** also performed the analysis of National Center for Biotechnology Information (NCBI) and The Cancer Genome Atas (TCGA) datasets, enzyme-linked immunosorbent assay (ELISA), production of lentivirus / construction of stable cell lines, and molecular cloning of doxycycline-inducing NEDD9 expression vector. Dr. Yang Long provided the constructs for NEDD9-CRISPR. Dr. Jie Su, with the assistance of Dr. Gregoire Morand, established the protocols and performed the *in vivo* animal experiments demonstrating the efficacy of doxycycline-induced NEDD9-knockdown. Dr. Sabrina da Silva and Dr. Alan Spatz oversaw collection, validation, and analysis of patient tissue samples. Immunohistochemical staining was performed by the Lady Davis pathology department by Dr. Naciba Benlimame. **Henry Yu**, Dr. Krikor Bijian, and Dr. Moulay A. Alaoui-Jamali conceptually developed the project and wrote the manuscripts.

For manuscript 2, **Henry Yu** performed cell-based experiments, including all western blot, immunofluorescence imaging, nuclear fraction, immuno co-precipitation, flow cytometric analysis, and the microtubule regrowth assay. **Henry Yu** also performed analysis of The Cancer Genome Atas (TCGA) datasets, production of lentivirus / construction of stable cell lines, and molecular cloning of STAT3/STAT3-CA expression vectors. **Henry Yu**, Dr. Krikor Bijian, and Dr. Moulay A. Alaoui-Jamali conceptually developed the project and wrote the manuscripts.

For manuscript 3, **Henry Yu** performed cell-based experiments, including all western blot, immunofluorescence imaging, aldehyde dehydrogenase enzymatic assay, flow cytometric analysis, tumorsphere formation assay, and microtubule regrowth assay.

Dr. Krikor Bijian oversaw the synthesis of novel Reversine derivatives and guided the *in vitro* selectscreen profiling of the small molecules. Dr. Dominik Wernic synthesized the small molecules. Dr. Sabrina da Silva and Dr. Alan Spatz oversaw collection, validation, and analysis of patient tissue samples. Dr. Jie Su and Dr. Gregoire Morand, established the protocols and performed the *in vivo* animal experiments demonstrating the efficacy of novel small molecules. **Henry Yu**, Dr. Krikor Bijian, and Dr. Moulay A. Alaoui-Jamali conceptually developed the project and wrote the manuscripts.

List of Figures

M1-Figure 6: NEDD9 upregulation in ALDH+ cells shut down micronuclei-rupture stimulated DNA sensing pathway by limiting STING protein expression

M1-Figure 7: shNEDD9-induced STING activation suppresses ALDH+ cell growth independently from shNEDD9-induced spindle multipolarity

M1-Figure 8: NEDD9-depletion selectively eliminates ALDH+ ATC cells and attenuates ATC spherogenic and tumor seeding potential

M1-Figure 9: NEDD9-depletion in ATC xenografts inhibits tumor growth, eliminates ALDH1A3 positive cells, promotes STING activation, and reduces chromosome missegregation

M1-Figure 10: Stemness-associated centrosome genes upregulation correlates with aneuploidy in multiple types of solid tumor

M1-Figure. S1: NEDD9-depletion hampers asymmetrical cell division in ALDH+ cells

M1-Figure. S2: ALDH enzymatic activity in THJ-16T is primarily via the ALDH1A3 isoform

M1-Figure. S3: Additional centrosome images

M1-Figure. S4: Low-magnification (20x) representative images of shNEDD9-induced multipolar spindles in ALDH+ cells.

M1-Figure. S5: Impact of CPAP/CENPJ knockdown in THJ-16T ALDH+ and ALDH- cells

M1-Figure. S6: STING upregulation contributes to shNEDD9-mediated cell death during interphase and mitosis

M1-Figure. S7: Impact of NEDD9-knockdown on MCF10-A non-transformed cell line

M1-Figure. S8: Inducible NEDD9-knockdown causes reduction of %ALDH+ in ATC xenograft

M1-Figure. S9: Gating strategy for flow cytometry analysis

Manuscript 2: Differential STAT3 regulation by NEDD9-interactome contributes to centrosome asymmetry in thyroid cancer stem-like cells

M2-Figure 1: NEDD9 and STAT3 mRNA levels are positive correlated across different types of cancer, including thyroid cancer

M2-Figure 2: NEDD9 distinguishes pSTAT3^{705} activation between ALDH- and ALDH+ ATC cells

M2-Figure 3: Only in ALDH+ cells, STAT3 is dephosphorylated in response to chemical inhibitors targeting the NEDD9-interactome

M2-Figure 4: AURKAi-induced pSTAT3^{705} dephosphorylation involves PTP-PEST phosphatase

M2-Figure 5: NEDD9/AURKA predominantly regulates cytoplasmic STAT3 activation in ALDH+ ATC cells

M2-Figure 6: STAT3 activation antagonizes centrosome microtubule-nucleation downstream of the NEDD9-interactome

M2-Figure 7: Both positive and negative regulation of STAT3 activation disturbs centrosome asymmetry in ALDH+ ATC cells

Manuscript 3: Targeting tumorigenic thyroid cancer stem cells through centrosome-activation-induced mitotic catastrophe

M3-Figure 1: Anaplastic thyroid cancer patient tissues contain γ-tubulin-deficient supernumerary centrosomes

M3-Figure 2: Identification of a small molecule MEAP that can activate γ-tubulin-deficient supernumerary centrosomes found primarily in ALDH+ ATC cells

M3-Figure 3: MEAP induces pericentriolar material accumulation at inactivated centrosomes during interphase

M3-Figure 4: MEAP preferentially induces multipolar spindles and G2/M arrest in ALDH+ ATC cells

M3-Figure 5: MEAP selectively eliminates ALDH+ ATC cells and attenuates spherogenic and tumorigenic potential

M3-Figure 6: MEAP eliminates ALDH+ ATC cells, increases PCM levels, induces spindle multipolarity, and reduces chromosomal instability in vivo

M3-Figure. S1: Additional representative images of γ-tubulin staining in papillary and anaplastic thyroid cancer patient samples. Original magnification: 100x. Scale bar = 10μm. The red arrows indicate the presence of highly asymmetrical centrosomes.

M3-Figure. S2: MEAP is a multikinase inhibitor which inhibits NEDD9-interactors Aurora Kinase A and FAK at a superior potency compared to Reversine:

Figure M3-S3: Additional low magnification of MEAP-induced centrosome-microtubule growth.

Fig. M3-S4: Impact of MEAP on pAURKA288 kinetics in cell cycle synchronized cells.

List of Key Recurring Abbreviations

AURKA - Aurora Kinase A

ALDH - Aldehyde dehydrogenase

ACD - Asymmetrical cell division

ATC - anaplastic thyroid cancer

CD - cluster of differentiation

CIN - Chromosomal instability

CSC - Cancer stem cells

DNA - Deoxyribonucleic acid

EMT/MET - Epithelial mesenchymal transition / mesenchymal epithelial transition

FAK - Focal adhesion kinase

iPSC - Induced pluripotent stem cell

Mir - MicroRNA

MTOC - Microtubule organizing center

NEDD9 - Neural Precursor Cell Expressed, Developmentally Down-Regulated 9

STING - Stimulator of interferon genes

Introduction

As cancer progresses into advanced stages, two recurrent traits often emerge often irrespective of the tissue of origin: 1) gradual accumulation of traits normally restricted to tissue-resident stem cells or progenitor cells 2) increase in chromosomal instability leading to large-scale genomic alterations. Although these two traits are often acquired in parallel, their interplay is poorly understood.

The first chapter of this thesis is composed of four main segments. The first (1.1) examines the empirical evidence that cancer development is ultimately driven by the unresolved interplay between factors promoting intratumoral heterogeneity. This segment demonstrates cancer stemness and genomic instability as two overlapping factors that co-determine emergent tumors' eventual property. The second segment (1.2) reviews current studies that have shown that stem cell-associated factors have impacts on canonical "cancer hallmarks," thus providing evidence for why cancer cell fitness could benefit from aberrant activation of stem cell-intrinsic network, resulting in overall increased "stemness" as cancer progresses. The third segment (1.3) reviews the mechanisms of asymmetrical cell division - a unique property of stem-like cells that is essential to their usual replication paradigm, whereby their cell division produces one daughter cell that retains the stem cell identity and another more differentiated daughter cell. This segment illustrates that asymmetrical cell division is a tightly regulated stem cell program whose contribution to cancer development is only beginning to be understood. The final (1.4) segment describes the unique properties of centrosomes - a pair of organelles with encompassing functions in intracellular trafficking and mitotic spindle morphology/orientation. This segment reviews evidence that centrosomes have unique properties in the context of both stem cell biology and cancer.

These introductory chapters lay the foundation for chapter 2, which builds upon these existing studies to investigate the centrosomes as a critical linkage between cancer stemness and chromosomal instability.

1. Background: Interplays among tumor heterogeneity, stemness, and centrosome abnormalities during cancer progression

1.1 Cancer "stem" cells are a non-genetic source of tumor heterogeneity and drug resistance

1.1.1 Cancer cells can retain differentiation paradigms of their original tissue

Evidence that malignant tumors are composed of phenotypically distinct subpopulations, with specific clones resembling stem cells, has existed for over 60 years [1] [2]. Cumulative studies have revealed that cancer cells extensive vary in cell surface markers [3], proliferation potential[4], therapy resistance [5] and mutational landscape [6] . As a result, cancer can no longer be viewed as simple amalgamations of rapidly proliferating cells. Instead, cancer is formed of a complex ecosystem collectively referred to as the tumor microenvironment, with “cancer stem cells” (CSC) playing an integral supporting role in the architecture of these neoplastic tissues.

The notion that cancer cells' properties are linked to stem cells and developmental pathways originated from early observations that cancer cells can, to some extent, exhibit differentiation patterns of their original tissue. Studies in teratocarcinoma showed, for instance, that the F9 model can be induced to undergo differentiating morphological changes upon induction with shallow doses (10^{-9}M) of retinoic acid [7]. Meanwhile, the breast cancer cell line Rama 25 was also maintained in an undifferentiated state at low density but then underwent spontaneous differentiation into secretory and myoepithelial lineages at high density [8,9] . These findings indicated that cancer cells could partially retain the differentiation potential of their original tissues.

Early studies which identified CSCs were based on lineage markers used for their parental tissue; for instance, enrichment of both leukemic stem cells and hematopoietic stem cells can both be accomplished using CD34+CD38- status [10]. Functionally, there are many similarities between tumor cell propagation and stem cell propagation models: in both leukemia and hematopoietic stem cells models, a rare subset of slow-cycling cells retain unlimited proliferation capacity but can produce rapidly proliferating "transit-amplifying" progenitor cells to expand total cell numbers [9,11,12] [13]. More recent studies in pediatric brain tumors have demonstrated that solid tumors can

also recapitulate the differentiation paradigms of the tissue lineages from which they are derived [14].

If cancer cells can retain the differentiation paradigms of their original tissue, then it follows that, when taken to the most dedifferentiated extreme, cancer cells would acquire the functional analogy of adult/somatic stem cells - rare cells whose role is to act as a relatively unlimited source of tissue regeneration[15]. The interest in CSCs largely stems from the initial speculation that, much like how somatic stem cells can rejuvenate a tissue after injury, so can CSCs act as the root source of cancer relapse [5].

1.1.2 Cancer stem cells are a source of tumorigenesis, self-renewal, and cellular hierarchy

Physiologically, a typical adult stem cell's role is to act as a reservoir of self-regenerating cells to maintain long-term tissue homeostasis. The cancer stem cell model essentially proposes that certain cancer cells have analogous functions to normal stem cells but are malignant. Currently, there is no precise definition for CSC, particularly as those criteria differs between experimental and clinical settings. Ideally, a CSCs is defined as cancer cells that also display qualities of stem cells, such as multipotency (the capacity to differentiate) and self-renewal (replicating while maintaining stem cell identity). However, applying this definition is challenging if a cancer cell only partially displays stem cell features. A compelling definition of CSCs are cells that share similar transcriptional programs as the resident somatic stem cells of the parental tissue from which the cancer was derived[16]; this likely offers the most direct evidence that a cancer cell has an activated transcriptional signature, though the phenotypic impact of having a stem-like transcriptional signature can only be indirectly inferred. On the other hand, clinically, CSCs are more appropriately defined as cancer cells which can functionally initiate tumors. Indeed, the golden standard for assessing the presence of CSCs is via limited-dilution and serial transplantation assay, and it was via this functional definition that the earliest prospective CSCs were isolated in leukemia in 1994 [17], breast cancer in 2003 [18], and a plethora of other cancer thereafter [19-23]. This functional definition of CSC is most relevant to treatment of cancer patients; however, this definition focuses only on tumorigenicity and overlooks other supportive roles that CSCs could play within the tumor microenvironment.

Self-renewal potential is tightly associated with cellular hierarchy. That is, cells with the most self-renewing potential (i.e., stem cells) are primarily, though perhaps not always

independently, are the ones capable of generating all other resident cell types of that tissue [13,24]. Some of the best-studied models of stem cells, such as hematopoietic stem cells, intestinal stem cells, and hair follicle stem cells, exemplify the capacity of a single stem cell to establish a complex multicellular organ or organoids (**Figure 1a-e**). CSCs display this function as well. When a small population of CSCs is transplanted into a new host, the secondary tumors generated will often mimic the original tumor's functional heterogeneity and relative composition[25]. The dynamics of cancer hierarchy have been carefully dissected using fate-mapping in glioblastoma models, which found that irrespective of any genetic mutations, the tumorigenesis dynamics generally involved slow-cycling cells, giving rise to a rapid-cycling progenitor population, which then give rise to non-dividing cells [25].

Tumor hierarchy can be maintained by relatively conserved epigenetics programs consisting of DNA, histone, and nucleosome modification factors alongside non-coding RNA to regulate gene expression patterns that dictate cell fate [26]. Various epigenetic factors either suppress or promote self-renewal [27]. For instance, the histone linker H1.0 and the histone demethylase KDM5B were downregulated in CSCs and restrict proliferative and differentiation potential [28 29]. Meanwhile, epigenetic factors which sustain self-renewal are often associated with the Polycomb complex, including EZH2, Bmi1, and PRC1.1; in most cases, these factors themselves have not undergone any mutation and instead become hyperactivated and confer malignant properties via their canonical functions. Other key players are the SWI/SNF chromatin remodeling complex, which has been shown to promote stemness via activation of c-MYC[30], and various microRNAs, which regulate the stem cell phenotype by modulating the activation of key signaling pathways such as JAK/STAT and Wnt/β-catenin [31]. Aside from these epigenetic factors, intrinsic variations in gene/protein expression levels (i.e., noise) and environmental factors also contribute to variations in stem-like functionalities. The latter is particularly important in solid malignancies where the topological location of distinct clones has a substantial impact on function [32,33], with hypoxic conditions, in particular, being a major contributing factor to the maintenance of stem-like phenotype of the cells in the inner regions of the tumor [34,35].

There is also mounting evidence that the hierarchical structure is not entirely rigid in both stem cells and cancer stem cells, and that the reverse (i.e., dedifferentiation) does also occur as rare events. In certain models, cancer cells within different transcriptional states can reach an equilibrium [36] determined by the relative probability of each state. This plasticity blurs the

definition of CSCs, as even cells in "non-stem like" states *in vitro* could establish *in* vivo tumors in certain environments, and thus fit the functional definitions of CSCs.

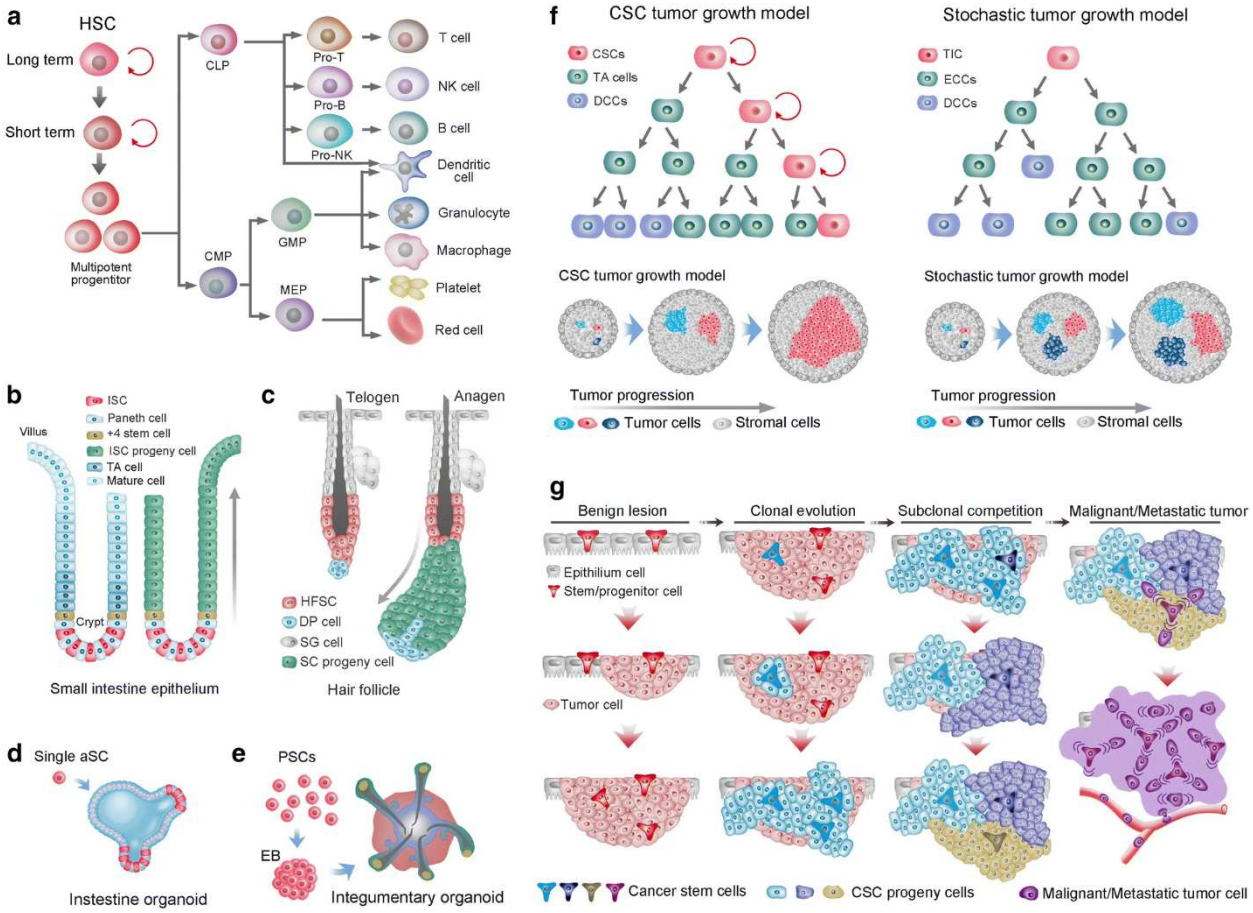

Figure 1: Stem cells in tissues, organoids, and cancer are defined by their capacity to establish a cellular hierarchy **a.** Cells of the hematopoietic system are derived from differentiation of hematopoietic stem cells into progenitor cells (e.g., common lymphoid progenitors CLP), which then eventually transition to terminally differentiated cells (e.g., mature T cells). **b.** At least two types of intestinal stem cells lineages (including the Lgr+ stem cells and the Bmi1+ stem cells at the +4 position) residing at the crypt of the small intestines divide ~every 24h to generate rapidly proliferating transit-amplifying (TA) cells that in turn differentiate into mature epithelial cells (e.g., the secretory Paneth cells) [37]. Upon extreme tissue damage such as exposure to radiation, the cells above the crypt can revert towards a dedifferentiated "ISC progeny cell" state to repopulate crypt-villus [38] **c.** Slow-cycling CD34+ hair follicle stem cells (HFSC) form a bulge underneath the epithelial layer and maintain quiescence during the resting (telogenic) phase. During the growth phase (anagen), HFSCs generate rapidly cycling Lgr5+ progeny cells that in turn differentiate into mature determa papilla (DP) and sebaceous gland (SG) cells. SC progeny cells can also reciprocally repopulate the HFSC compartment and suggest distinct yet equally multipotent stem cell compartments. **d-e.** Stem cells, under certain conditions, can grow into self-organized tissues called organoids *in vitro,* exemplifying their intrinsic capacity for

multipotency. **f.** Under the hierarchical model of tumor growth, cancer stem cells (CSCs) self-renew indefinitely while also producing transit-amplifying cells that differentiate into non-proliferative cancer cells. Under the stochastic model of tumor growth, all cancer cells have the potential to exist as either a CSC or non-CSC and fluidly transition between these states. **g.** A model under which CSC and stochastic tumor growth models are unified postulates that genetically similar cancer cells form a differentiation hierarchy while simultaneously, clonal variants compete via natural selection. This figure is reproduced from "Stem cells in tissues, organoids, and cancers" by Xusheng Wang, Cellular and Molecular Life Sciences (2019) [39], under the terms of the Creative Commons Attribution 4.0 International License (http://creativecommons.org/licenses/by/4.0/)

1.1.3 Cancer stem cells in parallel with clonal evolution increase phenotypic/transcriptomic heterogeneity in a cancer cell population

Cellular hierarchy generally assumes genetically identical clones that exist in different states of differentiation. However, in cancer, mutations occur frequency, and such event can gradually introduce new clonal variants that have an altered hierarchical paradigm [40 41]. Clonal evolution, the idea that cancer evolves through a combination of natural selection of cancer clones generated via random mutations, pre-dates CSCs hypothesis as a way to explain the existence of intratumoral heterogeneity[40 41]. While it was contested whether CSCs or clonal evolution is majorly responsible for intratumoral heterogeneity, modern understandings suggest that tumor heterogeneity is a simultaneous product of stable genetic differences and transient epigenetic states. Indeed, recent findings using advanced genome sequencing have established that cancer cells within single patients consist of a heterogeneous combination of genetically distinct subclones, which are the product of branching evolution, resulting in functionally diverse clones with uniquely acquired driver mutations [40 41]. The integration of both models proposes that the state of differentiation/maturation further stratifies distinct genetically distinct clones within a tumor.

1.1.4 Cancer stem cells contribute to the remodeling of tumor microenvironment niches

Solid tumors can be subdivided into histological types, molecular subtypes, and functionally distinct compartments based on topology and interaction with non-cancerous cells [42,43]. The most common niches are the hypoxic region, perivascular area, and the invasive front. Distinct CSC populations have been shown to sustain the integrity of these different niches, thus conferring functional diversification in CSCs within tumors[44-51] (**Fig. 2**). In this manner, CSCs seem functionally analogous to normal stem cells in terms of communicating to their respective niches for maintaining tissue homeostasis [52,53]. The implication here is that once cancer has progressed to a stage where it can form a self-sustaining microenvironment, it gradually acquires the complexities and nuances of healthy organs. These regional-specific interactions are complicated by certain solid tumors such as medulloblastoma, manifesting genetically distinct clones within spatially distinct compartments, which further varies cancer cell behavior within

solid tumors[54]. CSC's specific interactions within each niche will be elaborated in sections further below that address the impact of CSCs on angiogenesis, metastasis, and immune evasion.

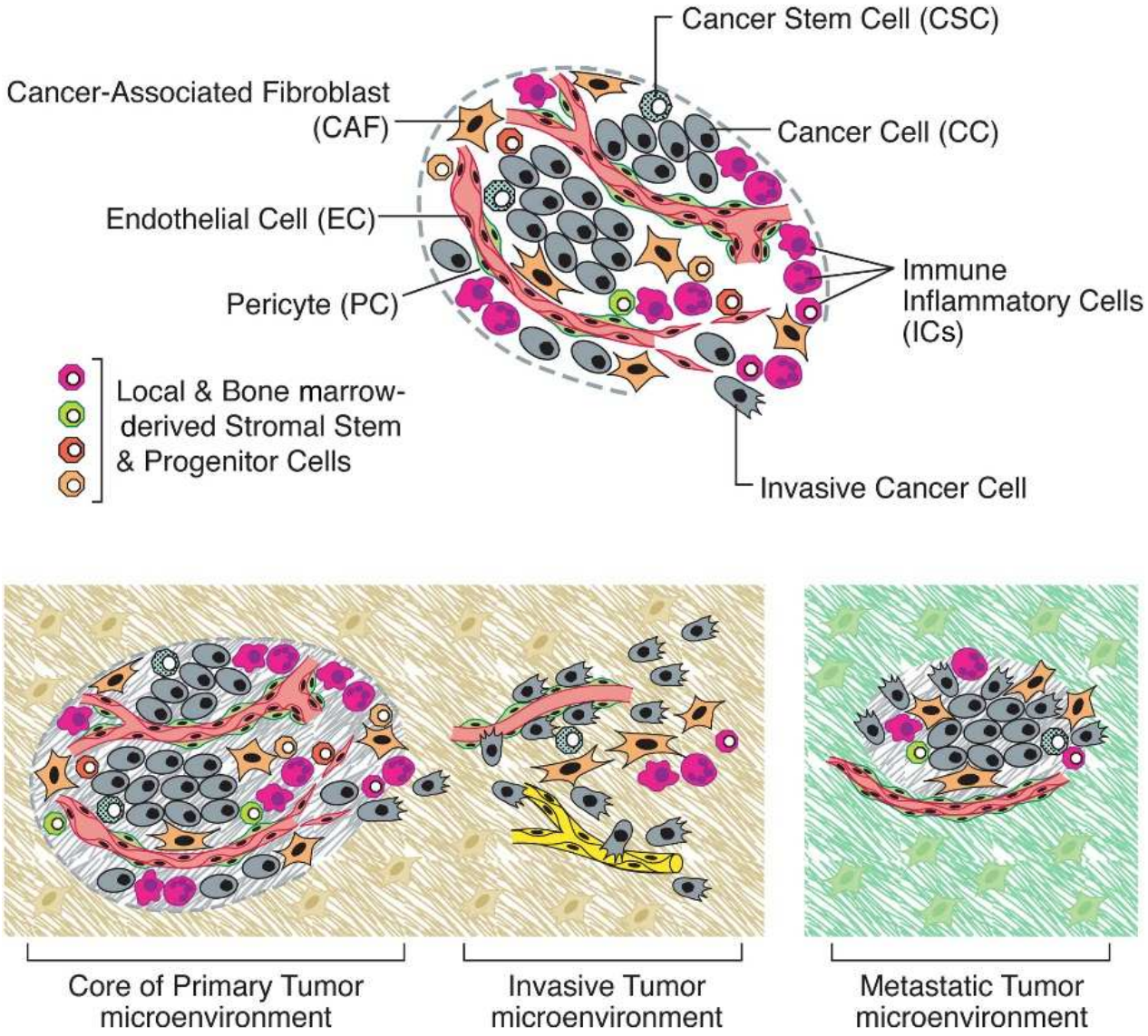

Figure 2: Cancer stem cell functions with a tumor microenvironment (upper) Most solid tumors are composed of an aggregate of tumor cells, stromal cells, parenchymal cells, and immune cells that communicate via cell-cell contact / paracrine signaling to drive cancer progression. (Lower) The tumor microenvironment shifts during tumor progression and metastasis, altering the phenotypic state of cancer cells and cancer stem cells. Image is reproduced from "Hallmarks of Cancer: The Next Generation" by Douglas Hanahan and Robert Weinberg, Cell (2011) **[55]**, with permission from Elsevier.

1.2 Cancer "stemness" arises from both intrinsic and extrinsic factors driven by an integrated program and governs each hallmark cancer property

Cancer develops via the gradual acquisition of "cancer hallmarks" - properties that aid in overcoming checkpoints that gatekeep healthy cells from malignant transformation (**Fig. 3**). Progress towards resolving the molecular basis of cancer acquisition has unveiled remarkable new insight into how these hallmarks can be acquired intrinsically via mutations, signaling alterations, and aberrant extrinsic interaction with the tumor microenvironment. The following sections of the thesis highlights recent evidence that "stemness" is a cancer property that directly or indirectly impacts each stage of tumor development by modulating the manifestation of cancer cell hallmarks.

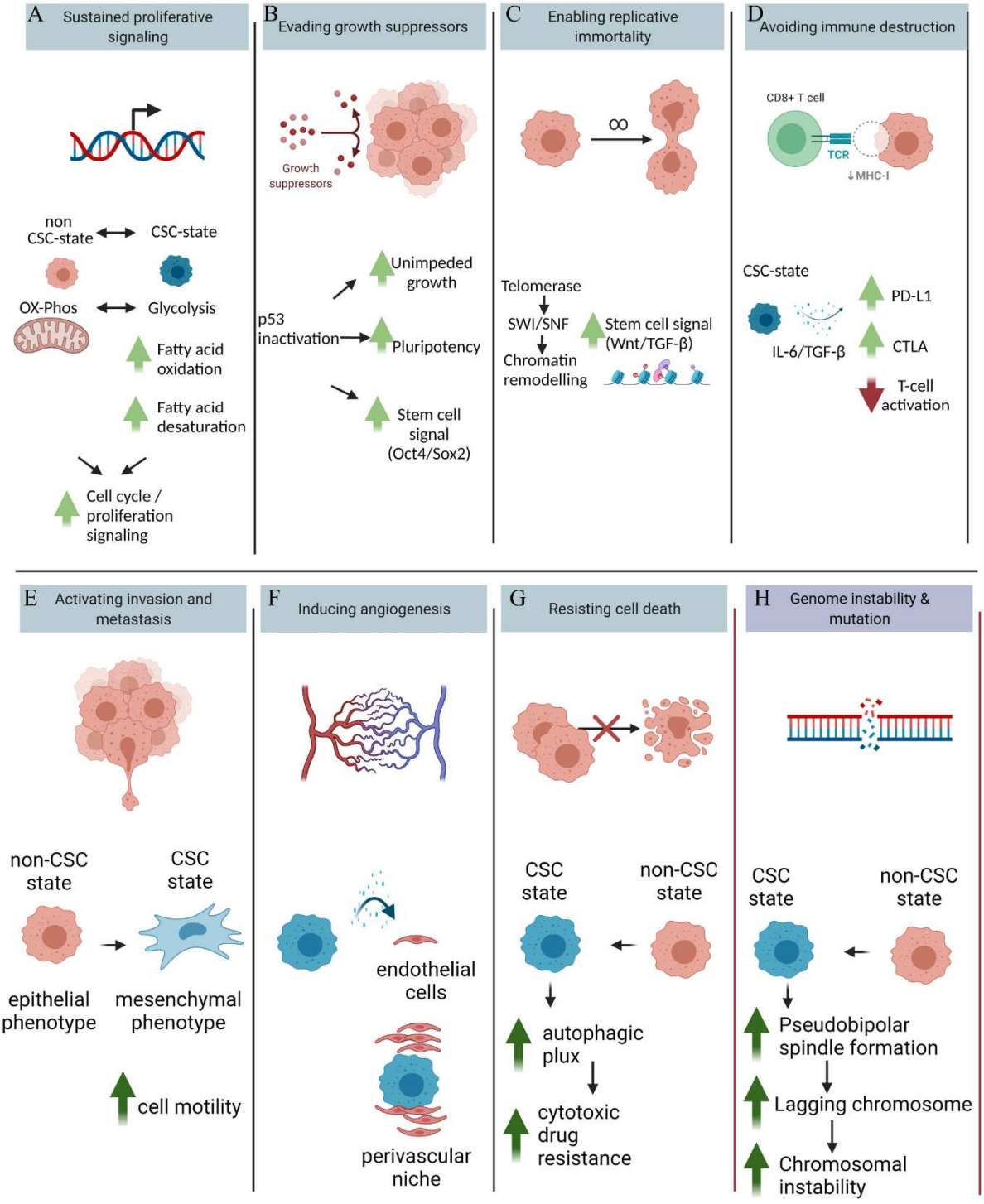
A Sustained proliferative signaling
non CSC-state
CSC-state
OX-Phos
Glycolysis
Fatty acid oxidation
Fatty acid desaturation
Cell cycle / proliferation signaling
B Evading growth suppressors
Growth suppressors
Unimpeded growth
p53 inactivation
Pluripotency
Stem cell signal (Oct4/Sox2)
C Enabling replicative immortality
∞
Telomerase
SWI/SNF
Chromatin remodelling
Stem cell signal (Wnt/TGF-β)
D Avoiding immune destruction
CD8+ T cell
TCR
↓MHC-I
CSC-state
IL-6/TGF-β
PD-L1
CTLA
T-cell activation
E Activating invasion and metastasis
non-CSC state
CSC state
epithelial phenotype
mesenchymal phenotype
cell motility
F Inducing angiogenesis
endothelial cells
perivascular niche
G Resisting cell death
CSC state
non-CSC state
autophagic plux
cytotoxic drug resistance
H Genome instability & mutation
CSC state
non-CSC state
Pseudobipolar spindle formation
Lagging chromosome
Chromosomal instability

Figure 3: The cancer stem cell phenotypic state modulates oncogenic hallmarks of cancer. Oncogenic properties are acquired through collective gains of cancer cell "hallmarks" required for malignant growth. Studies have shown that cancer cells that are in a stem cell-like phenotypic state manifests these hallmarks differently than cancer cells that are not in a stem cell-like phenotypic state **A)** Distinct metabolic programs drive cSCs proliferation compared to non-CSCs, such as switching between ox/phos or glycolytic mode of generating ATP, or the use of lipid metabolism. **B)** The central tumor growth suppressors such as p53 are also gatekeepers against cells acquiring pluripotency and the activation of stem cell signaling pathways, linking the stem cell state with increased avoidance of tumor suppressors **C)** Replicative immortality can be achieved through the activity of telomerase, which reverses telomere erosion that normally occurs due to the inability of cells to synthesize DNA sequences at the end of chromosomes. Recently, telomerase has been shown to directly promote stem cell signaling by activating chromatin remodeling complexes such as SWI/NSF. **D)** Cancer cells can better evade cell death by cytotoxic immune cells such as CD8 T cells and natural killer cells by upregulating immune checkpoint proteins such as PD-L1 and CTLA, which attenuate immune cell activation. Presently, there is evidence of a positive correlation between the CSC-state and the expression of immune checkpoints, suggesting that the CSC-state may favor immunosuppression. **E)** Metastasis is a multistep process that can be facilitated by acquiring several properties, including cell motility. The CSC-state is closely associated with the epithelial cell's plasticity to transition from epithelial to a motile mesenchymal morphology accompanied by increased cell motility. The bidirectional conversion between epithelial to mesenchymal states weakens lineage commitment and increases the likelihood of cancer cells to adopt a CSC-state. **F)** CSCs can secrete pro-angiogenic factors such as VEGF to stimulate endothelial cells via paracrine to establish a perivascular niche supporting the tumor microenvironment. **G)** Certain CSCs have increased autophagic flux, increasing their ability to metabolize cytotoxic drugs to avoid cell death. **H)** Increased genome instability and mutation is an emergent hallmark of cancer that genomic altering events in cancer gradually become easier to tolerate due to cancer-specific adaptations to tolerate the deleterious consequences of genomic insults. The impact of cancer stemness on this cancer hallmark is the main concept studied in the doctoral thesis (chapter 2), where our findings show that cancer stem cells can downregulate centrosome activity to facilitate pseudobipolar spindle formation, a type of mitosis that is highly prone to lagging chromosomes and chromosomal instability, leading to large-scale changes in genomic composition.

1.2.1 Proliferation

Sustainable proliferation is the most fundamental attribute of cancer. While CSCs are defined by long-term self-renewing potential, non-CSCs can often demonstrate superior short-term proliferation potential [9,11,12] [13,37]. Since proliferation tends to push cells towards differentiation intrinsically [10,11], stem cells require specific measures to ensure they do not lose differentiation potential, such as maintaining relative quiescence, asymmetrical cell division, or limiting expression of differentiation factors[56]. The stem-like state cannot be easily distinguished by the proliferation rate alone, though studies have shown that many CSCs rely on signaling pathways associated with developmental programs, such as Wnt/Beta-catenin [57-59], Notch [60] Hippo [61]. These pathways activate proliferation signals during embryonic or tissue development [62-65] and maintain crosstalk between stem cell identity regulation and proliferation signaling. The increased reliance on developmental pathways to drive proliferation, in turn, implies a reduced dependence on tissue-specific pathways (e.g., the estrogen receptor pathway in breast cancer cells), hence offers leeway for these endocrine tissue-derived tumors to develop resistance to anti-hormone therapy[66].

Cell proliferation is also dependent on sustainable energy sources. Recent studies have shown that CSC can exhibit distinct metabolism signatures that can be targeted[67]. The two main cellular pathways for generating energy (ATP) is glycolysis and oxidative phosphorylation (OXPHOS). Interestingly, the preferred metabolic program of CSCs appears to be tissue-specific: breast cancer and nasopharyngeal carcinoma CSCs rely on glycolysis [68,69], while CSCs in glioma, glioblastoma, lung, leukemia, and pancreatic CSCs rely on mitochondrial OXPHOS [70-73]. Similar parallels are also observable in normal stem cells; for instance, hematopoietic stem cells, in contrast to their more differentiated myeloid progenitor counterparts, uniquely rely on Lkb1-mediated OXPHOS for their maintenance [74]. There is also evidence that certain CSCs can reversibly switch between both metabolic programs: breast CSCs utilize AMPK-HIF1α and NRF2-thioredoxin pathways to evade the effects of glycolysis or OXPHOS inhibitors[75], and pancreatic CSCs use reciprocal activation of MYC and PGC-1α transcriptomic programs to acquire resistance to Metformin. Although notably, the pool of pancreatic cells with metabolic plasticity was smaller than that of cells with self-renewing capacity[72].

There is also evidence that CSCs can be distinguished by their dependence on lipid metabolic pathways, including fatty acid synthesis, oxidation, and desaturation in many types of cancer. Fatty acid synthesis via peroxisome proliferator-activated receptor-γ (PPARγ) and sterol

regulatory element-binding protein 1 (SREBP1) has been shown to be essential for the maintenance of breast and glioblastoma CSCs [76-78]. Meanwhile, fatty acid oxidation was rate-limiting for breast CSCs and promoted paracrine signaling from breast adipocytes [79]. Likewise, the nutritional sensor farnesoid x receptor (FXR) governs bile acid homeostasis and promotes fatty acid oxidation and Lgr5+ colorectal cancer stem-like cell proliferation [80]. The increased reliance on lipid metabolism may be related to activation of NANOG, a master regulator of the pluripotent state[81], since it appears to reprogram normal stem cells to use fatty acid oxidation, Acadvl, Echs1, and Acads [82].

Additionally, fatty acid desaturation via the stearoyl-CoA desaturase (SCD) enzymes is a central converging factor for multiple stem cell-specifically pathways such as Nanog, Wnt/Beta-catenin, and YAP/TAZ/Hippo, further implicating lipid desaturation as a critical functional biomarker for stem cells and CSCs [83-85]. However, stem cells/CSCs reliance on lipid metabolism may extend beyond needing an alternative energy source, as lipids also affect cell membrane fluidity. Desaturated lipids reduce membrane tension, potentially facilitating polarization, asymmetric division, and migration[86 87]. Cancer cells with "softer" membranes appear more tumorigenic [88], further supporting a mechanical function for lipid metabolism in CSCs.

1.2.2 Evading tumor cell growth suppressors

In normal tissues, proliferation signaling can be attenuated via proliferation-triggered senescence and growth-inhibitory factors[89]. Consequently, the inactivation of "master" growth suppressors occurs early during cancer development [89]. However, recent studies have demonstrated that these master tumor suppressors also have vital roles in limiting self-renewal and pluripotency in stem cell models, suggesting that these growth suppressors could also moonlight to limit cancer cells' stemness.

RB, the first discovered tumor suppressor, is best known for driving cell cycle-exit by inhibiting the E2F transcription factors [90]. However, aside from the cell cycle, RB can also regulate cell differentiation through Runx2 and PPAR-gamma [91,92]. Furthermore, in induced pluripotent stem cell models, RB has also been found to regulate chromatin conformation of pluripotency genes to limit cellular plasticity [93].

p53 is another critical tumor suppressor whose function is abrogated in most cancer; it is usually activated in response to DNA damage, oncogene activation, hypoxia [94]. While initially viewed as a safeguard mechanism against DNA damage to avert oncogenic mutations, more recent studies on the subtle roles of P53 in stem cell development have raised intriguing new parallels between the stem cell state and tumorigenesis. The importance of p53 to the stem cell state is perhaps surprising, given that *Trp53* null mice are viable, though they will generally develop spontaneous tumors within ~18 months [95]. However, five independent studies published in 2009 (reviewed in[96]) irrevocably showed that p53 inactivation potentiates the process of generating induced pluripotent stem cells (iPSC) from more differentiated cells. In addition to inhibiting pluripotency, other studies found p53 to limit cell quiescence[97] and asymmetrical division [98]. As such, there is copious evidence that activation of p53 in stem cells limits stem cell-like properties, raising the possibility that it may similarly also limit stemness in cancer cells. A prove of principle study in breast CSCs found that p53 is required to repress the expression of CD44 – a cell surface marker that is commonly associated with the cancer stem cell phenotype. The repression of CD44 is, in return, critical to the growth-inhibitory effects of P53[99]. Moreover, in thyroid [100], breast [101], and liver cancer [102], p53 mutation or inactivation correlated with a dedifferentiated or stem-like phenotype.

As the functions of classical tumor suppressor genes continue to be studied, it becomes increasingly clear that they function with a complex interdependent network of metabolic regulators and stem cell signaling. For instance, it has been shown that Oct4, a master regulator of pluripotency, promotes deactivation of p53 via Sirtuin-1 - a deacetylase that is also integral to metabolic pathways [103], illustrating how activation of a stem cell program could limit the tumor-suppressive functions of p53 through altering the cell metabolic state. Another study in pancreatic cancer showed that the pluripotency regulators Sox2 and Myc can drive a tumorigenic metabolic program because p53 function is ablated. Thus, the gradual acquisition of stem cell-like properties may be an invariable outcome of cancer progression given the extensive crosstalk between stem cells and collectively, assuming that the weakening of tumor-suppressive barriers is a prerequisite to cancer growth tumor-suppressive factors.

1.2.3 Resistance to cell death

Programmed cell death (apoptosis) is a physiologically critical mechanism to ensure tissue homeostasis by removing damaged, infected, or excess cells [104]. Cell death can be triggered following stress, nutrient deprivation, infection, or intracellular damage and elicits a programmed response either via extrinsic signals (i.e., via Fas ligands/receptors) or intrinsic signals (e.g., caspases) and are counterbalanced by anti-apoptotic factors (e.g., Bcl-2) [104]. Hyperactivation of many oncogenes, such as Myc, would trigger apoptosis without anti-apoptotic factors [105]. There is considerable variation in both pro and apoptotic signals reflecting the wide range of challenges that a cell experiences. Many of these apoptotic regulators have roles in mitochondrial maintenance, as it is mostly the permeabilization of the mitochondrial outer membrane that mediates intrinsic apoptosis pathways. As previously stated, CSCs often exhibit distinct metabolic requirements, and as such, it is unsurprising for them to display differential sensitivity to apoptotic factors. For instance, human leukemia stem cells were found to require high levels of Bcl-2 to balance a low rate of reactive oxygen species, thus sensitizing this population to apoptosis when Bcl-2 is inhibited [73].

While apoptosis induces cell death, its primary function is to ensure tissue homeostasis. Consequently, in principle, the net goal of triggering apoptosis should be maintaining a constant number of cells. At least in epithelial cells, this is accomplished via apoptosis-induced proliferation, a compensatory mechanism where dying cells secrete mitogens such as epithelial growth factors, IL-6, and Wnt to stimulate proliferation of neighboring cells [106,107]; this is further supported by evidence that in many cases, dying cells, even the ones fated to be eventually removed, remain metabolically active for some time [108]. Multiple factors in stem cell maintenance have been implicated in apoptosis-triggered proliferation, including Hedgehog, Notch, and Jak-STAT3. These pathways allow tissue regeneration after injury through the apoptosis-triggered proliferation of tissue-resident stem cells. Given the parallels between tissue regeneration and tumorigenesis, it is conceivable that apoptosis-induced proliferation is highly relevant to oncogenic growth, as cancer cell growth is often dependent on similar secretory profiles as those seen during apoptosis-induced proliferation [109,110].

A crucial link between apoptosis-induced proliferation and CSC propagation is the c-Jun N-terminal kinases (JNK). JNK, and its interactor p38 MAPK, are critical regulators of both

extrinsic and intrinsic apoptosis signaling [111] and are shown in *Drosophila* and animal disease models as required for apoptosis-induced proliferation [112]. JNK also promotes the CSC phenotype in glioma, glioblastoma [113], triple-negative breast cancer [112], and normal stem cells. A recent genome-wide CRISPR screening identifies the JNK pathway as a critical factor in limiting ESC differentiation into the endodermal lineage by co-occupying ESC enhancers OCT4, NANOG, and SMAD2/3 to prevent their dissociation, thus forcing the ESC to maintain its pluripotency[114]. Aside from these activities, JNK also frequently converges with WNT signaling to regulate differentiation [115]. It remains to be formally elucidated how JNK's regulation of stem cell identity interacts with its role in regulating apoptosis. This connection is complicated by JNK's role in regulating the inflammatory response, which itself is also a function that controls the pro/anti-apoptosis signaling via paracrine signaling, as evidenced by IL-4's anti-apoptotic activities for maintaining colorectal CSCs[116].

Another form of cell death that is pertinent to CSCs is anoikis. Anoikis, like apoptosis, is a form of programmed cell death and is triggered in response to the loss of anchorage from the extracellular matrix. Given that CSCs are often characterized by their capacity to grow in low-attachment conditions as spheroids, those cells must intrinsically be anoikis-resistant. Mechanistically, anoikis resistance arises, in part, from overexpression of c-FLIP - a caspase and TRIAL antagonist that is generally downregulated during cells detach [117,118]. Breast CSCs are shown to have innately upregulated c-FLIP, which confers them resistant to TRIAL-mediated anoikis/apoptosis[117,118]. Acquisition of a mesenchymal phenotype, including upregulation of transcription factors Snail and Twist, is very common in CSCs [119] and has been found to contribute to anoikis resistance [120]. Lastly, studies have shown that CSCs could also promote anoikis resistance via secretion of anti-apoptotic factors such as IL-6 [119]. Consequently, the CSC-state appears to confer distinct survival advantage under adhesion-free growth, likely contributing to their capacity to self-renew under spheroid conditions.

Activation of pro-apoptotic pathways can be averted by multiple cell-intrinsic mechanisms to tolerate stress and insults, most notably are the components that contribute to: "DNA damage response," the "unfolded protein response," and "autophagy."

DNA is structurally sensitive to spontaneous hydrolysis reactions causing cytosine to be converted to uracil and susceptible to damage via oxidative species and radiation, thus requiring constant repair[121]. Multiple DNA pathways exist, including non-homologous end joining,

homologous recombination, nucleotide excision repair, base excision repair, and mismatch repair to address these various DNA lesions. When facing DNA damage, stem cells need to balance rapid cell death for genome integrity conservation versus upregulation of anti-apoptotic factors for the stem cell pool rescue. Many studies across different types of somatic stem cells have revealed that the mechanism, response, and consequences vary greatly among stem cells originated from different tissues, which is partially due to the different environments imposing unique challenges to those stem cells. For instance, epidermal stem cells that are constantly bombarded with ultraviolet radiation are more resistant to DNA damage than intestinal stem cells, which readily undergo apoptosis in response to DNA lesions. Some evidence suggests that CSCs from breast and glioblastoma are resistant to radiation therapy[120-122] and possess better tolerance against DNA damage via a more robust activation of DNA-damage checkpoint proteins [122,123]. However, a more transparent connection between DNA repair pathways and the stem cell program has not been established yet.

Autophagy – the cellular process of "self-eating" to recycle organelle and proteins into biomass - is a fundamental mechanism for cell survival that has received considerable attention recently. Three forms of autophagy are known to exist: chaperone-mediated autophagy, microautophagy, and macroautophagy (the process where double-membrane vesicles form around a section of the cytoplasm and deliver their content to autophagosomes; from here on called "autophagy"). Autophagy has a complex relationship with apoptosis; although autophagy alone can promote cell death, in some cases, autophagy operates in concert with apoptosis. While in other cases, autophagy serves as a survival mechanism to prevent the activation of apoptotic pathways [124,125]. Interestingly, in the context of stem cells, autophagy is more often found to be protective, though autophagic-cell death does also occur [126]. In hematopoietic stem cells (HSC), autophagy is critical under fasting or cytokine withdrawal [127]. Inhibition of autophagy in aged HSCs prevents the degradation of excess mitochondria, resulting in an active metabolic state that promotes HSC depletion through induced differentiation [128]. In mesenchymal stem cells, basal autophagy levels decrease following differentiation [129] and protect against irradiation injury [130]. Likewise, many studies in CSCs also found autophagy to be protective such as protecting CD133+ liver CSCs against nutrient and oxygen deprivation [131] and colorectal CSCs against chemotherapy [132]; likewise, inhibition of autophagy via compounds such as chloroquine usually result in depletion of the CSC population[133,134].

Closely related to autophagy is the unfolded protein response: a mechanism of quality control that ensures protein integrity. As a convergent point for multiple sources of cellular stress, activation of the UPR triggers activation of several pathways (PERK, IRE1, and ATF6) to halt protein synthesis, induce degradation of misfolded proteins, and upregulate chaperone proteins to restore endoplasmic reticulum homeostasis. Hematopoiesis models revealed that HSCs, in contrast to their progenitors, are highly sensitive to UPR-induced cell death, indicating a low tolerate for misfolded protein in the stem cell compartment [135]. Consistent with this, activation of UPR causes CSCs to differentiate and lose stem cell properties [136,137], though notably, UPR-induced CSC differentiation does not necessarily involve cell death.

In summary, there is copious evidence that the CSC-state is associated with altered sensitivity to cell-death triggers. Assuming that CSC and non-CSCs are interconvertible states, any cytotoxic treatments administered on a heterogeneous cancer model need to be effective against both states to eradicate cancer successfully.

1.2.4 Replicative cell immortality

The replicative lifespan of a normal cell is limited to around 50-70 cell divisions [138]. Due to the eventual shortening of the telomeres, the guanine-rich DNA repeats at the end of linear chromosomes that maintain chromosome stability. The telomeres of somatic cells are gradually shorter after each cell division due to the inability of the DNA replication machinery to fully replicate the 3' end of DNA, thus contributing to aging. Stem cells and cancer cells overcome this limit via activating telomerase to restore eroded telomeres. Somewhat paradoxically, telomeres shortening can also be oncogenic [139,140] as the shortening of telomere leads to loss of chromosome-capping, resulting in chromosome instability and mutagenesis.

Reactivating telomerase to gain replicative immortality can be considered one of the first stem cell-specific properties that cancer cells acquire. Despite this apparent connection, evidence that telomerase activity contributes explicitly to the CSC phenotype or that CSCs have distinct telomere length from non-CSCs is sparse. Indirectly, inhibition of telomerase activity has been shown to selectively eliminate CSCs in a few cancer models, including ALDH+ lung CSCs, CD24-CD44+ESA+ breast CSCs, CD24+CD44+ESA+ pancreatic CSCs [141,142], and in glioma stem cells[143].

Intriguingly, it has become increasingly evident that telomerase activity is not limited to its DNA elongation function but also has additional roles in regulating the transcriptomic state of the cell. In mouse epidermal stem cells, telomerase activation has been shown to directly modulate the SWI/SNF chromatin remodeling proteins and Wnt complex to regulate stem cell activity in mouse gastrointestinal tract [144]. Similar non-telomere specific roles of telomerase were found in CSCs, where the hTERT enhances the self-renewing properties of GCSCs by activating EGFR [145] or by enhancing the TGF-β and β-catenin pathways in gastric cancer [146], and via c-Myb in glioma cancer[143]. The non-reverse transcription role of telomerase gives further evidence that stemness arises from integrating all the individual molecular programs associated with stem cells. As such, reactivation of telomerase in cancer may be an early step towards acquiring cancer stemness.

1.2.5 Angiogenesis

The development of the tumor microenvironment will necessitate vascularization to offer nutrient support and waste disposal. Typically, this process occurs via the differentiation of endothelial cells (vasculogenesis) and the branching expansion of existing blood vessels (angiogenesis). Both vasculogenesis and angiogenesis occur very early during embryonic development [147] and early tumor development stages, sometimes before any histologically evident malignancy [148] [149]. Angiogenesis is regulated by pro (e.g., vascular endothelial growth factors, VEGF) and anti-angiogenic (e.g., thrombospondin 1, TSP1) factors, ensuring that vascular branching is triggered only transiently to injury in normal tissues. Hypoxic conditions and oncogenic signaling drives activation of pro-angiogenic factors, resulting in excess and enlarged vessels[150,151].

Tissue-resident stem cells play an intimate role in driving the formation of blood vasculature. The connection between angiogenesis and the CSC phenotype is supported by observations that pro-angiogenic factors promote cancer stemness. CSCs often reside in a "perivascular niche" adjacent to endothelial cells [152-154]. For instance, CD34+ epithelial CSCs express high VEGF levels, which helps maintain the tumor microenvironment through two modalities: via paracrine signaling on endothelial cells to promote the perivascular niche and via autocrine signaling to upregulate CSC self-renewing properties. Similar findings were reported in CD133+ hepatocellular carcinoma CSCs, which were found to self-renew via the VEGF-VEGFR2 pathway leading to downstream activation of Nanog [155-157]. Endothelial cell-to-CSC

communication appears to be supported by other key regulators such as Notch, Hedgehog, and Stat3[158]. Reciprocally, the pro-angiogenic factors secreted by CSCs benefit the expansion and activation of those endothelial cells, thus constituting an interdependent relationship between endothelial cells and CSCs [159]. Perhaps more remarkably, the observation that many endothelial cells in glioblastoma carry the same genetic alterations as cancer cells confirms that endothelial cells could be derived from glioblastoma cell transdifferentiation [160]; this "vascular mimicry" has also been described in breast cancer, melanoma, and colorectal cancer [161-163].

Pericytes are cells that wrap around the endothelial cells and regulate blood vessel stability and homeostasis via contact-mediated and paracrine signaling. Pericytes share many similarities with mesenchymal stem cells, both fibroblast-like, have multilineage potential, and the identity of pericyte and mesenchymal stem cells often overlap [164] [165]. Perhaps the most direct evidence of CSCs supporting the vasculature of the tumor microenvironment was when it was found that CSCs can differentiate into pericytes just as they can be made into endothelial cells; fluorescence in-situ hybridization analysis of pericytes in primary glioblastoma tissues confirmed the familiar presence of cancer-associated genetic alterations within glioblastoma-associated pericytes, confirming that cancer cell transdifferentiation into functional pericytes occurs in primary human tumors **[166].** Importantly, it has been shown that pericytes derived from glioma stem cells form tight junctions around tumor-infiltrating blood vessels, limiting the delivery of chemotherapy drugs [167].

Somewhat paradoxical to the notion that endothelial cells and vascularization (high O2/nutrient) are interdependent with CSCs is the observation that the hypoxic niche (low O2/nutrient) also supports CSC maintenance. [122] [168,169]. The hypoxic conditions favor the reprogramming of cancer cells towards a stem-like state, as the quiescence and metabolic plasticity are favorable traits to survive nutrient-scarce conditions. Hypoxic conditions can trigger the secretion of pro-angiogenic factors via a negative feedback response, suggesting that CSCs in the hypoxic niche could promote the maintenance of the perivascular niche [159]. The potential interplay between CSCs of different niche compartments is not well understood but is likely to reveal key insight into the dynamic formation of the tumor architecture.

1.2.6 Activation of cancer cell invasion and metastasis

Metastasis is a multistage process involving local invasion, intravasation into nearby blood vessels, surviving the vascular system, and eventually colonizing a new site. CSCs acting as seeds

for tumor growth at distant destinations is unsurprising; after all, the self-renewing properties of CSC make them conceptually ideal for initiating tumorigenesis. Indeed, measurement of cancer cell's capacity to initiate tumorigenesis via methods such as the limiting dilution transplantation assay remains the golden standard for functionally measuring stemness[170].

Beyond tumor seeding at the distal sites, the stem-like phenotype is also implicated in earlier stages of cancer metastasis, such as invasion and intravasation. Physiologically, normal stem cells acquire motile features to fulfill their function during development and tissue regeneration. Epiblast cells during gastrulation acquire this motile phenotype to ingress and differentiate into mesodermal/endothelial layers. Likewise, neuroepithelial cells are mobilized during neural crest delamination to give rise to the different layers of glial and neuronal cells [171]. This mobile state is also observed during wound-healing of injured tissues; for instance, activation of liver stem cells (which have high tissue telomerase activity) results in their spreading throughout the liver tissues to regenerate the damaged organ[53]. The enrichment of stem cells by transdifferentiation programs shared by stem cell wound-healing activities offer an attractive framework to understand why cancer stem cells can be induced under conditions of cellular stress.

The programmed acquisition of cell motility by stem cells and CSCs-alike is enabled by a developmental program called epithelial-mesenchymal transition (EMT). As the name implies, EMT refers to a phenotype shift from an epithelial-like state (E-state), where cells exhibit tight cell-cell junctions and apical-basal polarity, to a mesenchymal state (M-state) characterized by front-rear polarity, reduced cell-cell adhesion, and greater motility[171]. The EMT program was strongly implicated to play a role in cancer metastasis based on the observation that cancer cell models with invasive potential often exhibited traits of mesenchymal cells and reduced levels of epithelial markers, particularly E-cadherin [172,173]. The first evidence that EMT and the CSC-state are linked is via the seminal studies in mammary gland models, which showed that inducing EMT via overexpression of specific transcription factors (Snail, Twist) or treatment with TGF-β can induce the cells to acquire stem cell properties such as expression of CD24-/CD44+ surface markers, tumor seeding potential, and tumorsphere growth[174]. Similarly, it was found that the EMT transcription factor Snail2 (Slug) plays a role in the self-renewal capacity of mammary stem cells, the loss of which will promote differentiation into the epithelial lineage, illustrating the connection between EMT and stemness in both stem cell and CSC context [175]. It is important to stress one important caveat regarding EMT: the lack of formal evidence that traces the entire process of a

single epithelial cancer cell undergoing EMT at the primary tumor followed by reinitiating MET at the colonization [176]. Thus, this plasticity-driven model of metastasis is currently supported by primarily indirect/circumstantial evidence.

At its core, EMT involves activating several key transcription factors, including Snail, Twist, and Zeb, in conjunction with microRNAs and epigenetic factors to reprogram the cell. The overall process bears a striking resemblance to CSC re-programming into distinct lineages and hierarchies (discussed in Chapter 1). Indeed, many EMT-promoting transcription factors such as Twist and Zeb1 have also been shown to modulate stemness, propagation, and tumorigenesis directly. For instance, Twist1, a prototypical EMT-inducing transcriptional factor, has been carefully dosed to show that lower levels of Twist1 were sufficient to promote cancer cell proliferation, whereas higher doses of Twist1 induced EMT[177]. Moreover, Twist1 and Zeb1 promote EMT and stemness through regulating the chromatin silencing factor Bmi1 via microRNAs (specifically miR-200) to [178] [179] [180]. Due to these functional crossovers, the line between EMT-promoting transcriptional factor and a CSC-promoting transcriptional factor cannot always be delineated.

Reprogramming fibroblasts (M-state committed cells) into iPSCs can offer clues regarding EMT and the CSC-state connection. Overexpression of the pluripotency factors of Oct4, Klf4, Sox2, and c-Myc drives fibroblasts into iPSC state over several weeks, throughout which extensive morphological and epigenetic changes occur. Notably, fibroblast dedifferentiation into the iPSC state requires the cell first to enter a transitory epithelial state [181]. Overexpression of pro-EMT factors forced iPSC to commit to M-state, which resulted in a reduction of stemness[181]. Since EMT also promotes the emergence of stem-like properties in cells that begin in the E-state, these observations collectively suggest that the transition process between E and M state drives dedifferentiation and acquisition of stemness. Further evidence emerged in breast cancer models where E-like and M-like CSCs can be isolated from the same cell model, supporting that stemness is not intrinsically tied to either state [182].

The plasticity of EMT/MET is exemplified by the reversibility of the process and the existence of multiple "intermediate" stages [183] between being completely E or M-states. [171,184,185]. This transitory E-M hybrid phenotype could be observed during development, where certain stem cells acquire a motile phenotype while maintaining some degree of cell-cell adhesion with neighboring cells [184-188]. In the context of cancer, these hybrid E-Ms are often reported to be more

metastatic than either fully E-committed or M-committed cells, with the highest degree of malignancy found in hybrid cells that are biased towards the E-state [183,189], [176]; these findings support the notion that the capacity to transition between both states is ideal for the entire invasion-metastasis cascade [171,183-185]. Notably, in a squamous cell carcinoma model, it was shown that although the stemness and metastatic potential are higher in the hybrids, the tumor initiation potential is similar among the hybrids and the M-committed cells, supporting the notion that tumorigenesis is acquired earlier in the cancer progression process than plasticity and metastatic potential[183]. Generally, the M-state has been linked to better invasiveness and survival of cancer cells in circulation while the E-state is linked to superior macro-metastasis colonization; simultaneously, hybrids exhibit the advantages of both states[190-192]. In accordance, cancers expressing both epithelial and mesenchymal markers appear to have the worst prognosis [193]. This continuum-model of E-M states may also explain the puzzling observation that sarcomas (mesenchymal-like cancers to begin with) can still undergo further EMT to acquire invasive properties[194 195]. Overall, these findings highlight that the EMT program combined with stem-like plasticity form a deadly paradigm of heightened metastatic dissemination.

Remarkably, it appears that rather than being randomly distributed, each different E-M intermediate resides in distinct niches within the tumor microenvironment, with E-state cell regions being relatively devoid of endothelial, inflammatory, and immune cells relative to M-state and E-M hybrid regions. The degree of stromal cell integration correlated with cytokine levels secreted in each region and is consistent with the extensive list of studies showing the importance of paracrine signaling (fibroblasts, mesenchymal stem cells) in driving EMT and stemness [196,181,197]. In another study in head and neck carcinoma, cells exhibiting partial-EMT were also shown to have higher invasive potential and stemness and resided at the invasive front[198]. In summary, although the details are unclear, there is strong evidence that loosening of lineage-commitment from either EMT or EMT raises cancer cell stemness and metastatic potential, implicating CSCs as a critical target in the development of anti-metastatic treatment.

1.2.7 Escaping tumor immunosurveillance

Immune cell's ability to recognize and eliminate neoplastic cells has been speculated over a century ago[199]. Transcriptomic analysis revealed that across multiple cancer that gene signatures associated with "stemness" predict a reduced anti-tumoral immune response[200]. Although the

causative link between CSCs-state and immunoregulation is not fully elucidated, evidence shows that CSCs adopt a multifaceted approach to promote the immunosuppressive state: quiescence, downregulating antigen-presenting pathways, and secreting of immunosuppressive factors, are identified.

Studies conducted using normal stem cells support the notion that CSC would be intrinsically equipped to evade immune surveillance due to quiescence. Recently, it has been shown that T-cells will generally eliminate cycling stem cells while sparing quiescent ones in the intestine, breast, and ovary[201]. This finding links quiescence, a property indeed manifested by certain cancer stem cells, to immune evasion[202]. Due to their disposition for maintaining quiescence, it is speculated that CSCs are the earliest cancer cell variants with immune evasion capacity.

Emerging studies also reveal that CSC/EMT programs can modulate the expression of immune suppressive proteins, such as PD-L1 and CTLA-4, on the cancer cell membrane. For instance, glioblastoma stem-like cells showed downregulated antigen-presenting major histocompatibility complex (MHC), induced self-antigen pathways, and antigen-processing machinery [203]. In general, Wnt, STAT3, and HGMA have been proven to regulate PD-L1 expression; moreover, a reciprocal relationship has been observed between PD-L1 and CSC-marker expression in breast, lung, colorectal, and head and neck cancers [204] [205,206] [207,208]. In return, the presence of PD-L1 is also required to express the pluripotent stem cell factors Nanog and Oct4[209]. More recently, an in-depth investigation using single-cell RNA-seq and lineage tracing has shown that TGF-β activation causes upregulation of CD80 – a CTLA ligand, to dampen T cell activation [210]. The downregulation of antigen-presenting factors may be closely related to quiescence, as quiescent stem cells have been shown to downregulate MHC on the cell surface compared to cycling cells[201].

Lastly, just as CSCs play a role in modulating the activity of endothelial cells and fibroblasts, there is also clear evidence that CSCs could form an interdependent relationship with tumor-infiltrating immune cells, including monocytes/macrophages, neutrophils, and myeloid cells [211-213]. In general, many cytokines that induce stem cell properties in cancer (e.g., IL-6 and TGF-β) are immunosuppressive [174,214] [215,216]. The secretion of these cytokines by CSCs help recruit innate immune cells to form a homeostatic state that permits the establishment of CSC-niche; reciprocally, immune cells (e.g., dendritic cells) secrete cytokines (e.g., CXCL1) which can

promote transcriptional activation of pluripotency pathways (e.g., NANOG, OCT4, SOX2, MYC) to enhance the CSC phenotype [217].

1.2.8 Current status of targeting cancer stem cells as a therapeutic

From the perspective of targeting CSCs as a therapeutic approach, a longstanding challenge has been to identify them within cancer patients. In cell lines, markers including CD24, CD44, CD133, aldehyde dehydrogenase, and EpCAM are widely used to infer the CSC phenotype of marker-positive cells; however, these markers are not 100% definitive [19-23], and the reliability of these markers vary among cell lines from the same cancer subtype. Monitoring the CSC content of patient tissues by markers alone would require many rounds of invasive biopsies. Furthermore, since stemness also requires extensively phenotypic validations in addition to marker-based measurements, it is largely unfeasible to assess these traits in real cancer patients at the time of their diagnosis.

There is also little progress in translating therapies that are selective against CSCs in cellular models into clinical applications [218,219]. A major reason for this lack of success is that many clinical-based studies were initiated prematurely before the biological understanding of CSCs is adequate. For instance, companies such as OncoMed and Verastem were founded in the early 2000s following the initial identification of cancer stem cells in solid tumors and quickly initiated several clinical trials to test the efficacy of small molecules selectively target CSCs, such as the focal adhesion kinase inhibitor VS-6063 (defactinib) [219,220]. The proposed outcome of using anti-CSC therapy was to eliminate the tumor by depriving them of cells offering long-term sustenance; thus, it would offer slower tumor shrinkage than conventional therapy but with the merit of less relapse. Instead, the efficacy of the monotherapy was, at best, a modest response, which exposed several flaws of CSC-targeted therapy. First, there is the difficulty mentioned above in teasing out the clinical effect of targeting CSCs. Most candidates targeted known oncogenic pathways such as FAK, Notch, or DLL3, so their clinical effects could have been due to inhibition of tumor growth in general and not related to targeting CSCs [218,219]. Secondly, the rationale for CSC-targeted treatment is rooted in the original CSC model, which worked under the assumption that *only* CSCs are drivers of tumor growth, metastasis, and relapse. As more biological studies on CSCs emerged, it became evident that the promise of targeting CSCs alone would prevent tumor metastasis/relapse is faulty because 1) these aggressive features also manifested to a lesser extent in non-stem-like

cancer cells and 2) the potential of dedifferentiation, which allows non-CSCs to regenerate CSCs via cancer cell plasticity [218,219].

Overall, the unmet expectations with the initial rounds of anti-CSCs therapy undermined the enthusiasms for the field; however, recent advancement in a basic understanding of CSC biology, with the help of single-cell sequencing and better visualization of rare cell populations, may yet lead to a renaissance for the field in the future.

1.3 Asymmetrical cell division in stem cells and cancer

The notion that cancer hallmarks are drastically altered in cancer cell variants possessing stem cell phenotypes is strongly supported by literature evidence (reviewed in segment 1.2). Perhaps ironically, the oncogenic functions of the actual "phenotypes" associated with stemness are poorly understood due to difficulties in conducting controlled studies on those phenotypes without affecting other cellular functions. Multiple phenotypes are canonically associated with stem cell identity, including self-renewal, plasticity, and asymmetry; presently, the asymmetrical aspect of stem cell identity is arguably the least understood in the context of cancer progression.

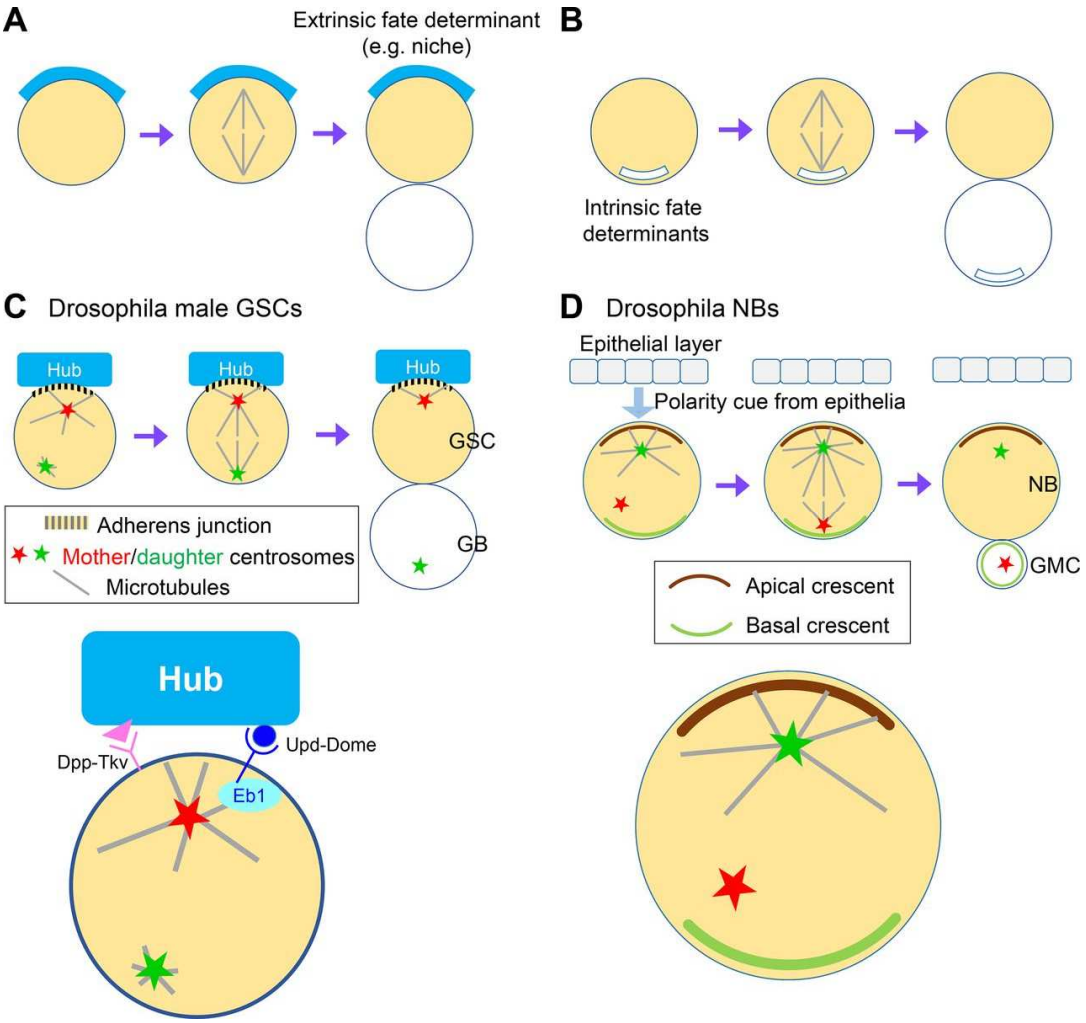

Figure 4: Principles of asymmetrical cell division. Asymmetrical cell division is driven by A) extrinsic factors originating from outside the cell (such as by paracrine factors secreted by the stem cell niche) or B) intrinsic factors originating from inherent asymmetries present within the stem cell itself. Much of the study of asymmetrical cell division is conducted in *Drosophila* models. In *Drosophila* germline stem cells (GSC), the GSCs interact with the stem cell niche (or "hub cells") via adherens junctions. The hub cell secretes factors such as Dpp and Upd to dictate the organization of astral microtubules (microtubules that extends from the centrosomes to the cortex of the cell membrane) to dictate the positioning of the centrosome and the orientation of the mitotic spindle. In *Drosophila* neuroblasts D) cell-fate determinants are intrinsically segregated to two cell poles during interphase based on polarity cues from the epithelial cell layer. These polarized fate-determinants (e.g., Par3/par6) captures microtubules emanating from one specific centrosome (e.g., daughter centrosome) to direct the mitotic spindle parallel to the apical-basal axis. Asymmetrical cell division self-renew the neuroblast while generating a ganglion mother cell (GMC). The image is reproduced from Emerging mechanisms of asymmetric stem cell division by Zsolt G Venkei and Yukiko M Yamashita, Journal of Cell Biology (2018) [221] with permission from Rockefeller University Press.

1.3.1 Cell division asymmetry is a fundamental property of stem cells

In stem cells, asymmetrical cell division (ACD) is a choreographed process where one cell division yields two daughter cells with distinct cell fates. It is fundamental to all kingdoms of life, ranging from prokaryotes (bacteria, yeast, flagellates) to more complex multicellular organisms. In unicellular organisms, ACD must partition the old or damaged ribosomal DNA and proteins into one cell while rejuvenating another, thus maintaining the long-term proliferative potential of the organism [222-224]. In more complex multicellular organisms, this asymmetry is essential during development for enabling a single fertilized egg to self-renew and differentiate into distinct cell lineages and maintain tissue homeostasis in adults by maintaining a stable pool of tissue-resident stem cells[222-224]. Disruption of ACD has been linked to both stem cell depletion and cancer [225].

ACD was initially recognized as a mechanism for maintaining tissue homeostasis. By dividing strictly asymmetrically to generate one stem cell and one non-stem cell, the stem cell can produce differentiated progenies without a net change in stem cell numbers. However, studies on stem cell population dynamics during development and in adult tissues has challenged this premise with a different "population asymmetry" model, which proposes that homeostasis in stem cell population within tissues is instead maintained at the population level via "stochastic" (randomly determined) transitions between stem-like and non-stem-like state utilizing a combination of ACD, symmetrical self-renewing (producing two stem-like daughter cells), and symmetrical differentiating (producing two non-stem cells), with each stem cells having the equipotent capacity to transition between these states [226-228]. Under such a model, some stem cells could become depleted (symmetrical differentiating). In contrast, others become expanded (symmetrical self-renewing), with the probabilities of these events balancing each other out to maintain a stable pool of stem cells.

Asymmetry applies to a set of differential assets or properties inherited by the two daughter cells ranging from size, differentiation status, proliferation potential, old-new cellular components, epigenetic factors, and positioning within the tissue architecture [222-224]. Studies in *Caenorhabditis elegans*, *Drosophila*, and mammalian cells have collectively elucidated many different paradigms under which asymmetry is generated, maintained, and amplified, and together indicate that the "core frameworks" of ACD are well-conserved among different organisms. This core framework refers to a specific set of events that eventually lead to ACD: an

initial (intrinsic or extrinsic stimuli) breaking cellular symmetry, leading to polarization and asymmetrical partitioning of fate-determinant factors during interphase, which is then finalized by the establishment of the mitotic spindle and cytokinesis perpendicular to the plane of polarization such that the two asymmetrical sides are partitioned into different progenies [222-224].

Cell polarity-driven asymmetry should be distinguished from "left-right" (LR) asymmetry, another form of asymmetry that arises from the chirality of the molecular building blocks. Microtubules, for instance, are helical structures that can have chirality (non-superimposable mirror images), and therefore are intrinsically asymmetrical at the molecular level [229]. The impact of this asymmetry is demonstrated in the case of the bacterium flagellum; Due to the asymmetry of the helix, a counter-clockwise rotation will hydrodynamically bundle the individual flagellar filaments causing a straight-line motion, while the reverse clockwise spin will cause uncoordinated motions of the filaments, leading to dissociation of the bundle thus results in random "tumble" motion [230]. Unlike polarity-based asymmetry, which involves blatant segregation of factors into two extreme ends, the impact of left-right asymmetry is much more subtle. However, this molecular chirality has propagating effects on all cell levels (e.g., the microtubules being chiral causes the mitotic spindle to also be chiral) [231], which can bias the rotational movements cell within a 3D environment [232]. For instance, the importance of left-right asymmetry is best understood in the context of cardiac tissue morphogenesis, where chirality contributing to cell rotational bias appears to be essential for direct the "looping" of the tubes within the heart [233].

It is especially noteworthy that the basal bodies/centrioles – the organization centers of microtubules, consistently exhibit the same chirality across all known organisms, and there is recent evidence that this intrinsic chirality within the centriole/basal body can cause the emergence of polarity in the absence of spatial cues [234]. While the chirality of cells remains an emerging and poorly understood property, an important implication of these intrinsically chiral centers is that asymmetry in cells never has to be generated *de novo* and could instead be amplified from these subtler differences.

1.3.2. Breaking cell division asymmetry

The initial signal that breaks symmetry varies from intracellular fate determinants to environmental stimuli (e.g., cytokines). Extracellular stimuli are generally contributed by a stem

cell niche such as the basal layer of an epithelium sheet [221,225]. The niche can act as a positioning cue to direct ACD, such that stem cell identity is only retained in the daughter cell close to the niche after division. This paradigm is best studied in *Drosophila* germline cells, where the niche is comprised of non-dividing "hub" cells that secrete the ligand "Unpaired" (Upd, an analog of Jak/STAT ligands), and Decapentaplegic (Dpp, analog of bone morphogenic protein, BMP, ligands) [235] [236] [237]. Aside from paracrine signaling, the extrinsic cues could also be in an extracellular membrane and basement membranes [238], or mechanical forces (e.g., membrane stiffness) [239].

While these extrinsic signals help direct and facilitate polarization, stem cells are observed to undergo asymmetrical division in culture in the absence of extrinsic factors, indicating that the cell-intrinsic polarity – often tied to developmental programs - can be sufficient to drive asymmetrical division [240] [241]. The best-studied model for the intrinsic generation of asymmetry is the *Drosophila* neuroblast. Cell division is preceded by the polarization of several identified fate-determining factors, including Numb, Prospero, and Brat will prim the daughter cell eventually differentiate into the ganglion mother cell [242] [243]. These cell-fate determinants are aggregated into a complex and are localized to the inner face cell membrane (cortex). In these models, polarization occurs intrinsically but can be accelerated by supplementation extracellular stimuli, suggesting that multiple layers of regulation fine-tune the extent of polarization [225, 226].

It is worth noting that, even without extrinsic factors, asymmetry is at least to some extent inherent from a previous cell division or environmental context. In the case of neuroblasts, the neuroepithelial cells (symmetrically dividing neural stem cells) from which they are derived are already apico-basally polarized at that stage. Thus, even before neuroblast delamination from the epithelium, the localization of the polarity complex (e.g., Par-aPKC at the apical side) is positioned at their polarized location [221,223]. Indeed, it can be viewed as that the entire developmental cascade is borne from a single asymmetrical event, that being the sperm fertilization of the egg at a singular unmirrored point [221,223,244], thus acting as an initial source of asymmetry.

1.3.3 Cell polarization and fate-determinants

Polarization and asymmetrical partitioning of cell-fate determinants is the most defining moment of asymmetrical division. It refers to the active shuttling of RNA, proteins, and nutrients

to one side of the cell such that those molecules will be inherited primarily by only one of the two daughter cells.

Polarity and asymmetrical division mechanisms possibly evolved as a mechanism to combat aging. In unicellular organisms which propagate by asymmetrical division (e.g., *Saccharomyces cerevisiae)*, it has been observed that the mother cell will retain oxidatively damaged proteins during cytokinesis so that the progeny is effectively "rejuvenated" [245]. Such a mechanism would likely be more energetically efficient versus simply degrading all proteins that accumulated some amount of damage. The absence of such a mechanism could lead to the eventual aging of the entire lineage [246,247]. The mechanism through which this effect is achieved in these unicellular organisms is still under investigation. However, it is suspected that it may involve anchoring cytoplasmic protein aggregates to transmembrane proteins predominantly associated with the older (inherited) pole rather than the new (de novo synthesized) pole[248]. Similarly, stem cell asymmetry likely also exists to maintain the longevity of the tissue lineage by partitioning damaged components away from the original stem cell.

Fundamentally, cell polarization is possible because the skeleton and trafficking "highway" of the cell (actin filament and microtubules) are "polarized" in the sense that they have one fast-growing and one slow-growing ends [229]. Microtubules, for instance, are structures formed from the assembly of alpha and beta-tubulin dimers in an alternating pattern. The polymerized form will have one end with alpha-tubulin exposed and the other with beta-tubulin exposed. This results in one fast-growing end (+ end) and one slow-growing end (- end). Actin filaments are likewise polarized. This directionality is having clear implications for the trafficking of organelles along the microtubule highway since the motor proteins (dynein and kinesin) travel in a specific direction along the microtubule [249].

The prototypical signaling axis for epithelial cell apical-basal polarity is the Par3, Par6 (Par, partition defective), and atypical protein kinase C (aPKC) complex, which works with the cell division control protein CDC42 to regulate the apical-basal membrane border[250]. The apical membrane is regulated by crumbs complex (CRB), which consists of transmembrane protein CRB with the cytoplasmic component MPP5. The basolateral plasma domain is regulated by the large disc homolog (DLG) complex [251,252]. These complexes act in a reciprocally antagonistic manner in conjunction with cell-cell adhesion proteins (e.g., E-cadherin expression on the apical-side) to drive cell polarity within the epithelium layer [252]. These polarity complexes are also operational in

Drosophila neuroblasts ACD to aid in restricting the stem cell factors towards the apical side and the differentiation factors to the basal side, exemplifying the connection between asymmetrical division and cell polarity.

Cell-polarity complexes integrate signals from the cell membrane and are mediated via intracellular trafficking. The membranes at the apical (facing the lumen), lateral (facing cells in the parallel layer), or basal (facing subjacent cells) have specialized components. For instance, the outer leaflet of the apical membrane is enriched in regulatory lipids phosphatidylinositol-4,5-bisphosphate (PtdIns(4,5)P2) [253] [254]. These "side-specific" components are sorted out in the trans-Golgi network and distributed to the correct regions via different cargo carriers, sometimes requiring an additional sorting step subsequently within Rab8a and Rab11a positive endocytic carriers [255,256]. The molecular mechanisms through which cells can recognize the intended destination of these proteins are not well-understood but were found to involve some site-specific protein motifs such as YXXØ for basolateral sorting 255 or N/O-linked glycosylation apical sorting[257].

1.3.3 Asymmetrical cell division in cancer

Among all the definitive properties of stem cells, (ACD) is arguably the one whose role in cancer is least understood, mainly due to the difficulty of capturing this rare event right at the moment of cancer cell division. Irrespective of asymmetrical division, the polarity complex has been established mostly as an essential regulator of tumor suppression and occasionally as oncogenic signaling [258]. Epithelial cell polarity is established via similar polarity complexes as those observed in other organisms such as *Drosophila.* For instance, the Par complex and tight junction proteins are also included in forming an intracellular seal, defined as the apical-lateral boundary and preventing intermixing membrane-bound proteins [259]. Par3 is frequently deleted in esophageal squamous cell carcinoma, and this deletion was found correlated with loss of cell-cell contact, positive lymph node metastasis, and poor differentiation [260]. Likewise, in breast cancer, the Par-complex also promotes cell-cell adhesion [261] and limits epithelial-mesenchymal transition via SNAIL degradation [262]. Moreover, tight junction proteins such as occludins, claudins, and nectins were also discovered to serve tumor-suppressive function [263-265].

Given that tumorigenesis is generally believed to arise from loss of polarity/asymmetry, the notion that CSCs would both display the asymmetrical properties of stem cells and act as tumorigenic seeds is somewhat paradoxical. Nevertheless, asymmetrically dividing cells have indeed been observed in lung cancer [266 187], prostate cancer [267], thyroid cancer [268], glioblastoma[269], and breast cancer [270], and in each case, the asymmetrically dividing population are correlated with stem-cell properties such as expression of CSC-markers, pluripotent gene signature, self-renewal, or elevated hierarchical positioning. This phenomenon is best understood in the model for colorectal cancer, where genetic perturbation of the adenomatous polyposis coli (APC) gene is widespread. APC is a regulator of the polarity complex and Wnt signaling and a potent tumor suppressor [271]. The balance between symmetrical and asymmetrical division in colorectal cancer is regulated by fine-tuning the level of Notch activation via Mir-34a. Excess Mir-34a results in two differentiated daughter cells, while low Mir-34a results in two dedifferentiated daughter cells[272,273]. Thus, only an ideal level of Mir-34a would result in the asymmetrical outcome of one stem cell and one non-stem cell[272,273]. Viewed this way, it suggests that tumorigenesis at least requires cancer cells that have the *potential* to divide asymmetrically even if every division they perform is not asymmetrical. At the same time, the act of breaking asymmetry itself can ultimately result in either expansion or depletion of tumorigenic cancer cells depending on the expression of fate-determinant. This model helps reconciles the contradiction that is asymmetrically dividing cells and the breaking of asymmetry both appear to favor and inhibit tumorigenesis. Overall, the dynamic relationship between cancer stemness, asymmetry, and tumorigenesis remains far from being elucidated.

1.4 The role of centrosomes in stem cell biology and cancer

A central component to stem cell ACD is a pair of innately asymmetrical organelles called centrosomes. Centrosomes are animal cell microtubule-organizing centers (MTOC), dictating cell shape, polarity and motility, spindle formation, chromosome segregation, and cell division [274-276], [277]. They are structurally amorphous, composed of a pair of centrioles embedded within "pericentriolar materials" (PCM) that contains ~100 different proteins [277]. Centrioles exist as part of the centrosome and as basal bodies at the root of cilia and flagella; thus, centrioles and

centrosomes are critical elements in development and physiology, whose deregulation can be linked to various diseases, including cancer, ciliopathies, and microcephaly [278].

1.4.1 Centriole structure, biogenesis, and asymmetries

Centriole/basal bodies are cylindrically shaped organelles constructed from nine microtubule triplets organized in a "ninefold symmetrical configuration reinforced by a cartwheel-like structure"; this structure is evolutionary conserved across eukaryotes but was lost in certain branches such as yeast and vascular plants [274-276,279].

During normal cell cycle progression, the centrosome needs to be replicated exactly once during the S-phase, reminiscent of DNA [274-276]. Traditionally, centriole replication is thought to depend on the existence of a template centriole[274-276]. However, centrioles can also form spontaneously "*de novo*" in animal cells, particularly in the absence of pre-existing centrioles, albeit with a higher frequency of errors [280-282]. These findings imply that centriole numbers are maintained by active suppression of excessive centriole biogenesis, though the mechanism that accomplishes this is not fully understood.

Despite the large number of proteins residing within the centrosome, RNAi screening in *C. elegans* revealed only a fraction (~5) of those components which are essential for the formation of the centriole, including ZYG-1 (human ortholog: PLK4), SPD-2 (Cep192), SAS-4 (CPAP/CenpJ), SAS-5 (STIL), and SAS-6 (SASS6)[283]; the function of these gene products are generally conserved in *Drosophila* and human models [283].

Centriole duplication is "licensed" during the end of a prior mitosis cycle, starting with a process called "centriole disengagement," whereby the protein Separase is required to break the S-phase to M-phase (S-M) linker that orthogonally binds a centriole pair [284]. During the subsequent S phase, new "procentrioles" will begin to be generated in the vicinity of pre-existing "mother centrioles" (inherited from the previous cell division). The new daughter centrioles will then be linked to the lateral base of the mother centrioles via new S-M linkers. They will continue to mature throughout G2 and M-phase via elongation and appendage assembly at the distal ends.

1.4.2 Asymmetrical centrosome behaviors in normal stem cells

Perhaps the most captivating attribute of centrosomes, particularly in the context of stem cell biology, is the capacity of centrosome pairs to behave distinctly from one another. It has been observed that in stem cells, more so than in differentiated cells, one of the centrosomes will invariably have more robust microtubule-organizing center (MTOC) activity compared to the second centrosome [274,285-287].

A critical parameter that determines the centrosome's MTOC activity is the age of the centrosome itself [274]. Within a single cell resides three distinct generations of centrioles. At the end of mitosis, the centriole pair inherited during the previous cell division was a mother-daughter pair (here can be indicated by M1 and D1); during the subsequent S-phase, the two new centriole pairs generated would be (M1-D2, and D1-D2) [274]. While M1 and D1 are both inherited during a previous cell division and act templates for new centrioles, studies have shown subtle differences in their function: the younger D1 centriole lacks certain appendages at the distal ends found in the M1 centriole[274]; this means that centrioles fully matured only after two complete cell cycles. Several studies have shown that the mother centrosome maintains higher MTOC activity in most mammalian cell types, perhaps due to the maturation process gradually endowing centrosomes with more capacity to bind and nucleate. In multiple stem cell models, such as *Drosophila* germ cells, the daughter cell that retains self-renewing properties will invariably inherit the mother centrosome [285], suggesting that age differences between centrosomes are communicated to cellular factors regulating ACD.

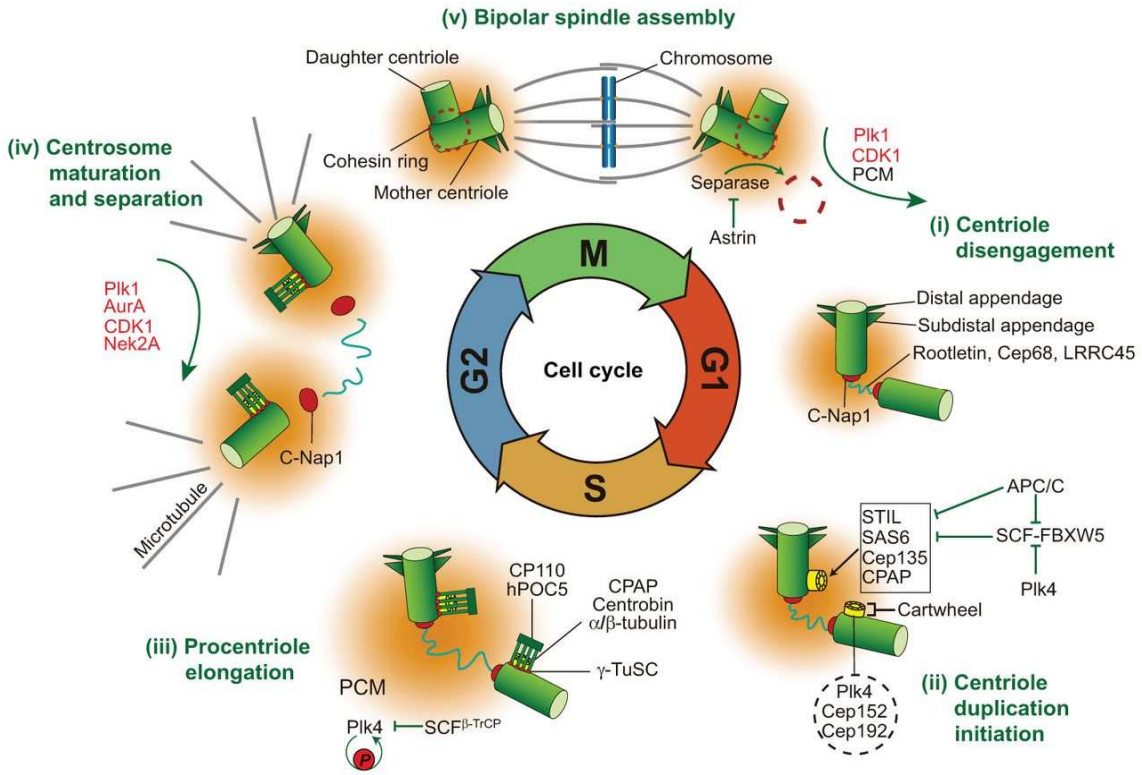

Figure 5: The centrosome cycle is interconnected with the cell cycle. At the beginning of interphase (G1), a cell normally contains only one centrosome consisting of a centriole pair. Before centrosome duplication, the two centrioles need to be separated via centriole disengagement, where the two centriole pairs transition from being linked to being only loosely tethered. During the late G1 and early S-phase, centriole replication is initiated by proteins PLK4 recruited by proteins such as PLK4 to the centrosomes. A new centriole is founded on a 9-fold symmetrical "cartwheel" structure formed by proteins such as SAS6, Cep135, and CPAP at the proximal end of an existing centriole. This cartwheel behaves as a template for forming a new centriole (procentriole) from the gradual formation of tubulin polymers at the ends of 9 spoke arms attached to the cartwheel. Tubulin polymerization is aided by centrobin, which stabilizes a/b tubulin dimers to promote centriole elongation. Procentriole elongation lasts from the late-S phase to mitosis. During G2, the two centriole pairs mature by assembling pericentriolar materials such as γ-tubulin and pericentrin and begin distancing from one another in preparation for mitosis. Protein kinases such as Aurora Kinase A, PLK1, and Nek2 are important regulators of this stage. During early mitosis (prophase to metaphase), both centrosomes act as nucleation sites for microtubule polymers, producing the mitotic spindle. During anaphase, Separase is recruited to cleave cohesion subunits at the centrosomes to initiate the process of centriole disengagement that will be completed at the beginning of the following interphase. Pericentriolar materials are also rapidly discarded from the centrosomes at the end of mitosis. Image is from " The role of mitotic kinases in coupling the centrosome cycle with the assembly of the mitotic spindle" by Gang Wang, Qing Jiang, and Chuanmao Zhang, Journal of Cell Science 2014 [288], and reproduced with permission from The Company of Biologists Ltd.

The difference in MTOC activity between the two centrosomes has two critical implications in cell behavior during cell division. Firstly, the centrosome with low MTOC activity generally moves extensively during interphase, while the centrosome with higher MTOC is relatively stationary [289,290]. In several models, the centrosome with the stronger MTOC is positioned near the side closer to the stem cell niche. Secondly, the centrosome with higher MTOC activity forms the mitotic spindle earlier during early mitosis [289,290]. This latter trait appears to be part of a coordinated effort to ensure that the stem cell retains the template DNA during asymmetrical cell division[289,290].

Aside from differences in MTOC activity, centrosomes also differ in their molecular composition. Presently, several proteins have been identified as being only enriched in either the mother or daughter centrosomes, including Klp10A, Alms1a, Ninein, outer dense protein 2 (ODF2), and centrobin [291-295]. In *Drosophila* models, knockdown of genes that express proteins such as Klp10A or Almb1a led to abnormal elongation of the mother, but not daughter centrosomes, indicating that centrosome behaviors could indeed be affected by different molecular compositions. Furthermore, cell-fate determinants, such as Mindbomb1 (Mib1), have also been observed [296]to segregate to a specific centrosome for correctly partition into the prospective daughter cell during asymmetrical cell division. Likewise, mRNAs coding for cell-fate determinants such as *IoDpp*, *IoEve*, and *IoTld* have also been shown to be partitioned to centrosomes [297]. These collective findings portray the centrosome as a critical member in the toolbox that stem cells utilize to dictate progeny cell fate.

Despite the vast amount of evidence linking the asymmetrical behavior of centrosomes to stem cells and their capacity to conduct asymmetrical cell division, the molecular mechanisms that govern asymmetrical centrosome behavior is difficult to dissect precisely. A major challenge is that perturbation of centrosome proteins can lead to pleiotropic changes to intracellular trafficking or mitotic fidelity, obfuscating the effects of centrosome asymmetry.

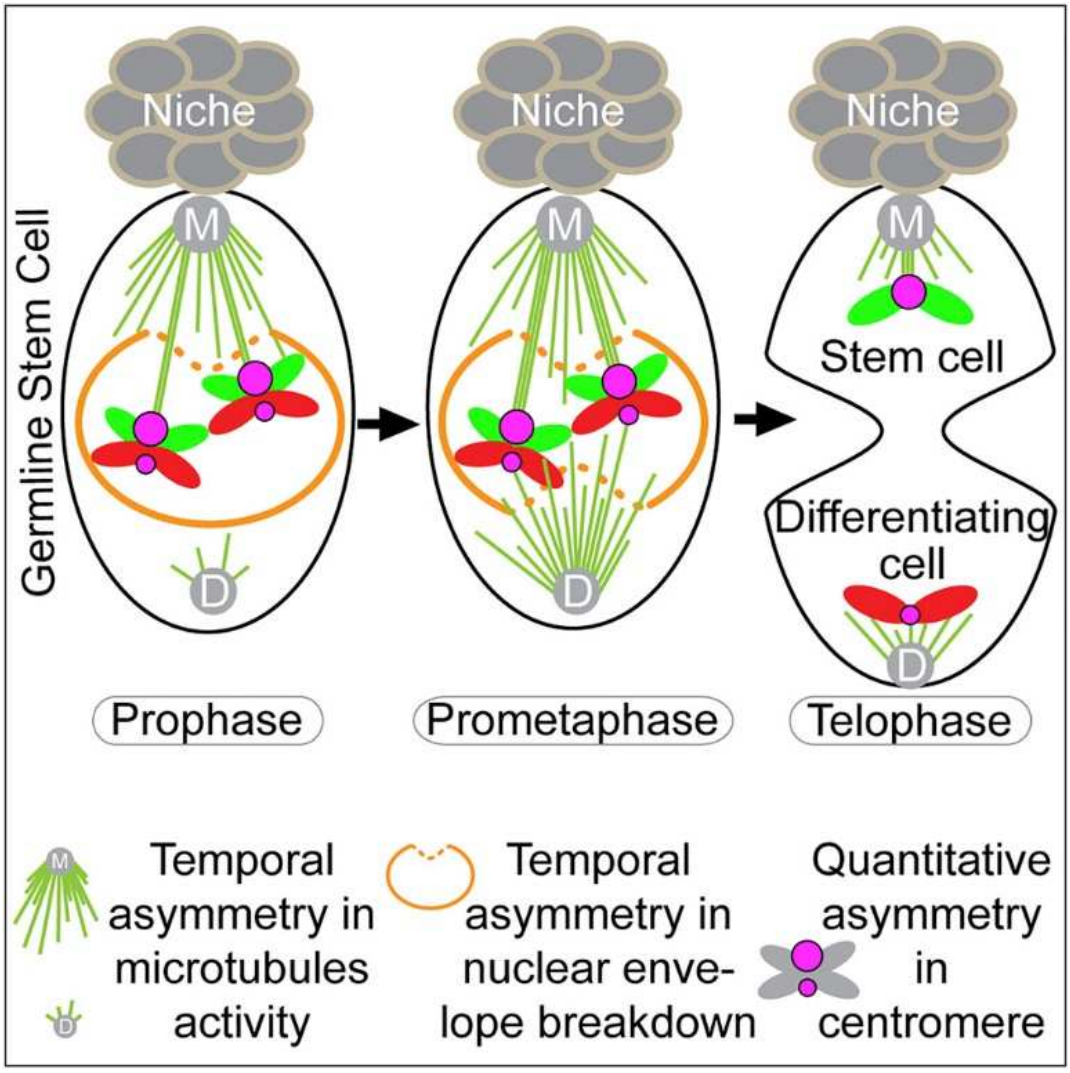

Figure 6: Differences between mother and daughter centrosomes drive asymmetrical mitotic cascades in asymmetrical-dividing stem cells. In Drosophila germline stem cells, the mother centrosome exhibits a robust microtubule organization center (MTOC) activity during interphase and early prophase. In contrast, the daughter centrosome shows comparatively weak MTOC activity. During the early prophase, the mother centrosome forms the mitotic spindle slightly earlier than the daughter centrosome, leading to a short period where only a single spindle is formed and attaches to chromatids. The mother centrosome anchors selectively to the template, rather than replicated DNA, via epigenetic marks present only on template DNA centromeres. Following cell division, the mother centrosome is inherited by the cell that remains near the stem cells niche, which retains stem cell identity and the template DNA strand. Image is reproduced from "Asymmetric Centromeres Differentially Coordinate with Mitotic Machinery to Ensure Biased Sister Chromatid Segregation in Germline Stem Cells" by Rajesh Ranjan, Jonathan Snedeker, and Xin Chen, Cell Stem Cell 2019 [290], with permission from Elsevier.

1.4.3 Centrosomes regulate asymmetrical cell division via spindle pole orientation

The formation of the mitotic spindle apparatus is arguably the primary function of centrosomes. The mitotic spindle is an assembly of microtubule (-) ends radiating from (usually) two poles at the opposite ends of the cell during mitosis that coordinate the segregation of sister chromatids into respective daughter cells. Three distinct microtubules are radiating from the spindle: kinetochore microtubules that attach to chromosomes, interpolar microtubules that bind the two poles together, and astral microtubules that attach to the cell cortex (inner side of the cell membrane) [298,299]. By regulating the organization of these microtubules, centrosomes positioning can inform the orientation of the mitotic spindle, which determines the cytokinesis happening site and ultimately how cell-fate determining factors get portioning in respective daughter cells[298,299].

During asymmetrical cell division, repositioning the mitotic spindle by the polarity protein complexes occurs once before mitotic spindle assembly and a second time during anaphase [300,301]. The first step involves aligning the spindle with the polarity complex; this process is highly conserved and observable in both *C. elegans* and *Drosophila* neuroblasts. The Par complex (e.g., Par3, Par6, aPKC) is pre-sequestered to the apical cortex and, there, interacts with TPR/GoLoco domain protein GPR-1/2 (Pins in flies; LGN/AGS-3 in mammals) via a linker protein Inscrutable (Insc)[300,301]. GRP1 and the membrane-bound G protein (Gα) reciprocally activate each other, leading to the recruitment of the scaffolding protein Disc large homolog (Dlg) and the activation of the downstream cascade of the motor proteins Khc73 dynein via NuMA and Lis1. These events resulted in the anchoring of one centrosome to one of the cell "poles" [301,302]. The second step is to position the mitotic spindle such that cytokinesis occurs off-center, producing daughter cells of different sizes. This function may have evolved from convergent evolution, as different organisms show distinct approaches to shift the spindle off-center; for instance, *C. elegans* achieves this asymmetry by anchoring the spindle away from the center itself, whereas *Drosophila* cells achieve this asymmetry by having the two spindle arms be of different sizes. This step also appears to have several levels of regulatory redundancy, as either Pins-Gα or the Par3/6 complex alone was shown to be sufficient [298,299].

In the event that a mispositioned spindle progressed as far as anaphase, stem cells appear to have evolved one last checkpoint during telophase, called "telophase rescue," as a final effort to relocate fate-determinants to preserve the asymmetrical partitioning scheme. This pathway is governed by a pathway controlled by the scaffolding protein Dlg, the motor protein Khc73, Snail,

Tumor necrosis factor, and Eiger (Egr) [303] [304,305] to actively shuttles the fate-determinants themselves into the newly positioned axis or correct the spindle angle itself[306].

1.4.3 Pseudobipolar spindle formation in centrosome amplified cancer cells drive genotypic heterogeneity by promoting chromosomal instability

Centrosome amplification, the acquisition of >2 centrosomes by a cell, is a common feature of multiple types of cancer and is generally more common in advanced cancers [307]. Centrosome amplification can arise from several non mutually exclusive mechanisms. Errors in the centrosome cycle can lead to centriole overduplication or *de novo* centriole genesis, while errors in cytokinesis can generate polyploid cells with extra pairs of centrosomes [308].

Centrosome amplification generally leads to increased aneuploidy - a change in the number of chromosomes in a cell, sometimes leading to spontaneous tumorigenesis [309,310],[311,312]. Mechanistically, supernumerary centrosomes cause aneuploidy by increasing the number of spindle poles formed during mitosis; this occurs due to increased merotelic attachments - a type of error in spindle-chromosome binding whereby a single kinetochore is mistakenly attached to microtubules radiating from multiple spindle poles, resulting in lagging chromosomes during anaphase [313,314].

Although the formation of multipolar spindles promotes CIN/aneuploidy, multipolar mitosis (where a cell divides into three or more daughter cells) almost always leads to unviable cells [315,316]. Cancer cells avert this catastrophe by preventing multipolar spindles from progressing beyond metaphase; instead, a process called "centrosome clustering" is utilized to assemble mitotic spindles into one of two poles [317,318]. The resultant "pseudobipolar spindle" retains merotelic attachments between spindles/kinetochores without committing to multipolar mitosis, thus effectively propagate CIN/aneuploidy while avoid generating unviable daughter cells.

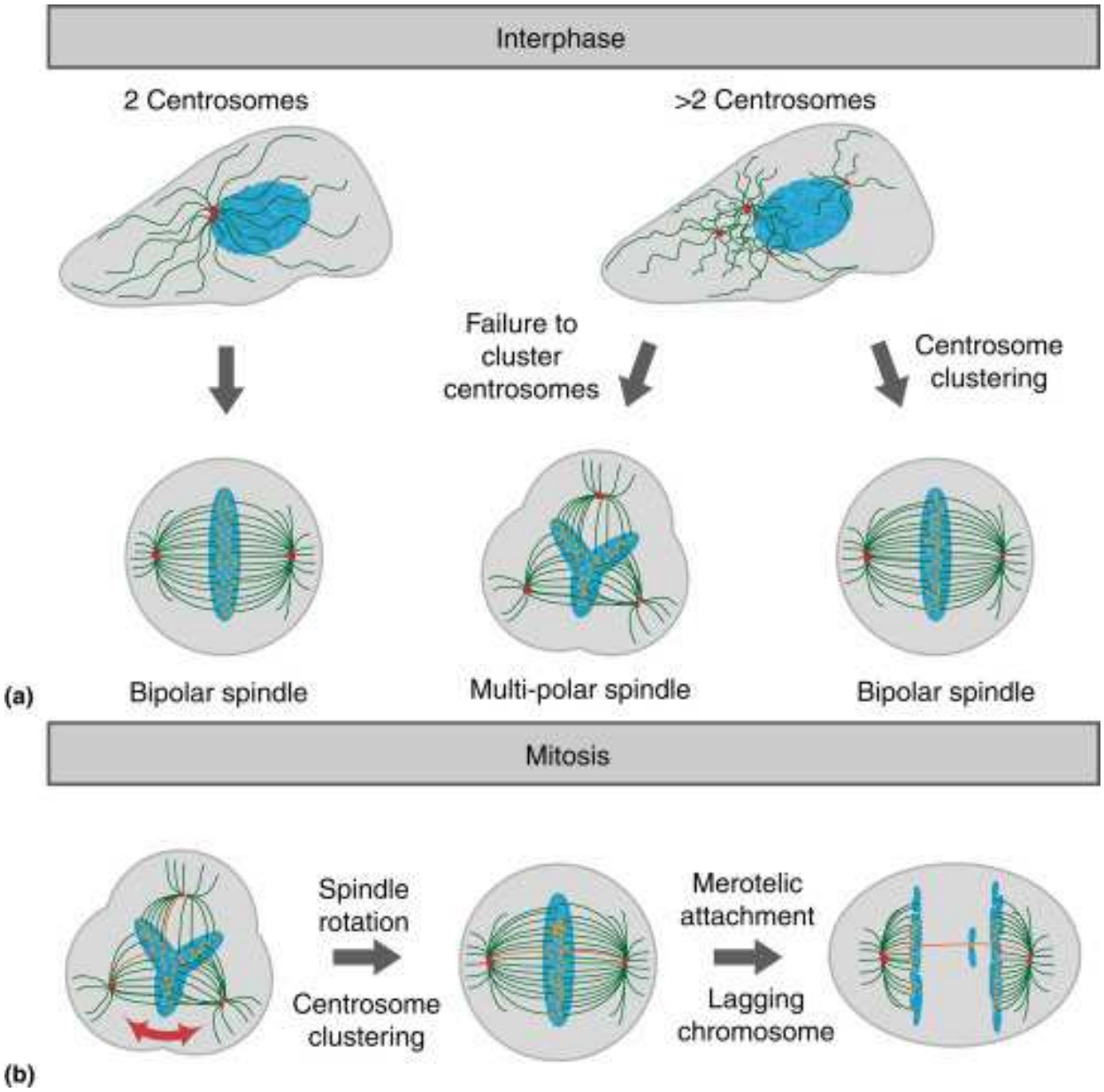

Figure 7: Mechanistic link between centrosome amplification and chromosomal instability **a)** When centrosome amplification occurs, extra mitotic spindles are generated during mitosis. At this point, a chain of events called "centrosome clustering" involving spindle assembly checkpoint, motor proteins, kinetochore proteins, and spindle tension sensors will attempt to resolve spindles into a (pseudo)bipolar spindle; if centrosome clustering occurs, then multipolar spindles only transiently manifests but if centrosome clustering fails, then multipolar persists, leading to either extended mitotic arrest or (usually) fatal multipolar mitosis. **b)** When centrosomes are successfully clustered into pseudobipolar spindles, chromosomes can easily become attached to microtubules originating from >1 pole (merotelic attachment). Merotelic attachments are highly likely to produce lagging chromosomes during anaphase, leading to chromosomal instability. From volume 2 of Encyclopedia of Cell Biology pages 649-659 "Centrioles and the Centrosome" by J. Sillibourne and M Bornens [319], with permission from Elsevier.

Since centrosome amplification occurs primarily in cancer cells but not healthy cells, identifying factors required for centrosome clustering became a very appealing approach to uncover cell-specific vulnerabilities. Multiple studies have attempted to identify proteins required for centrosome clustering. Functional RNAi screening revealed that centrosome clustering is via proteins that can generally be classified as sensors of spindle tension, regulators of spindle assembly checkpoint, or motor proteins[320]. Another recent study revealed that drugging CPAP-tubulin interaction also prevented the formation of pseudobipolar spindles in centrosome amplified in breast cancer and lung cancer cells [321]; however, a vital distinction of this study is that the small molecule did not appear to block centrosome clustering directly but to promote centrosome declustering by hyper activating supernumerary centrosomes. Collectively, these findings show that cancer cells enable pseudobipolar spindle formation via at least two currently known mechanisms: centrosome clustering and centrosome inactivation.

2. Investigation of centrosome-dependent signaling axis driving stemness and chromosomal instability of ALDH-positive cancer stem-like cells

2.1 Purpose and rationale

The studies reviewed in **Chapter 1** establishes several key concepts. The first is that cancer stemness is a major contributor to aggressive cancer progression and a root cause of intratumoral heterogeneity. While there remain important questions regarding the identity and precise nature of CSC involved (**section 1.1**), there is sufficient evidence to support that stem-like cells exist as a distinct phenotypic state that cancer cells can adapt to survive and progress. Supporting this are many studies that found that stemness is a property that can modulate many of the classical hallmarks associated with oncogenesis (**section 1.2**).

The studies laid out in chapter 1 highlight a few gaps in the present understanding of the connection between CSCs and the oncogenic properties of cancer. Firstly, most of the connections built between CSCs and cancer oncogenic properties compared cancer cells identified as "CSCs" based on the expression of cell-surface markers (e.g., CD133), enzymatic markers (e.g., ALDH), or canonical stem cell markers (e.g., Bmi1, Nanog, Oct4). Although this approach offers valuable evidence to the knowledge that the CSC-state behaves sufficiently distinct from having altered cancer hallmarks, it does not add to our understanding of how stem cell properties themselves contribute to oncogenesis. What is particularly lacking is a solid understanding of how asymmetrical cell division (ACD), a definite feature of stem cells, affects CSCs (**section 1.3**). Moreover, a solid understanding of how cancer stemness could impact chromosomal instability (CIN) is also largely missing, despite both features co-manifesting tremendously in cancers with extensive intratumoral heterogeneity.

Based on the established findings that centrosomes act as a critical regulator for both ACD and CIN in stem cells and cancer cells, respectively (**section 1.4**), we postulated that centrosome regulation in CSC could potentially bridge stemness and CIN status together in cancers.

2.2. Summary of key findings

Manuscript 1

The first manuscript entitled "Asymmetrical centrosome behavior and DNA sensing coregulation link stemness to chromosomal instability during thyroid cancer progression," investigates a central hypothesis proposed by our introductory chapters: that asymmetrical centrosome behaviors in stem cells could impact CIN due to centrosomes also being a critical factor in the formation of spindle pole during mitosis. This study identified that the stem-like cell population is the primary CIN source in the highly advanced thyroid cancer, anaplastic thyroid cancer (ATC). We probed for centrosome-related genes upregulated in the stem-like cell compartment. We found that the centrosome-related scaffolding protein "NEDD9" was a dual regulator of stemness and CIN in this cancer model. Our findings that ALDH+ ATC cells (characterized as stem-like by their superior capacity to perform asymmetrical cell division, grow as tumorsphere, and seed tumors) transcriptionally upregulate NEDD9 due to retinoic acid signaling and are dependent on NEDD9 to acquire exceptional tolerance to both centrosome amplification and micronuclei - two key barriers which limit CIN-propagation.

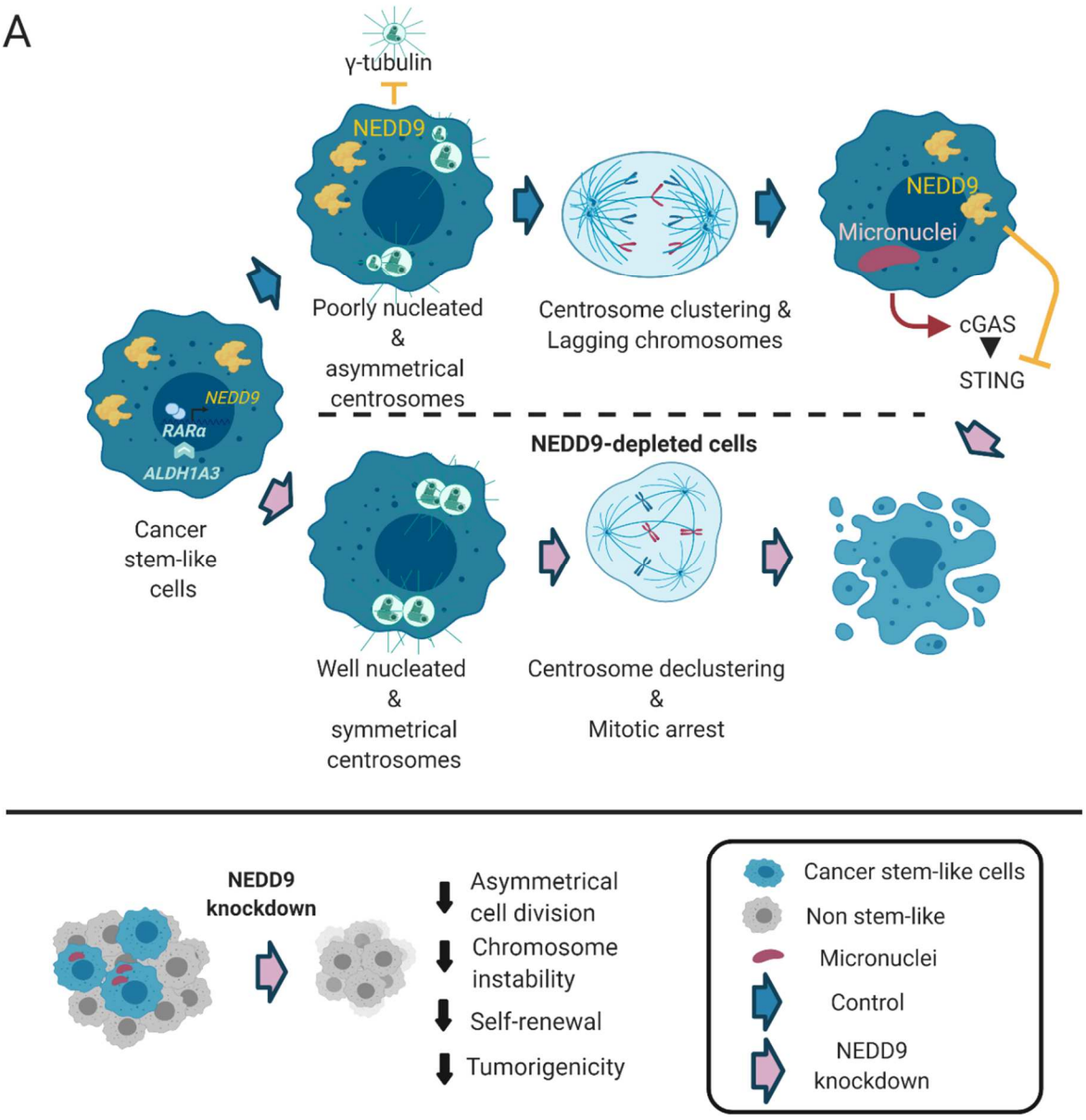

Figure 8: Graphical abstract depicting key findings in manuscript one entitled " Asymmetrical centrosome behavior and DNA sensing coregulation links stemness to chromosomal instability during thyroid cancer progression **"**

Manuscript 2:

In the second manuscript entitled "Differential STAT3 regulation by NEDD9-interactome contributes to centrosome asymmetry in thyroid cancer stem-like cells", we investigate more deeply the downstream pathways through which NEDD9 interactome is distinguished in ALDH+ thyroid cancer stem-like cells. This study aims to clarify some of the downstream molecular events contributing to NEDD9's effects observed in manuscript 1. We identify that among known NEDD9-regulated oncogenes, STAT3 was the key effector whose activation is distinguished by NEDD9 in ALDH+ cells. Remarkably, our study finds that in contrast to conventional STAT3 signaling, STAT3 activation in ALDH+ cells occurred primarily in the cytosol. Consequently, NEDD9-STAT3 signaling did not substantially affect STAT3's function as a nuclear transcription factor but did affect STAT3's cytosolic function as a regulator of cytoskeletal dynamics, including centrosome microtubule-nucleation. Moreover, a precise level of STAT3 is required to maintain asymmetrical centrosomes in ALDH+ cells, as both overexpression of constitutively activated STAT3 or STAT3-knockdown disturbed centrosome asymmetry.

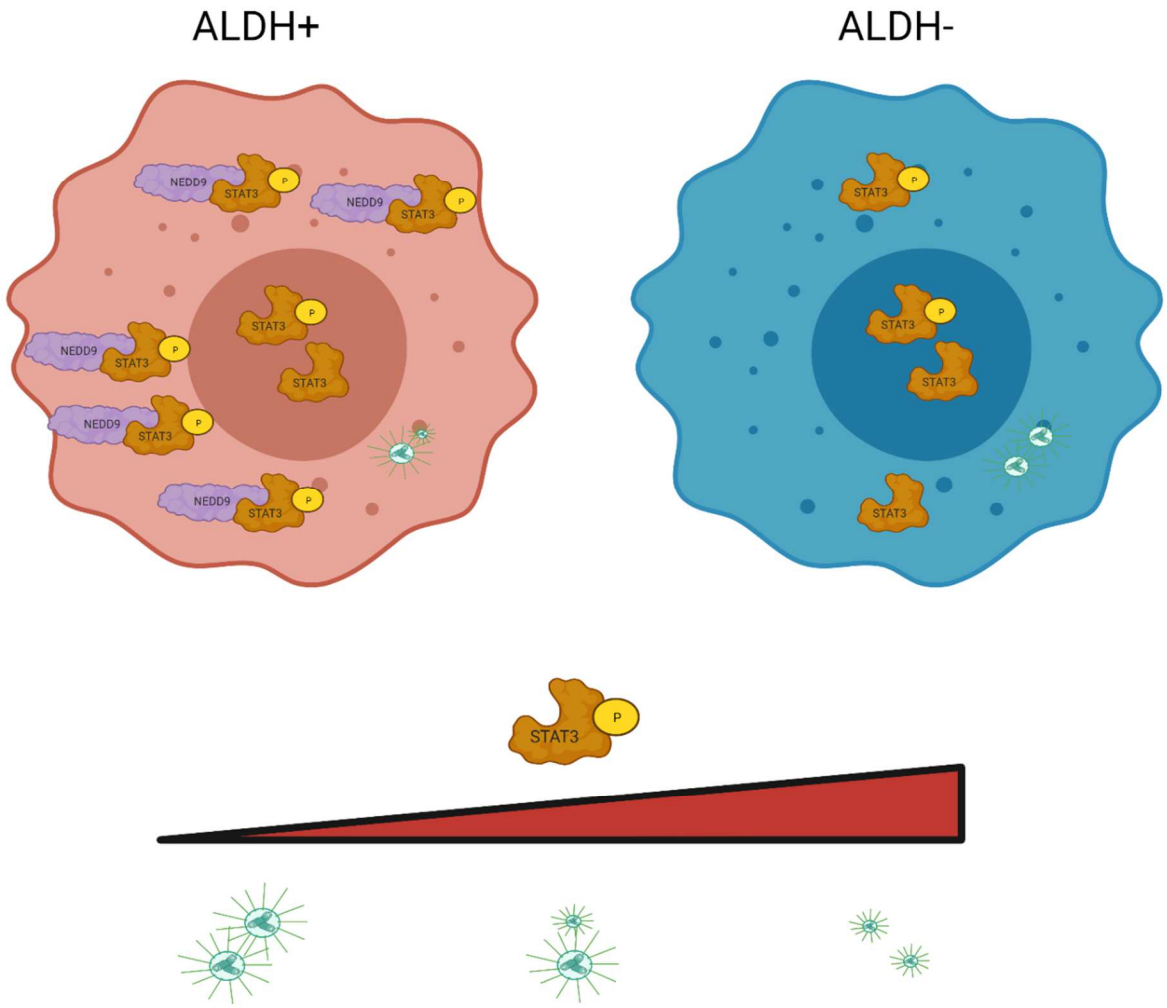

Figure 9: Graphical abstract depicting key findings in manuscript two entitled " Differential STAT3 regulation by NEDD9-interactome contributes to centrosome asymmetry in thyroid cancer stem-like cells"

Manuscript 3:

Clinically, ATC is regarded as a highly aggressive disease that currently lacks effective treatment options. The third manuscript, "Targeting tumorigenic thyroid cancer stem cells through centrosome-activation-induced mitotic catastrophe," aims to explore the pharmacological usage of key regulatory factors identified in manuscripts 1 and 2 to eliminate CSCs in our preclinical ATC models through disrupting the centrosome inactivation pathways (**Fig. 9**). We screened for compounds targeting NEDD9-interactome for candidates that could best recapitulate the centrosome hyperactivation effect observed when we knocked down NEDD9 (manuscript 1). The lead candidate, a novel multikinase inhibitor "MEAP," was discovered to induce supernumerary centrosome hyperactivation and mitotic arrest selectively in ALDH+ ATC stem-like cells, leading to an overall reduction in stemness features such as spherogenesis and tumorigenesis. MEAP significantly reduced ALDH1 positive cancer cell clusters, induced multipolar spindles, and attenuated tumor growth in an ATC xenograft model when administered intraperitoneally.

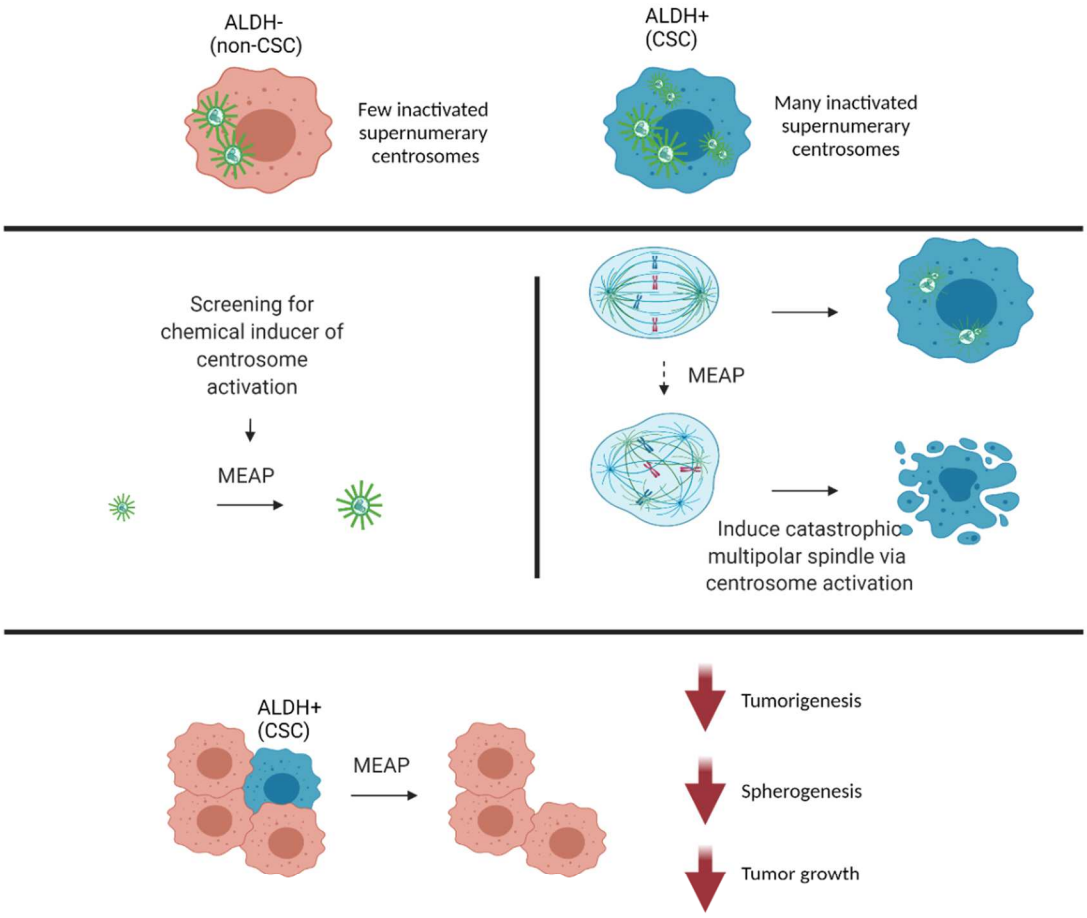

Figure 10: Graphical abstract depicting key findings in manuscript 3 entitled: " Targeting tumorigenic thyroid cancer stem cells through centrosome-activation-induced mitotic catastrophe "

`

2.3 Challenges encountered

The project was an exploratory work investigating the potential connection between stemness and CIN in ATC - a disease where both hallmarks are highly enriched. This approach is relatively open-ended, offering the advantage of having many novel aspects to explore each finding. As a result, several unexpected and interesting observations were made, such as NEDD9's inverse relationship with STING activation, the non-canonical cytoplasmic NEDD9-STAT3 pathway, and STAT3 being a phosphatase-regulated downstream mediator of AURKA/FAK inhibitors.

Given the exploratory nature of the work, much of the initial effects were spent probing for novel findings from different angles. Although the thesis presented the work as three manuscripts, these studies were originally a single concept whose scope outgrew the limit of a single manuscript.

Although the phenotypes we observed upon NEDD9-knockdown were highly remarkable, much work was required to delineate the precise mechanisms that caused those effects due to the large number of effects that ended up occurring. Stemness, CIN, and centrosome clustering are all phenotypes requiring extensive experiments to prove and further to rule out alternative hypotheses. For instance, our proposed hypothesis that CSCs were induced to undergo centrosome declustering required first 1) proving that these cells were not experiencing centrosome fragmentation (whereby the centrosomes are not clustered, but instead a piece of the pericentriolar material breaks off from the centrosome and acts as supplementary MTOC). Moreover, as the study aimed to examine mechanisms specific to thyroid CSCs, each experiment required ALDH- counterpart control, thus doubling the amount of data required to conclude.

Another key challenge was the observation that only ~50% of the ALDH+ cell death triggered by NEDD9 knockdown could be attributed to centrosome-mediated mitotic catastrophe. To explain the mechanistic cause of the other 50% of ALDH+ cell death, we eventually uncovered that the secondary killing was due to activating cGAS/STING signaling; this introduced another complicated aspect to the system that, on the one hand, could not be ignored (due to it accounting for half of the effects), yet also necessitated a large number of experiments. Thus, although the study covered large grounds, the full-depth investigation for many aspects is prohibitive (such as exploring the mechanistic basis for how NEDD9 specifically controlled centrosome activity).

Lastly, the cancer model itself, while being a highly convenient model due to its ease of isolating CSC population via ALDH marker-based sorting, is not well-studied; as such, many basic

cell parameters (e.g., proliferation rate, centrosome amplification rate, etc.) did not have well-defined benchmarks in literature. In addition, while ALDH+ ATC cell's "stemness" is well acknowledged to experts in the field of ATC, it is less broadly recognized among researchers conceptually studying CSCs; this resulted in much additional work required to characterize ATC stemness, whereas these steps could have been shorted if findings were conducted in a more prominent model such as CD24-/CD44+ breast cancer stem cells.

Overall, in many ways, this study exemplified both advantages and disadvantages of an open-ended exploratory study. While it uncovered significant novel conceptual insights into the interplay between two heterogeneity-promoting cancer hallmarks (stemness and CIN), many findings demand further, more in-depth investigation to fully elucidate.

2.4 Manuscript 1: Asymmetrical centrosome behavior and DNA sensing coregulation links stemness to chromosomal instability during thyroid cancer progression

Co-regulation of centrosome asymmetry and DNA-sensing links stemness to chromosomal instability during thyroid cancer progression

Authors: Henry G. Yu, Krikor Bijian, Sabrina D. da Silva, Jie Su, Gregoire Morand*, Alan Spatz and Moulay A. Alaoui-Jamali

Affiliations:

Departments of Medicine, Oncology, Pathology and Otolaryngology-Head and Neck Surgery, Lady Davis Institute for Medical Research and Segal Cancer Centre, the Sir Mortimer B. Davis-Jewish General Hospital, Faculty of Medicine, McGill University, Montreal, Canada.

* Department of Otorhinolaryngology-Head & Neck Surgery, University Hospital Zurich, Switzerland**.**

Corresponding author

Moulay A. Alaoui-Jamali, PhD

E-mail: moulay.alaoui-jamali@mcgill.ca

Abstract

Background: Oncogenic dedifferentiation and chromosomal instability (CIN) are both hallmarks that contribute to intratumoral heterogeneity in advanced cancers such as anaplastic thyroid cancer (ATC). The centrosomes, a pair of organelles that organize microtubules and the spindle apparatus, play a unique role in stem cell biology and promoting CIN. The interplay between stemness/CIN and the involvement of centrosomes therein is poorly understood.

Methods: Transcriptomic datasets from the National Center for Biotechnology Information (NCBI) and The Cancer Genome Atlas (TCGA) were analyzed to identify the centrosome-related scaffolding protein "NEDD9" as a potential ATC stemness and CIN dual regulator. NEDD9 upregulation alongside the stem-like cell marker ALDH1A3 was evaluated by immunohistochemical staining of the patient specimen. In patient-derived ATC cell lines THJ-11T and THJ-16T, stem-like cells were isolated by flow cytometry using ALDH as a marker. Stemness was evaluated via tumorsphere formation, asymmetrical cell division, and tumorigenesis. CIN was assessed by lagging chromosomes and micronuclei rate. Immunofluorescent confocal image and live-cell imaging were used to evaluate NEDD9-knockdown's impact on centrosome/chromosome/spindle dynamics. The *in vivo* effect was confirmed by doxycycline-inducible shNEDD9 in ATC xenografts and immunohistochemistry.

Results: ALDH+ stem-like cells possess triple the CIN of ALDH- bulk cells in ATC models. ALDH1A3/NEDD9 co-upregulation correlated with thyroid cancer progression/dedifferentiation. NEDD9 was transcriptionally upregulated exclusively in ALDH+ ATC cells to promote stem cell-like asymmetrical centrosome dynamics. Leveraging this function, ALDH+ cells staggered activation of supernumerary centrosomes during mitosis, limiting the severity of multipolar spindles, thus increasing the success of CIN-prone mitosis. Moreover, NEDD9 further promoted CIN tolerance by suppressing STING, thus attenuating cell death caused by micronuclei-stimulated type 1 interferon secretion. Simultaneous inhibition of stemness and CIN could be achieved through NEDD9-depletion *in vitro* and *in vivo*. Lastly, analysis of patient transcriptomic datasets revealed that upregulation of "stemness-related centrosome genes" also correlated with aneuploidy across multiple types of solid tumors.

Conclusions: ALDH+ stem-like ATC cells are highly CIN-tolerant. NEDD9 overexpression in those cells co-regulates stemness and CIN tolerance by suppressing centrosome activation and cytosolic DNA sensing. Stemness-related centrosome pathways could be effective targets for advanced cancers.

Introduction

Cancer encompasses remarkable cell heterogeneity featuring genetically and phenotypically distinct cells having different impacts on clinical outcomes. Tumor heterogeneity can arise from, in part, 1) genome-altering events such as chromosomal instability (CIN) [1], and 2) oncogenic dedifferentiation driving a stem-cell-like phenotypic state [2,3]. Existing studies find that CIN-high and cancer stem-like cells can act as drivers of tumor heterogeneity and evolution [4-6]. There is evidence that acquiring stemness or progression to a poorly differentiated state involves a parallel increase in the degree of CIN [7,8]. Furthermore, stemness and CIN are frequently increased in advanced/metastatic forms of cancer such as thyroid, prostate and breast cancer [3,9-14], suggesting that the interplay between stemness and CIN may exist. However, mechanistic links between these hallmarks are yet to be elucidated.

Both stem cell phenotype and CIN can, in principle, be promoted through distinct behaviors of the centrosomes - a pair of organelles that coordinate the orientation and assembly of the microtubule network and the mitotic spindle [9]. In *Drosophila* stem cell and neuroblastoma models, asymmetries in centrosome inheritance and microtubule-organizing center (MTOC) activity are integral to asymmetrical cell division (ACD). ACD is a specialized cell division currently understood to be unique to stem/progenitor cells whereby one daughter cell retains stem cell identity, while another differentiates [10-16]. On the other hand, centrosomes are also unique in cancer cells, as cancer cells frequently acquire an excess of centrosomes via numerous mechanisms such as centriole overduplication and endoreplication [17]**.** In such cases, supernumerary centrosomes can lead to erroneous attachment of chromatids to microtubules at the kinetochores, resulting in missegregated chromosomes found in the spindle midzone during anaphase [18-20], increasing the rate of CIN. It is presently unclear if and how asymmetries in centrosome behavior affect cancer cells with supernumerary centrosomes or CIN.

For cancer cells with centrosome amplification to successfully propagate CIN, at least two sequential challenges need to be overcome. First, during mitosis, supernumerary centrosomes need to form pseudo-bipolar spindles, where failure can lead to unresolvable multipolar spindles, mitotic catastrophe, and cell death [19,21-23]. Second, during the following interphase, chromosome missegregation will often lead to micronuclei formation, whereby chromosomes enclosed within the micronuclei envelope can be exposed to DNA damage and cytosol leakage [24]. The presence of

cytosolic double-stranded DNA (dsDNA), through DNA sensing cGAS-STING pathway activation, promotes anti-tumor immunity [24,25] and cell-autonomous cell death [26].

As stem-like cancer cells are often phenotypically distinct from non-stem-like cells [2], a question arises as to whether cancer stemness could modulate CIN tolerance in cancer types where both traits are present, such as in anaplastic thyroid carcinoma (ATC). Though rare, ATC accounts for the majority of death from thyroid cancer[27]. Median survival for ATC patient is merely six months, with most patients dying of suffocation, and standard treatments such as chemotherapy, radiation therapy, and surgery offer only marginal benefits[27]. ATC is presently diagnosed by their extensive dedifferentiation and nuclear atypia [27] and could be viewed as a prototypical example of advanced cancer with a high degree of both stemness and CIN. Compared to less aggressive thyroid cancer subtypes, ATC harbors a relatively high proportion of tumorigenic "stem-like" clones with high levels of aldehyde dehydrogenase activity (ALDH) [28-32], an enzyme biomarker used for prospective identification of cancer stem-like cells in multiple cancer models [7,31,33,34]. These ALDH+ cells are important for the stemness-associated traits of ATC, such as their tumorsphere forming potential and tumorigenesis [28-32,35,36], but it is presently unknown if they also contribute to CIN. This study finds that ALDH+ ATC cells are strikingly tolerant to CIN compared to non-stem-like ALDH- cells. We traced both CIN tolerance and stem-like properties to the upregulation of NEDD9 – a scaffolding protein that coordinates cytoskeletal dynamics [37-47]. Our finding proposes that the stem-like state in this cancer model can directly influence CIN tolerance and highlight the centrosome-regulatory network in ALDH+ ATC cells as a critical target to limit aggressive properties associated with this disease.

Results

ALDH+ anaplastic thyroid cancer cells exhibit stem-like features, divide asymmetrically, and harbor a higher rate of chromosomal instability

We began by characterizing two patient-derived ATC cell lines: THJ-11T and THJ-16T sorted by ALDH-status (**M1-fig. 1a**). ALDH1A3, the ALDH isoform commonly associated with high ALDH activity in cancer stem cells, was upregulated in ALDH+ compared to ALDH- cells and shRNA-mediated knockdown ALDH1A3 ablated ALDH enzymatic activity (**M1-fig. 1c**). By

benchmarking tumorsphere forming capacity, we found that compared to ALDH- cells, ALDH+ cells formed tumorsphere at an increased rate of about 4-fold (**M1-fig. 1d)**. A comparison of BrdU/DAPI co-staining showed that the rate of proliferation and overall cell cycle distribution in asynchronous ALDH- and ALDH+ sorted cells are similar, indicating their disparity in spheroid growth is likely due to differences in stemness rather than proliferation potential (**M1-fig. S1a**). These results agree with previous studies postulating that ALDH was an effective marker for cancer stem-like cells in ATC [28-32,35,36].

When we tracked the ALDH+/- status of sorted cells, we noticed that ALDH+ cells were substantially better at recapitulating heterogeneity compared to ALDH- cells, as purely sorted ALDH+ cells (99%) produced a population of 46% ALDH+ after ten passages, whereas purely sorted ALDH- cells (99%) remained ~90% ALDH- within the same timeframe (**M1-fig. 1b)**. This suggested that the dynamics of ALDH+ and ALDH- cells likely follow an interconversion-capable phenotypic equilibrium model seen in many other cancer models with a stem-like cell population [48,49]. The capacity for ALDH+ cells to be highly effective at generating ALDH+/- daughter cells suggested that they may be more capable of asymmetrical cell division - a type of division used by normal stem cells. ACD is known to result in non-random segregation of fate-determining factors and [49] template DNA segregation [13,14] [50]. We seeded single cell-sorted ALDH+/- cells and assessed the ALDH-status of the resulting daughter cells after one cell division. ALDH+ cells divided into an ALDH+ and one ALDH- daughter cells ~10-15% of the time, whereas this occurred less than 1% of the time for ALDH- cells (**M1-fig. 1e**). To confirm ALDH+ cell's disposition for ACD, we stained ALDH+ dividing cells for ALDH1A3, as well as BrdU pulse-chase assay [50], with both assays indicating that ~10% of ALDH+ cell divisions were asymmetrical in contrast to no observable ACD in ALDH- counterpart (**M1-fig. S1b to S1c**).

To deepen our characterization of ALDH+ versus ALDH- cells, we used FUCCI (*Fluorescent* Ubiquitination-based Cell Cycle Indicator) probes [51] to monitor cell-cycle and mitotic transitions in real-time (**M1-fig. 1f**). In both ALDH+ and ALDH- cells, most (>80%) daughter cells re-entered S-phase simultaneously (within 1h) of each other (**Video 1**), but in ALDH+ cells exclusively, in ~8% of cases, one of the daughter cells re-entered the cell cycle. In contrast, the other daughter cell remained non-proliferative for at least 12h (**Video 2, M1-fig. 1e-f, s1d).** Furthermore, analysis of FUCCI-expressing cells revealed that ALDH+ cells displayed a much higher rate of lagging chromosomes and anaphase bridges (**M1-fig. 1f**), leading to daughter

cells harboring visible micronuclei. To better resolve these CIN features, we used immunofluorescence imaging of fixed cells stained with DAPI/ALDH1A3 to quantify the rate of lagging chromosomes and micronuclei between ALDH+ and ALDH- cells. Per FUCCI-analysis, both these CIN indicators were significantly higher in THJ-16T ALDH+ cells (lagging chromosome: 26%, micronuclei: 23%) versus ALDH- cells (lagging chromosome: 9.8%, micronuclei: 6.8%) **(M1-fig. 1g, 1h)**. Similar trends were observed in THJ-11T cells.

NEDD9 is transcriptionally upregulated by ALDH1 enzymatic activity in ALDH+ cells and NEDD9/ALDH1A3 co-upregulation is correlated with thyroid cancer progression

Given that ALDH+ cells were relatively more prone to both ACD and CIN, we hypothesized that at least some of these features were likely due to differential regulation of centrosomes, since this organelle is intrinsically required to augment asymmetry in stem cells, as well as being a major cause of CIN by causing spindle defects during mitosis[13,14,19,20].

To explore this possibility, we examined an existing transcriptomic dataset comparing the expression patterns of ATC bulk cells (cells growing as monolayers) versus stem-like cancer cell-enriched (cells grown as tumorsphere) for genes that code for centrosome-located products [52]. Out of a set of 234 centrosome-related genes based on the text-based COMPARTMENTS database [53], using a cut-off of standardized value > 0.5, 21 genes were differentially downregulated in the stem-like fraction**.** At the same time**,** only 4 (TUBA1A, NEK7, HAUS6, and NEDD9) were upregulated **(**using an adjusted p-value threshold of <0.001**) (M1-fig. 2a, supplemental table 1)**. We opted to investigate NEDD9 as it is the only differentially-regulated gene with a known retinoic acid response element (RARE) in the promoter region 54, thus directly regulated by the retinoic acid enzymatic product of ALDH activity [54]. Analysis of several thyroid cancer cell lines revealed that the basal rate of %ALDH+ cells well-matches the overall level of NEDD9 in thyroid cancer models, with the aggressive ATC models having an overall higher rate of ALDH/NEDD9 compared to the less aggressive papillary thyroid cancer models (**M1-fig. 2b**).

Stimulation of the RAR pathway via all-trans-retinoic acid (ATRA) or retinaldehyde at 0.1μM induced *NEDD9* mRNA and protein expression in ALDH+ cells (**M1-fig. 2c, S2a**). Chromatin immunoprecipitation using anti-RARα antibody demonstrated a 2-fold enrichment of RARα comparing to IgG control at the NEDD9-RARE [54,55] (p=0.0115), but not at the NEDD9-exon region, confirming the direct binding of RARα to NEDD9-RARE in ALDH+ cells (**M1-fig.**

S2b). Reciprocal depletion of NEDD9 and ALDH1A3 showed NEDD9 to be downstream of ALDH1A3, consistent with the latter's function in synthesizing retinoic acid (**M1-fig. 2d**). Likewise, retinoic acid receptor alpha knockdown also led to reduced NEDD9 expression and attenuated retinoic acid induced NEDD9 expression (**M1-fig. S2c**). Collectively, these findings demonstrated that RAR signaling, supported by ALDH1A3's enzymatic activity, constitutively drives high expression of NEDD9 in ALDH+ ATC cells.

To extend the clinical significance of NEDD9/ALDH1A3 co-upregulation in ATC cell lines, we examined their protein expression in normal, papillary, and ATC patient tissues, using ki-67 as a control to confirm the high proliferation index of ATC tumors (**M1-fig. 2e**). Immunohistochemical staining of ALDH1A3 and NEDD9 on papillary thyroid cancer (n=5), and ATC samples (n=5); (**M1-fig. 2f**) revealed that both NEDD9 and ALDH1A3 were heterogeneously expressed in normal and cancerous thyroid tissues, with ATC tissues harboring visibly more cells with a high level of NEDD9 and ALDH1A3 **(supplemental table 2, 2f)**. Expression of ALDH1A3, and to a lesser extent NEDD9, in thyroid cancer tissues looked hierarchically distributed; where cells with a very high level of ALDH1A3 expression are relatively rare and surrounded by cells with a moderate and low level of ALDH1A3. Normal thyroid tissues exhibited mostly nuclear NEDD9-staining, whereas cytoplasmic and surface staining of NEDD9 increased from normal to PTC and more so in ATC. By performing linear correlation on NEDD9/ALDH1A3 mRNA expression in papillary thyroid cancer patients (TCGA, n=482), [56], we noted that *NEDD9* expression was positively correlated with *ALDH1A3* (Pearson = 0.375) (**M1-fig. 2g**), but not *CD44* or *CD133*: two other putative thyroid cancer stem-like cell marker. Also, *NEDD9* and *ALDH1A3* expression were positively correlated with lower thyroid differentiation scores, a more advanced cancer stage and the presence of extrathyroidal extension. Their expressions were also higher in the histological variants most likely to progress to ATC (tall cell) and lower in the variant less likely to progress (follicular) (**M1-fig. 2h**) [57-59]. Overall, these findings suggested that NEDD9/ALDH1A3 co-upregulation was correlated with thyroid cancer dedifferentiation and progression to ATC.

NEDD9-depletion disrupts centrosome asymmetry and asymmetrical cell division in ALDH+ ATC cells

To test if NEDD9 upregulation in ALDH+ cells impacted their centrosome characteristics, we visualized centrosomes of ALDH+ and ALDH- cells each treated with shRNA or CRISPR-mediated depletion of NEDD9. Centrosomes are composed of a pair of centrioles surrounded by pericentriolar material (PCM), including γ-tubulin, which acts as a nucleation site for the minus end of tubulin polymers [60-63]. Asymmetries in centrosome MTOC activity is a known requisite for ACD in many stem cell models, [9,14] so we began by assessing the asymmetries in γ-tubulin accumulation (via immunofluorescence intensity) (**M1-fig. 3a**) or microtubule growth organizing center (MTOC) activity (via microtubule regrowth assay. **fig 3b-e**) between the centrosome pairs. We remarked that ALDH+ cells, compared to ALDH- cells contained centrosomes with significantly more disparity in both γ-tubulin staining and microtubule regrowth rate at the two centrosome pairs. By co-staining for centriole/PCM, we noted that in most cases, two centrosomes with unequal levels of PCM contained an equal number of centrioles, indicating that the differences in MTOC activity we observed was not caused by an uneven aggregation of centrioles (**M1-fig. S3a**). Using GFP-tagged α-tubulin, we tracked the dynamics of centrosome MTOC activity in real-time, using the different metaphase spindle structure as a landmark "time 0". In ALDH- cells, both centrosomes began showing visible MTOC simultaneously, ~30 minutes before metaphase. In contrast, in ALDH+ cells, only one of the two centrosomes acquired visible MTOC activity before mitosis (**M1-fig. 3f, video 5**). Based on evidence from the microtubule regrowth and centrosome staining experiment, we saw that although shCT cells showed a centrosome with relatively weak MTOC, the distance between the two centrosomes at ~the late G2 stage was not affected, suggesting that the spindle formation dynamics we observed during live-cell imaging is due to a delayed formation of the second spindle, rather than delayed centrosome separation. NEDD9 knockdown in ALDH+ cells broke centrosome asymmetry, resulting in spindle forming dynamics resembling ALDH- cells (**M1-fig. 3f, video 6**).

To further consolidate our findings, we assessed whether the breaking of centrosome asymmetry would lead to ALDH+ cells losing the capacity to perform ACD. Indeed, FUCCI, BrdU chase, or ALDH1A3 partitioning experiments showed that shNEDD9 severely hampered ALDH+ cell's capacity to undergo ACD (**M1-fig. S1a-c**). Therefore, these findings collectively showed

that ALDH+ cells, through transcriptional upregulation of NEDD9, maintained asymmetrical centrosome activation dynamics typical of normal stem cells that are likely required for these cells to perform ACD.

NEDD9 inhibits the activation of a subset of supernumerary centrosomes to limit the severity of spindle multipolarity

Centrosome amplification is one of the major mechanisms which leads to CIN due to the potential spindle defects it introduces during mitosis; however, CIN, in this case, would only accumulate if viable daughter cells are produced following cell division [19]. Given that NEDD9 upregulation conferred distinct centrosome dynamics to ALDH+ cells, we hypothesized that an extension of this effect might impact the behavior of supernumerary centrosomes and thus CIN [19]. By staining for centriole pairs (centrin1) and PCM (pericentrin), respectively, we noted that compared to ALDH- cells, ALDH+ cells displayed significantly more centrosome amplification (19.6% vs. 6.5%) **(M1-fig. 4a-b)**. However, approximately a third of the supernumerary centrosomes in ALDH+ cells consisted of centriole pairs highly deficient in pericentrin or γ-tubulin, analogous to the weaker centrosome when only two centrosomes were present*;* this was in contrast to ALDH- cells, where centriole pairs were generally evenly nucleated **(M1-fig. 4a-b)**. Using centrosome-pair distance to control the interphase cell cycle stage, we measured PCM intensity during various cell cycle stages, finding that ALDH+ cells intrinsically possessed weaker PCM accumulation than ALDH- cells during G1 and G2 but is normalized by metaphase (**M1-fig. 4c-e**). NEDD9-depletion restored ALDH+ centrosome PCM levels during interphase, indicating that the weaker supernumerary centrosomes in ALDH+ cells are mediated by NEDD9 upregulation (**M1-fig. 4c-e**). Microtubule regrowth assay confirmed that the trends in centrosome MTOC activities matched PCM levels during interphase (**M1-fig. S3b**).

Next, we examined how ALDH-status and NEDD9 expression affected the configuration of the mitotic spindle. In THJ-16T ALDH+ cells, ~18% of metaphase cells exhibited a "pseudo-bipolar spindle configuration, 3% of metaphase cells are found in a multipolar spindle configuration, while the remainder were normal bipolar spindles **(M1-fig. 4f-g)**. In ALDH- cells, 4% of metaphase cells were pseudobipolar while 6% were multipolar, which indicates that although ALDH- cells exhibited fewer overall centrosome amplification, centrosome amplification in these cells was ~12-times more likely to manifest as multipolar spindles **(M1-fig.**

4g). Meanwhile, NEDD9 depletion in ALDH+ cells but not ALDH- cells led to a sharp increase in multipolar spindles (from 3 to 27%), concordant with decreased pseudo-bipolar spindles **(M1-fig. 4g, M1-fig. S4)**. Similar trends were confirmed in THJ-11T cells **(M1-fig. 4g)**. Using centrin/pericentrin co-staining, we ruled out these differences in spindle formation caused by centrosome fragmentation (**M1-fig. 5c**). We also ruled out that these phenotypes were not simply due to ALDH+ cells having intrinsically fragile spindles by benchmarking knockdown of CPAP- a master regulator of spindle pole integrity [16,64,65], which yielded no selectivity towards ALDH+ cells for spindle abnormalities (**M1-fig. S5**).

In ALDH+ control (shCT) cells that formed pseudo-bipolar spindles, we noted that ~70% of the centrosomes were located at the two pseudo-spindle poles, while the remaining ~30% were found dispersed generally around the metaphase plate **(M1-fig. 4f)**; notably, these non-polarized centrosomes appeared to possess minimal spindle forming capacity. Following NEDD9 knockdown, no "inactive" mitotic centrosomes were observed **(M1-fig. 4f)**. To better resolve this phenomenon, we performed microtubule regrowth assays and examined specifically the MTOC activity of supernumerary centrosomes during mitosis. Consistent with our spindle staining, we found ~30% of mitotic centrosomes in ALDH+ shCT cells, but not in ALDH+ shNEDD9 cells or ALDH- cells were non-polarized and lacked MTOC activity (**M1-fig. 4h,4i**). Collectively, our data show that NEDD9 limited the severity of multipolar spindles, likely by delaying the activation of supernumerary centrosomes.

NEDD9 facilitates supernumerary-centrosome-harboring ALDH+ cells complete mitosis and increases the rate of CIN

Centrosome amplification can only cause CIN propagation if the cell successfully divides rather than being arrested at metaphase by unresolvable multipolar spindles or eliminated through multipolar cell division[19]. Using centrin1/pericentrin co-staining, we observed that NEDD9 knockdown induced a sharp increase in the ratio of centrosome amplified cells at metaphase yet decreased supernumerary centrosomes in the later stages of mitosis (from 23% in ALDH+ shCT to 2% in ALDH+ shNEDD9) (**M1-fig. 5a-b**). This accumulation of centrosome amplification during metaphase indicates those cells are likely arrested at that stage.

Confirming this, live-cell imaging using eGFP-α-tubulin was used to examine the fate of cells that manifested multipolar spindles during mitosis. In ALDH+ cells, visible supernumerary centrosomes often did not migrate apart at the G2/M transition and instead remained tightly clustered before metaphase (-60'min to 0'min) **(M1-fig. 5d, video 7)**. Subsequently, ALDH+ shCT cells manifested a transient multipolar spindle during mitosis, observable only for one frame (-10') (**M1-fig. 5d, video 7**). Importantly, this transient multipolar spindle formation did not delay exit into the anaphase/telophase stage in many cases. In contrast, NEDD9-knockdown caused the supernumerary centrosomes to be more scattered at the G2/M transition (-60'min), resulting in the formation of multipolar spindles at metaphase (0'min) that persisted until cell death (-390'min) (**M1-fig. 5d, videos 8-9**). Quantifying the rate of these events, we found that ~5% of ALDH+ cells and ~35% of ALDH- cells manifesting multipolar spindles ended in unresolved mitotic arrest. After NEDD9-knockdown, these rates spiked to 80% for ALDH+ cells while remaining relatively unchanged (~30%) in ALDH- cells (**M1-fig. 5e**). Importantly, mitotic arrests were rarely observed in cells that only displayed two centrosomes, indicating mitotic defects occurred due to failures in resolving spindle multipolarity. These findings were consistent with the relative rate of pseudo/multipolar spindles measured in these groups (**M1-fig. 4g**) and support NEDD9 to be required for preventing unresolvable multipolar spindles.

To rule out the possibility that shNEDD9-induced mitotic arrest was only triggered by ectopic expression of eGFP-tubulin, we also assessed the incidence of mitotic arrest using FUCCI live-cell imaging. Following NEDD9 depletion, a spike in the mitotic arrest was observed (ALDH+ shCT **video 3,** ALDH+ shNEDD9**: video 4**) (from 14 $\pm$ 2% to 26 $\pm$ 4%) **(M1-fig. 5f-g)**, lasting between >6h and was followed by the disappearance of the nucleus rather than transition into G1 (Cdt1+ state), confirming that the fate of mitotically arrested cells is mostly cell-death, not mitotic slippage; furthermore, while chromosomes were visibly aligned at the metaphase plate, the clover-geminin probe was not degraded by the anaphase-promoting complex, indicative that mitotic arrest is likely triggered by the activation of the spindle assembly checkpoint[66] (**video 4**).

Lastly, we quantified the frequency of chromosome missegregation in ALDH+ versus ALDH- cells following NEDD9-depletion. While shNEDD9 did not substantially impact the rate of CIN in ALDH- cells (11.2%), it significantly reduced CIN (from 27% to 13%, $p<0.01$) in ALDH+ cells (**M1-fig. 5i-j**); this was consistent with our above observations that NEDD9-depletion selectively perturbed ALDH+ cell centrosome activation and prevented spindle

assembly in ALDH+ cells. Moreover, in agreement with the previous studies[19], anaphase cells that displayed centrosome amplification were ~3 times more prone to demonstrate CIN compared to cells with the normal number of centrosomes, indicating that the observed differences in CIN are primarily impacted by the fate of cells carrying supernumerary centrosomes during mitosis (**M1-fig. 5k**). These findings collectively indicate that ALDH+ cell's tolerance for CIN is contributed by their unique centrosome-activation dynamics favoring the successful completion of mitosis in cells with supernumerary centrosomes.

NEDD9 upregulation in ALDH+ cells inhibit the micronuclei-rupture stimulated DNA sensing pathway by limiting STING protein expression

The successful exit of mitosis following pseudobipolar spindle formation is required for CIN-propagation; however, this is not always sufficient, as lagging chromosomes often turn into micronuclei that can activate pro-apoptotic DNA sensing pathway [24-26]. Based on our data, ALDH+ cell's CIN tolerance could not be explained by a disparity in mitotic success rate between ALDH-/+ cells alone. Firstly, compared to ALDH- cells, ALDH+ cells harboring micronuclei were significantly more resistant to spontaneously interphase cell death (**M1-fig. 5g**). As these cell deaths occurred in cells in the S/G2 phase, this points to their death not simply being a delayed outcome of defective mitoses (**M1-fig. 5g, 5a**). Secondly, when arrested during metaphase, ALDH+ cells had a much longer mitotic life span than ALDH- cells (average time in mitosis before cell death: ALDH+ 12.5h, ALDH- 5h) (**M1-fig. S6a**). These observations suggest ALDH+ cells to have somehow attenuated cGAS-STING (cyclic GMP-AMP synthase-stimulator of interferon genes) signaling, as recent studies reveal this primordial pathway can link micronuclei to pro-apoptotic signaling [24-26] and accelerate cell death during mitotic arrest [67].

Since the cGAS-STING pathway can be rate-limited by their expression[68], we started by probing for the respective protein levels of these two proteins in ALDH+ and ALDH- cells and found that ALDH+ cells expressed drastically less STING protein but not cGAS (**M1-fig. 6b**). Remarkably, NEDD9 depletion in ALDH+ cells restored STING to a level comparable to ALDH- cells (**M1-fig. 6b**), observed in several ATC models (**M1-fig. 6c**). STING expression levels are factors that tune the magnitude of downstream TBK1-STAT1 signaling and type I IFN signaling [68]. To probe if shNEDD9 promoted STING pathway activation across ATC models, we used an interferon-β reporter system, observing that shNEDD9 indeed led to increased IFN-β transcription in THJ-11T, THJ-16T, and 8505c cells (**M1-fig. 6d**). qPCR and western blot were used to validate

that interferon-stimulated gene (ISG) expression and pTBK1 and pSTAT1 activation-induced shNEDD9, indicating that the canonical STING pathway is activated by NEDD9-depletion (**M1-fig. 6f**). Moreover, ALDH+ cells with intact levels of NEDD9 were insensitive to low doses of dsDNA, whereas the same dose of dsDNA was sufficient to stimulate ISG transcription in shNEDD9 cells, indicating that shNEDD9 could overcome STING quiescence in ALDH+ cells (**M1-fig. 6e**).

Consistent with these observations, shNEDD9 also enabled a more sustained stimulation of pTBK1 and pSTAT1 activation in response to dsDNA, as well as damaged self-DNA caused by cisplatin [69] (**M1-fig. 6f)**. Overexpression of STING alone, via a puno1 expression vector, was sufficient to stimulate the STING pathway without perturbing NEDD9, confirming STING expression as a key limiting factor for STING pathway activation (**M1-fig. 6g**). Furthermore, CRISPR-mediated STING knockout (STING-KO) could completely ablate shNEDD9-induced IFN-β reporter activity, indicating that STING upregulation alone could account for shNEDD9-induced IFN-β expression (**M1-fig. 6h**). As such, our findings reveal that NEDD9 suppresses STING pathway activation in ALDH+ cells by limiting the protein levels of STING.

Micronuclei-induced STING activation occurs due to micronuclei membrane rupture and subsequent recruitment of cGAS to those micronuclei [24,70,71]. To test if the endogenous ligands that activate the STING pathway in these cells are, in fact, the micronuclei, we exploited the overexpression Lamin B2 (LMNB2) approach, which could reinforce micronuclei membranes to minimize DNA leakage without substantially perturbing the nuclear membrane [24,70-72]. By overexpressing LMNB2 using a PCVM6 expression vector, we found that LMNB2 overexpression alone was remarkably sufficient to block most cGAS-micronuclei localization (~70% to ~15%) in both THJ-11T and THJ-16T cells (**M1-fig. 6i-j**). Using immunofluorescence imaging, we observed that both THJ-11T and THJ-16T cells displayed a comparatively high rate of cGAS positivity (50-60%) in micronuclei (**M1-fig. 6i-j**), and there was no discernable difference in micronuclei-cGAS-positivity following NEDD9-depletion (**M1-fig. 6j).** Furthermore, overexpression of LMNB2 was sufficient to negate shNEDD9-induced ISG (*IFNB1* and *TNF*) expression, indicating micronuclei rupture is indispensable for STING pathway activation following NEDD9-depletion (**M1-fig. 6k**). Taken together, these findings show that NEDD9 in ALDH+ cells limits cGAS-STING pathway activation, including its activation via micronuclei, by maintaining low STING protein levels.

shNEDD9-induced STING activation suppresses ALDH+ cell growth independently from shNEDD9-induced spindle multipolarity

Our above findings established that NEDD9 suppresses STING pathway activation in ALDH+ cells. Moreover, shNEDD9 resulted in increased sensitivity to growth-inhibition by dsDNA or cisplatin, implicating STING in shNEDD9-mediated growth inhibition **(M1-fig. S6b)**. We sought to investigate the impact of this NEDD9-micronuclei-STING relationship in regulating ALDH+ cell apoptosis. In ALDH+ cells with intact levels of NEDD9 (ALDH+ shCT cells), dsDNA treatment failed to induce apoptosis, consistent with these cells being in an intrinsically STING-quiescent state. NEDD9-depletion in ALDH+ cells led to a 4-fold increase in the basal rate of apoptosis (from 3% to 12%) and even further sensitized cells to dsDNA-induced apoptosis (from 12% to 17%) (**M1-fig. 7a**). Notably, STING-KO completely negated the additional apoptosis induced by dsDNA and significantly attenuated shNEDD9-induced apoptosis, confirming that STING plays an essential role in shNEDD9-mediated apoptosis (**M1-fig. 7a**). Consistently, overexpression of STING alone could also elevate the apoptosis rate (from 3-9%) (**M1-fig. 7b, S6d**). Furthermore, like STING-KO, LMNB2 overexpression also attenuated shNEDD9-induced apoptosis by a comparable amount (from 12% to 6%) (**M1-fig. 7c, S6e**). The comparable magnitude by which STING-KO and LMNB2 overexpression attenuated shNEDD9-induced apoptosis suggests that the STING-dependent portion of shNEDD9-induced apoptosis was potentiated mostly via micronuclei-rupture.

Therefore, our above findings show that shNEDD9 causes STING-dependent upregulation of interferon genes, known to have growth-impairing effects via an autocrine/paracrine mechanism [70,73-75]. To isolate any putative paracrine effects, we tested if conditioned media (CM) derived from shNEDD9 or STING-overexpression cells would negatively impair the growth of untreated cells (**M1-fig. 7d**). ELISA assay was used to confirm a significant increase in IFN-β concentration in the shNEDD9 CM compared to shCT CM **(M1-fig. 7e)**, consistent with the upregulation of the IFNB1 gene observed via qPCR analysis **(M1-fig. 6d-e)**. We found that for both THJ-11T and THJ-16T cell lines, CM derived from shNEDD9 impaired cell growth by ~30% after two days compared to CM derived from shCT. This effect could be abolished by the addition of IFN-β antibody to shNEDD9-derived CM, indicating that shNEDD9 cell-derived CM can cause growth

inhibition via STING-upregulation induced IFN-β secretion (**M1-fig. 7f**). In addition to this paracrine mechanism, STING can also affect cell growth by shortening the time to cell death in mitotically arrested cells [67]. We observed that in control cells, shNEDD9 (which induced STING upregulation) shortened the time to cell death of mitotically arrested cells from 11.2h to 8.4h. STING-KO extended the time to mitotic cell death for both groups to 13.2h (**M1-fig. S6b**).

Although we observed that STING-KO slightly extended the life of mitotically arrested cells, we did not observe significant changes to the rate at which multipolar spindles arise, as both control and STING-KO experienced a similar rate multipolar spindle-induction following shNEDD9 treatment (**M1-fig. 7g**). Consistently, STING-KO also did not impact shNEDD9-induced centrosome hyperactivation (**M1-fig. 7h**). STING-KO caused a minor increase in multipolar spindle frequency (**M1-fig. 7g**), ruling out shNEDD9-induced multipolar spindles to be dependent on STING-upregulation. Furthermore, STING-KO did not influence the rate of chromosome bridge or lagging chromosomes during anaphase, implying that this effect is tied to NEDD9's regulation of centrosome dynamics but not STING (**M1-fig. 7i**). These findings suggest that NEDD9's suppression of STING could be isolated from its suppression of spindle multipolarity, consistent with the above observation that STING-KO could not completely abrogate NEDD9-induced apoptosis yet could completely abrogate dsDNA-induced apoptosis (**M1-fig. 7a**).

As shNEDD9-induced spindle multipolarity and STING activation are both processes that could potentially lead to loss of micronuclei-bearing cells, we tested if STING-KO would impact the frequency of micronuclei bearing cells. We tracked the frequency of micronuclei-bearing cells in control and STING-KO, finding that STING-KO could only partially attenuate shNEDD9-mediated micronuclei loss. We then blocked the cells from entering mitosis using a double-thymidine block to arrest them at the S-phase, preventing micronuclei-bearing cells from being eliminated via multipolar-mediated mitotic arrest (**M1-fig. 7j**). Thymidine blocking was also insufficient to block shNEDD9-induced micronuclei depletion; however, a combination of STING-KO and thymidine block could abrogate most shNEDD9-induced micronuclei loss (**M1-fig. 7j**). These findings are consistent with the notion that NEDD9 has two distinct functions (centrosome dependent and STING dependent), enabling ALDH+ cells to tolerate CIN-imposed growth challenges (**M1-fig. 7k**).

NEDD9-depletion selectively eliminates ALDH+ ATC cells and attenuates ATC spherogenic and tumor seeding potential

Since our data suggested that NEDD9 was essential for ALDH+ ATC cells to tolerate CIN, it could be expected that depletion of NEDD9 would selectively eliminate this stem-like cell population. Indeed, NEDD9-knockdown in ATC cell lines THJ-11T and THJ-16T (**M1-fig. 8a**) caused rapid depletion of ALDH+ cells in an unsorted population (eliminating >90% of ALDH+ cells within 7days) (**M1-fig. 8b**). Consistent with our above results, STING-KO only partially rescued shNEDD9-induced %ALDH+ cell loss (**M1-fig. 8c**). As with shNEDD9-hairpin, CRISPR-mediated NEDD9-KO, but not shCPAP, also selectively eliminated ALDH+ cells in multiple ATC models (**M1-fig. 8d**). Neither NEDD9 depletion nor overexpression impacted ALDH- cell growth (**M1-fig. 8e**), nor did NEDD9-depletion affect %ALDH+ cells or microtubule nucleation in the non-transformed MCF10a cell line **(M1-fig. S7).** These findings confirm that ALDH+ ATC cells, which exhibit a high degree of CIN (**M1-fig. 1g-h**), are dependent on NEDD9 to sustain long-term growth.

To test if NEDD9 loss also led to a loss of stem-like properties, we tested the impact of NEDD9 on spherogenesis and tumorigenesis. NEDD9-knockdown significantly reduced tumorsphere forming potential of ALDH+ cells within seven days, while in comparison, NEDD9 overexpression in ALDH- cells did not significantly impact tumorsphere formation (**M1-fig. 8f**). Furthermore, via the limiting dilution transplantation assay [76], we found that $1x10^5$ shCT cells produced tumors in 3/5 mice. In contrast, it took $5x10^5$ shNEDD9 THJ-16T cells to seed 3/5 tumors (**M1-fig. 8h-i**), indicating that NEDD9-depletion reduced the tumor-initiating capacity by ~80%.

NEDD9-depletion in ATC xenografts inhibits tumor growth, eliminates ALDH1A3 positive cells, promotes STING activation, and reduces chromosome missegregation

To recapitulate our cell-based observations *in vivo*, we engineered THJ-11T and THJ-16T cells to express doxycycline-inducible NEDD9-knockdown (pLKO-tet-shNEDD9-2; shNEDD9-2 being a second shRNA construct targeting the same gene as shNEDD9) **(M1-fig. S8** for *in vitro*

characterization). We implanted THJ-11T and THJ-16T pLKO-tet-shNEDD9-2 stable cells subcutaneously into NOD-SCID mice and added doxycycline in their drinking water for seven days later. A significant decline in tumor growth rate was observed in the doxycycline-treated groups for both THJ-11T (p=0.037) and THJ-16T (p=0.007) xenograft monitored for 17 and 42 days (post-doxycycline treatment), respectively **(M1-fig. 9a-b**).

To mitigate interference from mouse stromal cells, we used flow cytometry measurements combined with human leukocyte antigen (HLA) staining to isolate THJ-11T/THJ-16T cells. Western blot analysis of HLA-positive sorted tumor cells confirmed dox-treatment to induce NEDD9-depletion concomitant with an upregulation of STING and STAT1 phosphorylation, consistent with our cell-based results (**M1-fig. 9c**). Flow cytometric measurement showed a significant decrease in HLA+ positive %ALDH+ cell for doxycycline-treated THJ-11T tumor (p= 0.022) and THJ-16T tumor (p=0.044) **(M1-fig. 9d, S8)**. These trends were confirmed using immunohistochemical staining of THJ-11T tumors, showing that highly positive ALDH1A3 cells were generally found in clusters and appeared surrounded by assorted moderately positive and ALDH1A3-negative cells, consistent with a cancer stem cell hierarchical model and our previous observation of ALDH1A3 cells having the capacity to divide asymmetrically (**M1-fig. 9e**). While this cannot discern the phenotypic impact of STING activation, particularly as this is an immunocompromised mouse model, it does indicate that NEDD9-depletion in ATC cells increases ATC tumor cell-autonomous STING activation along with decreased ALDH+ cell population.

Lastly, we assessed whether NEDD9-depletion impacts ATC tumor CIN levels. Micronuclei rates could not be precisely measured due to the potential of stromal cells infiltration; therefore, we focused on scoring only mitotic cells since they would likely encompass ALDH+ tumor cells (an assumption based on *in vitro* observation that THJ-11T ALDH- sorted cells are much less proliferative). We scored the impact of NEDD9-depletion on the relative rate of three mitotic events: cells in metaphase, cells post-metaphase (anaphase or later) exhibiting no chromosome missegregation, and cells post-metaphase exhibiting chromosome missegregation in THJ-11T cells **(M1-fig. 9f)** (THJ-16T dox-treated tumors were too small to score adequately). Our findings showed that doxycycline treatment caused a significant increase in the percentage of THJ-11T tumor cells in metaphase (from 75% to 85%, p=0.0321) and a decrease in post-metaphase cells exhibiting chromosome missegregation (from 17% to 4%, p=0.0013) (**M1-fig. 9g**), which is suggestive of the same metaphase-arrest mediated inhibition of CIN as observed during our cell-

based assays. Collectively, our finding indicates that loss of NEDD9 results in the elimination of stem-like cells and reduction in CIN rates in ATC tumors.

Stemness-associated centrosome genes upregulation correlates with aneuploidy in multiple solid tumor types

As our findings indicate that stem-like cancer cells can extend centrosome regulatory networks to acquire tolerance to CIN, we hypothesized that stemness-related centrosome genes might be able to predict aneuploidy in cancer patients. We parsed a list of 187 genes associated with a conserved stemness program [77] for centrosome-related genes (out of 162 COMPARTMENT [53] selected genes, shown in **M1-fig. 2a**). To minimize confounding factors that may arise from genes that are part of CIN-promoting gene signatures, we omitted any candidate overlapped with the CIN70 gene list[78]. This process led to a list of 7 "stemness-associated centrosome genes" (CDC25A, HAUS6, BUB1B, DLGAP5, CENPE, KIF11, KIF23) (**M1-fig. 10a, supplemental table 3**). Using breast cancer as a reference, we found that this set of stemness-associated centrosome genes was strongly correlated with aneuploidy (Spearman correlation vs. fraction genome altered >0.3) (**M1-fig. 10b**). By contrast, neither the stemness-related gene sets nor centrosome-related gene sets alone were effective as aneuploidy predictors (**M1-fig. 10b**). Upregulation of these genes is collectively correlated with aneuploidy across multiply types of human cancer, including sarcoma, breast, pancreatic, lung, and prostate cancer, illustrating the broad relevance of stemness-related centrosome genes upregulation to tumor genomic stability (**M1-fig. 10c**). These seven genes were often collectively upregulated in patients with a high degree of tumor aneuploidy but rarely mutated (**M1-fig. 10d**). Anaplastic thyroid cancer, a rare disease, does not have an existing transcriptomic dataset available for analysis; however, it has been observed that progression to ATC involves increased acquisition of both stemness and CIN[79], suggesting that these above trends may also hold for this disease.

Discussion

Recent studies using next-generation sequencing to characterize the genomic landscape of ATC has been a boon for identifying key driver mutations that enables their progression [80-83]. These findings show that ATC's landscape is highly diverse, consisting of extensive copy number

changes in many driver mutations, both common (e.g., p53, TERT[80-83]) and uncommon. A high mutation burden is clearly a hallmark of ATC that contributes to their difficult treatment, but how the thyroid cancer progresses from differentiated cells with low mutational burden to this state is largely unclear. Our findings offer critical insight into ATC pathogenesis by linking dedifferentiation/stemness - a common endpoint of cancer progression - to tolerance of CIN, a key source of large-scale mutagenesis.

This study illustrates that the ALDH+ cancer stem cell-like subpopulation in anaplastic thyroid cancer is uniquely tolerant to CIN, which was achieved by suppressing spindle multipolarity and STING activation. We showed that these effects could be dissociated, as STING-KO could rescue shNEDD9-induced micronuclei depletion, but not shNEDD9-induced centrosome multipolar spindles or chromosomal missegregation. As micronuclei formation is a common consequence of chromosomal missegregation caused by transient multipolar spindles, these two cell-protective effects serve complimentary roles during mitosis and interphase, respectively, to ensure the survival of ALDH+ cells. This survival advantage offered to ALDH+ cells under the pressure of persistent CIN may explain the high ratio of ALDH+ stem-like cells observed in anaplastic thyroid cancer compared to less aggressive thyroid cancer subtypes.

Although NEDD9 is known to be a centrosome regulating factor, how it affected centrosomes in ATC models was unexpected. Previous studies conducted in the luminal breast cancer cell line MCF-7 showed that NEDD9 expression was cell-cycle-dependent and promoted centrosome maturation by activating Aurora Kinase A and Nek2 - kinases which act as key regulators of centrosome replication and maturation [84]. In MCF-7 cells, NEDD9-knockdown caused monoastral spindles, whereas, in THJ-16T cells, NEDD9-knockdown had no effect in ALDH- cells while promoting centrosome activation in ALDH+ cells. Notably, unlike our ATC models, MCF7 cells are relatively well-differentiated with a low population of aldefluor-positive cells[85]. These disparities highlight the context-sensitive nature of NEDD9 [45].

The involvement of STING in this study was an unexpected departure from the initial premise of centrosome-specific phenotypes and illustrates that ALDH+ cells have at least two distinct mechanisms that promotes CIN-tolerance. Recent studies indicate that the stemness program is generally associated with immune suppression [86 87], which agrees with our finding that ALDH+ cells have innately attenuated STING expression. NEDD9's dual involvement in DNA

sensing and centrosome activation is not entirely surprising since the components of the canonical STING pathway, cGAS, and TBK1 localize at the centromere and centrosomes, respectively [88] [89].

The seven stemness-associated centrosome genes (CDC25A, HAUS6, BUB1B, DLGAP5, CENPE, KIF11, KIF23) included kinetochore-related (CENP-E, BUB1B) or spindle-related proteins [90]; thus, them having impact on CIN/aneuploidy is unsurprising. What is more interesting is that the predictive value of these genes on aneuploidy is not universal but appears to pertain only to some cancer subtypes. Moreover, in most cases, the individual predictive value of these seven genes for aneuploidy is consistent with one another (i.e., in cases where one has no predictive value, the rest do not either). These two factors favor the interpretation that these genes predict aneuploidy not necessarily through their direct function (in which case they would be more universal in their prediction of aneuploidy) but rather associated with a stem cell-related centrosome program. These patterns hint at the existence of a conserved stem cell-derived centrosome regulatory program that promotes cancer aneuploidy in certain cancer types, consistent with our primary finding here that stem-like ATC cells demonstrate a centrosome activation dynamic that resembles typical stem cell models.

Our results broaden the scope of how cancer stem cells can promote intratumoral heterogeneity. The existing paradigm largely follows the notion that cancer stem-like cells, via their potential to produce daughter cells of different cellular hierarchy, act can as a non-genetic source of intratumoral heterogeneity and independently from clonal evolution[2]. Our results propose that, by acquiring CIN tolerance through their unique centrosome regulatory pathways, ATC cancer stem-like cells could, in certain content, also become potent sources of genomic instability, thereby elevating their importance as therapeutic targets.

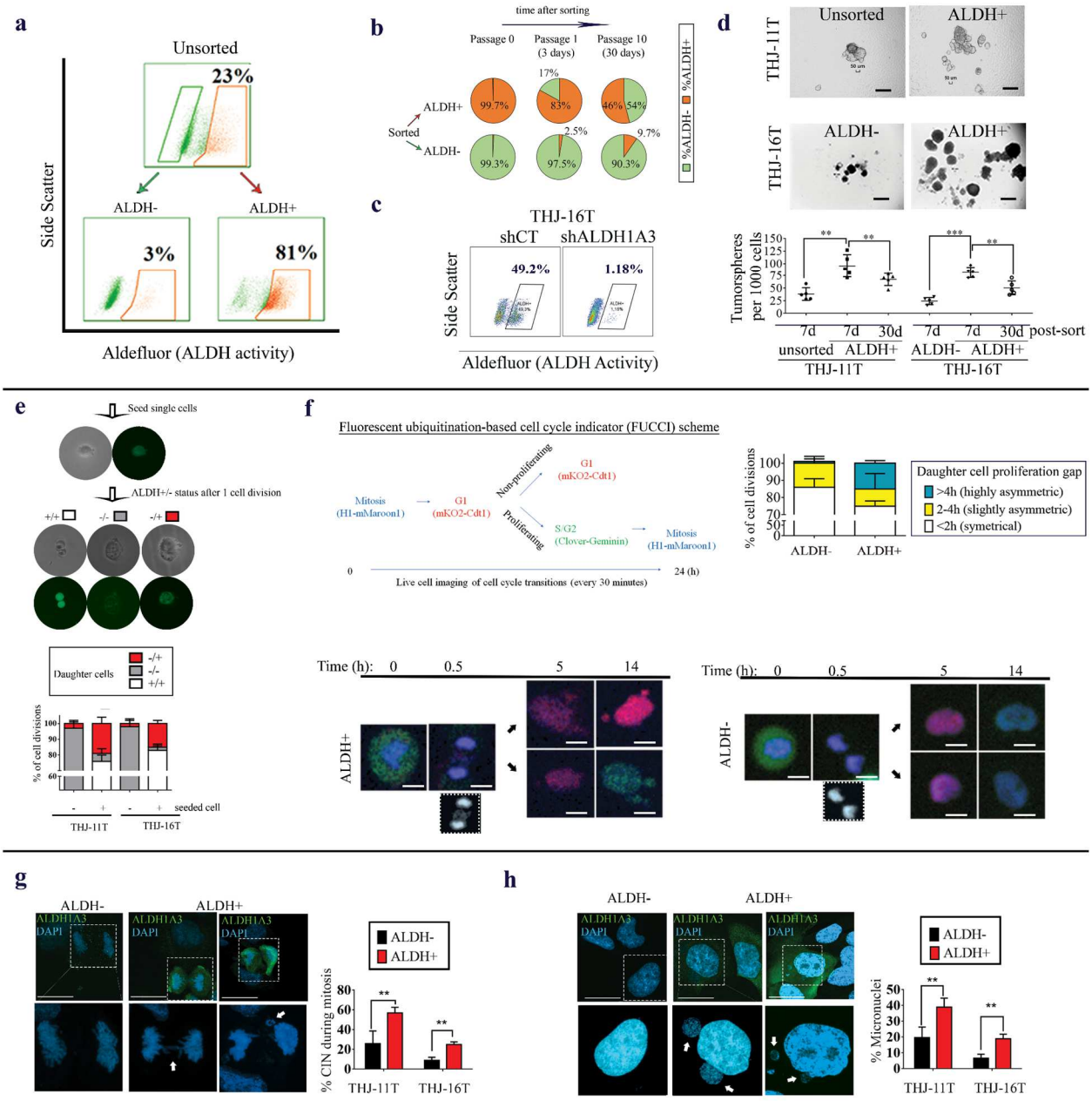
a
Unsorted
23%
Side Scatter
ALDH-
ALDH+
3%
81%
Aldefluor (ALDH activity)
b
time after sorting
Passage 0
Passage 1 (3 days)
Passage 10 (30 days)
Sorted
ALDH+
ALDH-
99.7%
17%
83%
46%
54%
99.3%
2.5%
97.5%
9.7%
90.3%
%ALDH-
%ALDH+
c
THJ-16T
shCT
shALDH1A3
Side Scatter
49.2%
1.18%
Aldefluor (ALDH Activity)
d
THJ-11T
Unsorted
ALDH+
THJ-16T
ALDH-
ALDH+
Tumorspheres per 1000 cells
7d
7d
30d
7d
7d
30d
post-sort
unsorted
ALDH+
ALDH-
ALDH+
THJ-11T
THJ-16T
e
Seed single cells
ALDH+/- status after 1 cell division
+/+
-/-
-/+
Daughter cells
-/+
-/-
+/+
% of cell divisions
seeded cell
THJ-11T
THJ-16T
f
Fluorescent ubiquitination-based cell cycle indicator (FUCCI) scheme
Mitosis (H1-mMaroon1)
G1 (mKO2-Cdt1)
Non-proliferating
Proliferating
G1 (mKO2-Cdt1)
S/G2 (Clover-Geminin)
Mitosis (H1-mMaroon1)
0
24 (h)
Live cell imaging of cell cycle transitions (every 30 minutes)
% of cell divisions
ALDH-
ALDH+
Daughter cell proliferation gap
>4h (highly asymmetric)
2-4h (slightly asymmetric)
<2h (symetrical)
Time (h): 0 0.5 5 14
ALDH+
Time (h): 0 0.5 5 14
ALDH-
g
ALDH-
ALDH+
ALDH1A3
DAPI
% CIN during mitosis
ALDH-
ALDH+
THJ-11T
THJ-16T
h
ALDH-
ALDH+
ALDH1A3
DAPI
% Micronuclei
ALDH-
ALDH+
THJ-11T
THJ-16T

M1-Figure 1: ALDH+ cancer stem-like cells exhibit stem-like features, asymmetry, and harbours higher rate of chromosomal instability

a. Depiction of FACS scheme where the patient-derived anaplastic thyroid cancer cell line THJ-16T cells was sorted into ALDH+ and ALDH- sub-cell lines. The number represents the %ALDH+ cell. **b.** Pie chart illustrating the %ALDH+ cell in sorted THJ-16T cells after 1 or 10 passages, each passage corresponding to 3-4 days. **c.** Impact of ALDH1A3-knockdown on ALDH enzymatic activity detected via aldefluor **d**: Representative image and quantification (n=3) of the relative tumorsphere forming capacity of THJ-11T/16T unsorted, ALDH- or ALDH+ FACS sorted cells seeded after 7 or 30 days in culture; 300 cells were seeded for THJ-16T, 200 cells was seeded for THJ-11T. Images were taken after 7 days, using 10x magnification. Scale bar = 100µm. **e.** Assessment of asymmetrical cell division based on ALDH+ status of daughter cells. Single ALDH+/- sorted THJ-11T or THJ-16T were seeded at 1 cell per well. The ALDH-status of daughter cells after 1 cell division is assessed by aldefluor and visualized by fluorescence microscopy. Divisions that produce 1 ALDH+ and 1 ALDH- daughter cells are considered asymmetrical. **f.** Schematic representing the strategy to discern the impact of NEDD9-knockdown (from t=24h to 48h) on cell cycle progression using FUCCI probes. Cell cycle transition between G1 and S is tracked by the expression of the replication licensing factors Ctd1 and Geminin, and mitosis is visualized using the linker histone H1.0. Cell cycle transitions is kinetically measured by live-cell time-lapse imaging of FUCCI-expression THJ-16T cells. Quantification for ratio of symmetrical and asymmetrical outcomes defined by the timing gap between two daughter cells re-expressing geminin (entering proliferative S-phase) following mitotic exit. Asymmetrical outcomes are defined by a timing gap >4h, while a symmetrical outcome is defined by timing gap <2h. Gaps between 2-4h are considered ambiguous. Representative images illustrate completed mitosis in ALDH+ and ALDH- sorted THJ-16T cells. The greyscale image shows only H1.0 to illustrate the presence of DNA materials in the anaphase midzone during mitosis, indicative of chromosomal missegregation. **g.** Representative image (THJ-16T cells) and quantification (THJ-16T and THJ-11T cells) of the ratio of ALDH+ cells and ALDH- cells (THJ-16T cells) exhibiting chromosomal missegregation (chromosome bridge or lagging chromosome) by the detection of apparent DNA strands during or following separation of the sister chromatid pairs. At least 100 mitotic cells were quantified for each group. Scale bars = 10µm. h**.** Representative image and quantification (THJ-16T and THJ-11T cells) of the ratio of ALDH+ and ALDH- cells harbouring visible micronucleus. At least 100 mitotic cells were quantified for each group. Micronucleis are defined as rounded DAPI positive structures less than one-third the diameter and with similar intensity/texture/plane as the nucleus For d-e, ALDH+ status is determined by first pre-sorting, and then further confirmed by ALDH1A3 staining. Scale bars = 10µm. Error bars represent $\pm$ SD. n= # of biological replicates.

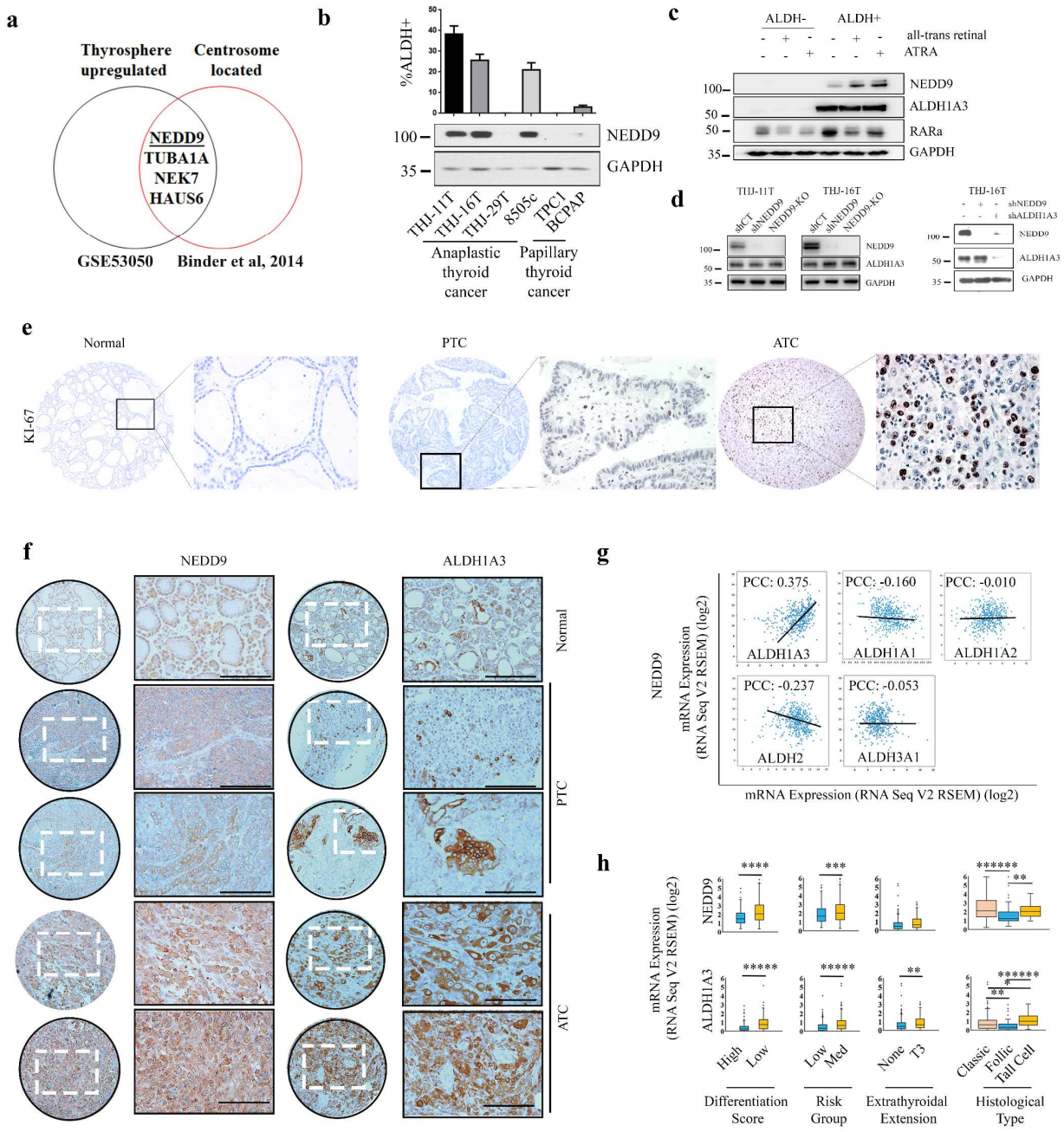
a
Thyrosphere upregulated
Centrosome located
NEDD9
TUBA1A
NEK7
HAUS6
GSE53050
Binder et al, 2014
b
%ALDH+
NEDD9
GAPDH
THJ-11T
THJ-16T
THJ-29T
8505c
TPC1
BCPAP
Anaplastic thyroid cancer
Papillary thyroid cancer
c
ALDH-
ALDH+
all-trans retinal
ATRA
NEDD9
ALDH1A3
RARa
GAPDH
d
THJ-11T
THJ-16T
shCT
shNEDD9
NEDD9-KO
shALDH1A3
e
Normal
PTC
ATC
KI-67
f
NEDD9
ALDH1A3
Normal
PTC
ATC
g
NEDD9
mRNA Expression (RNA Seq V2 RSEM) (log2)
PCC: 0.375
PCC: -0.160
PCC: -0.010
PCC: -0.237
PCC: -0.053
ALDH1A3
ALDH1A1
ALDH1A2
ALDH2
ALDH3A1
h
High
Low
Low
Med
None
T3
Classic
Follic
Tall Cell
Differentiation Score
Risk Group
Extrathyroidal Extension
Histological Type

M1-Figure 2: NEDD9 is upregulated in ALDH+ cancer stem-like cells and NEDD9/ALDH1A3 co-upregulation correlates with thyroid cancer progression

a. Pie chart representing the identification of centrosome-related genes (based on the COMPARTMENT text-based dataset using a threshold limit of >0.5) that were upregulated in THJ-11T tumorspheres (compared to cells grown as monolayers, based on GSE53050). List of genes and changes can be found in the supplemental data. **b.** Bar flow cytometry measurement of %ALDH+ cell ratio (n=3) and western blot images of NEDD9 protein expression levels in a panel of anaplastic and papillary thyroid cancer cell lines **c.** Western blot analysis illustrating the impact of 0.1uM retinaldehyde or retinoic acid (treated for 24h) on NEDD9 expression in THJ-16T cells. **d**. Impact of shRNA mediated NEDD9, CRISPR-mediated NEDD9-KO, or ALDH1A3 knockdown on their expression in ALDH+ cells; the levels were checked at t=24h. **e.** Representative KI-67 staining illustrating that ATC samples display characteristically high proliferation index **f.** Representative images of ALDH1A3 and NEDD9 immunohistochemistry staining in normal, PTC, and ATC patient samples. Images were captured at 20x and 40x magnification scale bar = 50μm**. g.** Correlation analysis for mRNA expression of NEDD9 and ALDH (multiple isoforms), using Pearson's Correlation Coefficient (PCC). Graph generated using cBioportal [91 92]. **h.** Box and whisker plot comparing *NEDD9* and *ALDH1A3* expression between papillary thyroid cancer patients categorized based on thyroid differentiation score (high > 0.5, *n=136*; low <-0.5, *n=156*), risk group as defined by MACIS (low = low risk, *n=166;* med = intermediate risk, *n=252*), extrathyroidal extension (none = no extension, *n=309*; T3 = minimal extension, *n=117*), or histological subtype (follic = follicular)

IHC images were taken using Leica DM LB2 at the noted magnification. **g-h** are based on the dataset: TCGA, Cell 2014[56], *n=486*. Statistical significance was determined using two-tailed Student's t tests (*P<0.05, **P<0.01, ***P<0.001).

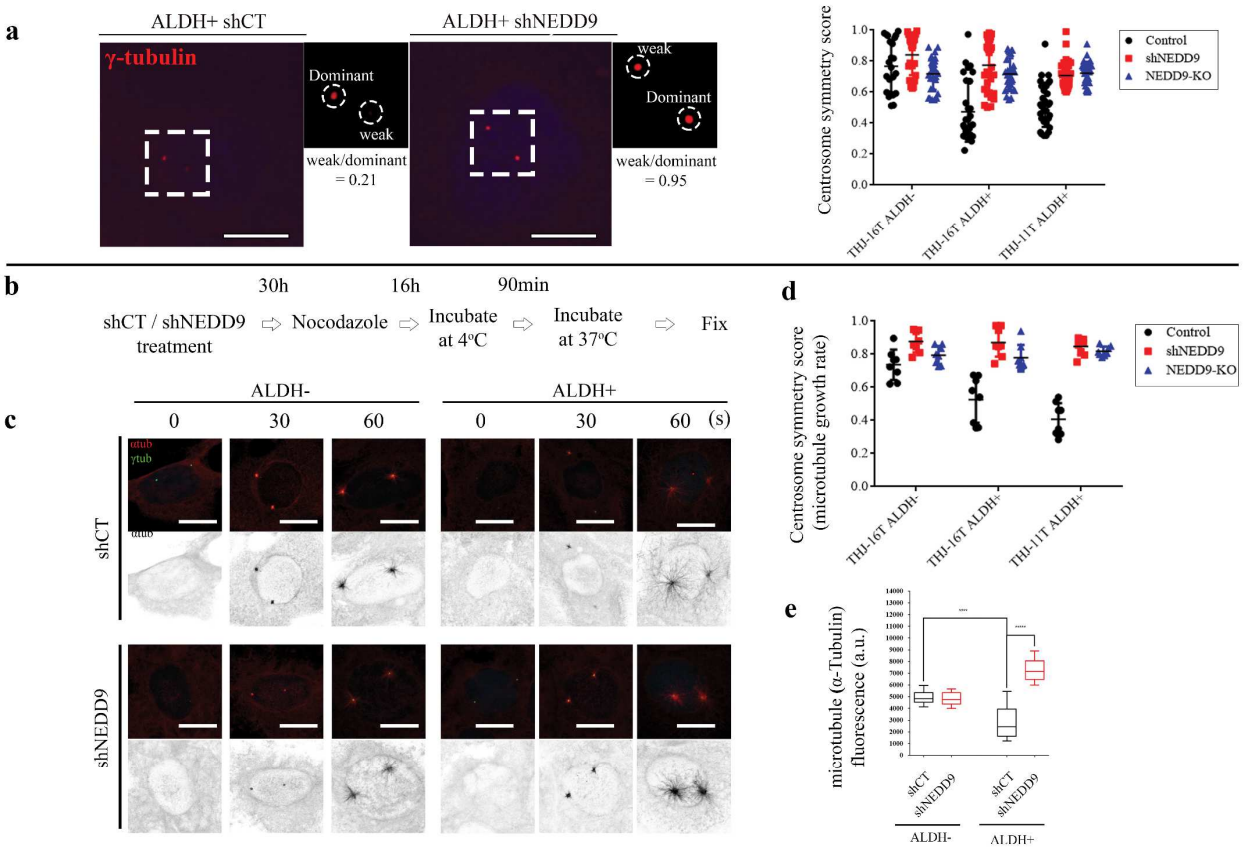
a
ALDH+ shCT
ALDH+ shNEDD9
γ-tubulin
Dominant
weak
weak/dominant = 0.21
weak
Dominant
weak/dominant = 0.95
Centrosome symmetry score
Control
shNEDD9
NEDD9-KO
THJ-16T ALDH-
THJ-16T ALDH+
THJ-11T ALDH+
b
30h
16h
90min
shCT / shNEDD9 treatment
Nocodazole
Incubate at 4°C
Incubate at 37°C
Fix
c
ALDH-
ALDH+
0
30
60
(s)
shCT
shNEDD9
αtub
γtub
d
Centrosome symmetry score (microtubule growth rate)
e
microtubule (α-Tubulin) fluorescence (a.u.)
shCT
shNEDD9
ALDH-
ALDH+

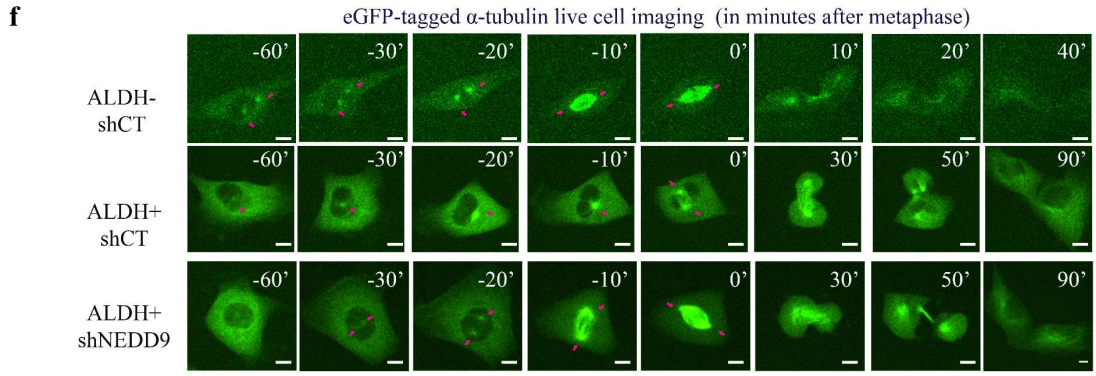
f
eGFP-tagged α-tubulin live cell imaging (in minutes after metaphase)
ALDH- shCT
ALDH+ shCT
ALDH+ shNEDD9
-60'
-30'
-20'
-10'
0'
10'
20'
30'
40'
50'
90'

M1-Figure 3. NEDD9-depletion disrupts asymmetrical centrosome behavior in ALDH+ cells

a. Representative immunofluorescence image and quantification of γ-tubulin symmetry by calculating the ratio of γ-tubulin intensity between centriole pairs (formula: intensity of weak centrosome / intensity of strong centrosome) **b.** Experimental scheme of microtubule regrowth assay **c.** Representative images of microtubule regrowth at 3 different timepoints following nocodazole washout. α-tubulin images were color-inverted to grayscale for visual clarity. **d.** Quantification of centrosome microtubule nucleation asymmetry (formula: intensity of weak centrosome / intensity of strong centrosome), 60seconds after induction of microtubule regrowth. At least 30 centrosomes were used to determine microtubule growth rate for each condition, n=3. Centrosome pairs that were >4μm apart but still within the edge of the nucleus, where the nucleus was still uncondensed was selected. **e.** Quantification of relative centrosome microtubule-nucleation activity based on intensity of tubulin staining. **f.** Live cell time-lapse of eGFP-labeled α-tubulin of cells treated with shCT or shNEDD9 (shRNA treatment timeline: t=24h to 48h), visualize the dynamics of spindle formation. For mitotic progression timeline, we used the visible metaphase-like spindle configuration as landmark. Note the asymmetrical dynamics in spindle formation in ALDH+ cells, and not ALDH- cells, which was disrupted by NEDD9-depletion.

shRNA treatment timeline: Cells were treated with shNEDD9 or shCT (scramble control) lentivirus during seeding; after 1day, the lentivirus is removed and replaced with fresh media, at a timepoint designated as t=0h. n= # of biological replicas. Scale bars = 10μm.

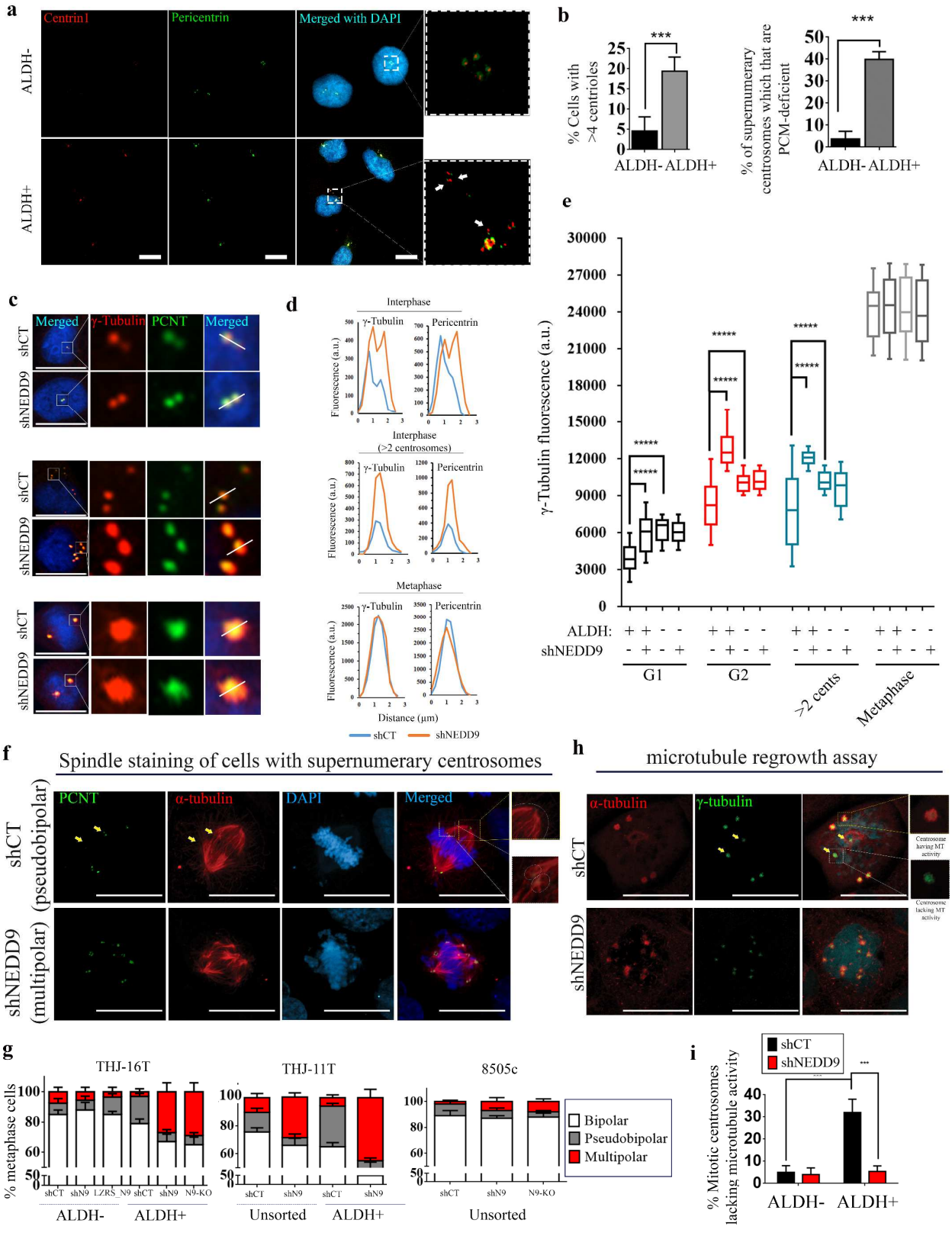
a
Centrin1
Pericentrin
Merged with DAPI
ALDH-
ALDH+
b
% Cells with >4 centrioles
***
ALDH- ALDH+
% of supernumerary centrosomes which that are PCM-deficient
***
ALDH- ALDH+
c
Merged
γ-Tubulin
PCNT
Merged
shCT
shNEDD9
d
Interphase
γ-Tubulin
Pericentrin
Fluorescence (a.u.)
Interphase (>2 centrosomes)
Metaphase
Distance (μm)
shCT
shNEDD9
e
γ-Tubulin fluorescence (a.u.)
*****
ALDH:
shNEDD9
G1
G2
>2 cents
Metaphase
f
Spindle staining of cells with supernumerary centrosomes
shCT (pseudobipolar)
shNEDD9 (multipolar)
PCNT
α-tubulin
DAPI
Merged
h
microtubule regrowth assay
α-tubulin
γ-tubulin
shCT
shNEDD9
Centrosome having MT activity
Centrosome lacking MT activity
g
THJ-16T
THJ-11T
8505c
% metaphase cells
shCT shN9 LZRS_N9 shCT shN9 N9-KO
ALDH- ALDH+
shCT shN9 shCT shN9
Unsorted ALDH+
shCT shN9 N9-KO
Unsorted
Bipolar
Pseudobipolar
Multipolar
i
shCT
shNEDD9
***
% Mitotic centrosomes lacking microtubule activity
ALDH- ALDH+

M1-Figure 4: NEDD9 inhibits the activation of a subset of supernumerary centrosomes to limit the severity of spindle multipolarity

a. Representative centriole (centrin1) and pericentriolar material (pericentrin) co-staining images of ALDH+ and ALDH- cells with supernumerary centrosomes during interphase. Original magnification: 63x. Note the proximity of many supernumerary centriole pairs within a single pericentrin-positive structure, as well as additional pairs of centrioles with very low pericentrin staining that are located further away (indicated by arrows) **b.** Quantification of centrosome amplification in THJ-16T cells at t=36h, and the frequency of supernumerary centrosomes with unusually weak PCM levels (where PCM intensity is <20% of the most dominant centrosome). Centrosome amplification is defined as cells with >4 pericentrin-colocalized centrin spots. At least 80 cells were scored for each condition, n=3 biological replicates **c.** Representative immunofluorescent image of interphase or mitotic centrosomes stained with pericentrin and γ-tubulin antibody. **d**. Representative line graph panel illustrating the impact of NEDD9-knockdown on the amount of pericentriolar material around centrosomes. The region quantified is depicted by a white line in (c). **e.** Quantification of shNEDD9's impact (t=36h) on centrosome γ-tubulin fluorescence in THJ-16T cells (n=3 biological replicates, 15 cells were scored for each repeat). For cells with normal number of centrosomes centrosomes, G1 centrosome was defined as two PCM-positive structure that were <1μm apart and directly adjacent to the nucleus. G2 centrosomes are defined as non-mitotic centrosomes that are more than 4μm apart but not any further than the edge of the nucleus, while the nucleus was still uncondensed. Mitotic centrosomes were scored during metaphase. Box limits indicate the 25th and 75th percentiles. Whiskers extend 1.5 times the interquartile range from the 25th and 75th percentiles. At least 30 centrosomes were analyzed per experiment, n=3. **f.** Representative immunofluorescent images of pseudobipolar and multipolar spindles, labeled with pericentrin (centrosomes), α-tubulin (spindle apparatus), and DAPI (nucleus)., Original magnification: 63x. Arrows point to centrosomes which are not polarized and show extremely weak spindle-forming capacity relative to the polarized centrosomes **g.** Quantification of relative frequency of bipolar, pseudobipolar, or multipolar spindles in ATC models (sorted where possible) following shNEDD9 treatment (t=36h). **h.** Microtubule regrowth assay measuring the microtubule nucleating activity of mitotic centrosomes. Microtubule regrowth assay is conducted as described in fig. 3b. Arrow point to non-polarized supernumerary centrosomes with very weak centrosome MTOC activity which resembles the centrosomes which lack spindle forming capacity in fig. (f) **i.** Quantification of supernumerary mitotic centrosomes that lacks microtubule nucleating activity, measured as the % of centrosomes that show weak microtubule nucleating activity / total number of centrosomes. Additional low-magnification images found in supplemental data. Calculation of statistical significance and shRNA treatment timeline are the same as in Figure. 3. Error bars represent $\pm$ SD. n= # of biological replicates. a.u. = arbitrary units. Scale bars = 10μm.

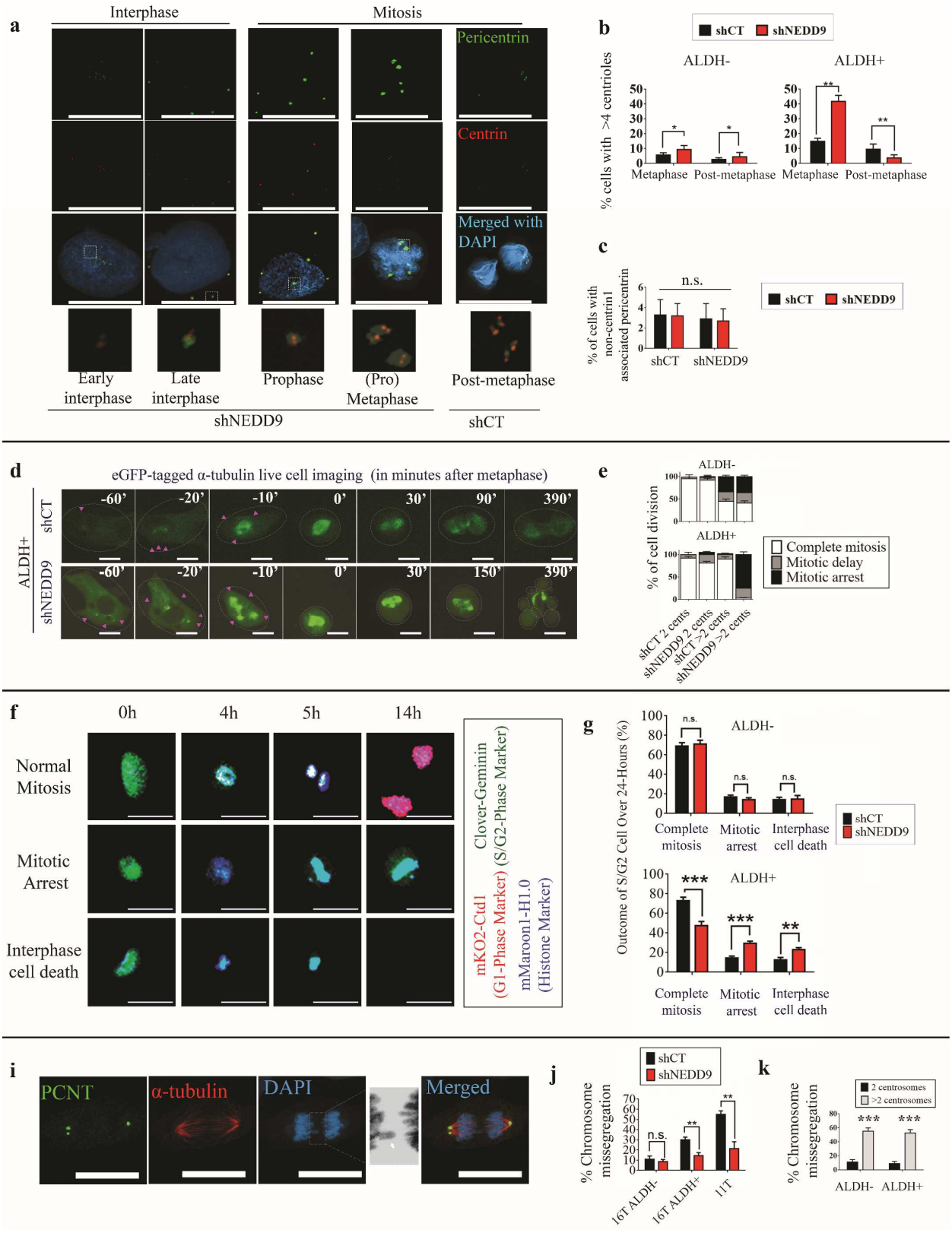
a
Interphase
Mitosis
Pericentrin
Centrin
Merged with DAPI
Early interphase
Late interphase
Prophase
(Pro) Metaphase
Post-metaphase
shNEDD9
shCT
b
shCT
shNEDD9
ALDH-
ALDH+
% cells with >4 centrioles
Metaphase
Post-metaphase
c
n.s.
% of cells with non-centrin1 associated pericentrin
shCT
shNEDD9
d
eGFP-tagged α-tubulin live cell imaging (in minutes after metaphase)
ALDH+
shCT
shNEDD9
-60'
-20'
-10'
0'
30'
90'
150'
390'
e
ALDH-
ALDH+
% of cell division
Complete mitosis
Mitotic delay
Mitotic arrest
shCT 2 cells
shNEDD9 2 cells
shCT >2 cells
shNEDD9 >2 cells
f
0h
4h
5h
14h
Normal Mitosis
Mitotic Arrest
Interphase cell death
Clover-Geminin (S/G2-Phase Marker)
mKO2-Ctd1 (G1-Phase Marker)
mMaroon1-H1.0 (Histone Marker)
g
ALDH-
ALDH+
Outcome of S/G2 Cell Over 24-Hours (%)
Complete mitosis
Mitotic arrest
Interphase cell death
shCT
shNEDD9
i
PCNT
α-tubulin
DAPI
Merged
j
shCT
shNEDD9
% Chromosome missegregation
16T ALDH-
16T ALDH+
11T
k
2 centrosomes
>2 centrosomes
% Chromosome missegregation
ALDH-
ALDH+

M1-Figure 5: NEDD9 helps supernumerary-centrosome-harbouring ALDH+ cells complete mitosis and increase the rate of CIN

a. Representative immunofluorescent images of centriole (centrin1) and pericentriolar material (pericentrin) co-staining in ALDH+ THJ-16T cells to illustrate dynamics of intact centriole pairs following NEDD9-depletion. Note that successful mitosis of centrosome amplified cells could be identified by post-mitotic daughter cells with >4 combined centrioles **b.** NEDD9-knockdown causes centrosome amplified cells to accumulate at metaphase, assessed by measuring the relative quantification of centrosome amplified cells found either during metaphase or post-anaphase (anaphase or telophase stage). Centrosome amplification is defined as >4 pericentrin-colocalized centrin spots between the two daughter cells. At least 80 cells were scored for each condition, n=3 biological replicates **c.** Quantification of the incidence rate of centrosome fragmentation at t=36h defined by the presence of areas with positive staining for PCM (pericentrin) but negative for centriole (centrin1). At least 80 cells were analyzed per group. **d.** Live cell time-lapse of eGFP-labeled α-tubulin to treated with shCT or shNEDD9 (shRNA treatment timeline: t=24h to 48h), to visualize outcomes of cells which experienced spindle multipolarity. For mitotic progression timeline, we used the visible metaphase-like spindle configuration as landmark. Note how supernumerary centrosomes in shCT cells were not polarized leading into prophase, whereas those in shNEDD9 cells do. In shCT cells, multipolar spindles were quickly resolved, and mitosis was completed, while in shNEDD9 cells, multipolar spindles persisted until cells died. **e.** Relative ratio of outcomes in cells which enter mitosis. 2 cents = cells with normal number of eGFP-tubulin positive structures, >2 cents = cells with more than 2 eGFP-tubulin positive structures. Mitotic delay is defined as a delay by more than 30 minutes but less than 2hrs. Mitotic arrest is defined as a delay by more than 2hrs, usually lasting until cell death. **f.** Representative images of three different outcomes in S/G2 (geminin-positive) cells occurring during the time-lapse experiment. Note that in the case of mitotic arrest, geminin is not degraded by the anaphase promoting complex, indicating that cells are arrested at metaphase. Images were captured at 20x magnification at low laser intensity to minimize cell harm. Scale bar = 10μm. **g.** Quantification of the four outcomes in S/G2 (geminin positive) cells occurring during the time-lapse experiment. At least 25 geminin-positive cells were analyzed per experiment, n=3 **i.** Representative image of a centrosome amplified cells in anaphase labelled with pericentrin (centrosomes), α-tubulin (spindle apparatus), and DAPI (nucleus). Inset is rendered greyscale and inverted for visual claritiy. Arrow is pointing to a lagging chromosome in the spindle midzone, identified as being visibly detached from chromosomes of either spindle poles **j.** Impact of NEDD9-depletion on % of sorted THJ-16T cells exhibiting chromosome missegregation during anaphase. At least 100 mitotic cells were quantified for each group. **k.** Rate of chromosome missegregation during anaphase in cells which either possesses or lacks visible centrosome amplification. Statistical significance was determined using two-tailed student's t-test (****P<0.0001, ***P<0.001, **P<0.01, *P<0.05 n.s.: not-significant. Error bars represent $\pm$ SD. Scale bars = 10μm. shRNA treatment timeline are the same as in Figure 3.

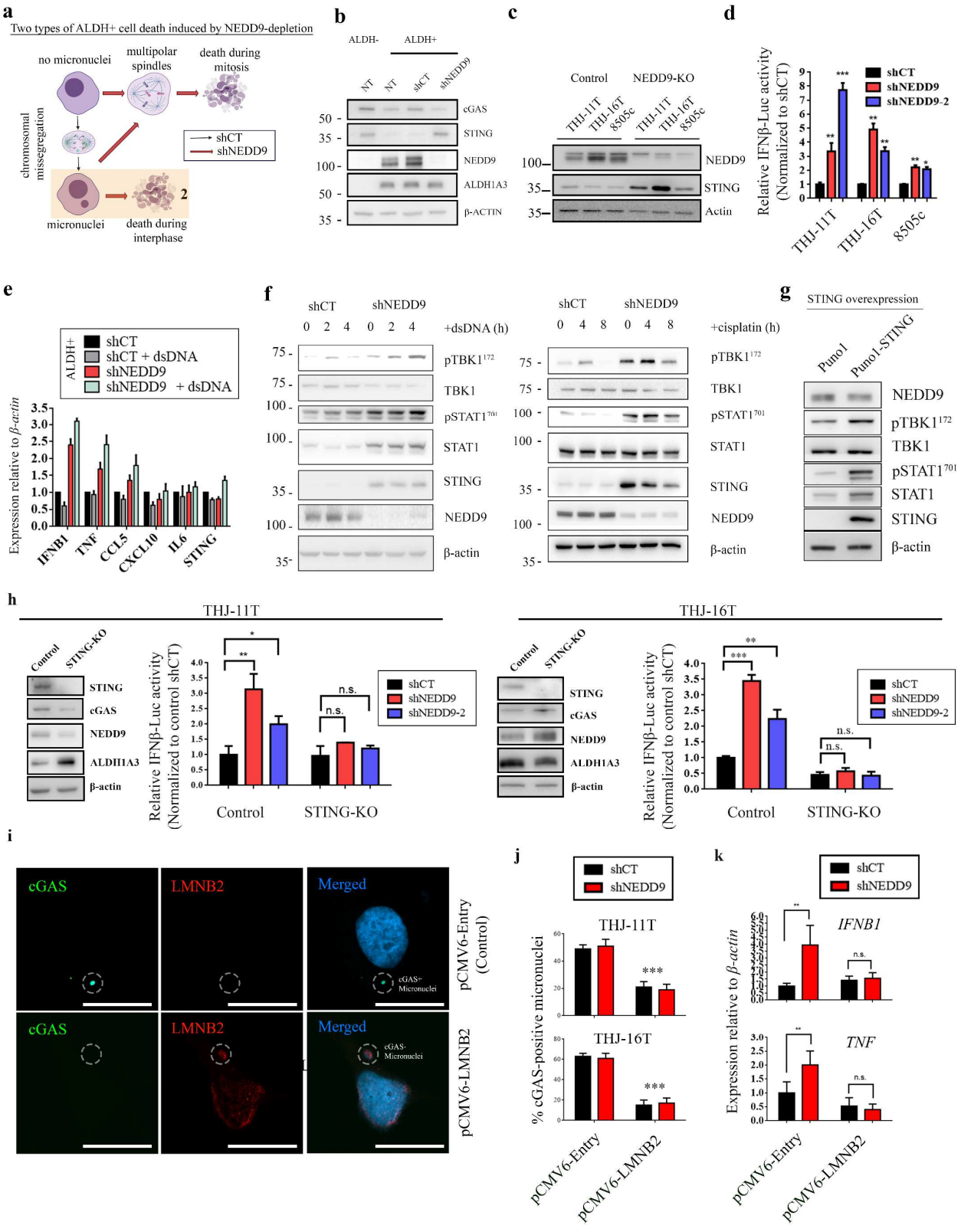
a
Two types of ALDH+ cell death induced by NEDD9-depletion
no micronuclei
multipolar spindles
death during mitosis
chromosomal missegregation
shCT
shNEDD9
micronuclei
death during interphase
2
b
ALDH-
ALDH+
NT
NT
shCT
shNEDD9
cGAS
STING
NEDD9
ALDH1A3
β-ACTIN
c
Control
NEDD9-KO
THJ-11T
THJ-16T
8505c
NEDD9
STING
Actin
d
Relative IFNβ-Luc activity (Normalized to shCT)
shCT
shNEDD9
shNEDD9-2
THJ-11T
THJ-16T
8505c
e
ALDH+
shCT
shCT + dsDNA
shNEDD9
shNEDD9 + dsDNA
Expression relative to β-actin
IFNB1
TNF
CCL5
CXCL10
IL6
STING
f
shCT
shNEDD9
+dsDNA (h)
+cisplatin (h)
pTBK1172
TBK1
pSTAT1701
STAT1
STING
NEDD9
β-actin
g
STING overexpression
Puno1
Puno1-STING
NEDD9
pTBK1172
TBK1
pSTAT1701
STAT1
STING
β-actin
h
THJ-11T
THJ-16T
Control
STING-KO
STING
cGAS
NEDD9
ALDH1A3
β-actin
Relative IFNβ-Luc activity (Normalized to control shCT)
shCT
shNEDD9
shNEDD9-2
n.s.
i
cGAS
LMNB2
Merged
cGAS+ Micronuclei
cGAS- Micronuclei
pCMV6-Entry (Control)
pCMV6-LMNB2
j
shCT
shNEDD9
THJ-11T
THJ-16T
% cGAS-posiitive micronuclei
pCMV6-Entry
pCMV6-LMNB2
k
shCT
shNEDD9
IFNB1
TNF
Expression relative to β-actin
pCMV6-Entry
pCMV6-LMNB2

M1-Figure 6: NEDD9 upregulation in ALDH+ cells shut down micronuclei-rupture stimulated DNA sensing pathway by limiting STING protein expression

a. Schematic summarizing the two models of cell death observed in ALDH+ cells following NEDD9-knockdown during interphase and mitosis respectively. **b.** Expression of the cytosolic DNA sensing pathway proteins cGAS and STING in ALDH-, ALDH+, and ALDH+ cells following NEDD9-knockdown (t=48h). ALDH+ cells express significantly less STING compared to ALDH- cells. Lentivirus treatment did not affect STING expression levels, while NEDD9-depletion restored STING level in ALDH+ cells to that of ALDH- cells, without affecting ALDH1A3 expression. **c.** Western blot analysis of STING protein levels in multiple ATC cell lines following CRISPR-mediated NEDD9-KO. **d.** Quantification of IFN-β activity via luciferase-based reporter system in multiple ATC cell lines following NEDD9-depletion **e.** Quantitative PCR analysis of downstream interferon gene expression in ALDH+ cells with or without NEDD9-depletion and treated with 10ng/mL dsDNA. **f.** Western blot analysis of STING signaling in ALDH+ cells with or without NEDD9-depletion and treated with 10ng/mL dsDNA or 10μM cisplatin n=3 **g.** Western blot analysis of STING signaling in ALDH+ cells following puno1-mediated STING expression. **h.** Western blot analysis and IFN-β reporter assay of THJ-11T and THJ-16T cells treated with shCT/shNEDD9 lentivirus in combination with STING-KO. Control cells are transduced with cas9 expressing vector only. **i.** Immunofluorescence images of THJ-16T cells transfected with control vector or pcmv6-LMNB2 (laminB2) overexpression vector. LMNB2 overexpression attenuates micronuclei rupture, limiting the cGAS recruitment to the micronuclei. **j.** Impact of LMNB2 overexpression on cGAS positivity in ATC cells. LMNB2-overexpressing stable cells were assessed for cGAS positivity using immunofluorescence imaging by probing for the presence of cGAS co-localization at the micronucleus. At least 30 micronuclei-bearing cells were scored per experiment, n=3. **k.** Impact of LMNB2 overexpression on shNEDD9-induced interferon stimulated genes (IFN-β1 and TNF) expression. THJ-16T cells with stable LMNB2 overexpress were treated with shCT or shNEDD9 lentivirus and the lysates were collected after 72h. n=5. Calculation of statistical significance and shRNA treatment timeline are the same as in Figure. 2. Error bars represent $\pm$ SD. n= # of biological replicates. a.u. = arbitrary units. Scale bars = 10μm.

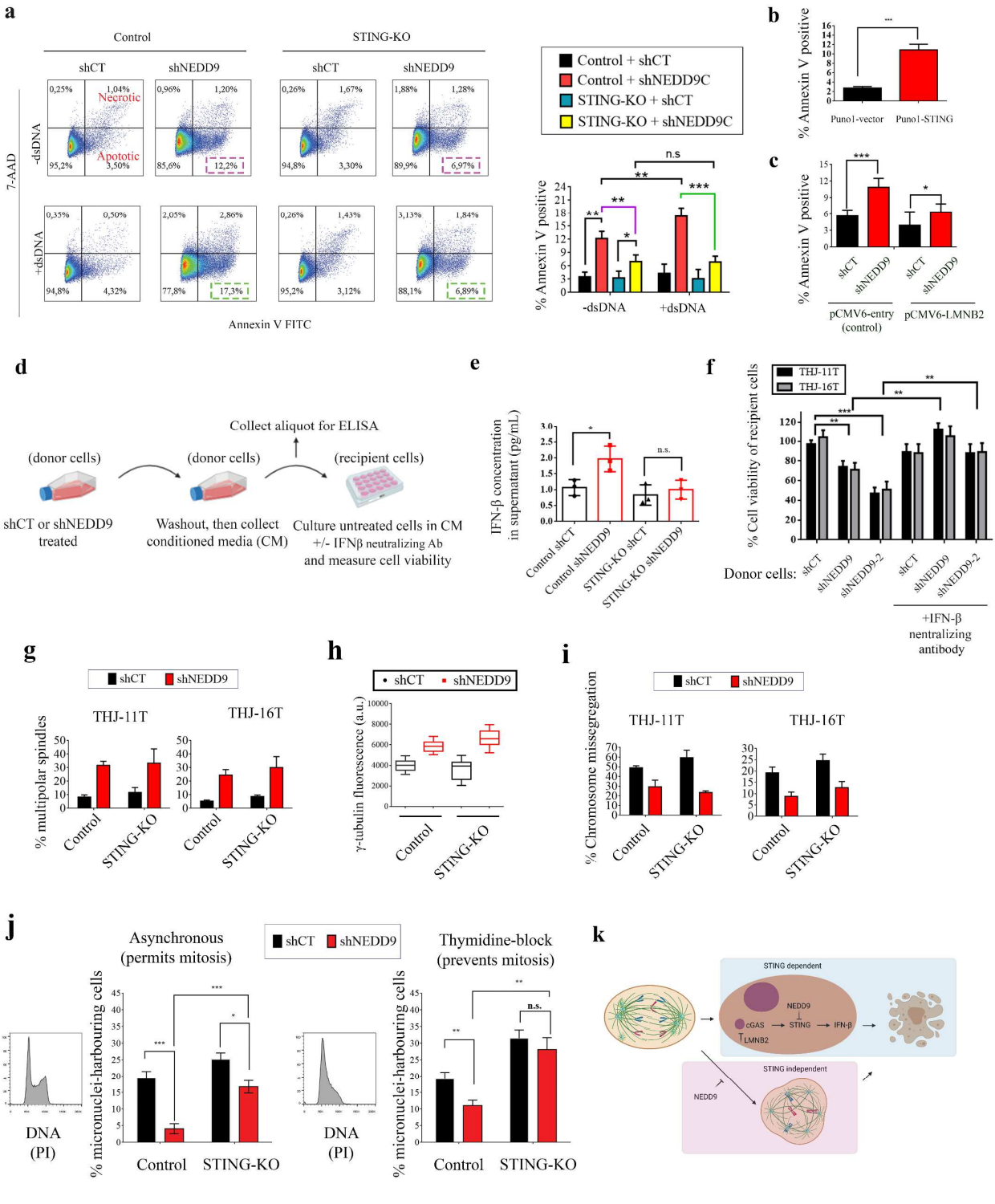
a
Control
STING-KO
shCT
shNEDD9
7-AAD
-dsDNA
+dsDNA
Necrotic
Apototic
Annexin V FITC
Control + shCT
Control + shNEDD9C
STING-KO + shCT
STING-KO + shNEDD9C
% Annexin V positive
-dsDNA
+dsDNA
b
% Annexin V positive
Puno1-vector
Puno1-STING
c
% Annexin V positive
shCT
shNEDD9
pCMV6-entry (control)
pCMV6-LMNB2
d
Collect aliquot for ELISA
(donor cells)
(donor cells)
(recipient cells)
shCT or shNEDD9 treated
Washout, then collect conditioned media (CM)
Culture untreated cells in CM +/- IFNβ neutralizing Ab and measure cell viability
e
IFN-β concentration in supernatant (pg/mL)
Control shCT
Control shNEDD9
STING-KO shCT
STING-KO shNEDD9
f
THJ-11T
THJ-16T
% Cell viability of recipient cells
Donor cells:
shCT
shNEDD9
shNEDD9-2
+IFN-β nentralizing antibody
g
shCT
shNEDD9
THJ-11T
THJ-16T
% multipolar spindles
Control
STING-KO
h
shCT
shNEDD9
γ-tubulin fluorescence (a.u.)
Control
STING-KO
i
shCT
shNEDD9
THJ-11T
THJ-16T
% Chromosome missegregation
Control
STING-KO
j
Asynchronous (permits mitosis)
Thymidine-block (prevents mitosis)
shCT
shNEDD9
DNA (PI)
% micronuclei-harbouring cells
Control
STING-KO
k
STING dependent
NEDD9
cGAS
STING
IFN-β
LMNB2
STING independent
NEDD9

M1-Figure 7: shNEDD9-induced STING activation suppresses ALDH+ cell growth independently from shNEDD9-induced spindle multipolarity

a. Representative flow cytometry panels and quantification illustrating that NEDD9-depletion sensitizes ALDH+ cells to dsDNA-mediated apoptosis in a STING-dependent manner. Annexin V apoptosis assay to measure cell death in ALDH+ cells control or STING-KO cells following NEDD9-depletion (t=48h) and in combination with double-strand DNA 10ng/mL (dsDNA). Note that NEDD9-depletion sensitizes ALDH+ cells to dsDNA-induced cell death, while STING-KO ablates this effect. **b.** Rate of apoptosis in THJ-16T cells after 72h after transfected with puno1-mediated STING overexpression. Representative FACS panels in supplemental data S6 **c.** Impact of LMNB2 overexpression on shNEDD9-induced apoptosis. ALDH+ cells with stable LMNB2 overexpression are treated with shCT/shNEDD9 lentivirus. Apoptosis is measured after 72h. Representative FACS panels in supplemental data S6 **d.** Representative schematic, illustrating the use of conditioned media derived from shCT/shNEDD9 treated donor cells on other untreated recipient cells and examining the impact of the conditioned media on overall cell viability after 48h. **e.** ELISA measurement of IFN-β concentration in conditioned media derived from shCT or shNEDD9-treated donor cells. **f.** Impact of shCT/shNEDD9 derived conditioned media on ATC cell growth. An IFN-β neutralizing antibody is used to abolish the effect of IFN-β in the media. **g.** Impact of STING-KO on shNEDD9-induced spindle multipolarity. At least 30 mitotic cells were scored per condition, n=3. **h.** Impact of STING-KO on shNEDD9-induced γ-tubulin accumulation at the centrosomes. γ-tubulin fluorescence intensity at centrosomes pairs that were <1μm apart and directly adjacent to the nucleus were measured. Box limits indicate the 25th and 75th percentiles. Whiskers extend 1.5 times the interquartile range from the 25th and 75th percentiles. At least 30 centrosome pairs were scored per condition, n=3 biological replicates **i.** Impact of STING-KO on shNEDD9-induced decrease in chromosomal instability. At least 30 anaphase cells were analyzed per condition. **j.** Quantification of the rate of micronuclei in ALDH+ control and STING-KO cells following NEDD9-depletion (t=48h). Thymidine block (2mM) was applied 18h prior to shNEDD9 treatment to arrest cells at S-phase, thus preventing micronuclei-bearing cells from being eliminated during mitosis. Micronuclei are defined as rounded DAPI positive structures less than one-third the diameter and with similar intensity/texture/plane as the nucleus. For g-j, cells with stable STING-KO were treated with shCT/shNEDD9, and analyzed for their respective assay. **k.** Schematic illustrating NEDD9 having two independent functions for enabling tolerance of chromosomal instability-imposed growth challenges in ALDH+ thyroid cancer stem cells.

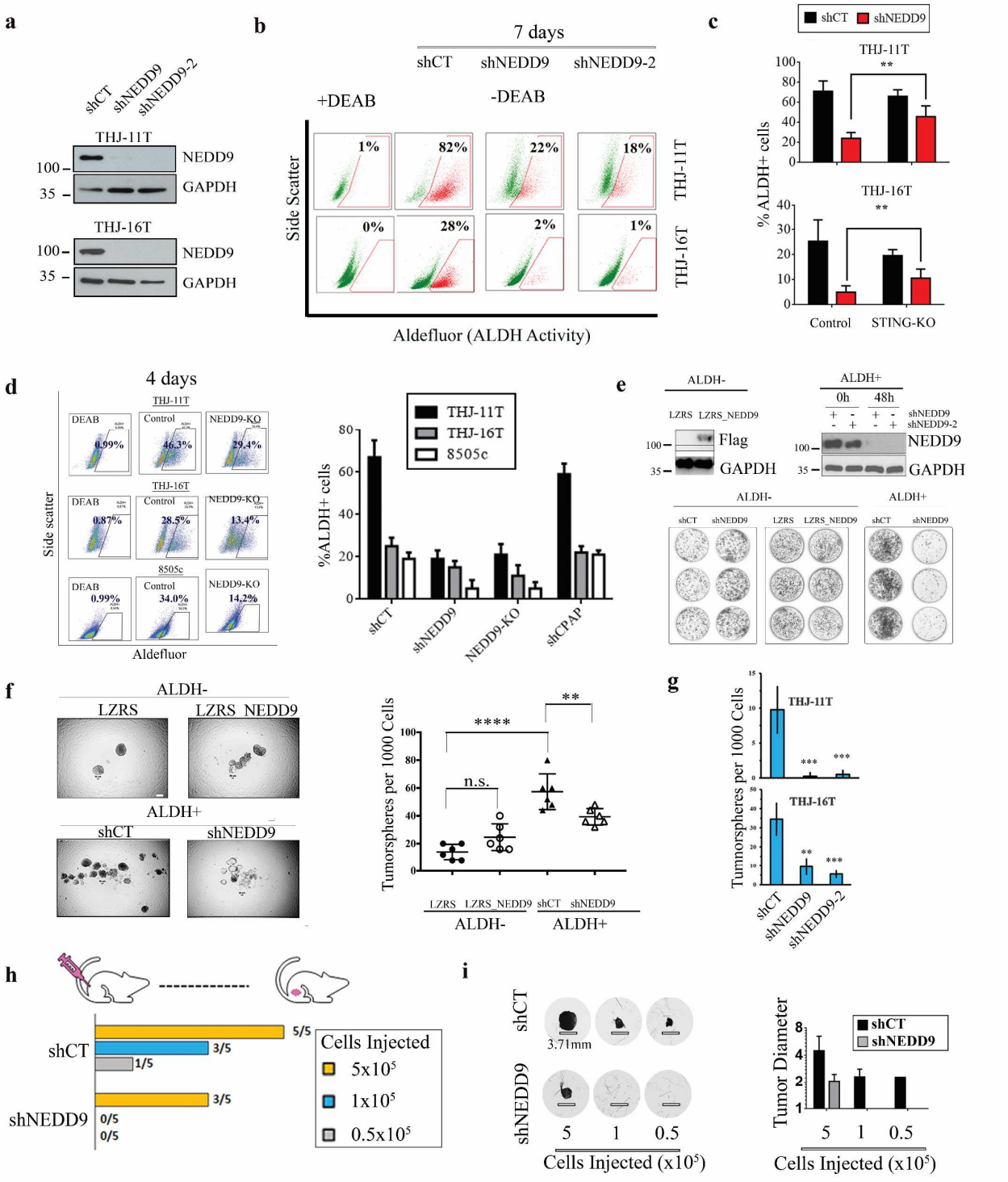
a
shCT
shNEDD9
shNEDD9-2
THJ-11T
NEDD9
GAPDH
100
35
THJ-16T
NEDD9
GAPDH
b
7 days
shCT
shNEDD9
shNEDD9-2
+DEAB
-DEAB
Side Scatter
1%
82%
22%
18%
0%
28%
2%
1%
THJ-11T
THJ-16T
Aldefluor (ALDH Activity)
c
shCT
shNEDD9
THJ-11T
**
THJ-16T
**
% ALDH+ cells
Control
STING-KO
d
4 days
THJ-11T
DEAB
0.99%
Control
46.3%
NEDD9-KO
29.4%
THJ-16T
DEAB
0.87%
Control
28.5%
NEDD9-KO
13.4%
8505c
DEAB
0.99%
Control
34.0%
NEDD9-KO
14.2%
Side scatter
Aldefluor
THJ-11T
THJ-16T
8505c
%ALDH+ cells
shCT
shNEDD9
NEDD9-KO
shCPAP
e
ALDH-
LZRS
LZRS_NEDD9
Flag
GAPDH
ALDH+
0h
48h
shNEDD9
shNEDD9-2
NEDD9
GAPDH
ALDH-
ALDH+
shCT
shNEDD9
LZRS
LZRS_NEDD9
shCT
shNEDD9
f
ALDH-
LZRS
LZRS_NEDD9
ALDH+
shCT
shNEDD9
Tumorspheres per 1000 Cells
****
**
n.s.
LZRS
LZRS_NEDD9
shCT
shNEDD9
ALDH-
ALDH+
g
Tumorspheres per 1000 Cells
THJ-11T
***
***
THJ-16T
**
***
shCT
shNEDD9
shNEDD9-2
h
shCT
5/5
3/5
1/5
shNEDD9
3/5
0/5
0/5
Cells Injected
5x10^5
1x10^5
0.5x10^5
i
shCT
3.71mm
shNEDD9
5
1
0.5
Cells Injected (x10^5)
Tumor Diameter
shCT
shNEDD9
5
1
0.5
Cells Injected (x10^5)

M1-Figure 8: NEDD9-depletion selectively eliminates ALDH+ ATC cells and attenuates ATC spherogenic and tumor seeding potential

a. NEDD9 knockdown using two shNEDD9 constructs (shNEDD9 and shNEDD9-2) in THJ-11T and THJ-16T (shCT = scramble control) cell lines. **b.** Representative FACS analysis of %ALDH+ cell after NEDD9-knockdowns (t=7days) in ATC cell lines, where the addition of the ALDH enzymatic inhibitor DEAB is used to establish background levels. **c.** Impact of NEDD9-knockdown on %ALDH+ cells in THJ-11T and THJ-16T control or STING-KO cells **d.** Representative flow cytometry panel and quantification of ALDH+ status in multiple ATC cell models after NEDD9 depletion. Knockdown of a different centrosome protein, CPAP, is used as control to assess the specificity of shNEDD9. Western blot validation for shCPAP in supplemental fig. s5. (t=4days) **e.** NEDD9 knockdown or ectopic expression in pre-sorted ALDH+ and ALDH- cell respectively, an approach which decouples the NEDD9 expression from ALDH-status. LZRS = LZRS_IRESGFP control, LZRS_NEDD9 = full-length NEDD9 cloned into LZRS-IRESGFP expression vector**.** Bottom panel: Impact of NEDD9 expression on the clonogenic growth of ALDH+ and ALDH- THJ-16T cells (t=5d), cells were seeded at 1000 cells per well **f.** Representative image (scale bar = 100 μm) and quantification of tumorsphere formation in ALDH+ or ALDH- sorted THJ-16T cells with either NEDD9-knockdown or ectopic overexpression after 7 days. Cells were treated with lentivirus, and after 24h, were detached and re-seeded with fresh tumorsphere growth media in polyhema coated plate. Cells were treated with shCT/shNEDD9 for 7 days then assessed for spherogenesis (n=5). **g.** Tumorsphere formation efficiency in THJ-11T and THJ-16T after shNEDD9. Cells were treated with shCT or shNEDD9. After 24h, cells were detached and re-seeded with fresh tumorsphere growth media in polyhema coated plate. Sphere formation efficiency assessed after 7 days **h.** Limiting dilution transplantation assay to compare tumor-seeding ability of THJ-16T cells treated with shCT or shNEDD9. Three different dilutions of THJ-16T ($5x10^5$, $1x10^5$ and $0.5x10^5$ cells, n=5 for each dilution) was injected into the right flank of NOD-SCID mice. Tumor growth was assessed by palpitation and examined by necropsy after 35 days. **i.** Tumor diameter measurement after sacrifice. Scale bar = 3.71mm. Error bars represent $\pm$ SD. Statistical significance was determined using two-tailed student's t-test (****P<0.0001, **P<0.01, *P<0.05 n.s.: not-significant).

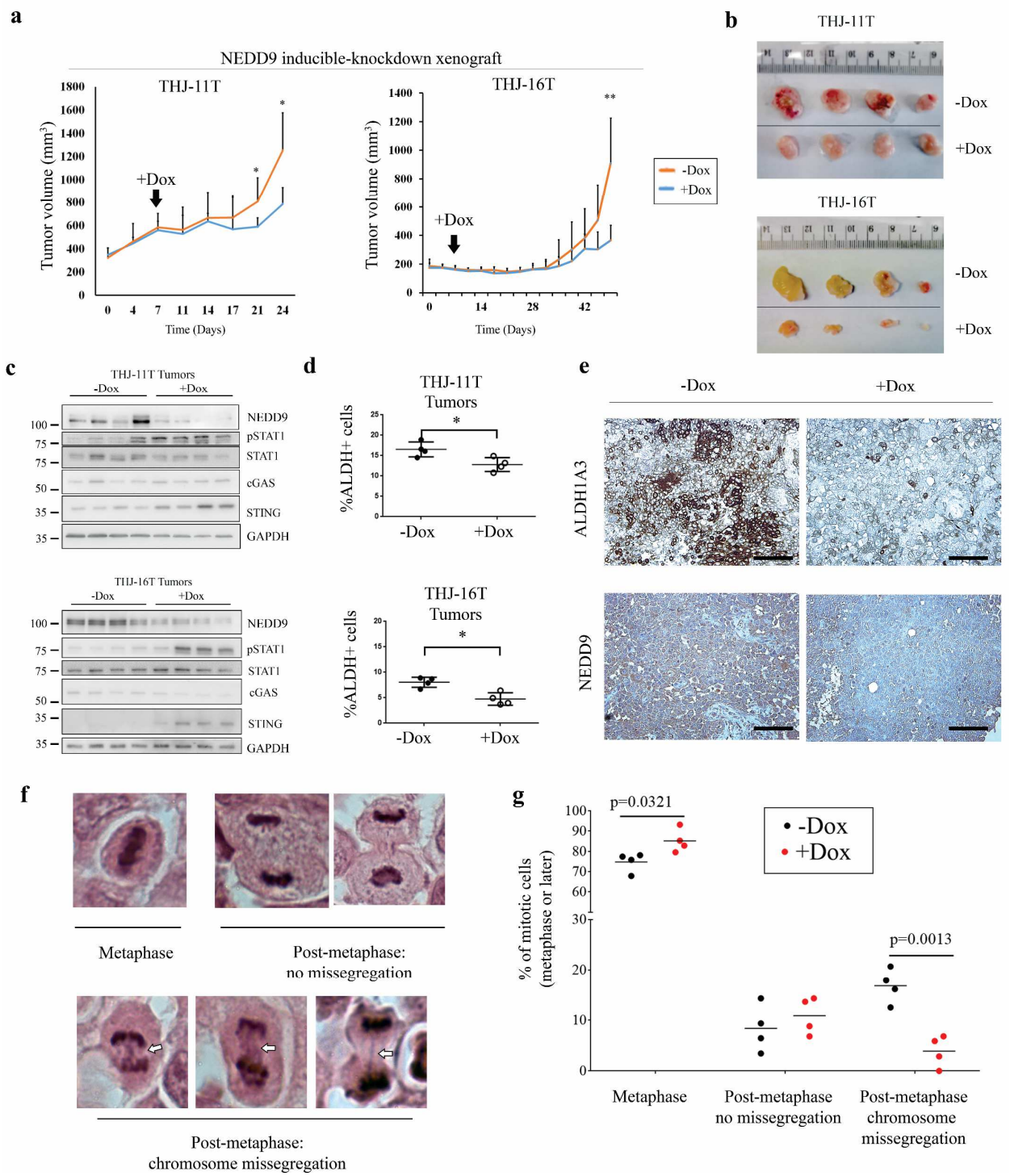
a
NEDD9 inducible-knockdown xenograft
THJ-11T
THJ-16T
Tumor volume (mm3)
+Dox
Time (Days)
-Dox
+Dox
b
THJ-11T
THJ-16T
-Dox
+Dox
c
THJ-11T Tumors
THJ-16T Tumors
-Dox
+Dox
NEDD9
pSTAT1
STAT1
cGAS
STING
GAPDH
d
THJ-11T Tumors
THJ-16T Tumors
%ALDH+ cells
e
ALDH1A3
NEDD9
f
Metaphase
Post-metaphase: no missegregation
Post-metaphase: chromosome missegregation
g
p=0.0321
p=0.0013
% of mitotic cells (metaphase or later)
Metaphase
Post-metaphase no missegregation
Post-metaphase chromosome missegregation

M1-Figure 9: NEDD9-depletion in ATC xenografts inhibits tumor growth, eliminates ALDH1A3 positive cells, promotes STING activation, and reduces chromosome missegregation

a. Tumor growth curve; 3×10^6 THJ-16T or THJ-11T cells were implanted subcutaneously into NOD-SCID mice (n=4), 7 days later, 2mg/mL of doxycycline (Dox) was added to drinking water together with 1% sucrose. THJ11T: p=0.037, THJ-16T: p=0.007 (n=4) **b**. Representative tumor images after sacrifice **c.** Protein expression in THJ-11T and THJ-16T xenografts after sacrifice. Single cell suspensions of tumor tissues were FACS sorted by HLA-A,B,C antibodies to remove mouse cells, then cultured in regular media for 24h before harvesting. **d.** %ALDH+ cell measured in THJ-11T and THJ-16T xenografts measured after sacrifice. Single cell suspensions of tumor tissues were used for assessing ALDH activity by Aldefluor assay, co-staining of anti-human HLA-A, B, C was used to gate out mouse cells; THJ11T: p=0.022, THJ-16T: p=0.044. (n=4) **e.** Representative images of ALDH1A3 and NEDD9 immunohistochemistry staining in THJ-11T tumors, taken at 20x magnification. Scale bar = 50μm. **f.** Representative haemotoxylin and eosin staining images illustrating metaphase, anaphase, or telophase cells in THJ-11T tumors. Arrows point to evidence of chromosome missegregation in the spindle midzone **g.** Quantification of the relative frequency of metaphase, post-metaphase cells, or post-anaphase cells exhibiting chromosome missegregation observed in THJ-11T tumors. At least 25 cells were scored per tumor. Error bars represent $\pm$ SD. Statistical significance was determined using two-tailed student's t-test (****P<0.0001, **P<0.01, *P<0.05 n.s.: not-significant).

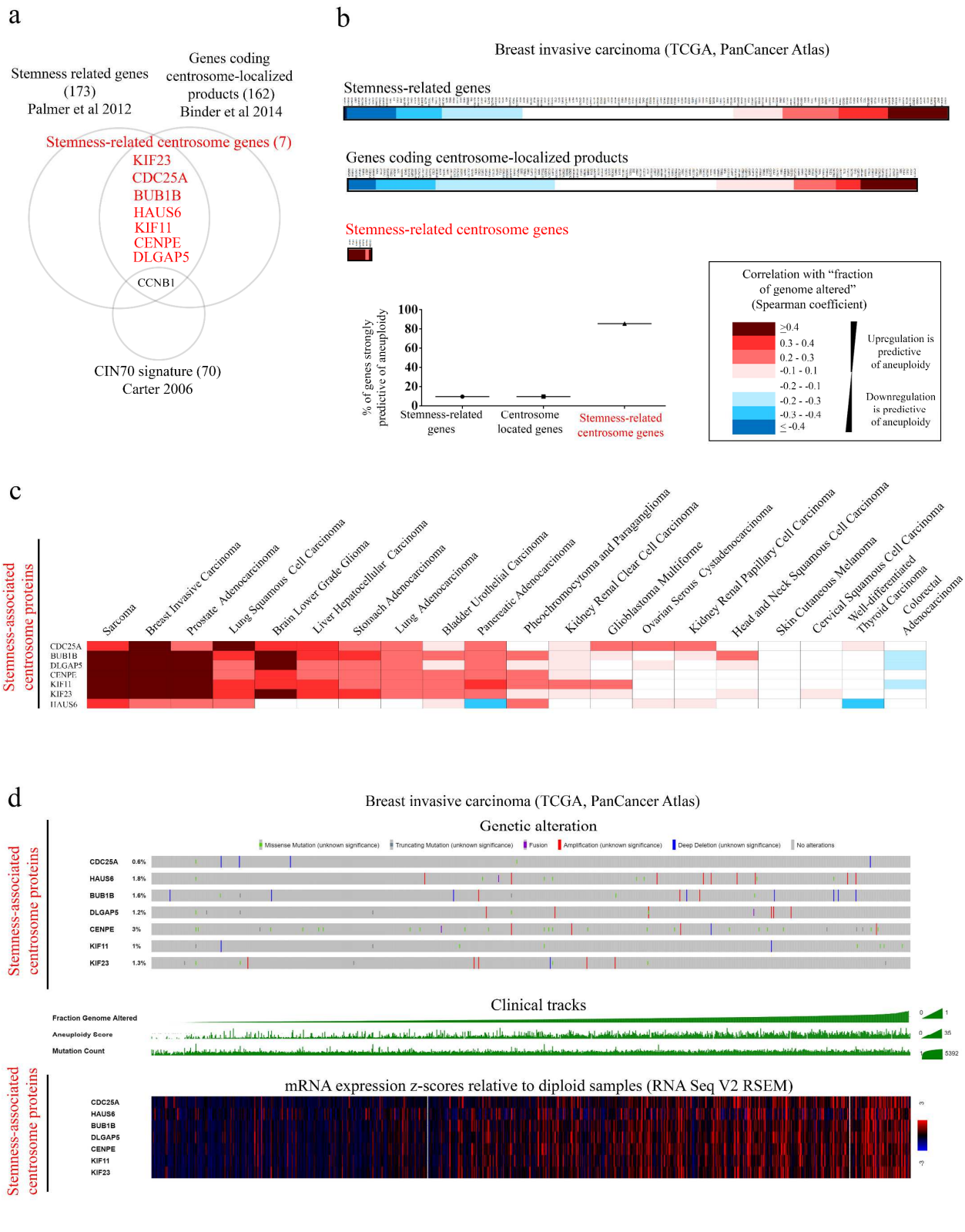
a
Stemness related genes (173) Palmer et al 2012
Genes coding centrosome-localized products (162) Binder et al 2014
Stemness-related centrosome genes (7)
KIF23
CDC25A
BUB1B
HAUS6
KIF11
CENPE
DLGAP5
CCNB1
CIN70 signature (70) Carter 2006
b
Breast invasive carcinoma (TCGA, PanCancer Atlas)
Stemness-related genes
Genes coding centrosome-localized products
Stemness-related centrosome genes
% of genes strongly predictive of aneuploidy
Stemness-related genes
Centrosome located genes
Stemness-related centrosome genes
Correlation with "fraction of genome altered" (Spearman coefficient)
≥0.4
0.3 - 0.4
0.2 - 0.3
-0.1 - 0.1
-0.2 - -0.1
-0.2 - -0.3
-0.3 - -0.4
≤ -0.4
Upregulation is predictive of aneuploidy
Downregulation is predictive of aneuploidy
c
Stemness-associated centrosome proteins
Sarcoma
Breast Invasive Carcinoma
Prostate Adenocarcinoma
Lung Squamous Cell Carcinoma
Brain Lower Grade Glioma
Liver Hepatocellular Carcinoma
Stomach Adenocarcinoma
Lung Adenocarcinoma
Bladder Urothelial Carcinoma
Pancreatic Adenocarcinoma
Pheochromocytoma and Paraganglioma
Kidney Renal Clear Cell Carcinoma
Glioblastoma Multiforme
Ovarian Serous Cystadenocarcinoma
Kidney Renal Papillary Cell Carcinoma
Head and Neck Squamous Cell Carcinoma
Skin Cutaneous Melanoma
Cervical Squamous Cell Carcinoma
Well-differentiated Thyroid Carcinoma
Colorectal Adenocarcinoma
CDC25A
BUB1B
DLGAP5
CENPE
KIF11
KIF23
HAUS6
d
Breast invasive carcinoma (TCGA, PanCancer Atlas)
Genetic alteration
Missense Mutation (unknown significance)
Truncating Mutation (unknown significance)
Fusion
Amplification (unknown significance)
Deep Deletion (unknown significance)
No alterations
Stemness-associated centrosome proteins
CDC25A 0.6%
HAUS6 1.8%
BUB1B 1.6%
DLGAP5 1.2%
CENPE 3%
KIF11 1%
KIF23 1.3%
Clinical tracks
Fraction Genome Altered
Aneuploidy Score
Mutation Count
mRNA expression z-scores relative to diploid samples (RNA Seq V2 RSEM)

M1-Figure 10: Upregulation of stemness-associated centrosome genes correlates with aneuploidy in multiple types of solid tumor

a. Cross-referencing a list of centrosome-located proteins (162 proteins based on Binder et al 2014 using a cut-off of 0.5 standardized value based on relevance to centrosomes), with stemness-related genes (based on a list of 173 genes predictive of a conserved stemness program, Palmer 2012). Candidates already known to be very strongly associated with chromosomal instability (based on the CIN70 gene list, Carter 2006) were excluded to omit genes already associated with CIN gene signature. This produced a list of 7 "stemness-related centrosome genes". **b.** Heatmap illustrating the predictive value of gene lists for "centrosome-located", "stemness-related", and "stemness-related centrosome genes" for aneuploidy. Values are determined by correlating each gene to the clinical track "fraction of genome altered" in invasive breast carcinoma, TCGA 2014 and presented as heatmap. High values indicate positive correlation between gene upregulation and aneuploidy. Quantification shows the % of genes from a specific genesets which have a >0.4 spearman correlation coefficient with fraction of genome altered, to indicate how predictive each gene sets are for aneuploidy **c.** Correlation between stemness-related centrosome genes and aneuploidy across multiple solid tumor datasets derived from TCGA Cancer Atlas datasets. The Spearman correlation coefficient between each gene and the clinical track "fraction of genome altered" was obtained from cBioportal and presented as heatmap. See panel c for the legends. **d.** Cbioportalk,[92] plot of invasive breast carcinoma patients arranged in order of increasing fraction of genome altered. Note the relative infrequency of mutations among the 7 stemness-related centrosome genes.

a

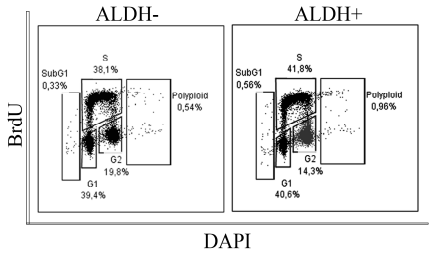

b

Asymmetry assessed by ALDH/ALDH1A3 partitioning (non-random partioning of fate-determinants)

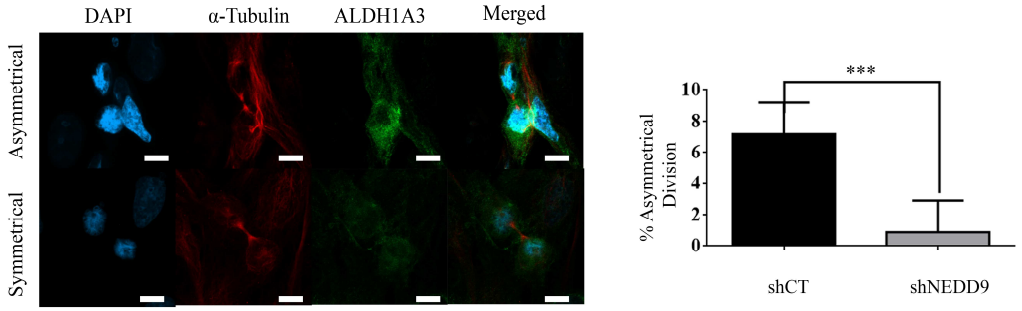

c

Asymmetry assessed by BrDU-pulase chase assay (rate of non-random sister chromatid segregation)

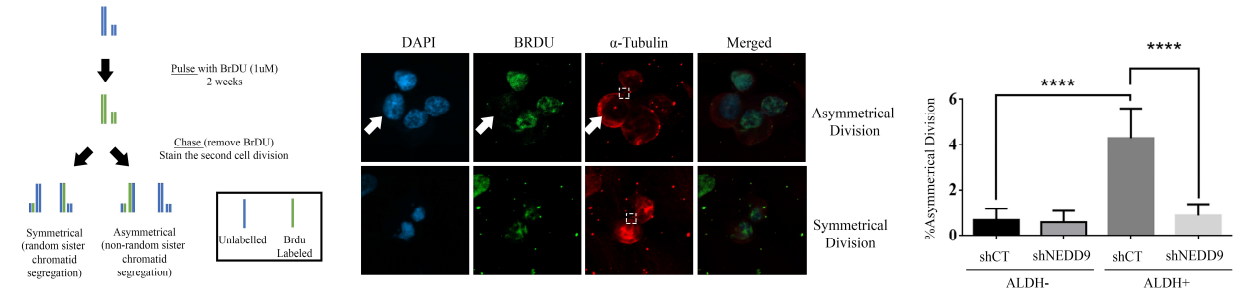

d

Asymmetry assessed by FUCCI (time for daughter cells to transition from G1 to S-phase)

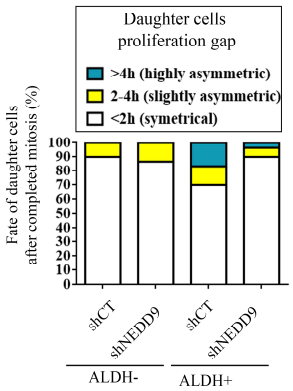

M1-Figure. S1: NEDD9-depletion hampers asymmetrical cell division in ALDH+ cells
a. Comparison of the basal cell cycle compartment between ALDH- and ALDH+ THJ-16T cells **b.** Quantification of proliferation gap differences following successful mitosis based on FUCCI assay. Asymmetry is assessed based on the relative timing when, after a successful cell division, the two daughter cells transition from a Ctdt1+ state into Geminin+ state via FUCCI imaging **c.** experimental scheme of the BrdU pulse-chase assay to assess asymmetrical partitioning of the parental DNA strand. **d.** representative images of symmetrical or asymmetrical partitioning BrdU partitioning; boxes highlight the midbody remnants to identity post-mitotic daughter cells. **e.** quantification of the frequency of asymmetrical partitioning **e.** Representative immunofluorescent images and **f.** quantification of symmetrical and asymmetrical division in THJ-16T ALDH+ cells based on ALDH1A3 partionining; ATC cells were labeled with ALDH1A3, α-tubulin, and DAPI. Post-mitosis daughter cells were identified via the midbody remnant. Original magnification: 63x. The cell model is all panels is THJ-16T. Calculation of statistical significance and shRNA treatment timeline are the same as in Figure. 2. Error bars represent $\pm$ SD. n= # of biological replicates. a.u. = arbitrary units. Scale bars = 10μm.

a

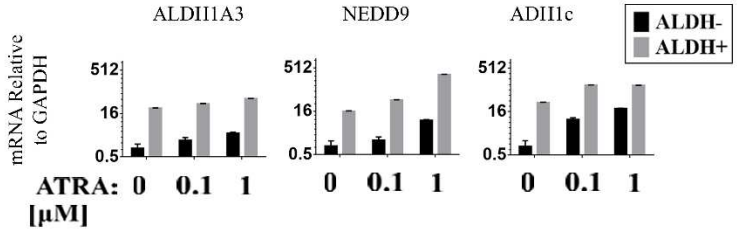
ALDII1A3
NEDD9
ADII1c
ALDH-
ALDH+
mRNA Relative to GAPDH
512
16
0.5
ATRA: 0 0.1 1
[µM]

b

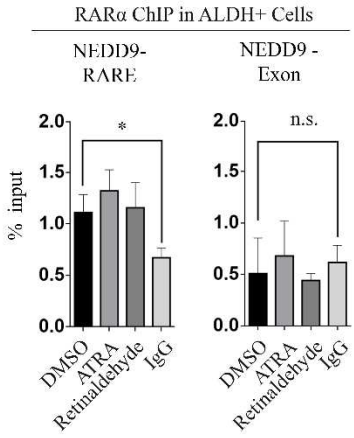
RARα ChIP in ALDH+ Cells
NEDD9-RARE
NEDD9 - Exon
% input
2.0
1.5
1.0
0.5
0.0
*
n.s.
DMSO
ATRA
Retinaldehyde
IgG

c

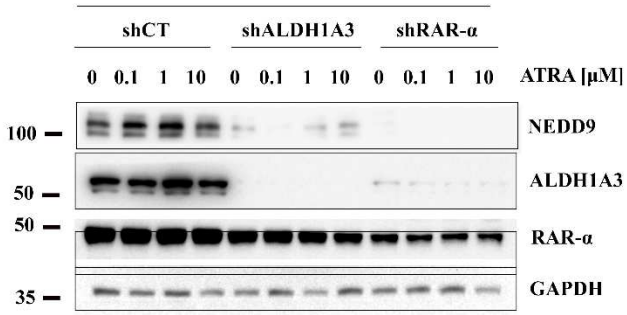
shCT
shALDH1A3
shRAR-α
0 0.1 1 10 0 0.1 1 10 0 0.1 1 10
ATRA [µM]
100
50
50
35
NEDD9
ALDH1A3
RAR-α
GAPDH

M1-Figure. S2: ALDH enzymatic activity in THJ-16T is primarily via the ALDH1A3 isoform

a. Quantitative PCR representing *NEDD9* and *ALDH1A3* mRNA expression in ALDH- and ALDH+ cells after treatment with 0.1 or 1µM retinoic acid for 24h, normalized to GAPDH. ADH1c is a positive control for retinoic acid receptor activation (n=3). **b.** ChIP assay for RARα protein enrichment on *NEDD9* RARE and exon ALDH+ THJ-16T cells were treated with DMSO, 0.1µM retinaldehyde or retinoic acid for 5h. (n=3). IgG is used as isotype control. **c**. Western blot representing the expression of NEDD9, ALDH1A3, and RARα in response to ALDH1A3 and RARα knockdown in combination with 0.1, 1 or 10 uM of all-trans retinoic acid in THJ-16T ALDH+ cells for 24 hours. Error bars represent $\pm$ SD, **P*<0.05

a

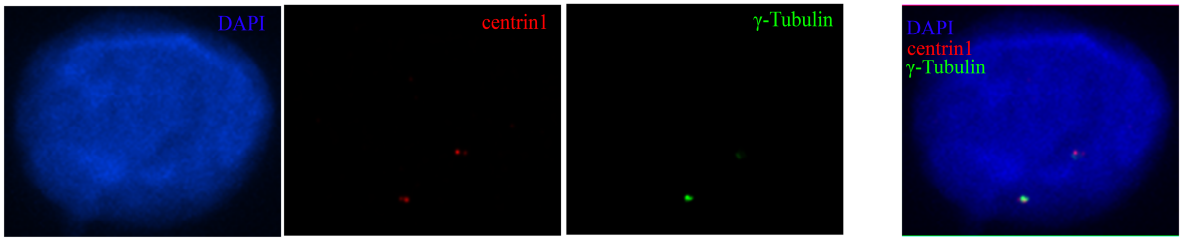
DAPI
centrin1
γ-Tubulin
DAPI
centrin1
γ-Tubulin

b

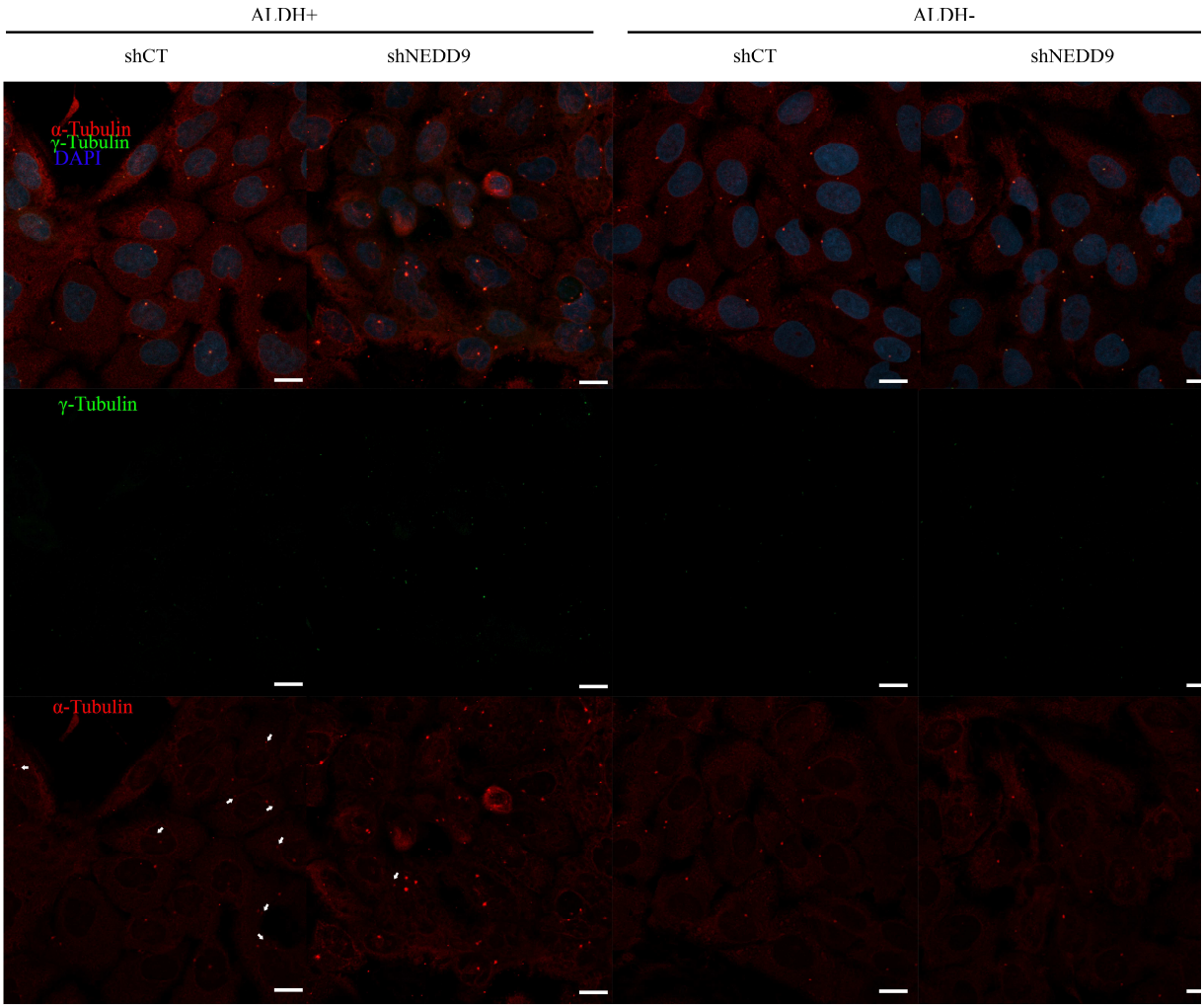
ALDH+
ALDH-
shCT
shNEDD9
shCT
shNEDD9
α-Tubulin
γ-Tubulin
DAPI
γ-Tubulin
α-Tubulin

M1-Figure. S3: Additional centrosome images

a. co-staining of centrin1 and γ-tubulin in ALDH+ shCT cells to illustrate that centrosomes with equal number of centrioles show distinct levels of pericentriolar material accumulation. **b.** Low magnification (20x) of microtubule regrowth assay in ALDH+ and ALDH- cells with or without NEDD9-knockdown, taken at 60s after induction of microtubule regrowth. Note the high occurrence of centrosomes (identified by γ-tubulin) with relatively weak microtubule nucleation (identified by a white arrow) compared to other centrosomes in the same cell in ALDH+ shCT cells. Images were captured using LSM 800.

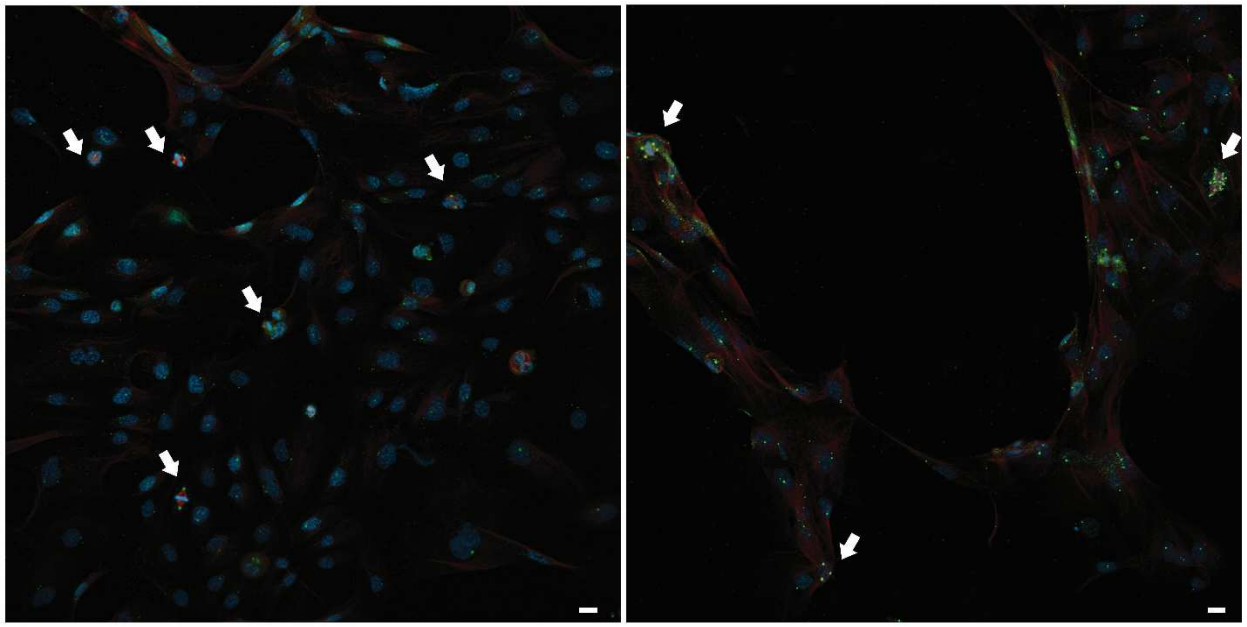

M1-Figure. S4: **Low-magnification (20x) representative images of shNEDD9-induced multipolar spindles in ALDH+ cells.** White arrows point to mitotic cells. Scale bar = 10μM. Images were captured using LSM 800.

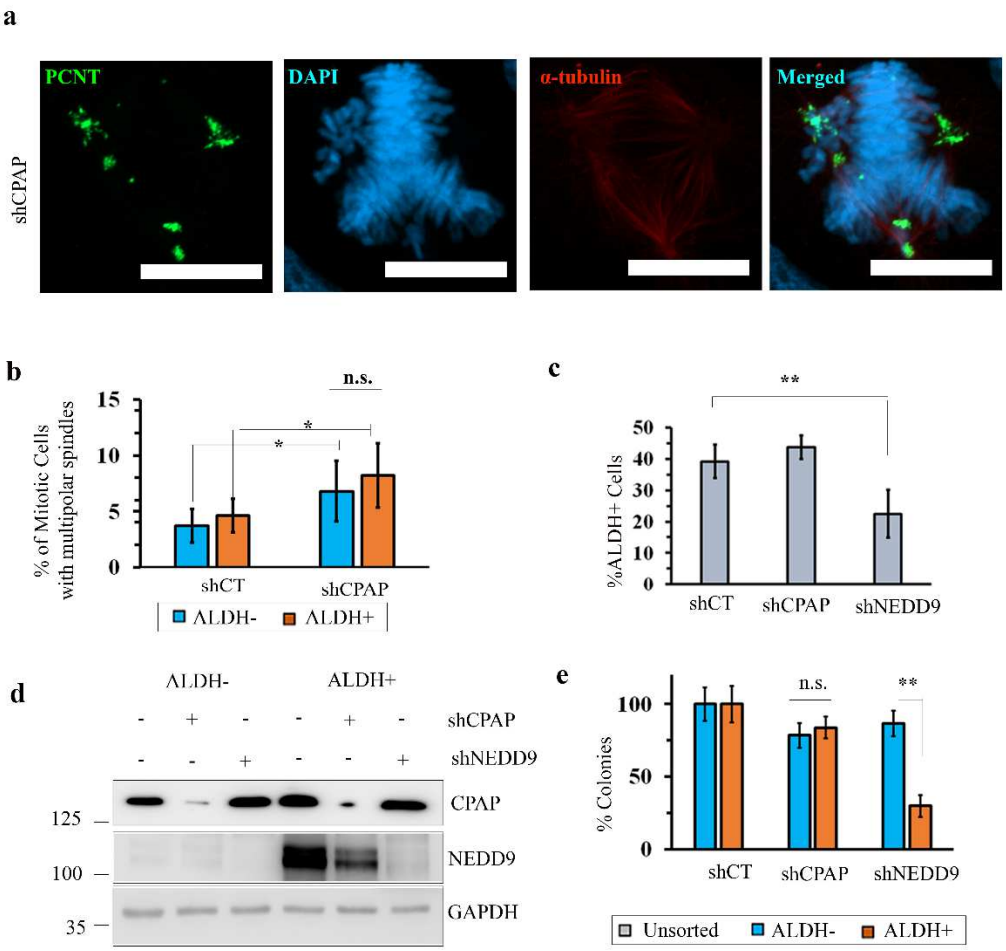

M1-Figure. S5: Impact of CPAP/CENPJ knockdown in THJ-16T ALDH+ and ALDH- cells
A. Representative immunofluorescence images of ALDH+ sorted THJ-16T cells illustrating the multipolar spindles observed following CPAP-knockdown **B.** Quantification of the incidence rate of multipolar spindles in ALDH+ and ALDH- THJ-16T following CPAP knockdown, (t=36h), pooled from 3 biological replicas **C.** Western blot of CPAP and NEDD9 expression levels in ALDH+ and ALDH- sorted THJ-16T cells following CPAP or NEDD9-knockdown. (t=36h) **D** Top: Quantification of the relative ratio of ALDH+ cells in unsorted THJ-16T following NEDD9 or CPAP-knockdown (t=5d) Bottom: quantification of the relative numbers of colony formed in ALDH+ and ALDH- sorted THJ-16T cells following NEDD9 or CPAP-knockdown (t=5d). 3 biological replicas each. Scale bars = 10µm. Error bars represent ± SD. Calculations of statistical significance and shRNA treatment timeline are the same as in Figure. 4

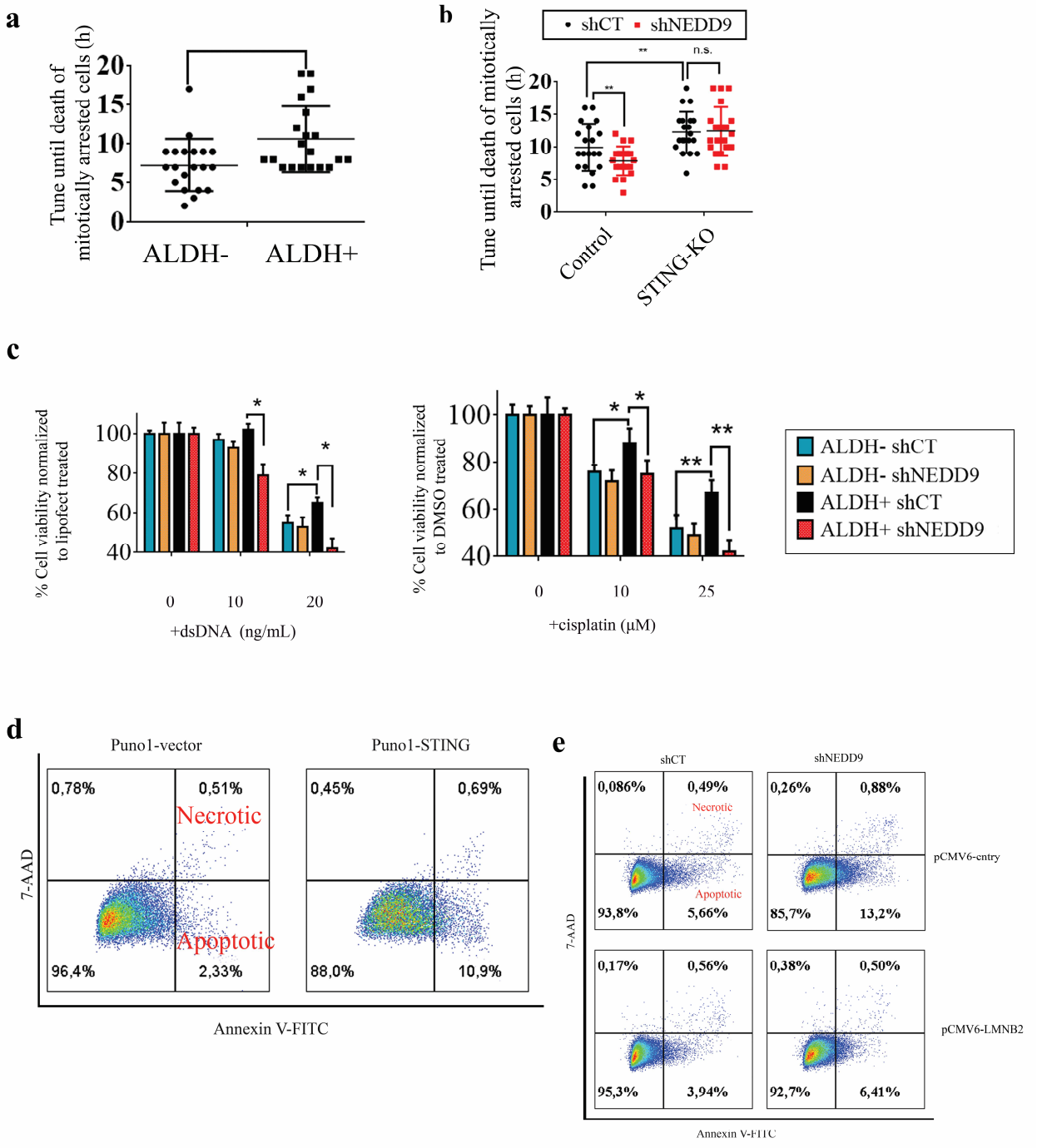
a
Tune until death of mitotically arrested cells (h)
20
15
10
5
0
ALDH-
ALDH+
b
shCT
shNEDD9
**
n.s.
**
Tune until death of mitotically arrested cells (h)
Control
STING-KO
c
% Cell viability normalized to lipofect treated
100
80
60
40
0
10
20
+dsDNA (ng/mL)
% Cell viability normalized to DMSO treated
0
10
25
+cisplatin (µM)
ALDH- shCT
ALDH- shNEDD9
ALDH+ shCT
ALDH+ shNEDD9
d
Puno1-vector
Puno1-STING
0,78%
0,51%
Necrotic
0,45%
0,69%
Apoptotic
96,4%
2,33%
88,0%
10,9%
7-AAD
Annexin V-FITC
e
shCT
shNEDD9
0,086%
0,49%
Necrotic
0,26%
0,88%
pCMV6-entry
Apoptotic
93,8%
5,66%
85,7%
13,2%
0,17%
0,56%
0,38%
0,50%
pCMV6-LMNB2
95,3%
3,94%
92,7%
6,41%
7-AAD
Annexin V-FITC

M1-Figure. S6: STING upregulation contributes to shNEDD9-mediated cell death during interphase and mitosis

a. Live cell imaging of eGFP-tubulin expressing cells was used to measure the time to cell death of mitotically arrested ALDH+ or ALDH- sorted cells. At least 20 mitotically arrested cells were analyzed per condition, n=3. **b**. Impact of STING-KO on shNEDD9-induced acceleration of mitotic cell death. Live cell imaging of eGFP-tubulin expressing cells was used to measure the time to cell death of mitotically arrested cells. At least 20 mitotically arrested cells were analyzed per condition, n=3. **c.** Cell viability of ALDH- and ALDH+ cells with or without NEDD9-depletion and treated with dsDNA or cisplatin. Cell viability for each group is normalized to shCT or DMSO treated. Cell viability is assessed by Cell Titre Glo 2.0. **d.** Representative flow cytometry panel illustrating the impact of STING overexpression on apoptosis. Puno1-STING was transfected into THJ-16T ALDH+ cells, and apoptosis was measured by AnnexinV/7-AAD co-staining after 72h. **e.** Representative flow cytometry panel illustrating the impact of LMNB2 overexpression on shNEDD9-induced apoptosis. Puno1-STING was transfected into THJ-16T ALDH+ cells. LMNB2-overexpressing stable cell lines was obtained following G418 selection. LMNB2-overexpressing cells were treated with shCT or shNEDD9 and apoptosis was measured by AnnexinV/7-AAD co-staining after 72h.

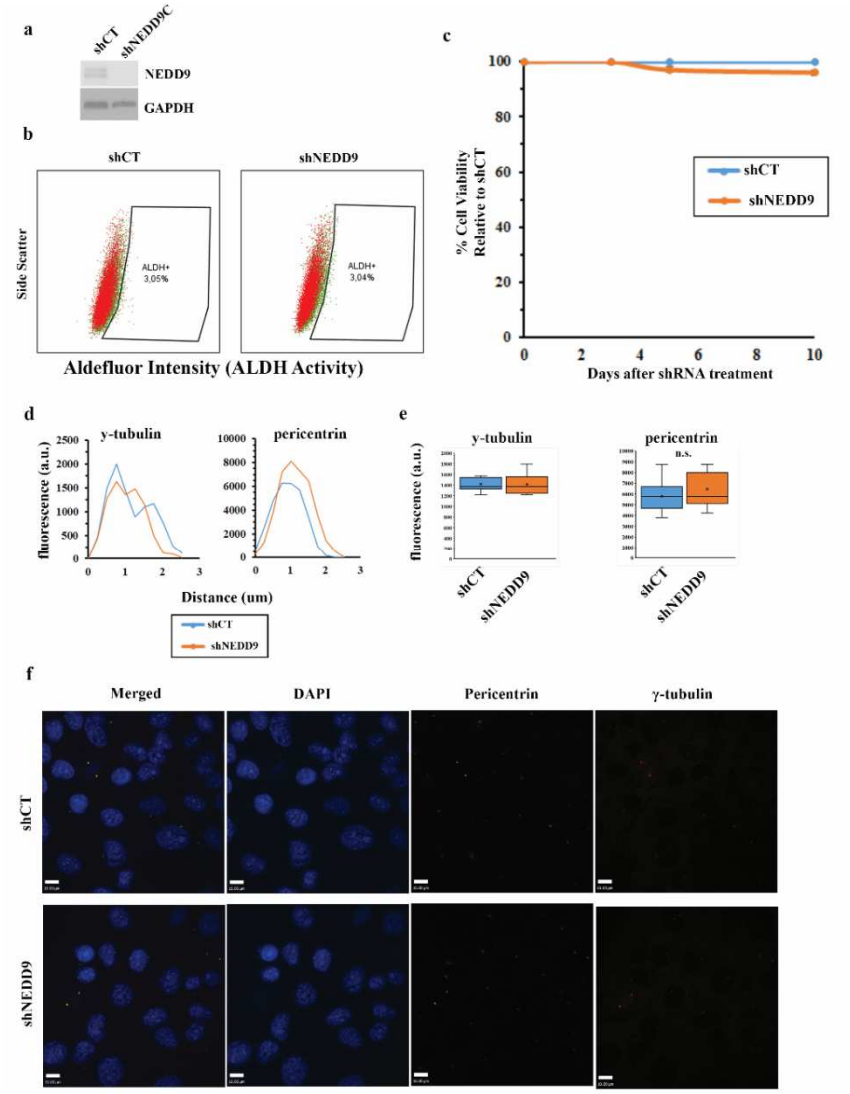

M1-Figure. S7: Impact of NEDD9-knockdown on MCF10-A non-transformed cell line

A Representation of NEDD9-knockdown (t=48h) in MCF10-A. **B** Representative FACS analysis of %ALDH+ cells after NEDD9-knockdown (t=10d) in MCF10-A, where the addition of the ALDH enzymatic inhibitor "DEAB" is used to establish background levels (overlaid in green) **C** Time-course of MCF10-A cell viability after NEDD9-knockdown, assessed by cell counting using trypan blue staining to discern non-viable cells **D** Representative Line graph panel indicating the intensity of centrosome pairs or individual centrosomes after NEDD9-knockdown (t=10d). **E** Quantification of γ-tubulin/ fluorescence of interphase centrosome in MCF10-A cells after NEDD9-knockdown (t=10days, 3 biological replicates, 15 cells were scored for each condition in each repeat). Measurements were conducted as described in Figure. 8A and B. **F** Low magnification representative image of pericentrin and y-tubulin immunofluorescence staining in MCF10-A (Scale bar = 10 μm). Calculations of statistical significance and shRNA treatment timeline are the same as in Figure. 4.

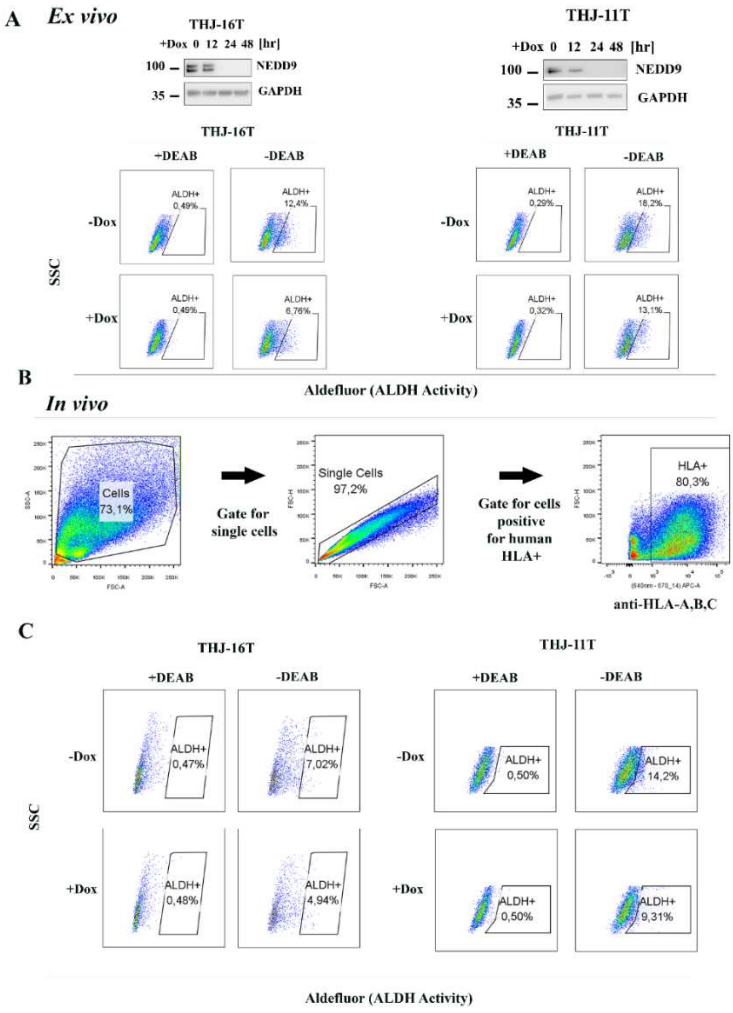

M1-Figure. S8: Inducible NEDD9-knockdown causes reduction of %ALDH+ in ATC xenograft

A. Representative western blot and flow cytometry panels illustrating the NEDD9 expression and ALDH activity levels of THJ-11T and THJ-16T pLKO-tet-shNEDD9D cells, which are inducible NEDD9-knockdown stable cell lines. For western blot, cells were treated with 300nM doxycycline for the indicated time. For FACS, cells were treated 300nM doxycycline for 7d. **B.** Scheme representing the strategy used to gate THJ-11T and THJ-16T pLKO-tet-shNEDD9D cells. At necrosis, tumors were digested with 0.25% trypsin to obtain single-cell suspensions, which were then stained with anti-HLA-A,B,C antibody to distinguish tumor cells from mouse cells. **C.** Representative flow cytometry panels illustrating the ALDH activity of THJ-11T and THJ-16T pLKO-tet-shNEDD9D cells derived from *in vivo* tumors. NOD-SCID mice implanted with tumors were treated with 2mg/mL doxycycline in drinking water. ALDH is measured from single-cell suspensions derived from tumors at necropsy, using the gating-strategy illustrated in panel B. DEAB, an ALDH enzymatic inhibitor, is used to establish background control.

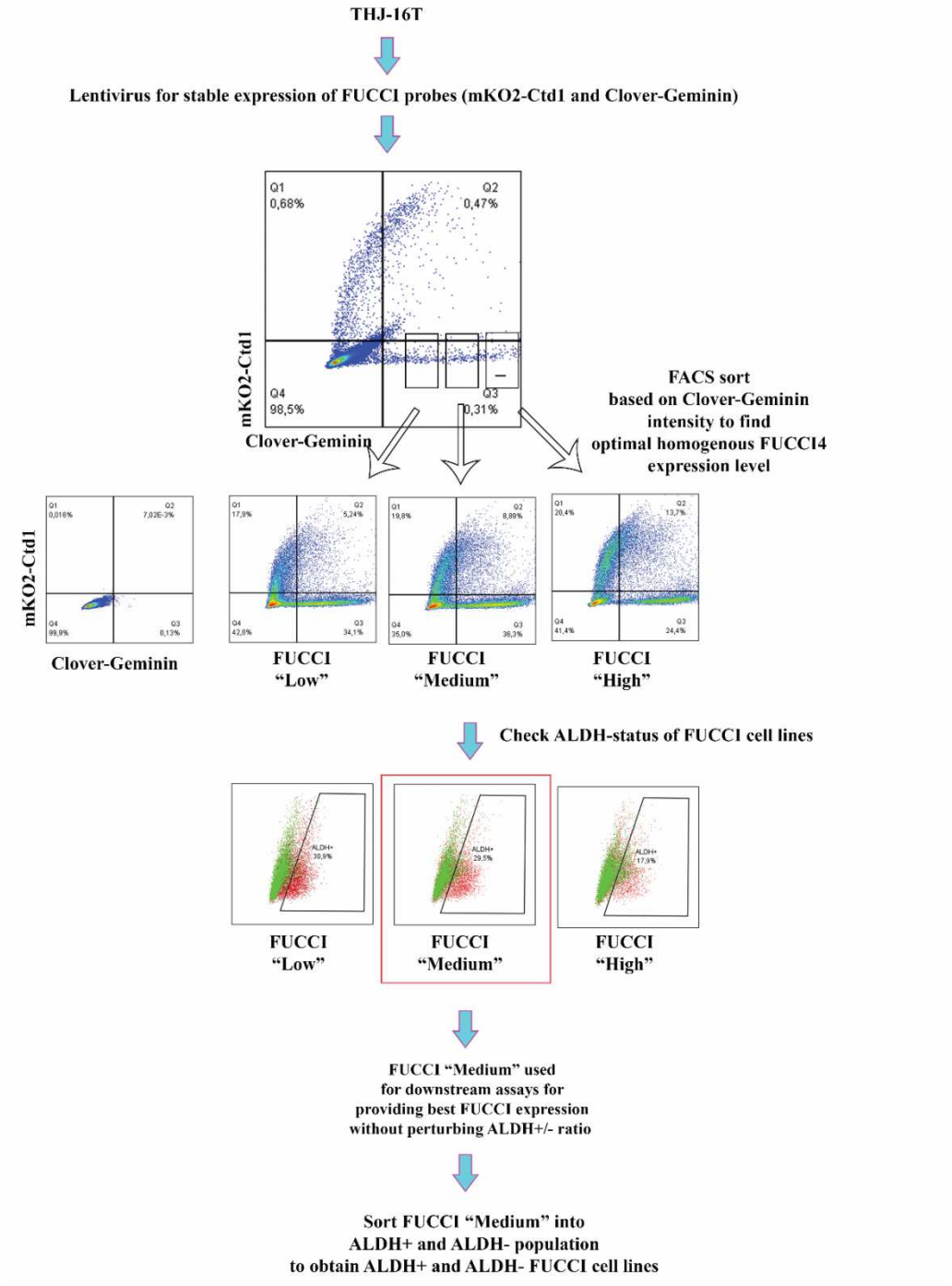

M1-Figure. S9: Gating strategy for flow cytometry analysis
Scheme representing the strategy used to generate ALDH+ and ALDH- sorted THJ-16T cell lines with stable expression of FUCCI probes.

Methods

Human study population and tissue microarray: Thyroid patient tissues was obtained from a retrospective cohort study approved by the Research Ethics Committee of the Jewish General Hospital – McGill University (Montreal, QC, Canada) through the protocol 13-093. The methods and experimental protocols of the present study were performed in accordance with the approved guidelines and informed consent was obtained from all human participants. Two sets of tissue samples were used: the 8 -patient cohort, with ATC samples, and the 169-patient cohort (Supplementary Table 2, including 13 benign thyroid tumors and 156 papillary thyroid cancer), with surgical samples for immunohistochemistry staining. The inclusion criteria were as follows: (a) (a) location of the tumor in the thyroid; (b) availability of surgical specimens in FFPE blocks; (d) treatment in single Institution; (e) no recurrence or distant metastasis in the moment of the diagnosis. The information collected from the medical records included the following: gender; age; subtype, variant, and laterality. Stained H&E histological slides were evaluated by two pathologists (AS, SDS).

Core biopsies were extracted from previously defined areas using a Tissue Microarrayer (Beecher Instruments, Inc., Sun Prairie, Wis). Tissue cores that measured 1.0 mm from each specimen were punched and arrayed in duplicate on a recipient paraffin block and tissue microarray (TMA) blocks used for immunohistochemistry as described earlier[93].

Cell culture: 8505c, TPC1, and BCPAP cell lines are a courtesy of Dr. M. Trifiro (Department of Endocrinology, Jewish General Hospital, McGill University), which were purchased from DSMZ—and maintained in culture in RPMI medium supplemented with 10% heat-inactivated fetal bovine serum (Wisent) and 1% penicillin-streptomycin . MCF-10A cells were purchased form ATCC and maintained in DMEM/12 supplemented with 5% horse serum, EGF, hydrocortisone, cholera toxin, insulin, and 1% penicillin-streptomycin. THJ-11T and THJ-16T were generously provided by Dr. J. Copland (Mayo Clinic, Jacksonville, Florida). These cell lines are derived from clinic anaplastic thyroid cancer patients and confirmed to match the primary tumor sample via DNA short tandem repeat analysis[94]. They are maintained in RPMI 1640x with 5% FBS, 1x non-essential amino acids, 1mM sodium pyruvate, and 10mM HEPES.

Microarray analysis: Dataset comparing transcriptomic profile of anaplastic thyroid cancer cells versus normal thyroid cells was obtained from GSE85457. The platform used was Affymetrix Human Genome U133 Plus 2.0 Array. Values were normalized using MAS.5 algorithm. NEDD9 probe: 202150_s_at. ALDH1A1 probe: 212224_at, ALDH1A2 probe: 207015_s_at, ALDH1A3 probe: 203180_at, ALDH2 probe: 201425_at, ALDH3A1 probe: 205623_at.

Flow cytometry quantification of ALDH activity and sorting by ALDH-status: ALDH activity was detected using ALDEFLUOR® staining kit (StemCell Technologies). Live cells were harvested after treatment, washed once with PBS, and resuspended in ALDH assay buffer before splitting into 2 tubes, one with DEAB and one without. The cells were incubated in 100µL of assay buffer + 1ul of 300nM aldefluor reagent and 1mL of DEAB reagent for 15-40min (optimized by cell line) at room temperature. The cells were then centrifuged and re-suspended in new assay buffer + 5µL of 7-AAD. 7-AAD staining is used to exclude necrotic cells during FACS analysis. The aldefluor intensity is measured using BD FACScalibur. The samples with DEAB was measured first, followed by the matching sample without DEAB added; positivity is determined by the difference in fluorescence between +DEAB and -DEAB sample. Cell sorting by ALDH-status was conducted using the same protocol in a sterile environment, using the BD-FACSAria machine. To ensure high purification rate, we recovered only the cell population with the 20% highest or lowest Aldefluor staining respectively. Sorted cells were allowed recovery for 3 days before being re-evaluated for ALDH+ positivity.

8505C, THJ-11T, and THJ-16T were sorted based on Aldefluor activity. 8505c had basal 20-30% rate of ALDH+ cells, but intensity-wise showed poor separation of the ALDH- and ALDH+ cells, thus could not be efficiently sorted. THJ-11T had a basal 20-40% rate of ALDH+ cells and exhibited good separation of ALDH+ and ALDH- cell population, but the ALDH- cells post sorting displayed only 20% of the doubling rate compared to ALDH+ cells. THJ-16T had a basal 20-40% rate of ALDH+ cells, exhibited strong separation of ALDH+ and ALDH- cell population, and displayed relatively equal double rating between the ALDH+ and ALDH- population post sorting, which was optimal for fair phenotype studies following genetic or pharmacological perturbations.

For apoptosis assay, cells were washed twice with Biolegend's Cell Staining Buffer, then responded in Annexin V binding buffer together with with FITC Annexin V (Biolegends 640905) for 20 minutes at room temperature, followed by treatment with 7-AAD before analysis by flow cytometry.

Immunofluorescence microscopy

For immunofluorescence microscopy, cells were fixed in 4% paraformaldehyde or 100% methanol and permeabilized using 0.2% triton-X. The centrosome, mitotic spindle, and DNA was visualized using anti-pericentrin (ab4448, Abcam, 1:2000), anti-α-Tubulin (DM1A, Millipore Sigma, 1:1000), anti-γ-tubulin (GTU-88, Abcam, 1:1000), anti-γ-tubulin (EPR16793, 1:1000), anti-Centrin (20H5, Millipore Sigma, 1:1000) and DAPI respectively. Immunofluorescence images were obtained using Quorum wave FX spinning disk (SD) confocal microscope or LSM800 Airyscan (Zeiss) confocal laser scanning microscope and analyzed using Volocity (PerkinElmer) or ImageJ.

To quantify declustered centrosomes in dividing cells, 60 or more random images across 3 biological replicas for each condition was taken at 40x or 63x magnification. At least 80 cells mitotic cells were counted per condition per replica. Representative images were captured at 63x magnification. Mitotic cells are discriminated by three criteria: chromosome condensation as visualized by DAPI, the appearance of the mitotic spindle as visualized by alpha-tubulin, and increased centrosome pericentriolar materials as visualized by pericentrin. Declustered centrosomes were identified based on the presence of >2 spindle poles radiating from distinct pericentrin foci in 1 cell. The number of declustered centrosomes is quantified as a percentage of total mitotic cells.

To quantify centrosome amplification, cells were co-stained with centrin and pericentrin antibodies and visualized at 63x magnification. A cell was defined as centrosome amplified by the presence of >4 centrin-positive dots that show co-localization with pericentrin. Images were captured using LSM800 Airyscan (Zeiss) confocal laser scanning microscope.

For centrosome proteins intensity assays, images were captured at 63x using focusing on the middle (maximal size and intensity) of an individual centrosome. Quantification was confirmed using two methods. The first is by drawing a circle around an individual centrosome in volocity software, measuring the sum integrated pixel intensity, then subtracting the background

fluorescence (measured by placing a circle of the same dimension away from the centrosome). The second way is, in ImageJ, drawing a 2.5um line through the center of one or two centrosomes then using the "plot profile" function of Fiji/ImageJ software to measure the integrated area after subtracting the background. For quantification involved 3 biological replicates in which 15 cells were scored for each condition in each repeat. Cells with 2 or more than 2 centrosomes were scored separately. For cells with 2 centrosomes, only centrosome pairs less than 1μm apart, directly adjacent to the nucleus were included. Centrosome nucleation symmetry is calculated using the formula (peak intensity of weak centrosome / peak intensity of strong centrosome) for cells with 2 centrosomes, or (average peak intensity of weaker 50% of the centrosomes / average peak intensity of the stronger 50% of centrosomes) in the case of centrosome amplification.

Live-cell visualization of cell cycle and mitosis events

Plasmids for FUCCI (Fluorescent Ubiquitination-based Cell Cycle Indicator) probes: pLL3.7m-Clover-Geminin(1-110)-IRES-mKO2-Cdt (30-120), pLL3.7m-mTurquoise2-SLBP(18-126)-IRES-H1-mMaroon1 were deposited by Dr. Michael Lin. Expressing eGFP-tagged alpha-tubulin (L304-EGFP-Tubulin-WT) was deposited by Dr. Weiping Han. Plasmids were used to generate lentivirus as described above. THJ-16T cells were infected with FUCCI probes, then allowed to recover for 7 days. Cells were then sorted by flow cytometry based on low, medium, or high geminin expression, to homogenize the expression of FUCCI probes to a level that did not perturb ALDH+/- population ratio, to avoid selective effects from FUCCI expression; cells were thereafter sorted into ALDH+ and ALDH- cell via Aldefluor assay as described above, to generate stable ALDH+ and ALDH- FUCCI cell lines (represented in **fig. S9**).

For the monitoring cell cycle and mitosis transitions, sorted cells stably expressing FUCCI or eGFP-tubulin were pretreated with shCT or shNEDD9 were seeded in normal growth media (RPMI + 5% FBS + Sodium Pyruvate + Non-essential amino acid + Hepes), on a multiwell chambered coverglass (LabTek). At the start of the time-lapse, the coverglass was directly placed on a heated stage with 5% CO2. Fluorescent images from 20 different fields per condition were captured every 10min (for eGFP tubulin) or 30min (for FUCCI) for 24h using a heated 20 X objective lens at WaveFX spinning disk confocal microscope system, using low intensity laser excitation (Quorum Technologies INC.).

Lentiviral generation and infection of cells: For shRNA-mediated knockdown, shRNA sequences cloned into pLKO.1-puro lentiviral vectors were co-transfected using *polyethylenimine* into 293T cells with psPAX2 and pMD2.G for lentiviral generation. Media was refreshed 12h after transfection. Thereafter, supernatant containing the lentivirus was collected and filtered every 24h and fresh media was added, repeated 3 times. Viral supernatant was added to low-passage cell lines together with polybrene in 1% serum. 24h after virus infection (t=0h for time-course assays), cells were refreshed with complete media and selection for infected clones was carried out using 0.5-2ug/mL puromycin. ALDH+ and ALDH- cells were confirmed not to have equal sensitivity to puromycin. Knockdown efficiency was confirmed by western blot using the corresponding antibodies. For doxycycline-inducible cell lines, stable cell lines were derived from a single clone isolated by single cell FACS sorting.
For LZRS retroviral vectors, LZRS or LZRS_NEDD9 (containing GFP sequence) was transfected into Phoenix cells using lipofectamine 2000. Supernatants containing the retrovirus were collected and filtered and added to low-passage cell lines together with polybrene. Infected cells were enriched by FACS-sorting for GFP-positivity, and expression of ectopic NEDD9 was confirmed using flag antibody to detect a 105kDa band.

Plasmid vectors

pLKO-shC (shNEDD9), pLKO-shD (shNEDD9-2), LZRS-hNEDD9-IresGFP, and LZRS-IresGFP were deposited by Dr. Lynda Chin. pLentiCRISPRv2 was deposited by Dr. Feng Zhang. pLentiCRISPRv2-STING_gRNA3 was deposited by Dr. Nicolas Manel. ShALDH1A3 (NM_000693.1-459s1c1), shRARA (NM_000964.2-594s21c1), shCPAP (NM_018451.2-2403s1c1) vectors were purchased from Sigma-Aldrich Corporation. To construct the plasmid for inducible NEDD9-knockdown, the shNEDD9-2 sequence (Forward 5' CCG GCC AGC AGA AAC CAG TGA GAA ACT CGA GTT TCT CAC TGG TTT CTG CTGG TTTTTG, Reverse 5' AATTCA AAAA CCA GCA GAA ACC AGT GAG AAA CTC GAG TTT CTC ACT GGT TTC TGC TGG) was cloned into the Tet-pLKO-puro vector (deposited by Dr. Dmitri Wiederschain). The lentivirus-construct expressing eGFP-tagged alpha-tubulin (L304-EGFP-Tubulin-WT) was deposited by Dr. Weiping Han.

Microtubule regrowth assay

The microtubule regrowth assay was performed as previously describe. Fluorescence activated cell sorted THJ-16T cells was treated with shCT or shNEDD9 for 36h, then treated with nocodazole for 16h. Cells were then given cold medium and placed on ice for 90 minutes. Thereafter, microtubule regrowth was then induced by pre-warmed media and placing the cells in 37ºC for the indicated time (30s – 60s), when they were subsequently fixed with 4% paraformaldehyde and stained for anti-α-tubulin and anti-γ-tubulin.'

Western-blot analysis: Sub-confluent cells were washed 3x with PBS, lysed in RIPA buffer (50 mM Tris-HCl at pH7.5, 150 mM sodium chloride, 1% tritonX-100, 0.1% SDS, 2mM EDTA and 25mM sodium fluoride) with 1mM PMSF and protease inhibitor cocktail (Roche) on ice for 30minand centrifuged at 13,000 rpm for 20min. Cell lysates was mixed with SDS buffer (Tris at pH 6.8, 20% glycerol, 5% SDS, bromophenol blue and β-mercaptoethanol) and boiled for 5 min, then loaded into 8-15% SDS-PAGE gels, transferred to PDVF membranes, and blotted with the primary antibodies. The primary antibodies used were as follows: anti-NEDD9 (Cell Signaling Technology, 4044), anti-ALDH1A3 (Novus Biologicals), anti-CPAP/CENPJ (Proteintech Group, 11517-1-AP), anti-RARα (Cell signaling, #62294) and anti-FLAG (Sigma Aldrich Corporation, F1804), p-TBK1 (cell signaling 54835), pSTAT1 (cell signaling 91675), TBK1 (cell signaling 35045), STAT1 (cell signaling 91725), STING (Cell signaling 13647), cGAS (abiocode 14085). Secondary antibodies for Western-blot assays: anti-mouse IgG-peroxidase-conjugated (Bio-Rad Laboratories, 172-1011), anti-rabbit IgG-peroxiase-conjugated (Bio-Rad Laboratories, 170-6515).

Reporter assay: Stable cell lines were transiently transfected (lipofectamine 3000) with human IFN-β firefly reporter plasmid [95], or TK-Renilla luciferase assay reporter to normalize the readings. Cell lysates were prepared, and reporter activity measured using the Dual Luciferase Assay System (Promega).

Immunohistochemistry: Immunohistochemistry was carried out as described earlier [96]. Incubations with the primary antibodies diluted in PBS were conducted overnight at 4ºC for: anti-NEDD9 (Abcam, 1:100), anti-ALDH1A3 (Novus Biologicals, 1:250), anti-Pericentrin

(Abcam, 1:5000), or anti-γ-tubulin (Abcam, 1:5000). The sections were washed and incubated with secondary antibodies (Advanced ™ HRP Link, DakoCytomation, K0690, Denmark) for 30min followed by the polymer detection system (Advanced ™ HRP Link, DakoCytomation) for 30mins at room temperature. Reactions were developed with a solution containing 0.6mg/mL of 3,3'-diaminobenzidine tetrahydrochloride (DAB, Sigma, St Louis) and 0.01% H_2O_2 and then counter-stained with Mayer's hematoxylin, dehydrated and mounted with a glass coverslip. Positive controls (a tissue known to contain the antigen under study) were included in all reactions in accordance with manufacturer's protocols. The negative control consisted in omitting the primary antibody and incubating slides with PBS and replacing the primary antibody with matching isotype. Quantification of γ-tubulin symmetry is based on ImageJ measurements of the relative DAB intensity of each centrosome pairs, following the same formula as for immunofluorescence measurements.

Tumorsphere-forming assays: The tumorsphere medium was prepared with DMEM-F12 (3:1, Invitrogen) containing 2% B27 supplement (Invitrogen), and 20 ng/mL epidermal growth factor (Sigma-Aldrich). Tissue culture dishes were coated with a polyhydroxyethylmethacrylate polymer (polyHEMA, Sigma-Aldrich) to facilitate sphere formation. Briefly, polyHEMA was dissolved in 95% ethanol at 12% (w/v). A working solution was made by further dilution of 1:10 in 95% ethanol and was added to 24-well plates at 0.1mL per well. A hydrophobic surface was formed after the polyHEMA solution dried out at room temperature in a tissue culture hood. Single-cell suspensions were seeded at two dilutions of 300 and 1000 cells per well in 6-replicas. For compound-treatment, drugs were mixed with initial cell-suspension. After ten days, the number of tumorspheres (>50µm) was microscopically counted and statically analyzed. Spheres were quantified using both seeding-dilutions where possible, though dilutions in which too few (<5) or too many (>50) spheres were not used for quantification. Representative images are generated from the same seeding-concentration.

Animal models: Animal experiments were performed in compliance with institutional and federal guidelines after approval from the McGill University Facility Animal Care Committee. (Protocol #5018). NOD-SCID mice were purchased from Charles River Laboratories (St. Zotique, Quebec, Canada). *Tumorigenesis Assay:* Exponentially growing THJ-16T cells were

resuspended as single-cells in PBS. 100uL of cell suspension containing the indicated cell number was injected subcutaneously into the right flank of NOD-SCID mice. The mice were sacrificed 35 days after injection and tumor formation was assessed by palpation and examined after necropsy for confirmation. To assess shNEDD9's impact on tumor initiation, THJ-16T cells were pre-treated with shNEDD9 *ex vivo* for 72h, followed by recovery in virus -free media for 5 days prior to injection. Representative tumor images were captured by placing the extracted tumors in 6-well plates and imaged using Gelcount machine and software (Oxford Optronix Ldt). No significant difference in cell viability between control and treated-cells was observed at time of injection via trypan blue staining.

Inducible NEDD9-knockdown model: 3 x 10^6 THJ-16T or THJ-11T cells tet-pLKO-puro-NEDD9D cells were injected subcutaneously into the right flank of NOD-SCID mice. To induce NEDD9-knockdown, 2mg/mL of doxycycline was administered in drinking water together with 1% sucrose, starting at 7 day after injection. Tumor volume was thereafter measured biweekly. At necropsy, tumors were digested in 0.25% trypsin/EDTA to obtain single-cell suspensions for FACS sorting. To distinguish human from mouse cells, cells were with anti-HLA-A,B,C antibody (Biolegend 311405). A subset of HLA-positive cells was purified for western blot analysis. A section of tumor was also removed from THJ-11T prior to trypsin-digest and fixed in 10% v/v formalin for immunohistochemical staining, while the same could not be done for THJ-16T due to the small size of the doxycycline-treated tumors.

Analysis of mitotic events in ATC xenograft tumor specimens

Hematoxylin and Eosin-stained (H&E) THJ-11T tumor samples was analyzed under a brightfield microscope at 100x magnification. Analysis was restricted to cells fixed while undergoing metaphase or later anaphase. Metaphase was defined by a clear condensed and aligned chromosomes. Anaphase or later is defined by two sets of condensed and aligned chromosomes within the same discernable cell. Chromosome missegregation in post-metaphase cells was defined by distinguishable hematoxylin staining presence between segregating chromosomes.

Quantitative PCR: 50×10^3 cells were plated in 6-well Corning® Costar® plates. Cells were either untreated or treated with 2-doses of all-trans retinoic acid. RNA was extracted 24h later using total RNA Mini Kit (Qiagen® FroggaBio ®) according to the manufacturers' instructions.

cDNA was synthesized from 500 ng of RNA using Superscript III reverse transcriptase (Invitrogen®) and oligo-dT primers (Invitrogen®). qRT-PCR was performed on the 7500 Fast Real-Time PCR System (Applied Biosystems) using GoTaq qPCR Master Mix (Promega) in 10 µL reaction volume. The reactions were carried out in triplicate. *GAPDH* was used as endogenous control. Following primers were used:

Gene	Forward Primer (5'-3')	Reverse Primer (5'-3')
ALDH1A3	ACC GAC TAT GGA CTC ACA GCA	GTT CTC TGC CAT TTC CTG ACA.
NEDD9	GAC GAC GCC AAA CAA CTG ACC AC	GGC TTA CTG TGG ACC TGG GCT TT
ADH1c	AAA GAG TTG GGT GCC ACT GAA	TTG TGC CAC ATG CCT CAT GAC AAC
STING	CCT GAG TCT CAG AAC AAC TGC C	GGT CTT CAA GCT GCC CAC AGT A
TNF-α	CTG CAC TTT GGA GTG ATC GG	CTC GGG GTT CGA GAA GAT GA
IL-6	CAG CCC TGA GAA AGG AGA CAT	GGT TCA GGT TGT TTT CTG CCA
CXCL10	GTG GCA TTC AAG GAG TAC CTC	TGA TGG CCT TCG ATT CTG GAT T
CCL5	CCA GCA GTC GTC TTT GTC AC	CTC TGG GTT GGC ACA CAC TT
IFN-β	AAA CTC ATG AGC AGT CTG CA	AGG AGA TCT TCA GTT TCG GAG G
Actin	ATG CAG AAA GAG ATC ACC GC	ACA TCT GCT GGA AGG TGG AC

Microarray analysis: Transcriptomic profiles of cancer patients were obtained from TCGA PanCancer Atlas datasets [97] and analyzed through Cbioportal[91,92].

BrDU pulse-chase assay

ALDH+ and ALDH- sorted THJ-16T cells were incubated together with 1µM bromodeoxyuridine (BrdU) for 2 weeks. Thereafter, cells seeded onto coverslips with shCT or

shNEDD9 lentivirus, and were allowed to attach for 24h before the culture media was refreshed, and cells were then cultured in virus and BrdU-free media for another 36h before being harvested. Slides were fixed in 70% ethanol for 2h at -20ºC, then washed 3x in PBS before being treated with 1.5M HCl for 15 minutes, washed another 3 times in PBS, and then stained with BrDU-FITC antibody, together with alpha-tubulin and DAPI as described in the immunofluorescence imaging methods section.

Chromatin immunoprecipitation assay: 50×10^3 cells were seeded in 150cm dish 48 hours before being treated with DMSO, 100nM all-trans retinaldehyde or 100nM all-trans retinoic acid (atRA) for another 5 hours. Cells were then harvested and cross-linked in 20mL PBS with 600ul of 37% Formaldehyde solution for 10 minutes, and later neutralized by adding 2.5mL of 1M glycine solution for 5 minutes. Cells were then lysed, and DNA was fragmented by extensive sonication. Immunoprecipitation of retinoic acid receptor alpha protein was performed using anti-RARα (Cell signaling, #62294) antibody together with Protein G Plus-Agarose Suspension (Millipore, IP04-1.5ML). Quantification of co-precipitated DNA was performed by qRT-PCR with the primers: *NEDD9*-RARE forward 5'- ATG TTC TGT GCT TCG CTG GA -3', reverse 5'- TTT GAC GGC TGG CAT TTC TA -3'; *NEDD9*-Exon forward 5'- ATG TCC ACG TCT TCC ACC TCC-3', reverse 5'- AGT GAC CAG TGC CAT TAG CGT G -3'.

Statistical analysis: For discrete variables showing normal distribution, means and standard deviations (SD) are given and comparisons were made using the t-test. In all statistical tests, $P<0.05$ was considered statistically significant.

References

1. Holland, A.J. & Cleveland, D.W. Boveri revisited: chromosomal instability, aneuploidy and tumorigenesis. *Nature reviews Molecular cell biology* **10**, 478 (2009).
2. Kreso, A. & Dick, J.E. Evolution of the cancer stem cell model. *Cell stem cell* **14**, 275-291 (2014).
3. Malta, T.M.*, et al.* Machine learning identifies stemness features associated with oncogenic dedifferentiation. *Cell* **173**, 338-354. e315 (2018).
4. Chen, H. & He, X. The convergent cancer evolution toward a single cellular destination. *Molecular biology and evolution* **33**, 4-12 (2016).
5. Bakhoum, S.F. & Landau, D.A. Chromosomal instability as a driver of tumor heterogeneity and evolution. *Cold Spring Harbor perspectives in medicine* **7**, a029611 (2017).
6. Morel, A.-P.*, et al.* A stemness-related ZEB1–MSRB3 axis governs cellular pliancy and breast cancer genome stability. *Nature medicine* **23**, 568 (2017).
7. Zhou, W.*, et al.* ALDH1 activity identifies tumor-initiating cells and links to chromosomal instability signatures in multiple myeloma. *Leukemia* **28**, 1155-1158 (2014).
8. Wilkens, L.*, et al.* Induction of aneuploidy by increasing chromosomal instability during dedifferentiation of hepatocellular carcinoma. *Proceedings of the National Academy of Sciences* **101**, 1309-1314 (2004).
9. Nigg, E.A. & Stearns, T. The centrosome cycle: centriole biogenesis, duplication and inherent asymmetries. *Nature cell biology* **13**, 1154-1160 (2011).
10. Yamashita, Y.M., Jones, D.L. & Fuller, M.T. Orientation of asymmetric stem cell division by the APC tumor suppressor and centrosome. *Science (New York, N.Y.)* **301**, 1547-1550 (2003).
11. Yamashita, Y.M., Mahowald, A.P., Perlin, J.R. & Fuller, M.T. Asymmetric inheritance of mother versus daughter centrosome in stem cell division. *Science (New York, N.Y.)* **315**, 518-521 (2007).
12. Cosenza, M.R.*, et al.* Asymmetric centriole numbers at spindle poles cause chromosome missegregation in cancer. *Cell reports* **20**, 1906-1920 (2017).
13. Morrison, S.J. & Kimble, J. Asymmetric and symmetric stem-cell divisions in development and cancer. *nature* **441**, 1068-1074 (2006).
14. Yamashita, Y.M. & Fuller, M.T. Asymmetric centrosome behavior and the mechanisms of stem cell division. *The Journal of cell biology* **180**, 261-266 (2008).
15. Izumi, H. & Kaneko, Y. Evidence of asymmetric cell division and centrosome inheritance in human neuroblastoma cells. *Proceedings of the National Academy of Sciences* **109**, 18048-18053 (2012).
16. Nigg, E.A. & Stearns, T. The centrosome cycle: centriole biogenesis, duplication and inherent asymmetries. *Nature cell biology* **13**, 1154 (2011).
17. Chan, J.Y. A clinical overview of centrosome amplification in human cancers. *International journal of biological sciences* **7**, 1122 (2011).
18. Lingle, W.L.*, et al.* Centrosome amplification drives chromosomal instability in breast tumor development. *Proceedings of the National Academy of Sciences* **99**, 1978-1983 (2002).

19. Ganem, N.J., Godinho, S.A. & Pellman, D. A mechanism linking extra centrosomes to chromosomal instability. *Nature* **460**, 278-282 (2009).
20. Milunović-Jevtić, A., Mooney, P., Sulerud, T., Bisht, J. & Gatlin, J. Centrosomal clustering contributes to chromosomal instability and cancer. *Current opinion in biotechnology* **40**, 113-118 (2016).
21. Leber, B.*, et al.* Proteins required for centrosome clustering in cancer cells. *Science translational medicine* **2**, 33ra38-33ra38 (2010).
22. Kwon, M.*, et al.* Mechanisms to suppress multipolar divisions in cancer cells with extra centrosomes. *Genes & development* **22**, 2189-2203 (2008).
23. Quintyne, N.J., Reing, J.E., Hoffelder, D.R., Gollin, S.M. & Saunders, W.S. Spindle multipolarity is prevented by centrosomal clustering. *Science (New York, N.Y.)* **307**, 127-129 (2005).
24. Mackenzie, K.J.*, et al.* cGAS surveillance of micronuclei links genome instability to innate immunity. *Nature* **548**, 461-465 (2017).
25. Ishikawa, H. & Barber, G.N. STING is an endoplasmic reticulum adaptor that facilitates innate immune signalling. *Nature* **455**, 674-678 (2008).
26. Hopfner, K.-P. & Hornung, V. Molecular mechanisms and cellular functions of cGAS–STING signalling. *Nature Reviews Molecular Cell Biology*, 1-21 (2020).
27. Molinaro, E.*, et al.* Anaplastic thyroid carcinoma: from clinicopathology to genetics and advanced therapies. *Nature Reviews Endocrinology* **13**, 644-660 (2017).
28. Nagayama, Y., Shimamura, M. & Mitsutake, N. Cancer stem cells in the thyroid. *Frontiers in endocrinology* **7**, 20 (2016).
29. Shimamura, M., Nagayama, Y., Matsuse, M., Yamashita, S. & Mitsutake, N. Analysis of multiple markers for cancer stem-like cells in human thyroid carcinoma cell lines. *Endocrine journal* **61**, 481-490 (2014).
30. Shimamura, M., Kurashige, T., Mitsutake, N. & Nagayama, Y. Aldehyde dehydrogenase activity plays no functional role in stem cell-like properties in anaplastic thyroid cancer cell lines. *Endocrine* **55**, 934-943 (2017).
31. Todaro, M.*, et al.* Tumorigenic and metastatic activity of human thyroid cancer stem cells. *Cancer research* **70**, 8874-8885 (2010).
32. Shiraiwa, K.*, et al.* JAK/STAT3 and NF-κB Signaling Pathways Regulate Cancer Stem-Cell Properties in Anaplastic Thyroid Cancer Cells. *Thyroid* **29**, 674-682 (2019).
33. Ginestier, C.*, et al.* ALDH1 is a marker of normal and malignant human mammary stem cells and a predictor of poor clinical outcome. *Cell stem cell* **1**, 555-567 (2007).
34. Mao, P.*, et al.* Mesenchymal glioma stem cells are maintained by activated glycolytic metabolism involving aldehyde dehydrogenase 1A3. *Proceedings of the National Academy of Sciences* **110**, 8644-8649 (2013).
35. Li, W., Reeb, A.N., Sewell, W.A., Elhomsy, G. & Lin, R.-Y. Phenotypic characterization of metastatic anaplastic thyroid cancer stem cells. *PloS one* **8**, e65095 (2013).
36. Todaro, M., Francipane, M.G., Medema, J.P. & Stassi, G. Colon cancer stem cells: promise of targeted therapy. *Gastroenterology* **138**, 2151-2162 (2010).
37. Shagisultanova, E., Gaponova, A.V., Gabbasov, R., Nicolas, E. & Golemis, E.A. Preclinical and clinical studies of the NEDD9 scaffold protein in cancer and other diseases. *Gene* **567**, 1-11 (2015).

38. Wang, Z.*, et al.* NEDD9 may regulate hepatocellular carcinoma cell metastasis by promoting epithelial-mesenchymal-transition and stemness via repressing Smad7. *Oncotarget* **8**, 1714 (2017).
39. Gabbasov, R.*, et al.* NEDD9 promotes oncogenic signaling, a stem/mesenchymal gene signature, and aggressive ovarian cancer growth in mice. *Oncogene*, 1 (2018).
40. Pugacheva, E.N., Jablonski, S.A., Hartman, T.R., Henske, E.P. & Golemis, E.A. HEF1-dependent Aurora A activation induces disassembly of the primary cilium. *Cell* **129**, 1351-1363 (2007).
41. Kim, M.*, et al.* Comparative oncogenomics identifies NEDD9 as a melanoma metastasis gene. *Cell* **125**, 1269-1281 (2006).
42. Feng, Y.*, et al.* The CRTC1-NEDD9 signaling axis mediates lung cancer progression caused by LKB1 loss. *Cancer research* **72**, 6502-6511 (2012).
43. Jin, Y.*, et al.* NEDD9 promotes lung cancer metastasis through epithelial–mesenchymal transition. *International journal of cancer* **134**, 2294-2304 (2014).
44. Ahn, J., Sanz-Moreno, V. & Marshall, C.J. The metastasis gene NEDD9 product acts through integrin β3 and Src to promote mesenchymal motility and inhibit amoeboid motility. *J Cell Sci* **125**, 1814-1826 (2012).
45. Singh, M.K., Cowell, L., Seo, S., O'Neill, G.M. & Golemis, E.A. Molecular basis for HEF1/NEDD9/Cas-L action as a multifunctional co-ordinator of invasion, apoptosis and cell cycle. *Cell biochemistry and biophysics* **48**, 54-72 (2007).
46. Pugacheva, E.N. & Golemis, E.A. The focal adhesion scaffolding protein HEF1 regulates activation of the Aurora-A and Nek2 kinases at the centrosome. *Nature cell biology* **7**, 937 (2005).
47. Izumchenko, E.*, et al.* NEDD9 promotes oncogenic signaling in mammary tumor development. *Cancer research* **69**, 7198-7206 (2009).
48. Dingli, D., Traulsen, A. & Pacheco, J.M. Stochastic dynamics of hematopoietic tumor stem cells. *Cell cycle* **6**, 461-466 (2007).
49. Gupta, P.B.*, et al.* Stochastic state transitions give rise to phenotypic equilibrium in populations of cancer cells. *Cell* **146**, 633-644 (2011).
50. Pine, S.R., Ryan, B.M., Varticovski, L., Robles, A.I. & Harris, C.C. Microenvironmental modulation of asymmetric cell division in human lung cancer cells. *Proceedings of the National Academy of Sciences* **107**, 2195-2200 (2010).
51. Bajar, B.T.*, et al.* Fluorescent indicators for simultaneous reporting of all four cell cycle phases. *Nature methods* **13**, 993-996 (2016).
52. Reeb, N. & Reigh-Yi, L. Microarray Analysis Identifies a Unique Molecular Signature of Human Thyroid Cancer Stem Cells. *Thyroid Disorders Ther* **4**, 2 (2015).
53. Binder, J.X.*, et al.* COMPARTMENTS: unification and visualization of protein subcellular localization evidence. *Database* **2014**(2014).
54. Knutson, D. & Clagett-Dame, M. atRA Regulation of NEDD9, a gene involved in neurite outgrowth and cell adhesion. *Archives of Biochemistry and Biophysics* **477**, 163-174 (2008).
55. Knutson, D.C. & Clagett-Dame, M. A complex RARE is required for the majority of Nedd9 embryonic expression. *Transgenic research* **24**, 123-134 (2015).
56. Agrawal, N.*, et al.* Integrated genomic characterization of papillary thyroid carcinoma. *Cell* **159**, 676-690 (2014).

57. Ganly, I.*, et al.* Prognostic implications of papillary thyroid carcinoma with tall-cell features. *Thyroid* **24**, 662-670 (2014).
58. Johnson, T.L., Lloyd, R.V., Thompson, N.W., Beierwaltes, W.H. & Sisson, J.C. Prognostic implications of the tall cell variant of papillary thyroid carcinoma. *The American journal of surgical pathology* **12**, 22-27 (1988).
59. Lloyd, R.V., Buehler, D. & Khanafshar, E. Papillary thyroid carcinoma variants. *Head and neck pathology* **5**, 51-56 (2011).
60. Kollman, J.M., Merdes, A., Mourey, L. & Agard, D.A. Microtubule nucleation by γ-tubulin complexes. *Nature reviews Molecular cell biology* **12**, 709-721 (2011).
61. Nigg, E.A. & Holland, A.J. Once and only once: mechanisms of centriole duplication and their deregulation in disease. *Nature reviews Molecular cell biology* **19**, 297 (2018).
62. Tang, N. & Marshall, W.F. Centrosome positioning in vertebrate development. *J Cell Sci* **125**, 4951-4961 (2012).
63. Nigg, E.A. & Raff, J.W. Centrioles, centrosomes, and cilia in health and disease. *Cell* **139**, 663-678 (2009).
64. Tang, C.-J.C., Fu, R.-H., Wu, K.-S., Hsu, W.-B. & Tang, T.K. CPAP is a cell-cycle regulated protein that controls centriole length. *Nature cell biology* **11**, 825-831 (2009).
65. Mariappan, A.*, et al.* Inhibition of CPAP–tubulin interaction prevents proliferation of centrosome-amplified cancer cells. *The EMBO journal* **38**(2019).
66. Shah, J.V. & Cleveland, D.W. Waiting for anaphase: Mad2 and the spindle assembly checkpoint. *Cell* **103**, 997-1000 (2000).
67. Zierhut, C.*, et al.* The cytoplasmic DNA sensor cGAS promotes mitotic cell death. *Cell* **178**, 302-315. e323 (2019).
68. Prabakaran, T.*, et al.* Attenuation of c GAS-STING signaling is mediated by a p62/SQSTM 1-dependent autophagy pathway activated by TBK1. *The EMBO journal* **37**, e97858 (2018).
69. Grabosch, S.*, et al.* Cisplatin-induced immune modulation in ovarian cancer mouse models with distinct inflammation profiles. *Oncogene* **38**, 2380-2393 (2019).
70. Lohard, S.*, et al.* STING-dependent paracriny shapes apoptotic priming of breast tumors in response to anti-mitotic treatment. *Nature communications* **11**, 1-16 (2020).
71. Bakhoum, S.F.*, et al.* Chromosomal instability drives metastasis through a cytosolic DNA response. *Nature* **553**, 467-472 (2018).
72. Hatch, E.M., Fischer, A.H., Deerinck, T.J. & Hetzer, M.W. Catastrophic nuclear envelope collapse in cancer cell micronuclei. *Cell* **154**, 47-60 (2013).
73. Fernandes-Alnemri, T., Yu, J.-W., Datta, P., Wu, J. & Alnemri, E.S. AIM2 activates the inflammasome and cell death in response to cytoplasmic DNA. *Nature* **458**, 509-513 (2009).
74. Paludan, S.R., Reinert, L.S. & Hornung, V. DNA-stimulated cell death: implications for host defence, inflammatory diseases and cancer. *Nature Reviews Immunology* **19**, 141-153 (2019).
75. Sistigu, A.*, et al.* Cancer cell–autonomous contribution of type I interferon signaling to the efficacy of chemotherapy. *Nature medicine* **20**, 1301-1309 (2014).
76. Eirew, P.*, et al.* A method for quantifying normal human mammary epithelial stem cells with in vivo regenerative ability. *Nature medicine* **14**, 1384-1389 (2008).

77. Palmer, N.P., Schmid, P.R., Berger, B. & Kohane, I.S. A gene expression profile of stem cell pluripotentiality and differentiation is conserved across diverse solid and hematopoietic cancers. *Genome biology* **13**, R71 (2012).
78. Carter, S.L., Eklund, A.C., Kohane, I.S., Harris, L.N. & Szallasi, Z. A signature of chromosomal instability inferred from gene expression profiles predicts clinical outcome in multiple human cancers. *Nature genetics* **38**, 1043-1048 (2006).
79. Salvatore, G.*, et al.* A cell proliferation and chromosomal instability signature in anaplastic thyroid carcinoma. *Cancer research* **67**, 10148-10158 (2007).
80. Landa, I.*, et al.* Genomic and transcriptomic hallmarks of poorly differentiated and anaplastic thyroid cancers. *The Journal of clinical investigation* **126**, 1052-1066 (2016).
81. Pozdeyev, N.*, et al.* Genetic analysis of 779 advanced differentiated and anaplastic thyroid cancers. *Clinical Cancer Research* **24**, 3059-3068 (2018).
82. Jeon, M.J.*, et al.* Genomic alterations of anaplastic thyroid carcinoma detected by targeted massive parallel sequencing in a BRAFV600E mutation-prevalent area. *Thyroid* **26**, 683-690 (2016).
83. Kunstman, J.W.*, et al.* Characterization of the mutational landscape of anaplastic thyroid cancer via whole-exome sequencing. *Human molecular genetics* **24**, 2318-2329 (2015).
84. Pugacheva, E.N. & Golemis, E.A. The focal adhesion scaffolding protein HEF1 regulates activation of the Aurora-A and Nek2 kinases at the centrosome. *Nature cell biology* **7**, 937-946 (2005).
85. Charafe-Jauffret, E.*, et al.* Breast cancer cell lines contain functional cancer stem cells with metastatic capacity and a distinct molecular signature. *Cancer research* **69**, 1302-1313 (2009).
86. Miranda, A.*, et al.* Cancer stemness, intratumoral heterogeneity, and immune response across cancers. *Proceedings of the National Academy of Sciences* **116**, 9020-9029 (2019).
87. Miao, Y.*, et al.* Adaptive immune resistance emerges from tumor-initiating stem cells. *Cell* **177**, 1172-1186. e1114 (2019).
88. Pillai, S.*, et al.* Tank binding kinase 1 is a centrosome-associated kinase necessary for microtubule dynamics and mitosis. *Nature communications* **6**, 1-14 (2015).
89. Gentili, M.*, et al.* The N-terminal domain of cGAS determines preferential association with centromeric DNA and innate immune activation in the nucleus. *Cell reports* **26**, 2377-2393. e2313 (2019).
90. de Wolf, B. & Kops, G.J. Kinetochore malfunction in human pathologies. *Cell Division Machinery and Disease*, 69-91 (2017).
91. Gao, J.*, et al.* Integrative analysis of complex cancer genomics and clinical profiles using the cBioPortal. *Sci. Signal.* **6**, pl1-pl1 (2013).
92. Cerami, E.*, et al.* The cBio cancer genomics portal: an open platform for exploring multidimensional cancer genomics data. (AACR, 2012).
93. Xu, Y.*, et al.* Filamin A regulates focal adhesion disassembly and suppresses breast cancer cell migration and invasion. *J Exp Med* **207**, 2421-2437 (2010).
94. Marlow, L.A.*, et al.* Detailed molecular fingerprinting of four new anaplastic thyroid carcinoma cell lines and their use for verification of RhoB as a molecular therapeutic target. *The Journal of Clinical Endocrinology & Metabolism* **95**, 5338-5347 (2010).
95. Fitzgerald, K.A.*, et al.* IKKε and TBK1 are essential components of the IRF3 signaling pathway. *Nature immunology* **4**, 491-496 (2003).

96. Saad, A.*, et al.* Insights into a novel nuclear function for Fascin in the regulation of the amino-acid transporter SLC3A2. *Scientific reports* **6**, 36699 (2016).
97. Weinstein, J.N.*, et al.* The cancer genome atlas pan-cancer analysis project. *Nature genetics* **45**, 1113 (2013).

2.5 Manuscript 2: Differential STAT3 regulation by NEDD9-interactome contributes to centrosome asymmetry in thyroid cancer stem-like cells

Rationale

Manuscript 1 identified NEDD9 as a key regulator of both stemness and CIN in the ATC model. However, NEDD9 is a scaffolding protein that has no known catalytic activity. As such, manuscript two is aimed to investigate the downstream signaling pathways associated with NEDD9's regulation of centrosomes in ALDH+ ATC cells.

Differential STAT3 regulation by NEDD9-interactome contributes to centrosome asymmetry in thyroid cancer stem-like cells

Authors: Henry G. Yu, Krikor Bijian, and Moulay A. Alaoui-Jamali

Affiliations:

Departments of Medicine, Oncology, Pathology and Otolaryngology-Head and Neck Surgery, Lady Davis Institute for Medical Research and Segal Cancer Centre, the Sir Mortimer B. Davis-Jewish General Hospital, Faculty of Medicine, McGill University, Montreal, Canada.

Corresponding author

Moulay A. Alaoui-Jamali, PhD

E-mail: moulay.alaoui-jamali@mcgill.ca

Study source of funding

This study was supported by the Quebec Breast Cancer Foundation

Efforts to target STAT3 for cancer treatment is hampered, in part, by unresolved heterogeneities in STAT3 regulation due to variances in cancer cell phenotypic states, such as the cancer stem cell state. Here, analysis of The Cancer Genome Atlas datasets exposed a positive correlation between STAT3 and NEDD9 transcription across several cancer subtypes, including thyroid cancer. Cancer-stem-cell marker-based sorting of patient-derived thyroid cancer cells reveals that STAT3 and NEDD9 are co-upregulated in aldefluor-positive (ALDH+) stem-like cells. Both shRNA-mediated NEDD9-knockdown or pharmacological inhibition of Aurora-A Kinase (AURKAi) - a NEDD9-interactor - rapidly promoted $pSTAT3^{705}$ dephosphorylation. A phosphatase RNAi screening identified that AURKAi-mediated $pSTAT3^{705}$ is dependent on PTP-PEST phosphatase. Strikingly, shNEDD9/AURKAi failed to decrease STAT3 transcriptional activity, and a nuclear fraction assay combined with immunofluorescence imaging confirmed that AURKAi/shNEDD9 reduced cytoplasmic but not nuclear $pSTAT3^{705}$. Compensatory functional studies using a constitutively activated STAT3 mutant (STAT3-CA) revealed that STAT3 acts downstream of AURKA/NEDD9 to antagonize centrosome activation in ALDH+ cells. Furthermore, both STAT3-knockdown or overexpression of STAT3-CA perturb centrosome asymmetry and biases cell division towards symmetrical rather than asymmetrical cell division, indicating that optimal centrosome asymmetry is achieved through balanced STAT3 activation. Our study collectively offers novel insight into STAT3-signaling heterogeneity and identifies a NEDD9-STAT3 regulatory axis driving asymmetrical properties in stem-like ALDH+ ATC cells.

.

Introduction

STAT (Signal Transducers and Activators of Transcription) is a large family of signal transduction proteins best known for regulating gene transcription in response to extracellular signals from hormones and cytokines [1-3]. STAT activation is fine-tuned in normal cells through the homeostatic activities of both STAT inducers such as JAK, SRC, and EGFR and negative regulation via phosphatases such as PTP1B and TCPTP [4-7]. Deregulation of STAT, especially STAT3, is widely associated with oncogenesis by regulating genes regulating cell proliferation, cell survival, invasion/metastasis, and shaping the tumor microenvironment through angiogenesis and immunomodulation [1-3,8]. Additionally, STAT3 has been non-transcriptional in regulating the microtubule, cytoskeletal, and centrosome dynamics [9 10 11 12 13].

Despite STAT3's prominence as an oncogene across a wide spectrum of cancer, including breast cancer [14], thyroid cancer [15], lung cancer [16], leukemia [17], and others [18-20], there is presently no STAT3 inhibitors in clinical development [21,22]. Key practical limitations include the stability of available STAT3-targeting agents, the selectivity of those candidates and not other STAT members such as STAT1, and the potential toxicity associated with inhibiting STAT3 in healthy cells [21,22]. Additionally, due to STAT3's wide number of molecular interactors [1-3], its activation is generally under a wide range of factors such that alternative activation pathways can overcome many approaches aimed at targeting STAT3. An important consideration is that cancer cells are not homogeneous, and by extension, the regulation of STAT3 across different phenotypically distinct cancer cell variants likewise differs. For instance, numerous studies have shown that cancer stem-like cells are especially dependent on JAK2/STAT3 signaling[23-30]. Resolving differences in STAT3 signaling within distinct cancer cell populations is therefore critical to identifying optimal approaches to targeting this oncogene.

In this study, we dissect the differentiation regulation of STAT3 in anaplastic thyroid cancer (ATC), an advanced form of thyroid cancer presently lacking ineffective forms of treatments [31-33]. In ATC, a reliable marker for cancer stem cells is aldehyde dehydrogenase (ALDH), as comprehensive studies have characterized ALDH+ cells as exhibiting stem-like properties, including differentiation, spherogenesis, and tumorigenesis potential [34 15,35]. We had previously found that in ALDH+ ATC, the scaffolding protein NEDD9 is highly overexpressed, while in ALDH- cells, NEDD9 is near undetectable. NEDD9 expression organically promotes numerous oncogenic and metastatic cascades via downstream effectors such as AURKA, SRC,

FAK, and STAT3 [36-46]. We investigate whether NEDD9 and its interactome can distinguish STAT3 signaling between the ALDH-/+ cell populations in ATC.

Results

STAT3 transcription positively correlates with NEDD9 across multiple cancer subtypes, including thyroid cancer

Our first indication of a potential biological connection between NEDD9 and STAT3 in thyroid cancer parsed the Cancer Genome Atlas (TCGA) dataset for thyroid cancer patient transcriptomic data. We previously identified that NEDD9 is strongly correlated with the cancer stem cell marker ALDH1A3 in thyroid cancer and that NEDD9 was required to sustain the stem-like cell phenotype in ATC cells. To obtain additional information on the molecular factors related to NEDD9 in ALDH+ cells, we further probed for striking correlations between NEDD9 and its oncogenic downstream effectors: AURKA, SRC, and STAT3[19]. Across the 451 patients, we found that NEDD9 mRNA levels strongly correlated with STAT3 (Pearson's correlation coefficient of 0.46, $p=1.26e^{21}$), but not with NEDD9 interactors Aurora A Kinase (AURKA) (p=0.145) or SRC (p=0.139) **(M2-fig. 1A)**.

Expanding our analysis to other cancers, we found that the positive correlation between NEDD9 and STAT3 expression extends across a wide range of cancer types. Out of 26 TCGA datasets with n>100, the NEDD9-STAT3 Pearson's correlation value exceeded 0.3 in 11 of them, with seven more in the 0.2 to 0.3 range. Notable examples include glioblastoma (0.68), pediatric neuroblastoma (0.39), prostate adenocarcinoma (0.37), and colorectal adenocarcinoma (0.31) **(M2-fig. 1B)**. In contrast, NEDD9 expression is generally not positively correlated with either SRC or AURKA **(M2-fig. 1B)**. Although these patient data only report STAT3 mRNA levels and not protein/activation status, the consistent correlation between NEDD9/STAT3 transcription levels may indicate some unresolved biological connection.

STAT3 and NEDD9 protein are both upregulated in ALDH+ ATC cells where NEDD9 positively regulates STAT3 activation

Our previous study in ATC models found that NEDD9 protein expression was not homogeneous but rather manifests as two extremes between being highly expressed in ALDH+ stem-like cells but lowly expressed in ALDH- cells. Since NEDD9 and STAT3 expression showed a strong positive correlation in thyroid patients, we sought to examine if STAT3 would likewise be overexpressed in ALDH+ cells. Using FACS to sort THJ-16T cells into ALDH- and ALDH+ cells **(M2-fig. 2A)**, we found that, indeed, STAT3 protein is also significantly upregulated in ALDH+ compared to ALDH- cells **(M2-fig. 2B)**.

We used shRNA targeting these proteins to interrogate the relationship between NEDD9 and STAT3 to examine the impact on STAT3, pSTAT3^{705}, and NEDD9. Knockdown of NEDD9, while impacting STAT3 protein expression, reduced pSTAT3^{705} levels in ALDH+ cells but strikingly had the opposite effect on ALDH- cells **(M2-fig. 2B)**. Conversely, knockdown of STAT3 in ALDH+ cells was also sufficient to reduce pSTAT3^{705} levels but had little impact on NEDD9 expression, suggesting that STAT3 activation is downstream of NEDD9 **(M2-fig. 2C)**.

We conduct a time-course analysis of shRNA-treated cells to better understand phosphorylation kinetics following NEDD9/STAT3 knockdown. We incubated the cells with a control shRNA (shCT), shNEDD9, or shSTAT3, allowed a 24h incubation period, then refreshed the media (a timepoint designated t=0h) then collected the lysates at designated time points. The phosphorylation patterns of these kinases fluctuated over the timepoints, so we compared the phosphorylation levels by matching each timepoint to shCT-treated control cells. With shNEDD9-treatment, we found that pSTAT3^{705} levels in ALDH+ cells decreased around the same time that NEDD9 protein was depleted and remained persistently lower than control shRNA-treated cells **(M2-fig. 2D)**. In contrast, AURKA and SRC only experienced a transient decline but recovered above shCT levels after a short time **(M2-fig. 2D)**. We also followed the phosphorylation patterns of the same kinases following STAT3 knockdown, finding that pSTAT3^{705} levels decreased while pAURKA/pSRC phosphorylation transiently spiked at t=24h followed **(M2-fig. 2E)**. These findings collectively reveal that STAT3 regulation is distinct between ALDH- and ALDH+ ATC cells and the regulation is distinguished, at least in part, through the NEDD9 interactome.

Only in ALDH+ cells, STAT3 is dephosphorylated in response to small molecules targeting NEDD9 interactors such as AURKA inhibitors

NEDD9 is an adapter protein with no known direct chemical inhibitor is reported. As an alternative approach to chemically interrogating the NEDD9 interactome, we used small molecules that targeted key oncogenic NEDD9-binding kinases and examined the consequential impact of STAT3 phosphorylation. We tested chemical inhibitors of major NEDD9 partners, namely FAK, SRC, and AURKA. Strikingly, 200nM of VX-680 (AURKA inhibitor), PF-573228 (FAK inhibitor), or PP2 (SRC inhibitor) each depleted the majority of $pSTAT3^{705}$ within 15 minutes in ALDH+ cell, but not in ALDH- cells (**M2-fig. 3A**). NEDD9-knockdown in ALDH+ cells significantly attenuated $pSTAT3^{705}$ inhibition by PF-573228 and VX-680, but only partially rescued $pSTAT3^{705}$ inhibition by PP2 (**M2-fig. 3A**), perhaps because SRC can also directly activate STAT3. Also noteworthy is that, unlike $STAT3^{705}$, other NEDD9 interactors became generally upregulated in response to these small molecules; AURKA inhibition led to increased SRC phosphorylation, while the SRC inhibitor led to increased pFAK/pAURKA phosphorylation **(M2-fig. 3A).** These phosphorylation changes were absent in ALDH- or shNEDD9 cells (**M2-fig. 3A**). Conversely, regardless of pFAK/pAURKA/pSRC phosphorylation levels, $pSTAT3^{705}$ decline remained similar (**M2-fig. 3A**).

We subsequently focused on AURKA inhibitor on the premise that this class of small molecules is presently under clinical investigation as a possible treatment for ATC. Using an alternative shRNA targeting NEDD9 (with a milder magnitude of knockdown), we confirmed that NEDD9-knockdown attenuated STAT3 dephosphorylation in response to AURKAi (**M2-fig. 3B**). Conversely, overexpression of NEDD9 in ALDH- cells that lack endogenous NEDD9 expression sensitized $pSTAT3^{705}$ levels to AURKA inhibition (**M2-fig. 3C**). We also confirmed these trends in an alternative cell line THJ-11T by comparing unsorted bulk THJ-11T cells with ALDH+ sorted THJ-11T cells (**M2-fig. 3D**).

We also sought to examine if AURKAi inhibition of $pSTAT3^{705}$ would be affected by induction via extracellular cytokines/growth factors. To test this broadly, we serum-starved ALDH- and ALDH+ cells pretreated the cells with AURKAi, and then induced the cells with 20% serum for 15 minutes before lysate-collection (**M2-fig. 3E**). Remarkably, we found that the level of $pSTAT3^{705}$ in ALDH- cells became induced by serum-stimulation, the $pSTAT3^{705}$ levels in ALDH+ cells did not change in response to serum (**M2-fig. 3E**). Under these conditions, AURKAi

still inhibited pSTAT3^{705} levels in a dose-dependent manner, indicating that pSTAT3^{705} inhibition by AURKAi is, likewise, not dependent on inhibiting extracellular-ligand induced pSTAT3^{705} signaling cascades (**M2-fig. 3E**).

AURKAi-induced pSTAT3^{705} dephosphorylation involves PTP-PEST phosphatase

Based on the timing of STAT3 dephosphorylation (<5 minutes) in response to AURKA inhibition, we hypothesized that a NEDD9-associated phosphatase mediated this phenomenon. To identify the specific phosphatase in the NEDD9-STAT3 pathway, we performed a small-scale RNAi screening using candidate phosphatases based on known interaction with NEDD9 or p130cas – NEDD9's better-studied paralog. These candidates included SHP1, SHP2, PTP1B, PTP-PEST, and TC-PTP. Our results showed that the knockdown of PTP-PEST prevented STAT3 dephosphorylation in response to AURKA or FAK inhibitors (**M2-fig. 4A**). By comparing the basal level of PTP-PEST between ALDH- and ALDH+ cells, we find that, unlike NEDD9, these two cell populations do not display differentiation expression of PTP-PEST, and that reciprocal knockdown of PTP-PEST or NEDD9 did not affect the expression of either protein (**M2-fig. 4B**). Interestingly, we noted that shPTP1B and shTCPTP, in fact, drastically increased basal pSTAT3^{705} phosphorylation but could not rescue AURKAi-induced STAT3 dephosphorylation (**M2-fig. 4A, 4C**). In contrast, shPTP-PEST was relatively unimpactful on basal pSTAT3^{705} but did affect the pSTAT3^{705} dephosphorylation in response to AURKAi (**M2-fig. 4A, 4C, 4D**). These findings indicate that pSTAT3^{705} in ALDH+ cells are generally suppressed by the activities of multiple phosphatases, of which only the activity of PTP-PEST is linked with AURKA.

To test if NEDD9/STAT3/PTP-PEST formed a protein complex, we performed immunoprecipitation using NEDD9 antibodies for pull-down. PTP-PEST showed high enrichment in the NEDD9 IP compared to mouse IgG control. STAT3 was also enriched in the NEDD9 precipitate, and interestingly, this interaction is weakened within minutes of cells being treated by AURKAi (**M2-fig. 4F**). Our positive control, SRC, was also highly enriched in the NEDD9 precipitate and dissociated from NEDD9 after 5 minutes (**M2-fig. 4F**).

NEDD9/AURKA predominantly regulates cytoplasmic STAT3 activation in ALDH+ ATC cells

Since STAT3's main function is to act as a transcriptional factor to induce targeted gene expression, we sought to examine how shNEDD9 and AURKAi affected the STAT3 transcriptional activity of a STAT3 reporter (pTATA TK-Luc). Strikingly, while the positive control shSTAT3 inhibited STAT3 transcriptional activity by ~80%, neither shNEDD9 nor AURKAi affected STAT3 transcriptional activity **(M2-fig. 5A)**.

To elucidate why AURKAi failed to affect STAT3 transcriptional activity despite reducing $pSTAT3^{705}$ levels, we collected cytoplasmic and nuclear fractions from AURKAi-treated THJ-16T lysates. Striking, the dominant localization for $pSTAT3^{705}$ was cytoplasmic. AURKAi inhibition only resulted in decreased cytoplasmic but not nuclear $pSTAT3^{705}$ (**M2-fig. 5B**). Other kinases such as pAkt were not significantly affected under these conditions.

To further confirm these observations, we performed immunofluorescence imaging of NEDD9 and $pSTAT3^{705}$, which confirmed that both NEDD9 and $pSTAT3^{705}$ were predominantly located in the cytoplasmic region of the cell, adjacent to, but not inside, the nucleus (**M2-fig. 5C, 5E**). Interestingly, a colocalization analysis of NEDD9/$pSTAT3^{705}$ staining shows both proteins are highly colocalized within ALDH+ cells (PCC ~ 0.79, **M2-fig. 5D**). When treated with AURKAi, two noteworthy changes occurred. The first was that cytoplasmic $pSTAT3^{705}$ staining became dim, and the staining appears nuclear-dominant, consistent with our nuclear-fraction data. Secondly, NEDD9 localization, while remaining in the cytoplasm, was no longer confined to a region near the nucleus and appeared more evenly scattered within the cytoplasm. Consequently, colocalization analysis shows AURKAi significantly reduces NEDD9/$pSTAT3^{705}$ colocalization (PCC ~ 0.29, **M2-fig. 5D**), consistent with our previous co-immunoprecipitation assay showing that AURKAi inhibits NEDD9-STAT3 direct interaction. Finally, compared to ALDH+ control cells, both ALDH- cells or ALDH+ cells with shNEDD9 showed reduced cytoplasmic $pSTAT3^{705}$ (**M2-fig. 5E**). These findings collectively indicate that NEDD9/AURKA interactome primarily governs STAT3 phosphorylation in the cytoplasm and not the nucleus, consistent with their lack of impact on STAT3 transcriptional activity.

STAT3 activation negatively regulates centrosome activation downstream of NEDD9/AURKA in ALDH+ ATC cells

Since our above findings suggest that perturbation to NEDD9-interactome negatively impacted cytoplasmic pSTAT3^{705} and that STAT3 transcriptional activity was not affected, we sought to evaluate STAT3's non-transcriptional functions. STAT3 is known to have cytoplasmic functions in regulating the ER [47] and centrosome/MT dynamics [9 10 11 12 13]. - the latter of these two functions is more closely related to the canonical function of NEDD9 and AURKA. To isolate the phenotypic impact of STAT3 activation in our model, we combined shNEDD9/AURKAi with ectopic expression of either wild-type or a constitutively activated form (STAT3-CA, with A662C, N664C point mutations) of STAT3 (**M2-fig. 6A**). This mutant form has been previously shown to be able to rescue non-transcription-based STAT3 activities [9].

A key functional hallmark of centrosome maturation/activation is the accumulation of γ-tubulin to act as minus-ends of tubulin to nucleate microtubule polymers, which is known to be regulated by cytoplasmic STAT3 activation. To assess centrosome maturation, we quantitatively measured the impact of NEDD9/STAT3 on the intensity of γ-tubulin at the centrosomes. Knockdown of either NEDD9, AURKAi, or STAT3 cause a ~3-fold increase in γ-tubulin fluorescence in ALDH+ cells. In ALDH- cells, a 1.6-fold increase in γ-tubulin levels was observed upon shSTAT3 but not shNEDD9 treatment. (**M2-fig. 6B**) Overexpression of STAT3-CA, but not wild-type STAT3, in ALDH+ cells prevented shNEDD9 or shSTAT3 induced γ-tubulin increase (**M2-fig. 6B**), indicating that STAT3 activation is required to limit centrosome γ-tubulin in ALDH+ cells.

We next sought to consolidate findings by quantifying the microtubule growth rate at the centrosomes, as centrosome MTOC activity is affected by γ-tubulin levels. Using the microtubule regrowth assay, we observed that overexpression of STAT3-CA, but not wild-type STAT3, suppressed centrosome microtubule-nucleation (**M2-fig. 6C, 6D**). Conversely, shNEDD9 induced centrosome microtubule-nucleation, which was attenuated by the overexpression of STAT3-CA but not wild-type STAT3 (**M2-fig. 6C**. **6D**). Additionally, γ-tubulin and MT-growth at the centrosomes also increased in response to AURKAi. They were likewise attenuated by STAT3-CA overexpression, consistent with our previous observation that both shNEDD9 and AURKAi led to decreased cytoplasmic pSTAT3^{705} (**M2-fig. 6E, 6F**). These findings collectively show that

STAT3 activation acts downstream of the NEDD9/AURKA interactome to antagonize centrosome activation in ALDH+ ATC cells.

Both positive and negative regulation of STAT3 reduces ALDH+ cell asymmetry

Asymmetries in centrosome behavior is a property of stem cells that we had previously shown to manifests in ALDH+ ATC in a NEDD9-dependent manner. Given that our findings above show that activation cytoplasmic STAT3 is regulated distinctly in ALDH+ cells, we considered that STAT3 activation might be related to the asymmetrical properties of ALDH+ cells.

Using microtubule regrowth assay, we show that, consistent with our previous findings, the two centrosomes in ALDH+ cells show highly specific MTOC activity, where the activity of the dominant centrosome is generally 3-4 times greater than that of the weaker centrosome. STAT3 knockdown. Interestingly, overexpression of STAT3-CA or STAT3-knockdown normalized MTOC levels between the two centrosomes, reducing asymmetry; however, a noteworthy distinction is that the centrosomes in STAT3-CA manifested as two weak MTOCs, while the centrosomes in shSTAT3 cells manifested as two robust MTOCs (**M2-fig. 7B**).

Lastly, since stem cells generally use centrosome asymmetry to perform asymmetrical cell division, we performed a cursory assessment to see if STAT3's effects on centrosomes translated to the disruption of asymmetrical cell divisions. We seeded single ALDH+ cells into 96 well plates and, over days, tracked the ALDH+/- status of the daughter cells. The ALDH+ positivity of the cells when they were single cells was confirmed using aldefluor staining combined with imaging, and the status of the daughter cells was then assessed once two cells were found in the well (**M2-fig. 7C**). In control and STAT3-WT overexpressing cells, ~10% of cell division asymmetrically produced one ALDH+ and one ALDH- cell. Overexpression of STAT3-CA or shSTAT3 reduced the rate of asymmetrical outcomes to 4.9% and 3.7%, respectively (**M2-fig. 7D**). Taken together, our findings support the notion that asymmetrical properties in ALDH+ cells are contributed by an optimal, balanced level of STAT3 activation.

Discussion

This study delineates a NEDD9/STAT3 regulatory axis uniquely activated in ALDH+ ATC cells, contributing to asymmetrical properties. Our findings offer novel insight into STAT3 signaling heterogeneity between phenotypically distinct cancer cells. Overall, our study supports

a model where STAT3 colocalizes with and is activated by NEDD9 in ALDH+ ATC cells under homeostatic conditions, supported by immunofluorescence co-immunoprecipitation, and RNAi studies supporting interactions between NEDD9/STAT3 being a factor that promotes STAT3 activation in ALDH+ cells. STAT3 phosphorylation was rapidly lost in response to perturbations to the NEDD9 interactome, as demonstrated by multiple small molecules targeting NEDD9-interactomes, including but not limited to AURKAi, effective at reducing pSTAT3^{705}. While some trepidations are needed when interpreting small molecule data due to potential pharmacological "off-targets" such as Jak2 [48], our findings firmly support that these inhibitors affect pSTAT3^{705} via NEDD9 NEDD9 expression being a determinant factor in whether pSTAT3^{705} will decline when treated by NEDD9-interactome inhibitors. This model is further supported by several noteworthy minor observations made in our study. Firstly, STAT3 activation in ALDH+ cells was unresponsive to serum starvation and stimulation by 20% FBS following serum-starvation, indicating that STAT3 regulation is primarily cell-autonomous. Secondly, knockdown of STAT3 also transiently induced pAURKA/pSRC activation, which supports pAURKA/pSRC being relevant to STAT3 homeostasis. Though not definitive, our study hints that the reason for NEDD9 to lose interaction with STAT3 is due to AURKAi causing NEDD9 being physically relocated in the cytoplasm to be more diffusely spread rather than concentrated adjacent to the nuclear region; however, since NEDD9 displacement caused pSTAT3^{705} to be lost entirely rather than displaced along with NEDD9, this suggests there may be additional factors governing NEDD9/STAT3 interaction specifically around the nuclear-adjacent area that is yet to be identified.

Our finding also identified an additional factor for STAT3 regulation in PTP-PEST. We deduced that loss of pSTAT3^{705} following AURKAi might be due to phosphatase activities due to the kinetics of pSTAT3^{705} loss since 5-minutes was enough to almost completely ablate pSTAT3^{705} levels. Aside from PTP-PEST, PTP1B and TCPTP also appears to be phosphatases that negatively regulate STAT3 activation, though they appear to act independently of NEDD9/AURKA. Though the relevance of NEDD9 to AURKAi/STAT3 interaction is implicated by the strong constitutive interaction between NEDD9/PTP-PEST in these cells, it is unclear how NEDD9's physical interaction with PTP-PEST contributes to STAT3 dephosphorylation. Mechanistic uncertainties aside, the extensive negative regulation of STAT3 activation by phosphatases in ALDH+ cells is consistent with STAT3 protein being heavily

upregulated relative to ALDH- cells. At the same time, pSTAT3^{705} levels are comparatively maintained a comparable baseline level.

An unusual finding in our study is that phosphorylated STAT3 in ALDH+ ATC cells is located predominantly in the cytoplasm, in contrast to a typical pSTAT3^{705} [49,50]. Since the nuclear import/export of STAT3 is constitutively imported into the nucleus by importins regardless of its phosphorylation status, [49], the number of nuclear pSTAT3^{705} maybe, to some extent, be rate-limited by the high amount of total STAT3 in ALDH+ cells. Based on our results, shNEDD9 and AURKAi inhibited cytoplasmic and not nuclear pSTAT3^{705}. In support of this, AURKAi/shNEDD9 appeared to impact STAT3's known function in regulating centrosome dynamics but had little impact on STAT3 transcription factor activities based on reporter assay. By combining shNEDD9/AURKAi with overexpression of either STAT3 or STAT3-CA, we were able to identify that STAT3 activation acts downstream of NEDD9-interactome to antagonize centrosome activation. Our findings also indicate that STAT3 homeostasis is crucial to maintaining asymmetrical centrosomes that are characteristic of ALDH+ ATC cells and many normal stem cells such as Drosophila germline stem cells [286], since both are characteristic reduction and increases to STAT3 activation appears to break this asymmetry. Although resolving the molecular basis for STAT3's effect on centrosome asymmetry is beyond the scope of this study, there is a strong possibility that this mechanism involves PLK1, which is a known target of STAT3 in regulating centrosomes and spindle dynamics [9,51], and is a key player in asymmetrically activation the centrosome pairs in normal stem cells [52-54]. Overall, however, ALDH+ cell's dependency on a precise level of STAT3 to achieve a stem cell-like centrosome configuration is consistent with the strict cell-autonomous regulation of STAT3 by the NEDD9-interactome that is identified by our study.

The NEDD9-STAT3 interaction observed in our study agrees with a recent study showing that, compared to NEDD9$^{-/-}$ ovarian cancers cells, Nedd9$^{+/+}$ cells have higher pStat3^{705} level when transplanted into a syngeneic mouse model, but lower pStat3^{705} level when grown in cell culture; interestingly, a correlation between NEDD9 and the expression of *aldh1a1* and *aldh1a2* was also observed in this model[55]. Our findings that NEDD9/STAT3 interactions are distinct between ALDH- and ALDH+ cells may account for some of the context-sensitive STAT3 activation patterns observed in that ovarian cancer model. Given that NEDD9 expression is directly impacted by ALDH enzymatic activity through retinoic acid signaling [38,46,55], ALDH

is broadly used as a stem cell-like marker across multiple types of cancer [56-63], its interaction with STAT3 may be broadly relevant to stem-like cells in different cancer models. In support of this, our study showed that the positive NEDD9/STAT3 mRNA correlation occurred in models besides thyroid cancer, such as glioblastoma, glioma, and neuroblastoma - cancer types in which NEDD9 has demonstrated oncogenic functions [64,65]. Further studies on this front in other models may broaden our understanding of STAT3 signaling particularities and functional contributions within the stem-like state in cancer cells.

A

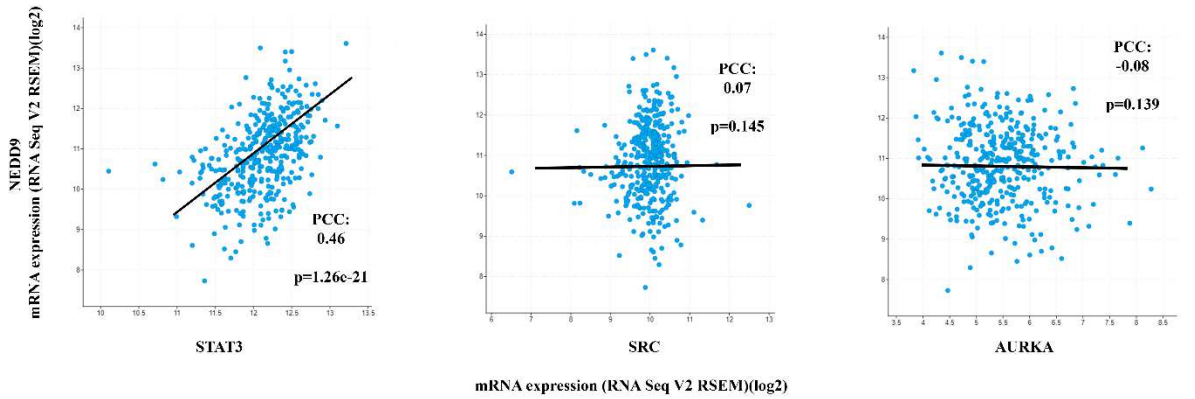

B

	NEDD9/STAT3		NEDD9/SRC		NEDD9/AURKA		
	PCC	P-value	PCC	P-value	PCC	P-value	n
Acute Myeloid Leukemia (OHSU, Nature 2018)	0.2	3.61E-05	0.09	0.0601	0.11	0.0281	451
Adult Soft Tissue Sarcomas (TCGA, Cell 2017)	0.28	8.72E-04	-0.12	0.0937	-0.26	1.55E-04	206
Bladder Cancer (TCGA, Cell 2017)	0	0.654	-0.08	0.108	-0.07	0.155	412
Brain Lower Grade Glioma (TCGA, Firehose Legacy)	0.42	8.28E-14	-0.15	0.0123	0.09	0.12	530
Breast Cancer (METABRIC, Nature 2012 & Nat Commun 2016)	-0.06	3.50E-03	-0.12	4.27E-07	-0.17	4.55E-14	1904
Breast Invasive Carcinoma (TCGA, Firehose Legacy)	0.21	2.16E-11	-0.09	4.56E-03	-0.34	3.49E-28	1100
Cervical Squamous Cell Carcinoma and Endocervical Adenocarcinoma (TCGA)	0.06	0.375	-0.11	0.12	-0.16	0.0325	306
Colorectal Adenocarcinoma (TCGA, PanCancer Atlas)	0.31	9.03E-13	-0.07	0.124	-0.35	3.43E-16	817
Glioblastoma (TCGA, Cell 2013)	0.68	9.41E-21	0.27	1.33E-03	0.29	4.36E-04	152
Head and Neck Squamous Cell Carcinoma (TCGA, Firehose Legacy)	0.08	0.0773	0.14	2.39E-03	-0.03	0.471	522
Kidney Renal Clear Cell Carcinoma (TCGA, Firehose Legacy)	0.32	6.12E-12	-0.4	8.90E-19	-0.5	2.78E-29	534
Liver Hepatocellular Carcinoma (TCGA, Firehose Legacy)	0.14	0.0101	0.15	4.98E-03	-0.04	0.438	373
Lung Adenocarcinoma (TCGA, Firehose Legacy)	0.25	1.05E-04	-0.09	0.155	-0.46	2.61E-13	517
Lung Squamous Cell Carcinoma (TCGA, Firehose Legacy)	0.22	2.70E-03	0.1	0.207	-0.13	0.0932	501
Ovarian Serous Cystadenocarcinoma (TCGA, Firehose Legacy)	-0.02	0.799	0.31	1.63E-05	-0.15	0.0403	307
Pediatric Neuroblastoma (TARGET, 2018)	0.39	1.89E-06	-0.2	0.0152	-0.42	3.01E-07	143
Pediatric Wilms' Tumor (TARGET, 2018)	0.39	2.19E-04	0.25	0.0135	-0.17	0.0881	130
Pheochromocytoma and Paraganglioma (TCGA, Firehose Legacy)	0.35	6.11E-06	-0.02	0.83	-0.08	0.312	184
Prostate Adenocarcinoma (TCGA, Firehose Legacy)	0.37	1.78E-17	0.18	7.37E-05	-0.24	1.24E-07	498
Sarcoma (TCGA, Firehose Legacy)	0.24	1.30E-04	-0.15	0.0226	-0.3	3.16E-06	263
Skin Cutaneous Melanoma (TCGA, Firehose Legacy)	0.26	7.38E-06	0.05	0.396	-0.09	0.143	472
Stomach Adenocarcinoma (TCGA, Firehose Legacy)	0.16	1.55E-03	0.11	0.0354	-0.13	0.0144	415
Testicular Germ Cell Tumors (TCGA, PanCancer Atlas)	0.36	7.17E-06	0.52	1.51E-11	-0.44	3.62E-08	149
Papillary Thyroid Carcinoma (TCGA, Cell 2014)	0.46	1.26E-21	0.07	0.145	-0.08	0.139	482
Thymoma (TCGA, Firehose Legacy)	0.48	3.44E-08	0.15	0.113	-0.53	8.36E-10	120
Uterine Corpus Endometrial Carcinoma (TCGA, PanCancer Atlas)	0.15	5.32E-04	0.15	6.98E-04	-0.09	0.0417	527

M2-Figure 1: NEDD9 and STAT3 mRNA levels are positively correlated across different types of cancer, including thyroid cancer

A. Correlation analysis for mRNA expression of NEDD9 and AURKA, SRC, or STAT3, using Pearson's Correlation Coefficient (PCC), based on the dataset: TCGA, Cell 2014[66], *n=451*. Graph generated using cBioportal [67] [68]. **B.** Table summarizing the PCC between NEDD9/STAT3, NEDD9/SRC, and NEDD9/AURKA in different cancer types based on TCGA datasets with available patient transcriptomic data with n>120. PCC values greater than 0.2 are highlighted in green.

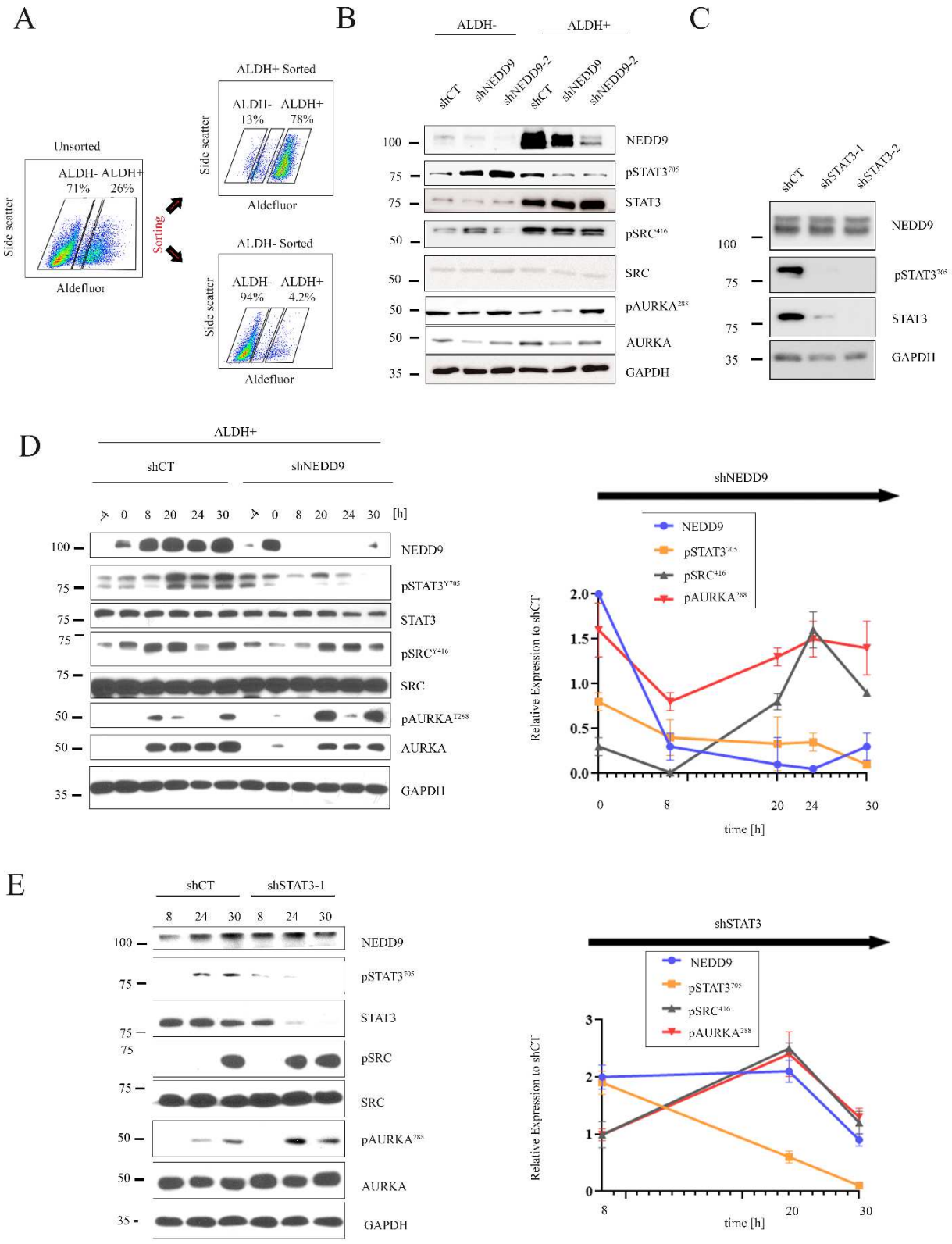
A
Unsorted
ALDH- ALDH+
71% 26%
Side scatter
Aldefluor
Sorting
ALDH+ Sorted
ALDH- ALDH+
13% 78%
Side scatter
Aldefluor
ALDH- Sorted
ALDH- ALDH+
94% 4.2%
Side scatter
Aldefluor
B
ALDH- ALDH+
shCT shNEDD9 shNEDD9-2 shCT shNEDD9 shNEDD9-2
100
75
75
50
50
50
35
NEDD9
pSTAT3705
STAT3
pSRC416
SRC
pAURKA288
AURKA
GAPDH
C
shCT shSTAT3-1 shSTAT3-2
100
75
75
35
NEDD9
pSTAT3705
STAT3
GAPDH
D
ALDH+
shCT shNEDD9
0 8 20 24 30 0 8 20 24 30 [h]
100
75
75
75
50
50
35
NEDD9
pSTAT3Y705
STAT3
pSRCY416
SRC
pAURKAT288
AURKA
GAPDH
shNEDD9
NEDD9
pSTAT3705
pSRC416
pAURKA288
Relative Expression to shCT
2.0
1.5
1.0
0.5
0.0
0 8 20 24 30
time [h]
E
shCT shSTAT3-1
8 24 30 8 24 30
100
75
75
75
75
50
50
35
NEDD9
pSTAT3705
STAT3
pSRC
SRC
pAURKA283
AURKA
GAPDH
shSTAT3
NEDD9
pSTAT3705
pSRC416
pAURKA288
Relative Expression to shCT
3
2
1
0
8 20 30
time [h]

M2-Figure 2: NEDD9 distinguishes pSTAT3^{705} activation between ALDH- and ALDH+ ATC cells

A. Representative scheme of fluorescence-activated cell sorting of THJ-16T ATC cells by ALDH+/- status using aldefluor staining **B.** Western blot analysis of STAT3, SRC, and AURKA protein and phosphorylation levels in ALDH+ and ALDH- cells responded to shNEDD9-mediated knockdown. Cells were treated with one of two shNEDD9 lentivirus constructs for 24h, at which point the media was refreshed, and the lysates were harvested after another 36h. **C.** Western blot analysis of NEDD9, STAT3, and pSTAT3^{705} levels in ALDH+ cells in response to shSTAT3. Cells were treated with one of two different shSTAT3 lentivirus vectors for 24h; after that, the media was refreshed, and the lysates were harvested after another 36h. **D.** Left: Representative time-course analysis of STAT3, SRC, and AURKA protein and phosphorylation levels in ALDH+ cells in response to shNEDD9. Cells were treated with shNEDD9 lentivirus vectors for 24h, at which point the media was refreshed (t=0h), and the lysates were harvested at the indicated timepoints. Right: Quantification of the relative total NEDD9, pSTAT3, pSRC, and pAURKA levels between shCT and shNEDD9-treated cells at matching timepoints, normalized to respective total proteins for the kinases and GAPDH for NEDD9. Values are the average of three biological replicas. **E.** Left: Representative time-course analysis of STAT3, SRC, and AURKA protein and phosphorylation levels in ALDH+ cells responded to shSTAT3. Cells were treated with shSTAT3 lentivirus vectors for 24h, after which the media was refreshed (t=0h), and the lysates were harvested at the indicated timepoints. Right: Quantification of the relative total NEDD9, pSTAT3, pSRC, and pAURKA levels between shCT and shSTAT3-treated cells at matching timepoints, normalized to respective total proteins for the kinases and GAPDH for NEDD9. Values are the average of three biological replicas.

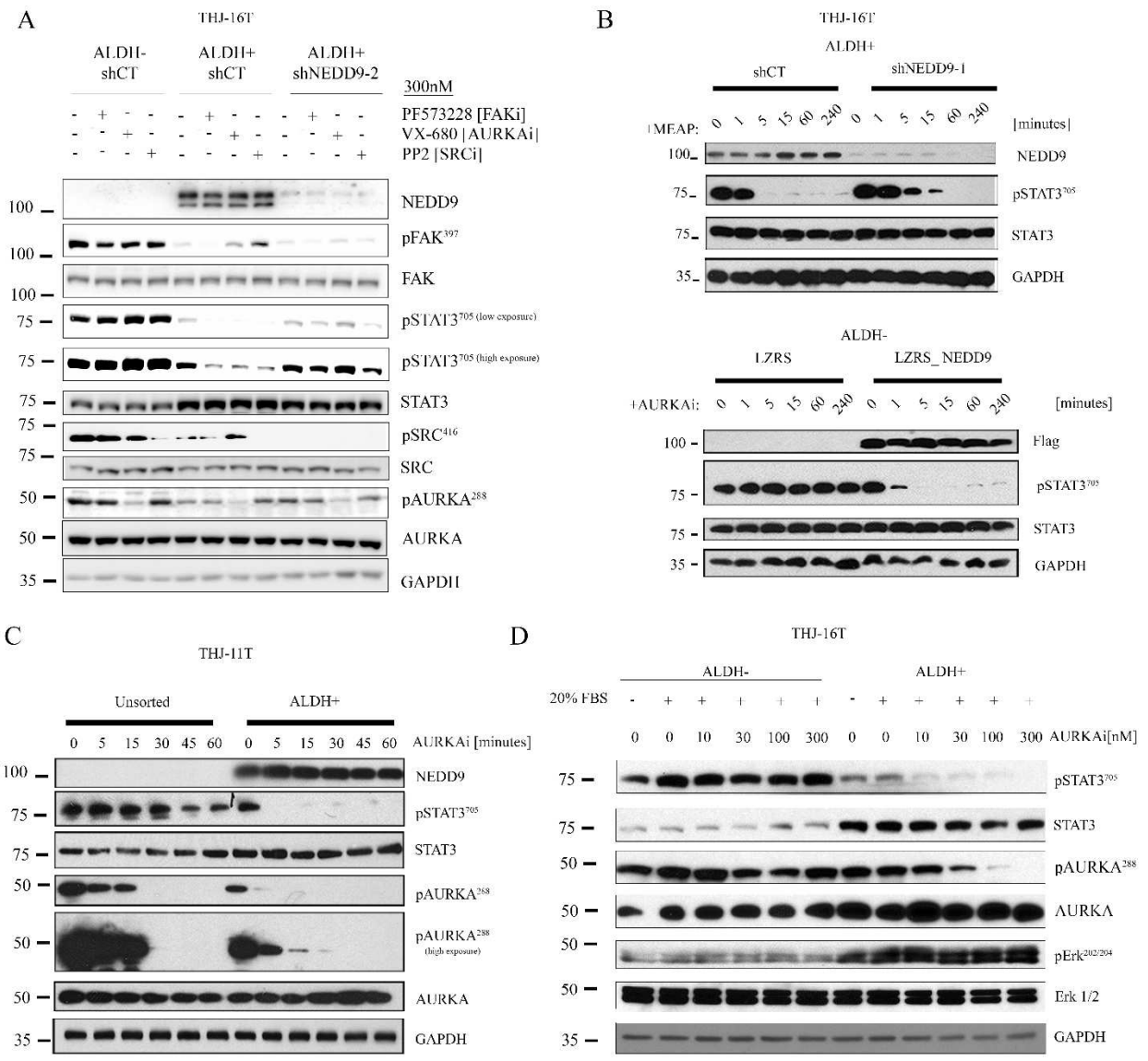
A
THJ-16T
ALDH-
shCT
ALDH+
shCT
ALDH+
shNEDD9-2
300nM
PF573228 [FAKi]
VX-680 |AURKAi|
PP2 |SRCi]
NEDD9
pFAK397
FAK
pSTAT3705 (low exposure)
pSTAT3705 (high exposure)
STAT3
pSRC416
SRC
pAURKA288
AURKA
GAPDH
B
THJ-16T
ALDH+
shCT
shNEDD9-1
[MEAP:
0 1 5 15 60 240 0 1 5 15 60 240
[minutes]
NEDD9
pSTAT3705
STAT3
GAPDH
ALDH-
LZRS
LZRS_NEDD9
+AURKAi:
0 1 5 15 60 240 0 1 5 15 60 240
[minutes]
Flag
pSTAT3705
STAT3
GAPDH
C
THJ-11T
Unsorted
ALDH+
0 5 15 30 45 60 0 5 15 30 45 60
AURKAi [minutes]
NEDD9
pSTAT3705
STAT3
pAURKA288
pAURKA288 (high exposure)
AURKA
GAPDH
D
THJ-16T
ALDH-
ALDH+
20% FBS
0 0 10 30 100 300 0 0 10 30 100 300 AURKAi[nM]
pSTAT3705
STAT3
pAURKA288
AURKA
pErk202/204
Erk 1/2
GAPDH

M2-Figure 3: Only in ALDH+ cells, STAT3 is dephosphorylated in response to chemical inhibitors targeting the NEDD9-interactome

(A) Western blot representing the impact of small molecule inhibitors targeting NEDD9-kinase partners AURKA (AURKAi, VX-680), FAK (FAKi, PF-573228), and SRC (SRCi, PP2) on signaling pathways in THJ-16T ALDH- (shCT) cells, ALDH+ (shCT) cells, and ALDH+ cells with stable NEDD9-knockdown (shNEDD9-2). Cells were treated with 200nM of each compound for 15 minutes. **(B)** Western blots illustrating that AURKAi ability to inhibit $pSTAT3^{705}$ in THJ-16T is dependent on NEDD9 expression. ALDH+ and ALDH- sorted cells were NEDD9-depleted or NEDD9-overexpressed respectively, then treated with 300nM AURKAi on corresponding time-points. (LZRS = LZRS_IRESGFP control, LZRS_NEDD9 = full-length NEDD9 cloned into LZRS-IRESGFP expression vector). **C.** Timecourse impact of AURKAi on pSTAT3 and pAURKA on either bulk unsorted THJ-11T cells or ALDH+ sorted THJ-11T cells. **E.** Impact of serum induction on signaling pathways in ALDH- and ALDH+ THJ-16T cells and their response to AURKAi. Sorted cells were serum-starved overnight before 1-hour treatment of escalating doses, then cells were given fresh 20% FBS media for 15 minutes to induce phosphorylation before harvest.

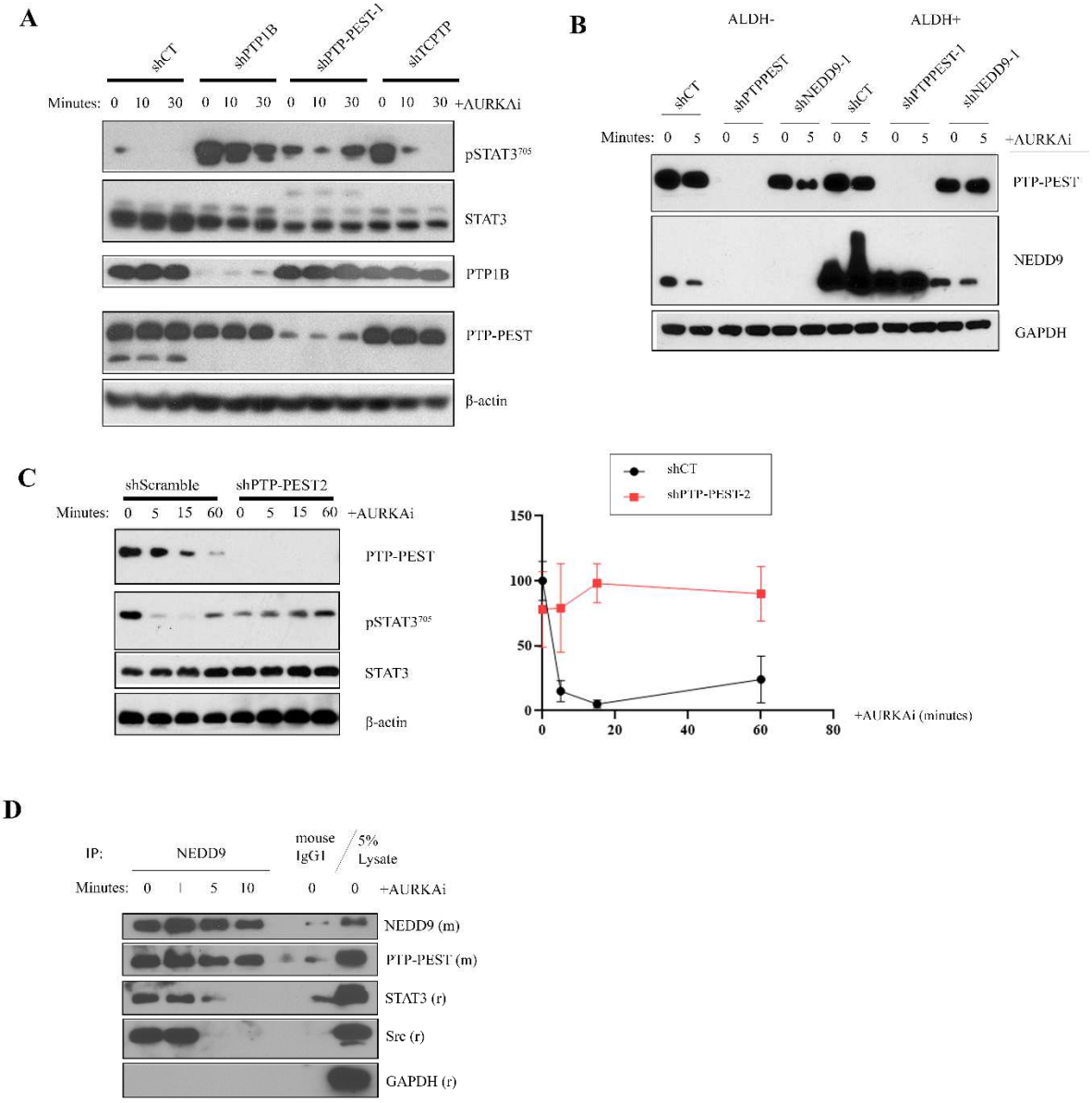
A
shCT
shPTP1B
shPTP-PEST-1
shTCPTP
Minutes: 0 10 30 0 10 30 0 10 30 0 10 30 +AURKAi
pSTAT3705
STAT3
PTP1B
PTP-PEST
β-actin
B
ALDH-
ALDH+
shCT
shPTPPEST
shNEDD9-1
shCT
shPTPPEST-1
shNEDD9-1
Minutes: 0 5 0 5 0 5 0 5 0 5 0 5 +AURKAi
PTP-PEST
NEDD9
GAPDH
C
shScramble
shPTP-PEST2
Minutes: 0 5 15 60 0 5 15 60 +AURKAi
PTP-PEST
pSTAT3705
STAT3
β-actin
shCT
shPTP-PEST-2
150
100
50
0
0
20
40
60
80
+AURKAi (minutes)
D
IP: NEDD9
mouse IgG1
5% Lysate
Minutes: 0 1 5 10 0 0 +AURKAi
NEDD9 (m)
PTP-PEST (m)
STAT3 (r)
Src (r)
GAPDH (r)

M2-Figure 4: AURKAi-induced pSTAT3^{705} dephosphorylation involves PTP-PEST phosphatase

(A) Western blot illustrating the impact of PTP1B, PTP-PEST, or TCPTP-depletion on the ability of AURKAi to inhibit pSTAT3^{705} in THJ-16T ALDH+ cells. Cells with stable phosphatase knockdown was treated with the indicated duration of AURKAi. **(B)** NEDD9/PTP-PEST protein levels between ALDH-/ALDH+ cells, in response to stable shNEDD9/shPTP-PEST-mediated knockdown, and when treated with 300nM AURKAi for 5 minutes. **(C)** Left: Validation of PTP-PEST's impact on AURKAi-mediated pSTAT3^{705} dephosphorylation using a second shRNA construct, right: quantification of pSTAT3^{705} levels in shCT and shPTP-PEST2 cells after AURKAi treatment normalized to total STAT3. **(D)** Immuno-coprecipitation with the NEDD9 monoclonal antibody in THJ-16T ALDH^{high} sorted cells treated with AURKAi (300nM) for the indicated duration. Mouse IgG1 was used as isotype control.

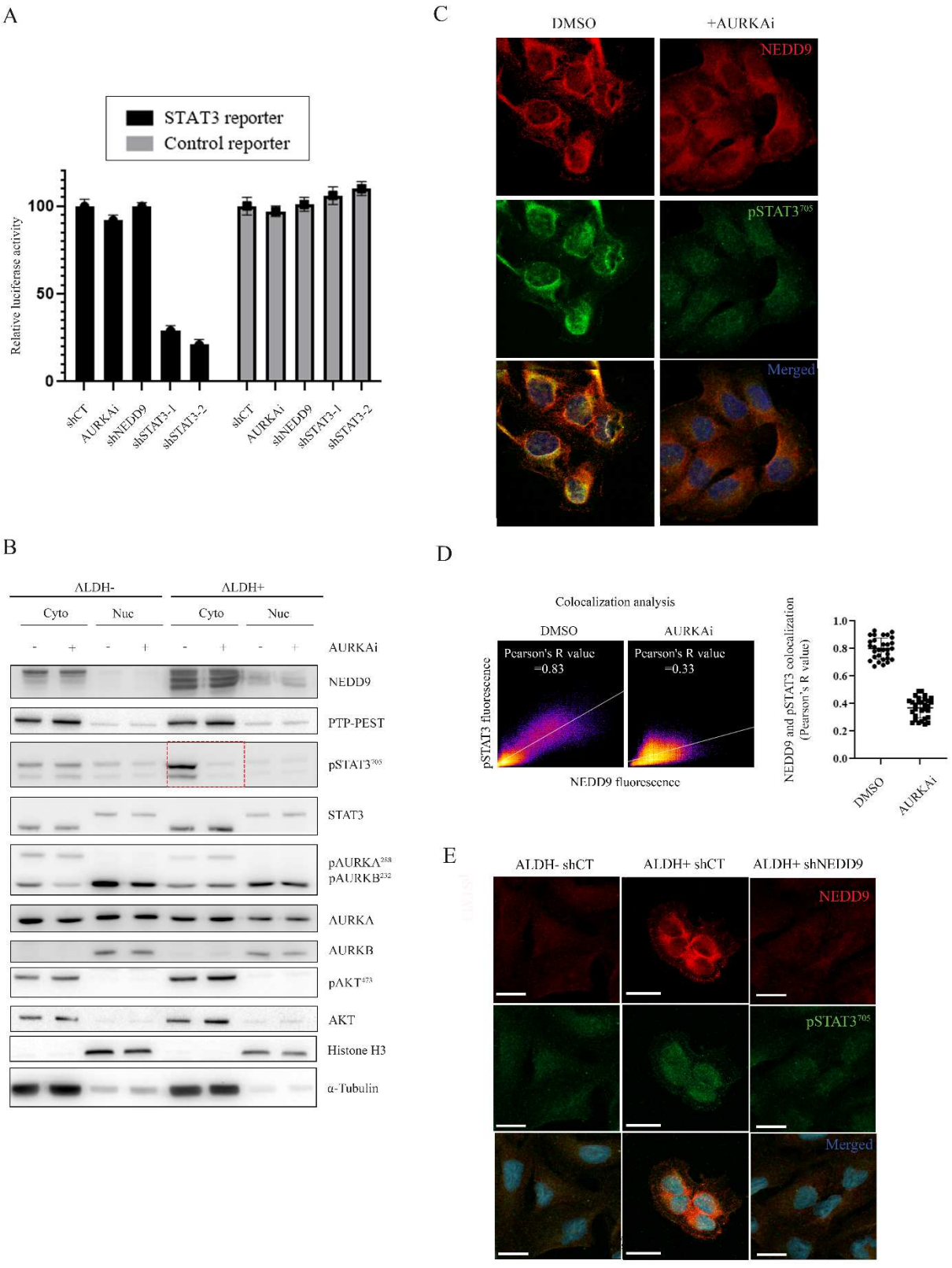
A
STAT3 reporter
Control reporter
Relative luciferase activity
100
50
0
shCT
AURKAi
shNEDD9
shSTAT3-1
shSTAT3-2
shCT
AURKAi
shNEDD9
shSTAT3-1
shSTAT3-2
B
ALDH-
ALDH+
Cyto
Nuc
Cyto
Nuc
- + - + - + - +
AURKAi
NEDD9
PTP-PEST
pSTAT3705
STAT3
pAURKA288
pAURKB232
AURKA
AURKB
pAKT473
AKT
Histone H3
α-Tubulin
C
DMSO
+AURKAi
NEDD9
pSTAT3705
Merged
D
Colocalization analysis
DMSO
AURKAi
Pearson's R value =0.83
Pearson's R value =0.33
pSTAT3 fluorescence
NEDD9 fluorescence
NEDD9 and pSTAT3 colocalization (Pearson's R value)
1.0
0.8
0.6
0.4
0.2
0.0
DMSO
AURKAi
E
ALDH- shCT
ALDH+ shCT
ALDH+ shNEDD9
NEDD9
pSTAT3705
Merged

M2-Figure 5: NEDD9/AURKA predominantly regulates cytoplasmic STAT3 activation in ALDH+ ATC cells

A. STAT3 transcriptional reporter activity of ALDH+ THJ-16T cells treated with AURKAi or shSTAT3, n=3 biological replicates. **B.** Western blot analysis of $pSTAT3^{705}$ levels in response to AURKAi treatment in ALDH- cells. Note that $pSTAT3^{705}$ levels are unchanged in control cells but become reduced in ALDH- cells where NEDD9 is ectopically expressed. **C.** Immunofluorescence images illustrating the impact of VX-680 (AURKAi) on $pSTAT3^{705}$ and NEDD9 cellular distribution. **D.** Representative panel and quantification of NEDD9/pSTAT3705 colocalization in ALDH+ cells treated with DMSO or AURKAi **E.** Immunofluorescent images of ALDH- ALDH+ and ALDH+ shNEDD9 cells stained for NEDD9 and $pSTAT3^{705}$.

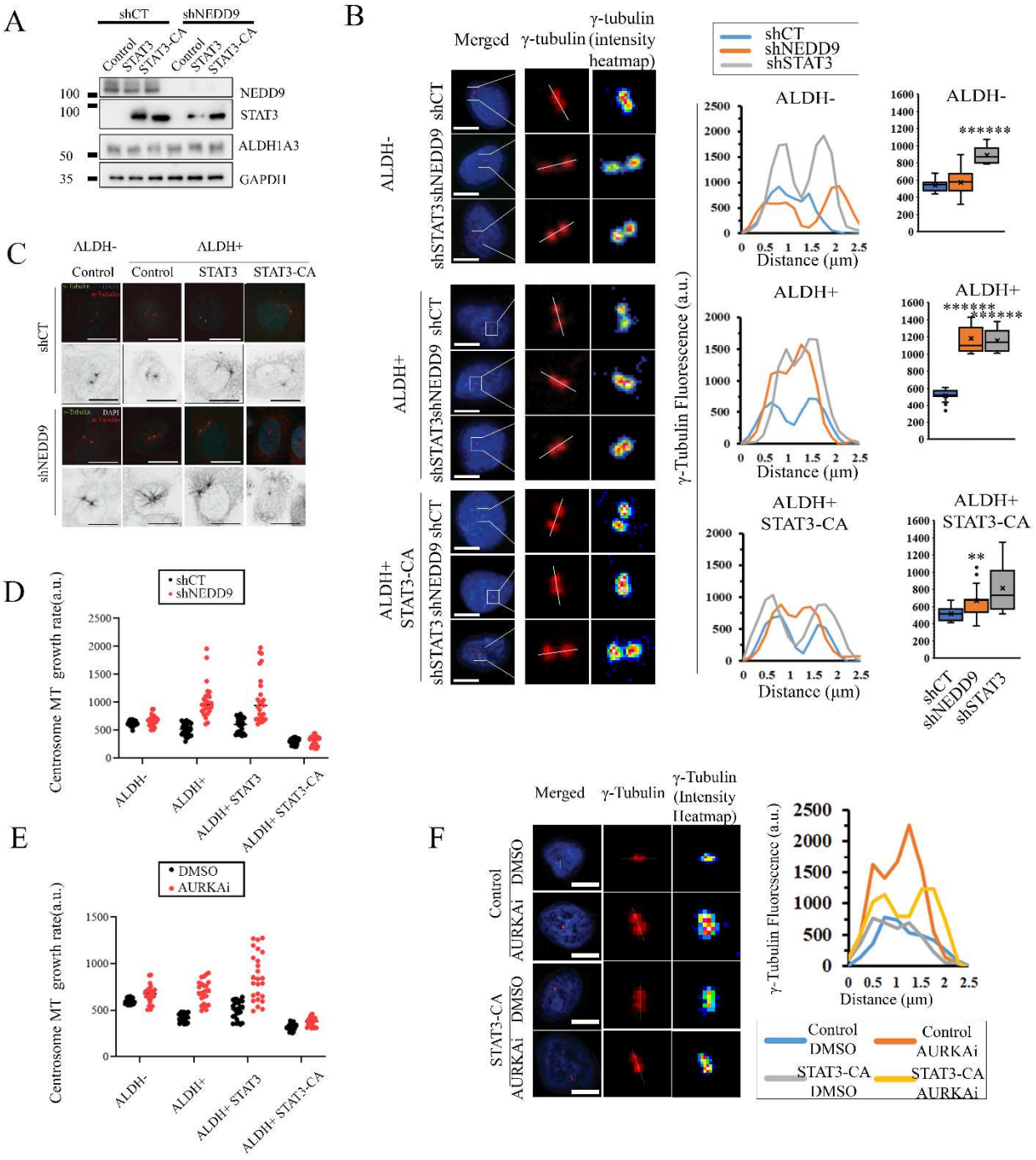
A
shCT
shNEDD9
Control
STAT3
STAT3-CA
Control
STAT3
STAT3-CA
100
100
50
35
NEDD9
STAT3
ALDH1A3
GAPDH
B
Merged
γ-tubulin
γ-tubulin (intensity heatmap)
shCT
shNEDD9
shSTAT3
ALDH-
ALDH+
ALDH+ STAT3-CA
γ-Tubulin Fluorescence (a.u.)
Distance (μm)
ALDH-
ALDH+
ALDH+ STAT3-CA
******
****
**
shCT
shNEDD9
shSTAT3
C
ALDH-
ALDH+
Control
Control
STAT3
STAT3-CA
shCT
shNEDD9
α-Tubulin
DAPI
α-Tubulin
D
shCT
shNEDD9
Centrosome MT growth rate(a.u.)
ALDH-
ALDH+
ALDH+ STAT3
ALDH+ STAT3-CA
E
DMSO
AURKAi
Centrosome MT growth rate(a.u.)
ALDH-
ALDH+
ALDH+ STAT3
ALDH+ STAT3-CA
F
Merged
γ-Tubulin
γ-Tubulin (Intensity Heatmap)
Control
STAT3-CA
DMSO
AURKAi
γ-Tubulin Fluorescence (a.u.)
Distance (μm)
Control DMSO
Control AURKAi
STAT3-CA DMSO
STAT3-CA AURKAi

M2-Figure 6: STAT3 activation antagonizes centrosome microtubule-nucleation downstream of the NEDD9-interactome

A. Western blot illustrating of NEDD9-knockdown in combination with STAT3 or STAT3-CA (constitutively activated mutant with A662C, N664C point mutations). B. Left: representative images and quantification of γ-tubulin levels after NEDD9 or STAT3-depletion in ALDH-, ALDH+ or ALDH+ STAT-3CA overexpressing THJ-16T cells. Centre: The line graph panels indicating the intensity of centrosome pairs or individual centrosomes of cells, measured using the "plot profile" function of Fiji/ImageJ software. The region quantified is depicted by a white line in the left panels. Right: Quantification of γ-tubulin/ fluorescence of interphase centrosome (n=3 biological replicates, where 5 cells were scored for each condition). Only centrosome pairs less than 1 μm apart, directly adjacent to the nucleus were scored. Box limits indicate the 25th and 75th percentiles. Whiskers extend 1.5 times the interquartile range from the 25th and 75th percentiles. **C.** Microtubule regrowth assay illustrating the impact of NEDD9 expression and STAT3 activation on microtubule-nucleating activities of centrosomes following NEDD9-depletion or STAT3 (wild type and constitutively active) ectopic expression. To ensure cell cycle parity, MT growth was compared between cells where the centrosomes were of similar distances apart and the chromosomes had yet to begin condensing. **D.** Quantification of microtubule growth rate at the centrosomes. The total fluorescent intensity of the microtubule emanating from centrosomes is calculated by summing the regional fluorescence subtracted by the background fluorescence. Cells that stable express control vector, STAT3-WT, or STAT3-CA were treated with shCT or shNEDD9 for 24h after which the media was refreshed and the cells were treated with nocodazole. 20h after nocodazole treatment, cells were placed in 4^{o}C ice condition to complete tubulin depolymerization before being placed in 37^{o}C nodozadole-free media to induce microtubule growth. **E.** Quantification of microtubule growth rate at the centrosomes. The total fluorescent intensity of the microtubule emanating from centrosomes is calculated by summing the regional fluorescence subtracted by the background fluorescence. Cells that stable express control vector, STAT3-WT, or STAT3-CA were treated with DMSO or AURKAi for 24h after which the cells were treated with nocodazole. 20h after nocodazole treatment, cells were placed in 4^{o}C ice condition to complete tubulin depolymerization before being placed in 37^{o}C nodozadole-free media to induce microtubule growth. **F.** AURKAi-induced γ-tubulin accumulation can be inhibited by ectopic expression of constitutively activated STAT3. Left: Representative images and quantification of γ-tubulin levels in DMSO or AURKAi-treated (100nM, 24h) control or STAT-3CA overexpressing ALDH+ THJ-16T cells. Right: line graph panel indicating the intensity of centrosome pairs or individual centrosomes of cells, measured using the "plot profile" function of Fiji/ImageJ software. The region quantified is depicted by a white line in the left panels. Statistical significance was determined using two-tailed Student's t tests. Error bars represent + SD. *****P<0.00001, ***P<0.001, **P<0.01.

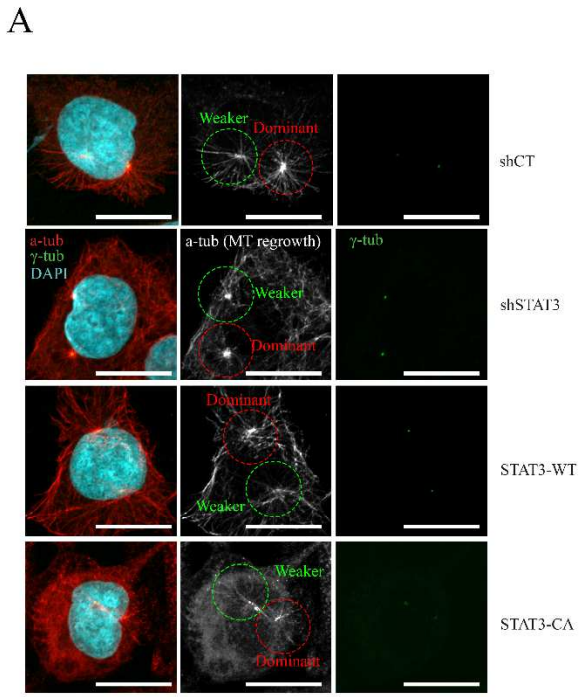
A
Weaker
Dominant
shCT
a-tub
γ-tub
DAPI
a-tub (MT regrowth)
γ-tub
Weaker
Dominant
shSTAT3
Dominant
Weaker
STAT3-WT
Weaker
Dominant
STAT3-CA

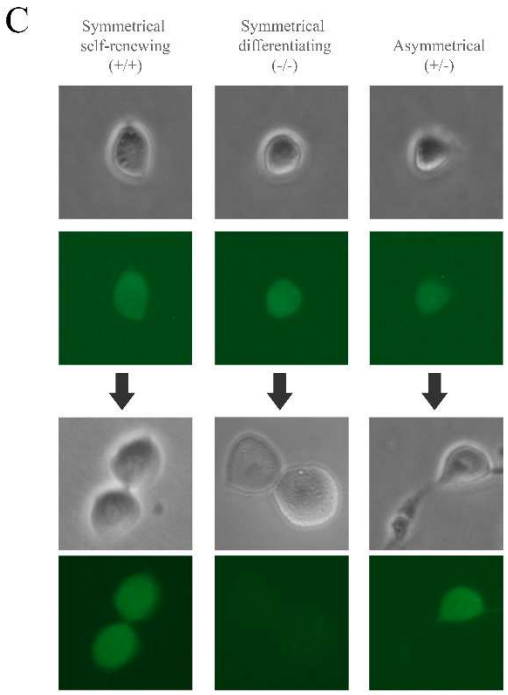
C
Symmetrical self-renewing (+/+)
Symmetrical differentiating (-/-)
Asymmetrical (+/-)

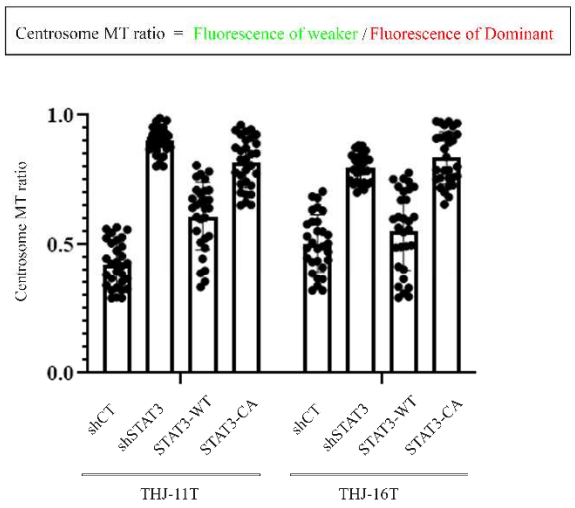
B
Centrosome MT ratio = Fluorescence of weaker / Fluorescence of Dominant
Centrosome MT ratio
1.0
0.5
0.0
shCT
shSTAT3
STAT3-WT
STAT3-CA
shCT
shSTAT3
STAT3-WT
STAT3-CA
THJ-11T
THJ-16T

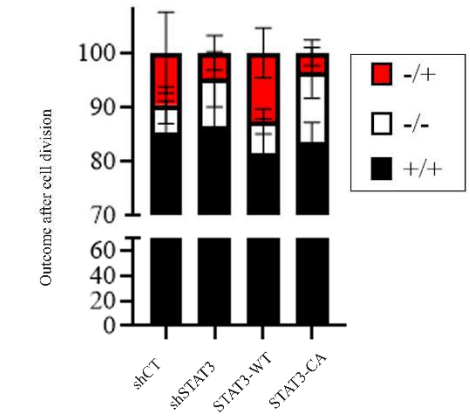
D
Outcome after cell division
100
90
80
70
60
40
20
0
-/+
-/-
+/+
shCT
shSTAT3
STAT3-WT
STAT3-CA

M2-Figure 7: Both positive and negative regulation of STAT3 activation disturbs centrosome asymmetry in ALDH+ ATC cells

A. Microtubule regrowth assay illustrating the impact of STAT3 activation on the microtubule-nucleating asymmetry between the two centrosomes. Red and green circles, respectively, highlight the dominant and weaker centrosomes. Cells that stable express control vector, shSTAT3, STAT3-WT, or STAT3-CA were treated with nocodazole for 20h, then were placed in 4^{o}C ice condition to complete tubulin depolymerization before being placed in 37^{o}C nodozadole-free media to induce microtubule growth. **B.** Quantification of centrosome asymmetry based on the relative regional fluorescence of microtubules emanating from each centrosome, calculated by dividing the fluorescence of the weaker centrosome by the fluorescence of the stronger centrosome; lower values indicate greater degrees of asymmetry. **c.** Representative images of symmetrical versus asymmetrical cell division based on the ALDH+ status of daughter cells. Single ALDH+/- sorted THJ-16T were seeded at 1 cell per well. The ALDH-status of daughter cells after 1 cell division is assessed by aldefluor and visualized by fluorescence microscopy. Divisions that produce 1 ALDH+ and 1 ALDH- daughter cells are considered asymmetrical. **d.** Quantification of outcomes represented in **c.** 192 ALDH+ cells per condition were scored.

Methods

Cell culture: 8505c, TPC1, and BCPAP cell lines are a courtesy of Dr. M. Trifiro (Department of Endocrinology, Jewish General Hospital, McGill University), which were purchased from DSMZ—and maintained in culture in RPMI medium supplemented with 10% heat-inactivated fetal bovine serum (Wisent) and 1% penicillin-streptomycin . MCF-10A cells were purchased form ATCC and maintained in DMEM/12 supplemented with 5% horse serum, EGF, hydrocortisone, cholera toxin, insulin, and 1% penicillin-streptomycin. THJ-11T and THJ-16T were generously provided by Dr. J. Copland (Mayo Clinic, Jacksonville, Florida). These cell lines are derived from clinic anaplastic thyroid cancer patients and confirmed to match the primary tumor sample via DNA short tandem repeat analysis[94]. They are maintained in RPMI 1640x with 5% FBS, 1x non-essential amino acids, 1mM sodium pyruvate, and 10mM HEPES.

Flow cytometry quantification of ALDH activity and sorting by ALDH-status: ALDH activity was detected using ALDEFLUOR® staining kit (StemCell Technologies). Live cells were harvested after treatment, washed once with PBS, and resuspended in ALDH assay buffer before splitting into 2 tubes, one with DEAB and one without. The cells were incubated in 100µL of assay buffer + 1ul of 300nM aldefluor reagent and 1mL of DEAB reagent for 15-40min (optimized by cell line) at room temperature. The cells were then centrifuged and re-suspended in new assay buffer + 5µL of 7-AAD. 7-AAD staining is used to exclude necrotic cells during FACS analysis. The aldefluor intensity is measured using BD FACScalibur. The samples with DEAB was measured first, followed by the matching sample without DEAB added; positivity is determined by the difference in fluorescence between +DEAB and -DEAB sample. Cell sorting by ALDH-status was conducted using the same protocol in a sterile environment, using the BD-FACSAria machine. To ensure high purification rate, we recovered only the cell population with the 20% highest or lowest Aldefluor staining respectively. Sorted cells were allowed recovery for 3 days before being re-evaluated for ALDH+ positivity.

8505C, THJ-11T, and THJ-16T were sorted based on Aldefluor activity. 8505c had basal 20-30% rate of ALDH+ cells, but intensity-wise showed poor separation of the ALDH- and ALDH+ cells, thus could not be efficiently sorted. THJ-11T had a basal 20-40% rate of ALDH+ cells and exhibited good separation of ALDH+ and ALDH- cell population, but the ALDH- cells post

sorting displayed only 20% of the doubling rate compared to ALDH+ cells. THJ-16T had a basal 20-40% rate of ALDH+ cells, exhibited strong separation of ALDH+ and ALDH- cell population, and displayed relatively equal double rating between the ALDH+ and ALDH- population post sorting, which was optimal for fair phenotype studies following genetic or pharmacological perturbations.

For apoptosis assay, cells were washed twice with Biolegend's Cell Staining Buffer, then responded in Annexin V binding buffer together with with FITC Annexin V (Biolegends 640905) for 20 minutes at room temperature, followed by treatment with 7-AAD before analysis by flow cytometry.

Immunofluorescence microscopy

For immunofluorescence microscopy, cells were fixed in 4% paraformaldehyde or 100% methanol and permeabilized using 0.2% triton-X. The centrosome, mitotic spindle, and DNA was visualized using anti-pericentrin (ab4448, Abcam, 1:2000), anti-α-Tubulin (DM1A, Millipore Sigma, 1:1000), anti-γ-tubulin (GTU-88, Abcam, 1:1000), anti-γ-tubulin (EPR16793, 1:1000), anti-Centrin (20H5, Millipore Sigma, 1:1000) and DAPI respectively.

Immunofluorescence images were obtained using Quorum wave FX spinning disk (SD) confocal microscope or LSM800 Airyscan (Zeiss) confocal laser scanning microscope and analyzed using Volocity (PerkinElmer) or ImageJ.

To quantify declustered centrosomes in dividing cells, 60 or more random images across 3 biological replicas for each condition was taken at 40x or 63x magnification. At least 80 cells mitotic cells were counted per condition per replica. Representative images were captured at 63x magnification. Mitotic cells are discriminated by three criteria: chromosome condensation as visualized by DAPI, the appearance of the mitotic spindle as visualized by alpha-tubulin, and increased centrosome pericentriolar materials as visualized by pericentrin. Declustered centrosomes were identified based on the presence of >2 spindle poles radiating from distinct pericentrin foci in 1 cell. The number of declustered centrosomes is quantified as a percentage of total mitotic cells.

To quantify centrosome amplification, cells were co-stained with centrin and pericentrin antibodies and visualized at 63x magnification. A cell was defined as centrosome amplified by

the presence of >4 centrin-positive dots that show co-localization with pericentrin. Images were captured using LSM800 Airyscan (Zeiss) confocal laser scanning microscope.
For centrosome proteins intensity assays, images were captured at 63x using focusing on the middle (maximal size and intensity) of an individual centrosome. Quantification was confirmed using two methods. The first is by drawing a circle around an individual centrosome in volocity software, measuring the sum integrated pixel intensity, then subtracting the background fluorescence (measured by placing a circle of the same dimension away from the centrosome). The second way is, in ImageJ, drawing a 2.5um line through the center of one or two centrosomes then using the "plot profile" function of Fiji/ImageJ software to measure the integrated area after subtracting the background. For quantification involved 3 biological replicates in which 15 cells were scored for each condition in each repeat. Cells with 2 or more than 2 centrosomes were scored separately. For cells with 2 centrosomes, only centrosome pairs less than 1μm apart, directly adjacent to the nucleus were included. Centrosome nucleation symmetry is calculated using the formula (peak intensity of weak centrosome / peak intensity of strong centrosome) for cells with 2 centrosomes, or (average peak intensity of weaker 50% of the centrosomes / average peak intensity of the stronger 50% of centrosomes) in the case of centrosome amplification.

Lentiviral generation and infection of cells: For shRNA-mediated knockdown, shRNA sequences cloned into pLKO.1-puro lentiviral vectors were co-transfected using *polyethylenimine* into 293T cells with psPAX2 and pMD2.G for lentiviral generation. Media was refreshed 12h after transfection. Thereafter, supernatant containing the lentivirus was collected and filtered every 24h and fresh media was added, repeated 3 times. Viral supernatant was added to low-passage cell lines together with polybrene in 1% serum. 24h after virus infection (t=0h for time-course assays), cells were refreshed with complete media and selection for infected clones was carried out using 0.5-2ug/mL puromycin. ALDH+ and ALDH- cells were confirmed not to have equal sensitivity to puromycin. Knockdown efficiency was confirmed by western blot using the corresponding antibodies.

For LZRS retroviral vectors, LZRS or LZRS_NEDD9 (containing GFP sequence) was transfected into Phoenix cells using lipofectamine 2000. Supernatants containing the retrovirus

were collected and filtered and added to low-passage cell lines together with polybrene. Infected cells were enriched by FACS-sorting for GFP-positivity, and expression of ectopic NEDD9 was confirmed using flag antibody to detect a 105kDa band.

Plasmid vectors

pLKO-shC (shNEDD9), pLKO-shD (shNEDD9-2), LZRS-hNEDD9-IresGFP, and LZRS-IresGFP were deposited by Dr. Lynda Chin.

Microtubule regrowth assay

The microtubule regrowth assay was performed as previously describe. Fluorescence activated cell sorted THJ-16T cells was treated with shCT or shNEDD9 for 36h, then treated with nocodazole for 16h. Cells were then given cold medium and placed on ice for 90 minutes. Thereafter, microtubule regrowth was then induced by pre-warmed media and placing the cells in 37ºC for the indicated time (30s – 60s), when they were subsequently fixed with 4% paraformaldehyde and stained for anti-α-tubulin and anti-γ-tubulin.

Western-blot analysis: Sub-confluent cells were washed 3x with PBS, lysed in RIPA buffer (50 mM Tris-HCl at pH7.5, 150 mM sodium chloride, 1% tritonX-100, 0.1% SDS, 2mM EDTA and 25mM sodium fluoride) with 1mM PMSF and protease inhibitor cocktail (Roche) on ice for 30minand centrifuged at 13,000 rpm for 20min. Cell lysates was mixed with SDS buffer (Tris at pH 6.8, 20% glycerol, 5% SDS, bromophenol blue and β-mercaptoethanol) and boiled for 5 min, then loaded into 8-15% SDS-PAGE gels, transferred to PDVF membranes, and blotted with the primary antibodies. The primary antibodies used were as follows: anti-NEDD9 (Cell Signaling Technology, 4044), anti-ALDH1A3 (Novus Biologicals), anti-CPAP/CENPJ (Proteintech Group, 11517-1-AP), anti-RARα (Cell signaling, #62294) and anti-FLAG (Sigma Aldrich Corporation, F1804), p-TBK1 (cell signaling 54835), pSTAT1 (cell signaling 91675), TBK1 (cell signaling 35045), STAT1 (cell signaling 91725), STING (Cell signaling 13647), cGAS (abiocode 14085). Secondary antibodies for Western-blot assays: anti-mouse IgG-peroxidase-conjugated (Bio-Rad Laboratories, 172-1011), anti-rabbit IgG-peroxiase-conjugated (Bio-Rad Laboratories, 170-6515).

Microarray analysis: Transcriptomic profiles of cancer patients were obtained from TCGA PanCancer Atlas datasets [97] and analyzed through Cbioportal[91,92].

Statistical analysis: For discrete variables showing normal distribution, means and standard deviations (SD) are given and comparisons were made using the t-test. In all statistical tests, $P<0.05$ was considered statistically significant.

References

1. Levy, D.E. & Lee, C.-k. What does Stat3 do? *The Journal of clinical investigation* **109**, 1143-1148 (2002).
2. Darnell, J.E. Validating Stat3 in cancer therapy. *Nature medicine* **11**, 595-596 (2005).
3. Bromberg, J.F.*, et al.* Stat3 as an oncogene. *Cell* **98**, 295-303 (1999).
4. Zhang, X.*, et al.* Identification of STAT3 as a substrate of receptor protein tyrosine phosphatase T. *Proceedings of the National Academy of Sciences* **104**, 4060-4064 (2007).
5. Shields, B.J.*, et al.* TCPTP regulates SFK and STAT3 signaling and is lost in triple-negative breast cancers. *Molecular and cellular biology* **33**, 557-570 (2013).
6. Silva, C.M. Role of STATs as downstream signal transducers in Src family kinase-mediated tumorigenesis. *Oncogene* **23**, 8017-8023 (2004).
7. Mali, S.B. Review of STAT3 (Signal Transducers and Activators of Transcription) in head and neck cancer. *Oral oncology* **51**, 565-569 (2015).
8. Yu, H., Pardoll, D. & Jove, R. STATs in cancer inflammation and immunity: a leading role for STAT3. *Nature reviews cancer* **9**, 798-809 (2009).
9. Morris, E.J.*, et al.* Stat3 regulates centrosome clustering in cancer cells via Stathmin/PLK1. *Nature communications* **8**, 1-15 (2017).
10. Metge, B., Ofori-Acquah, S., Stevens, T. & Balczon, R. Stat3 activity is required for centrosome duplication in Chinese hamster ovary cells. *Journal of Biological Chemistry* **279**, 41801-41806 (2004).
11. Ng, D.C.H.*, et al.* Stat3 regulates microtubules by antagonizing the depolymerization activity of stathmin. *The Journal of cell biology* **172**, 245-257 (2006).
12. Chen, R.-Y.*, et al.* CPAP promotes angiogenesis and metastasis by enhancing STAT3 activity. *Cell Death & Differentiation* **27**, 1259-1273 (2020).
13. Verma, N.K.*, et al.* STAT3-stathmin interactions control microtubule dynamics in migrating T-cells. *Journal of Biological Chemistry* **284**, 12349-12362 (2009).
14. Ma, J.-h., Qin, L. & Li, X. Role of STAT3 signaling pathway in breast cancer. *Cell Communication and Signaling* **18**, 1-13 (2020).
15. Shiraiwa, K.*, et al.* JAK/STAT3 and NF-κB signaling pathways regulate cancer stem-cell properties in anaplastic thyroid cancer cells. *Thyroid* **29**, 674-682 (2019).
16. Harada, D., Takigawa, N. & Kiura, K. The role of STAT3 in non-small cell lung cancer. *Cancers* **6**, 708-722 (2014).
17. Nakajima, K.*, et al.* A central role for Stat3 in IL-6-induced regulation of growth and differentiation in M1 leukemia cells. *The EMBO journal* **15**, 3651-3658 (1996).
18. Mora, L.B.*, et al.* Constitutive activation of Stat3 in human prostate tumors and cell lines: direct inhibition of Stat3 signaling induces apoptosis of prostate cancer cells. *Cancer research* **62**, 6659-6666 (2002).
19. Gabbasov, R.*, et al.* NEDD9 promotes oncogenic signaling, a stem/mesenchymal gene signature, and aggressive ovarian cancer growth in mice. *Oncogene* **37**, 4854-4870 (2018).
20. Wei, D.*, et al.* Stat3 activation regulates the expression of vascular endothelial growth factor and human pancreatic cancer angiogenesis and metastasis. *Oncogene* **22**, 319-329 (2003).

21. Siveen, K.S.*, et al.* Targeting the STAT3 signaling pathway in cancer: role of synthetic and natural inhibitors. *Biochimica et Biophysica Acta (BBA)-reviews on cancer* **1845**, 136-154 (2014).
22. Johnston, P.A. & Grandis, J.R. STAT3 signaling: anticancer strategies and challenges. *Molecular interventions* **11**, 18 (2011).
23. Hernandez-Vargas, H.*, et al.* Methylome analysis reveals Jak-STAT pathway deregulation in putative breast cancer stem cells. *Epigenetics* **6**, 428-439 (2011).
24. Doheny, D.*, et al.* Combined inhibition of JAK2-STAT3 and SMO-GLI1/tGLI1 pathways suppresses breast cancer stem cells, tumor growth, and metastasis. *Oncogene* **39**, 6589-6605 (2020).
25. Lin, L.*, et al.* STAT3 signaling pathway is necessary for cell survival and tumorsphere forming capacity in ALDH+/CD133+ stem cell-like human colon cancer cells. *Biochemical and biophysical research communications* **416**, 246-251 (2011).
26. Yang, Z.*, et al.* The KMT1A-GATA3-STAT3 circuit is a novel self-renewal signaling of human bladder cancer stem cells. *Clinical Cancer Research* **23**, 6673-6685 (2017).
27. Jiang, C.*, et al.* miR-500a-3p promotes cancer stem cells properties via STAT3 pathway in human hepatocellular carcinoma. *Journal of experimental & clinical cancer research* **36**, 1-13 (2017).
28. Liu, Y.*, et al.* HN1L promotes triple-negative breast cancer stem cells through LEPR-STAT3 pathway. *Stem Cell Reports* **10**, 212-227 (2018).
29. Shao, C.*, et al.* Essential role of aldehyde dehydrogenase 1A3 for the maintenance of non–small cell lung cancer stem cells is associated with the STAT3 pathway. *Clinical cancer research* **20**, 4154-4166 (2014).
30. Kroon, P.*, et al.* JAK-STAT blockade inhibits tumor initiation and clonogenic recovery of prostate cancer stem-like cells. *Cancer research* **73**, 5288-5298 (2013).
31. Perros, P.*, et al.* Guidelines for the management of thyroid cancer. *Clinical endocrinology* **81**, 1-122 (2014).
32. Salvatore, G.*, et al.* A cell proliferation and chromosomal instability signature in anaplastic thyroid carcinoma. *Cancer research* **67**, 10148-10158 (2007).
33. Smallridge, R.C.*, et al.* American Thyroid Association guidelines for management of patients with anaplastic thyroid cancer. *Thyroid* **22**, 1104-1139 (2012).
34. Todaro, M.*, et al.* Tumorigenic and metastatic activity of human thyroid cancer stem cells. *Cancer research* **70**, 8874-8885 (2010).
35. Nagayama, Y., Shimamura, M. & Mitsutake, N. Cancer stem cells in the thyroid. *Frontiers in endocrinology* **7**, 20 (2016).
36. Singh, M.K., Cowell, L., Seo, S., O'Neill, G.M. & Golemis, E.A. Molecular basis for HEF1/NEDD9/Cas-L action as a multifunctional co-ordinator of invasion, apoptosis and cell cycle. *Cell biochemistry and biophysics* **48**, 54-72 (2007).
37. Izumchenko, E.*, et al.* NEDD9 promotes oncogenic signaling in mammary tumor development. *Cancer research* **69**, 7198-7206 (2009).
38. Wang, Z.*, et al.* NEDD9 may regulate hepatocellular carcinoma cell metastasis by promoting epithelial-mesenchymal-transition and stemness via repressing Smad7. *Oncotarget* **8**, 1714 (2017).
39. Kim, M.*, et al.* Comparative oncogenomics identifies NEDD9 as a melanoma metastasis gene. *Cell* **125**, 1269-1281 (2006).

40. Li, Y., *et al.* HEF1, a novel target of Wnt signaling, promotes colonic cell migration and cancer progression. *Oncogene* **30**, 2633-2643 (2011).
41. Pugacheva, E.N. & Golemis, E.A. The focal adhesion scaffolding protein HEF1 regulates activation of the Aurora-A and Nek2 kinases at the centrosome. *Nature cell biology* **7**, 937-946 (2005).
42. Pugacheva, E.N., Jablonski, S.A., Hartman, T.R., Henske, E.P. & Golemis, E.A. HEF1-dependent Aurora A activation induces disassembly of the primary cilium. *Cell* **129**, 1351-1363 (2007).
43. Singh, M.K., *et al.* Enhanced genetic instability and dasatinib sensitivity in mammary tumor cells lacking NEDD9. *Cancer research* **70**, 8907-8916 (2010).
44. O'Neill, G.M., Seo, S., Serebriiskii, I.G., Lessin, S.R. & Golemis, E.A. A new central scaffold for metastasis: parsing HEF1/Cas-L/NEDD9. *Cancer research* **67**, 8975-8979 (2007).
45. Guerrero, M.S., Parsons, J.T. & Bouton, A.H. Cas and NEDD9 contribute to tumor progression through dynamic regulation of the cytoskeleton. *Genes & cancer* **3**, 371-381 (2012).
46. Shagisultanova, E., Gaponova, A.V., Gabbasov, R., Nicolas, E. & Golemis, E.A. Preclinical and clinical studies of the NEDD9 scaffold protein in cancer and other diseases. *Gene* **567**, 1-11 (2015).
47. Avalle, L., *et al.* STAT3 localizes to the ER, acting as a gatekeeper for ER-mitochondrion Ca 2+ fluxes and apoptotic responses. *Cell Death & Differentiation* **26**, 932-942 (2019).
48. Moore, A., Blagg, J., Linardopoulos, S. & Pearson, A. Aurora kinase inhibitors: novel small molecules with promising activity in acute myeloid and Philadelphia-positive leukemias. *Leukemia* **24**, 671-678 (2010).
49. Liu, L., McBride, K.M. & Reich, N.C. STAT3 nuclear import is independent of tyrosine phosphorylation and mediated by importin-α3. *Proceedings of the National Academy of Sciences* **102**, 8150-8155 (2005).
50. Cimica, V., Chen, H.-C., Iyer, J.K. & Reich, N.C. Dynamics of the STAT3 transcription factor: nuclear import dependent on Ran and importin-β1. *PloS one* **6**, e20188 (2011).
51. Morris, E.J., Gillespie, J.A., Maxwell, C.A. & Dedhar, S. A model of differential mammary growth initiation by Stat3 and asymmetric integrin-α6 inheritance. *Cell reports* **30**, 3605-3615. e3605 (2020).
52. Januschke, J., *et al.* Centrobin controls mother–daughter centriole asymmetry in Drosophila neuroblasts. *Nature cell biology* **15**, 241-248 (2013).
53. Gramates, L.S., *et al.* FlyBase at 25: looking to the future. *Nucleic acids research*, gkw1016 (2016).
54. Nair, A.R., *et al.* The microcephaly-associated protein Wdr62/CG7337 is required to maintain centrosome asymmetry in Drosophila neuroblasts. *Cell reports* **14**, 1100-1113 (2016).
55. Gabbasov, R., *et al.* NEDD9 promotes oncogenic signaling, a stem/mesenchymal gene signature, and aggressive ovarian cancer growth in mice. *Oncogene*, 1 (2018).
56. Xing, Y., Luo, D.-y., Long, M.-y., Zeng, S.-l. & Li, H.-H. High ALDH1A1 expression correlates with poor survival in papillary thyroid carcinoma. *World journal of surgical oncology* **12**, 29 (2014).

57. Charafe-Jauffret, E.*, et al.* Aldehyde dehydrogenase 1–Positive cancer stem cells mediate metastasis and poor clinical outcome in inflammatory breast cancer. *Clinical Cancer Research* **16**, 45-55 (2010).
58. Li, X., Wan, L., Geng, J., Wu, C.-L. & Bai, X. Aldehyde dehydrogenase 1A1 possesses stem-like properties and predicts lung cancer patient outcome. *Journal of Thoracic Oncology* **7**, 1235-1245 (2012).
59. Cheung, A.*, et al.* Aldehyde dehydrogenase activity in leukemic blasts defines a subgroup of acute myeloid leukemia with adverse prognosis and superior NOD/SCID engrafting potential. *Leukemia* **21**, 1423-1430 (2007).
60. Li, T.*, et al.* ALDH1A1 is a marker for malignant prostate stem cells and predictor of prostate cancer patients' outcome. *Laboratory investigation* **90**, 234-244 (2010).
61. Gao, F.*, et al.* The role of LGR5 and ALDH1A1 in non-small cell lung cancer: Cancer progression and prognosis. *Biochemical and biophysical research communications* **462**, 91-98 (2015).
62. Su, Y.*, et al.* Aldehyde dehydrogenase 1 A1–positive cell population is enriched in tumor-initiating cells and associated with progression of bladder cancer. *Cancer Epidemiology and Prevention Biomarkers* **19**, 327-337 (2010).
63. Yang, L.*, et al.* ALDH1A1 defines invasive cancer stem-like cells and predicts poor prognosis in patients with esophageal squamous cell carcinoma. *Modern Pathology* **27**, 775 (2014).
64. Speranza, M.C.*, et al.* NEDD9, a novel target of miR-145, increases the invasiveness of glioblastoma. *Oncotarget* **3**, 723 (2012).
65. Zhong, J., Bach, C.T., Shum, M.S. & O'Neill, G.M. NEDD9 regulates 3D migratory activity independent of the Rac1 morphology switch in glioma and neuroblastoma. *Molecular Cancer Research* **12**, 264-273 (2014).
66. Agrawal, N.*, et al.* Integrated genomic characterization of papillary thyroid carcinoma. *Cell* **159**, 676-690 (2014).
67. Gao, J.*, et al.* Integrative analysis of complex cancer genomics and clinical profiles using the cBioPortal. *Sci. Signal.* **6**, pl1-pl1 (2013).
68. Cerami, E.*, et al.* The cBio cancer genomics portal: an open platform for exploring multidimensional cancer genomics data. (AACR, 2012).

2.6 Manuscript 3: Targeting tumorigenic thyroid cancer stem cells through centrosome-activation-induced mitotic catastrophe

Rationale

Given that the first two manuscripts identified that NEDD9 uniquely regulates the centrosomes in ALDH+ cells, our final manuscript aims to exploit the NEDD9 interactome and the asymmetrical centrosome behavior in ALDH+ cells as a potentially novel way to treat ATC.

Targeting tumorigenic thyroid cancer stem cells through centrosome-activation-induced mitotic catastrophe

Authors: Henry G. Yu, Krikor Bijian, Jie Su, Sabrina D. da Silva, Gregoire Morand*, Dominic Wernic, Alan Spatz and Moulay A. Alaoui-Jamali

Affiliations:

Departments of Medicine, Oncology, Pathology and Otolaryngology-Head and Neck Surgery, Lady Davis Institute for Medical Research and Segal Cancer Centre, the Sir Mortimer B. Davis-Jewish General Hospital, Faculty of Medicine, McGill University, Montreal, Canada.

*Department of Otorhinolaryngology-Head & Neck Surgery, University Hospital Zurich, Switzerland**.**

Corresponding author

Moulay A. Alaoui-Jamali, PhD

E-mail: moulay.alaoui-jamali@mcgill.ca

Study source of funding

This study was supported by the McGill Interdisciplinary Initiative in Infection and Immunity (MI4) and Quebec Breast Cancer Foundation; GB Morand was supported by the Swiss Cancer League (BIL KFS-3002-08-2012)

Abstract

Centrosome amplification (CA) and stemness are both common hallmarks of advanced cancers. Due to being absent in normal cells, CA is regarded as an attractive anticancer target. However, it remains unknown if CA can be exploited to target cancer stem-like variants selectively. Our previous study showed that anaplastic thyroid cancer (ATC) - an advanced form of thyroid cancer - the stem cell-like ALDH+ subpopulation is enriched in supernumerary centrosomes deficient in pericentriolar material (PCM). Here, immunohistochemical staining revealed a high frequency of ALDH+ cells and PCM-deficient supernumerary centrosomes in ATC patient tissues but not in comparatively benign papillary thyroid cancer. On the premise that excess centrosome activation can be lethal to CA-bearing cells through hampering bipolar-spindle formation during mitosis, we evaluated a panel of small molecules for their ability to restore centrosome microtubule-nucleation activity to those PCM-deficient centrosomes enriched in ALDH+ cells. The leading candidate - a novel multikinase inhibitor "MEAP" - potentiated pericentriolar material accumulation and microtubule-nucleation activity of supernumerary centrosomes, thus inducing spindle multipolarity preferentially in ALDH+ cells. MEAP broadly and preferentially eliminated ALDH+ ATC cells, thus reducing spherogenesis/self-renewal. In vivo, MEAP eliminated ALDH+ cell clusters, attenuated ATC tumorigenesis and tumor growth rate, increased the rate of spindle multipolarity, and decreased chromosomal instability. These findings reveal the potential to target CA as a novel approach to eliminating thyroid stem-like cells, with therapeutic implications for managing the aggressive ATC disease.

Introduction

Centrosomes are the main microtubule-organizing centers (MTOC) in mammalian cells[1-3]. Physiologically, centrosomes are replicated once per cell division. The original and replicated centrosome mature by gradually acquiring pericentriolar materials (PCM) to nucleate microtubules during interphase and form the mitotic spindle during mitosis [1]. Centrosome amplification is common in high-grade tumors[4-6]; for cells with supernumerary centrosomes to replicate efficiently, the excess centrosomes need to be clustered into two opposite poles before metaphase failure to do so leads to multipolar spindles and mitotic catastrophe [7,8]. As centrosome amplification generally does not manifest in healthy cells, many approaches to targeting cancer cells with centrosome amplification have been developed, such as hindering the proteins required to cluster supernumerary centrosomes mechanistically [9-11], or by potentiating the microtubule nucleation activity of supernumerary centrosomes [12]; in either case, these strategies prevent pseudobipolar spindle formation, increases spindle multipolarity, and drives cells to mitotic catastrophe.

Centrosome amplification often manifests alongside cancer dedifferentiation as both are more common in treatment-refractory/advanced cancers [13,14,15,16]. Dedifferentiated cancers are frequently characterized by a larger population of cancer stem cell-like cells, with tumorigenic potential [13,14,15,16]. Physiologically, the centrosomes in normal stem cells often behave distinctly asymmetrical with one of the two centrosomes maturing (e.g., accumulating pericentriolar material) significantly ahead of the other until mitosis, where the weaker centrosome pair is delayed in forming the mitotic spindle [17-19]; the existence and significance of such mechanisms in cancer stem-like cells remains largely unclear. The cancer stem cell hypothesis postulates that stem-like cancer cells can be drivers of aggressive traits such as progression to metastasis, recurrence, and resistance to therapeutics [20,21,22]. Despite the correlative data between centrosome amplification and stemness [23,24], it is presently unknown if anticancer strategies which target centrosome amplification can selectively target stem-like cancer cells.

Thyroid cancer is the most common endocrine malignancy worldwide. Patients with well-differentiated thyroid cancer can achieve long-term survival by surgery alone or in combination with iodine-based therapy[25]. However, in some cases, progressive dedifferentiation of thyroid cancer cells can lead to anaplastic thyroid carcinoma, one of the most lethal types of cancer with a median survival of 6 months[25]. Conventional therapies, including surgery, radiotherapy, and chemotherapy, remain marginal benefits to ATC patients, and therefore the discovery of alternative therapeutic targets remains a priority for this disease [25]. Clinically, ATC commonly manifests as a mixture of differentiated and dedifferentiated cancer cells alongside a high rate of aneuploidy, atypical mitosis, and chromosomal abnormalities [25-27]. While ATC's pathogenesis is not entirely elucidated, most cases are believed to arise from progressive dedifferentiation of the more common papillary thyroid cancer (PTC). However, *de novo* cases are also believed to occur [25,28,29].

Aldehyde dehydrogenase (ALDH) is a polymorphic enzyme important for $NAD(P)^+$-dependent oxidation of aldehydes to respective carboxylic acids [30]. High ALDH activity can predict poor clinical prognosis across a wide range of cancer types [31-38] and is regarded as a reliable stem-like cell marker for ATC; multiple studied in this model indicated that ALDH+ cells are correlated with increased spherogenic, tumorigenic, or metastatic potentials [20,21,22,39 40,41]. In patient-derived ATC cell lines including THJ-11T and THJ-16T, the ALDH isoform primarily responsible for the high ALDH activity is ALDH1A3.

We had previously shown that ALDH+ ATC cells harbored poorly-nucleated supernumerary centrosomes, in contrast to ALDH- cells where structural/numeral centrosomes abnormalities were less frequent; these divergent centrosome-phenotypes were due to transcriptional upregulation [42,43] of the centrosome-associated protein "NEDD9" within ALDH+ ATC cells - a centrosome-associated scaffolding protein well-known to be an activator of metastatic signaling cascades via kinase partners such as Aurora Kinase A (AURKA), Focal Adhesion Kinase (FAK), and SRC [44-54]. Here, we expand upon those findings by first evaluating the expression levels of NEDD9/ALDH and the centrosome status of thyroid cancer patient tissue. After confirming our cell-based results through clinical samples/data, we considered if the poorly nucleated centrosomes in ALDH+ cells could be pharmacologically restored as a novel approach to target ALDH+ cells selectively, as centrosome activation has been shown to drive cancer cells with CA to mitotic catastrophe [12]. By evaluating the impact of small molecules on centrosome microtubule-nucleation, we identified/synthesized a novel multikinase inhibitor dual-targeting AURKA/FAK that potently increased supernumerary centrosome maturation, multipolar spindles, and mitotic arrest selectively in ALDH+ cells, consequently leading to attenuation of stemness-associated traits such as tumorigenesis.

Results

Anaplastic thyroid cancer patient progression is correlated with ALDH1A3/NEDD9 co-upregulation and a higher rate of γ-tubulin-deficient supernumerary centrosomes

Nuclear atypia is a hallmark of ATC that can diagnose ATC from more differentiated thyroid cancer variants and is commonly caused by centrosome abnormalities[55]. To examine the centrosome status of normal PTC versus ATC tissues, we stained for pericentrin (PCNT) and γ-tubulin, two widely-studied pericentriolar material (PCM) proteins (**M3-fig. 1A-B**). Based on PCM staining, centrosome amplification was not present in normal thyroid tissues; in contrast, an average of 1.9% CA was observed in papillary thyroid cancer, and 13.9% CA was observed in ATC tissues (n=3, **M3-fig. 1A**). In addition to the higher frequency of CA in the ATC samples, centrosomes in ATC patients were also much more asymmetrical than those found in PTC or normal thyroid tissues (**M3-fig. 1B, S1**). Calculating the intensity ratio between the weak: strong

centrosomes revealed that ATC centrosomes exhibited a ~0.5 (weak/strong) ratio while PTC and normal thyroid centrosomes displayed a ~0.8 ratio (**M3-fig. 1B, S1**). Although comparing the absolute centrosome intensity across samples is not entirely reliable, we estimated that the intensity of the stronger/dominant centrosomes is relatively similar between normal/PTC and ATC tissues, suggesting that the asymmetry primarily arose from the weaker centrosome. Although we could not evaluate the centrosome status of ALDH1A3^{high} cells distinctly from ALDH1A3^{low} cells in patient tissues, these trends indirectly support our previous cell-based results finding that poorly activated supernumerary centrosomes were especially enriched in ALDH+ ATC cells.

Identification of a novel Reversine analog "MEAP" displaying exceptional activation of centrosome microtubule-nucleation

We previously found that fluorescence-activated cell-sorting (FACS) could separate ATC cell lines into ALDH- and ALDH+ cells variants (**M3-fig. 2A**). Greater spherogenic potential was observed in the ALDH+ group, typical of stem-like cells (**M3-fig. 2B**). Remarkably, ALDH+ cells, which overexpressed ALDH1A3 and NEDD9 **(M3-fig. 2C)**, also harbored more CA, with those supernumerary centrosomes being typically poorly nucleated (**M3-fig. 2D**). Therefore, we hypothesized that pharmacological activation of centrosome microtubule-nucleation activity 322 could be a viable approach to targeting ALDH+ cells selectively.

To identify pharmacological agents that potentiate ALDH+ cell centrosome microtubule-nucleation, we evaluated a small molecule panel's impact on centrosome-nucleation using MT regrowth assay **(M3-fig. 2F)**. Our previous findings found that NEDD9 overexpression in ALDH+ cells distinguished centrosome regulation between these two cell populations. Since NEDD9, a scaffolding protein, cannot be directly drugged, our compound panel instead consisted of inhibitors targeting AURKA (Alisertib), FAK (PF-573228), and SRC (PP2) as these oncogenic kinases directly bind NEDD9. We further expanded our panel to include CW069 - an HSET inhibitor known to hinder centrosome clustering, Vandetanib [56], and Cabozantinib [57] (broad tyrosine kinase inhibitors - a class of compounds that show efficacy in inhibiting ATC), two small molecules which targeted canonical stem cell signaling pathways: IPW-2 (Wnt signaling inhibitor) and

RO4929097 (Notch signaling inhibitor), and lastly, two chemotherapy drugs cisplatin and paclitaxel.

In contrast to most small molecules in this panel that failed to affect MT nucleation, the small molecule "Reversine" was shown to be an exceptionally potent inducer of centrosome microtubule-nucleation (**M3-fig. 2G**). Reversine is a promiscuous agent that targets several notable kinases, including SRC, FAK, Aurora A, Jak2, and Mek1 [58,59] [58,59]. Chemically selective agents against AURKA (Alisertib) or FAK (PF-573228) partially recapitulated the effects of Reversine while small molecules targeting SRC (PP2), Jak2 (XL019) [60], or Mek1/2 (U0126) [61] showed no effect on centrosome microtubule-nucleation (**M3-fig. 2G**).

To improve Reversine's effects on ATC centrosomes, we chemically synthesized Reversine analogs with modifications to its side chains, intending to improve its inhibitory activity towards AURKA and FAK. By screening our library of analogs for their relative impact on MT growth, we identified one analog "MEAP" ((2-(4-Morpholinoanilino-6-[(2-exo-norbornyl)amino]-purine) (M3-fig. 2E) whose in vitro kinase inhibitory profiling show higher AURKA/FAK inhibitory efficiency compared to Reversine (**M3-fig. S2A**). Via MT regrowth assay, MEAP showed significantly improved activation of centrosome MT-growth compared to Reversine (**M3-fig. 2F-G, M3-fig. S3**). Importantly, MEAP's induction of centrosome-microtubule nucleation extended to cells with supernumerary centrosomes (**M3-fig. 2H**) and thus is relevant to ATC cells with CA. These findings collectively identity the multikinase inhibitor MEAP as a potent inducer of centrosome MT-nucleation in ATC cells.

MEAP increases pericentriolar material accumulation during interphase to increase the rate of nucleated centrosomes

A key determining factor for the centrosome MT-nucleation potential during interphase is accumulated pericentriolar material such as PCNT to support the nucleation of microtubule polymers [1,62-65]. To evaluate PCM accumulation during different stages of the centrosome cycle, we co-stained the centrin1 (centriole marker) together with PCNT and measured MEAP's impact on PCM levels via fluorescence intensity.

We first examined MEAP's effects on ATC cells with the normal number of centrosomes. By controlling for centriole replication-status and distance between centrioles as a control for

stages of the centrosome cycle, we found that MEAP led to a significant increase in PCNT/γ-tubulin levels after centriole disengagement (with two singlet centrioles), with the trend continuing throughout the G1-G2 centrosome maturation stage until early mitosis; conversely, MEAP did not affect PCM levels at the end of mitosis (telophase), ruling out any effect on PCM-shedding during mitotic-exit (**M3-fig. 3A, 3B**).

Next, we assessed MEAP's impact on the PCM of supernumerary centrosomes. Specifically, we measured whether MEAP would increase the ratio of centrioles that accumulate PCNT during interphase, as PCM-deficient centrioles were a remarkable characteristic of ALDH+ ATC cells. MEAP increased the rate PCM-nucleated interphase centrioles from 23+4% to 46+9% in THJ-11T and from 18+4% to 52+6% in THJ-16T (**M3-fig. 3C, 3D**). These findings collectively indicate that MEAP promotes centrosome PCM-recruitment, resulting in an increased frequency of activated supernumerary centrosomes during interphase.

MEAP induces transient loss of pAURKA followed by increased pAURKA in ALDH+ ATC cells

A puzzling finding was that MEAP increased centrosome PCM-accumulation since it showed AURKA inhibitory activity *in vitro*; phosphorylated-AURKA (achieved via pAURKA^{288} autophosphorylation) is an important promoter of centrosome maturation [66-68]. However, as pAURKA^{288} is not dependent on its autophosphorylation alone [69], we conducted a time-course to evaluate the actual kinetics of pAURKA^{288} in ATC cells exposed to MEAP. To avoid confounding effects from cell cycle changes, which are known to influence AURKA levels [67], we first synchronized treated cells via thymidine block (**M3-fig. S4A**). We observed in ALDH+ cells, treatment with MEAP lead to a decrease in pAURKA, but this decrease was transient, and longer exposure (>2h) led to an overall increase in pAURKA compared to basal levels (**M3-fig. S4B**). Similar trends were observed in ALDH- cells but with lesser magnitude in pAURKA fluctuation. These findings suggest pAURKA levels are overall increased following MEAP treatment, consistent with the observed increase in PCM at the centrosomes.

MEAP increases spindle multipolarity and G2/M arrest selectively ALDH+ cells

One of the most common causes of cell death associated with CA is mitotic catastrophe due to unresolved spindle multipolarity [9,70]. As the centrosome's spindle forming potential is dependent on PCM accumulation during interphase, it follows that MEAP would, in principle, increase the rate of multipolar spindles during mitosis. Indeed, about one-third of centrosomes in DMSO-treated THJ-11T and THJ-16T cells showed little to no spindle forming capacity (**M3-fig. 4A**). MEAP significantly increased the percentage of centrosomes forming robust mitotic spindles, thus increasing the severity of spindle multipolarity in affected cells (**M3-fig. 4A, 4C**).

The production of two viable daughter cells following a multipolar spindle mostly depends on assembling extra spindles into a "pseudo" bipolar configuration [9-11]. It has been shown that an increase in PCM accumulation during interphase interferes with the cell's capacity to form pseudobipolar spindles [12]. On that basis, we quantified the impact of MEAP on the ratio of bipolar/pseudobipolar/multipolar spindle configuration, finding that in THJ-11T THJ-16T alike, 48h treatment with 300nM MEAP increased multipolar spindles while decreasing pseudobipolar spindles (**M3-fig. 4B, 4F**), without substantially changing the overall rate of centrosome amplification (**M3-fig. 4D**); this suggests that by potentiating the spindle forming capacity of supernumerary centrosomes, MEAP impaired pseudobipolar spindle formation; in support of this interpretation, cells in a pseudobipolar spindle configuration displayed non-polarized spindle-deficient centrosomes while cells in multipolar spindle configuration displayed exclusively centrosomes that formed robust spindles (**M3-fig. 4B**). The multipolar spindles formed in MEAP-treated cells looked structurally typically **(M3-fig. 4B)**. MEAP did not affect the rate of non-centrin1 associated pericentrin (**M3-fig. 4E**), thus ruling spindle multipolarity due to PCM fragmentation.

Given that inactive supernumerary centrosomes were significantly more prominent in ALDH+ cells (**M3-fig. 2D, 4B, 4C**), MEAP's centrosome-related effects should proportionally more impact this cell population. Indeed, the comparative analysis showed that MEAP induced significantly more spindle multipolarity in ALDH+ compared to ALDH- cells (**M3-fig. 4F**). Furthermore, a cell-cycle compartment analysis found that ALDH+ but not ALDH- cells showed G2/M accumulation after exposure to MEAP, consistent with the observed spindle multipolarity (**M3-fig. 4G**). In contrast, MEAP caused a similar degree of apoptosis **(M3-fig. 4H)** and senescence **(M3-fig. 4I)** in both cell populations, indicating that unlike spindle multipolarity and

G2/M arrest, anti-proliferative effects via apoptosis/senescence were not selective against ALDH+ cells.

MEAP selectively eliminated ALDH+ cells and suppressed ATC spherogenesis and tumorigenesis

Several former studies have established that ALDH+ ATC cells possessed elevated stemness features such as self-renewal (e.g., the capacity to form tumorsphere) and initiated tumorigenesis [39], compared to bulk tumor cells[40,41]. As MEAP showed the capacity to induce multipolar spindles and G2/M accumulation preferentially in ALDH+ cells, we assessed its ability to deplete ALDH+ cells across ATC cell lines selectively. After 96h exposure to MEAP, THJ-11T, THJ-16T, and 8505c all lost >80% ALDH+ cells compared to DMSO-treated cells. MEAP's capacity to deplete ALDH+ cells outperformed Reversine. ALDH+ cell depletion was also partially recapitulated by Aurora A/FAK inhibitors. In contrast, inhibitors against SRC, Erk, tyrosine kinases, or chemotherapy drugs cisplatin/paclitaxel showed no either no effect on %ALDH+ cells or marginally increased ALDH+ cells (**M3-fig. 5A**). We confirmed that MEAP's elimination of ALDH+ cells were due to differential impact on cell growth (**M3-fig. 5B**), that the effect was dose-dependent (**M3-fig. 5C**) and ruled out any direct effect on ALDH enzymatic activity **(M3-fig. 5D**).

To evaluate if MEAP's selectivity against ALDH+ cell growth would consequentially attenuate stemness, we pretreated ATC cells with MEAP for 96h, then allowed the cells to recover for one week before assessing the spherogenic and tumorigenic potential of the recovered cell population. MEAP dose-dependently attenuated tumorsphere formation in THJ-11T, THJ-16T, and 8505c alike (**M3-fig. 5E**). Using the same pre-treatment conditions, we performed a limiting dilution transplantation assay to measure the impact of MEAP pre-treatment on ATC tumorigenesis. $1x10^5$ DMSO-treated THJ-16T cells were capable of initiating tumors in 3/5 mice. Simultaneously, it took $5x10^5$ MEAP-treated cells to achieve the same rate of tumorigenesis, with similar trends at other numbers of injected cells, suggesting an estimated ~80% decrease in tumorigenicity (**M3-fig. 5F**). Collectively, these observations indicate that MEAP is highly selective against ALDH+ ATC cells and could attenuate ATC stemness.

MEAP selectively eliminates ALDH+cells, induces spindle multipolarity, and inhibits chromosomal instability *in vivo*

To assess the preclinical efficacy of MEAP, we tested it on a preclinical orthotopic model of ATC. $5x10^5$ 8505c cells were injected into the right thyroid of NOD-SCID mice on day 0; mice were given 3-dosage of treated DMSO (Vehicle), Taxol (5mg/kg), or MEAP (30mg/kg) (n=3-5) on day 15, 17, and 20 (i.p.); mice were sacrificed, and necropsy was performed on day 30. We chose the 8505c ATC model over the THJ-16T since 8505c ATC cells had a higher take-rate (100% versus 75%) [71]. Via immunohistochemical staining, ALDH1-positive clusters were observed in both vehicle and taxol-treated 8505c tumors that were ablated in MEAP-treated tumors, indicating that MEAP's selectivity against ALDH+ cells can be recapitulated *in vivo* (**M3-fig. 6A**). γ-tubulin staining revealed that, analogous to our cell-based results, MEAP-treatment reduced asymmetry in γ-tubulin between the centrosome pairs **(M3-fig. 6B, C).** MEAP also significantly increased the frequency of multipolar spindles compared to DMSO or taxol-treated cells (**M3-fig. 6B, 6D**), again consistent with our cell-based findings. Additionally, hematoxylin and eosin staining (H&E) showed that MEAP reduced the rate of apparent chromosomal missegregation in anaphase/telophase cells (**M3-fig. 6E**). Since cell division in centrosome-amplified cells is a primary cause of chromosomal instability, this further supports the notion that MEAP induces mitotic catastrophe by hampering the mitosis of ATC cells with CA [72].

Lastly, we sought to test if administering MEAP against an already established ATC tumor would impair its growth. As orthotopic ATC models show high growth rate variance, we implanted ATC cells subcutaneously into NOD-SCID mice to evaluate MEAP's impact on tumor growth. When tumors became palpable, mice (n=8) were treated intraperitoneally with the vehicle, MEAP (30mg/kg), or Taxol (5mg/kg; a control for non-selective chemotherapy). 4 weeks of MEAP treatment (30mg/kg, three times per week) led to a 4-fold decline in growth of subcutaneously implanted 8505c tumors (**M3-fig. 6F-G**), without any sign of side effects or bodyweight loss (**M3-fig. 6H**), and outperforming 5mg/kg of Taxol. Taken together, our findings indicate that MEAP shows promising anti-tumoral effects associated with a reduction of tumor stemness, tumorigenesis, and growth potential without obvious host toxicity in the preclinical animal model tested.

Discussion

In this study, we illustrate a novel approach to eliminating tumorigenic ALDH+ ATC cells by exploiting the unique centrosome characteristics of these stem-like cells. We show that MEAP can potently induce centrosome maturation of supernumerary centrosomes that otherwise would be inactive; furthermore, we show that MEAP increased the severity of spindle multipolarity by increasing the rate of centrosome that can form a robust spindle during mitosis. As the successful formation of pseudobipolar spindles is generally observed alongside partially inactivated centrosomes, our findings overall propose that MEAP, by promoting supernumerary centrosome maturation, impairs the ability of cells to resolve spindle multipolarity, result in mitotic catastrophe. Our findings are consistent with previous studies showing that mitotic catastrophe could induce centrosome activation via inhibiting CPAP-tubulin interaction [12]. Here, we further show that this strategy of inducing centrosome activation in ATC was primarily effective against ALDH+ cells. This cell population is enriched in PCM-deficient or "inactive" centrosomes during interphase and thus is most affected by the PCM-inducing effect of MEAP. As such, MEAP selectively eliminated ALDH+ cells, resulting in overall attenuated stemness.

MEAP's identity as a multikinase inhibitor to some extent limits the conclusions that can be drawn at a molecular level. However, strong clues indicate its inhibition of Aurora-A to be predominantly responsible for any centrosome-related effects observed in this study[44-54]. Firstly, MEAP's effects were partially recapitulated by the Aurora-A selective inhibitor Alisertib. Secondly, Aurora A's is a known master regulator of centrosome maturation, particularly during interphase [66-68]. Lastly, Aurora-A is a canonical binding partner of NEDD9, consistent with the effects of MEAP being selective against ALDH+ cells which have upregulated NEDD9 [44-54]. However, we showed that despite being an AURKAi inhibitor *in vitro*, prolonged exposure to MEAP induces pAURKA[288] in ALDH+ cells, which highlighted an unexpected biological response. Our results do not exclude additional anti-proliferative effects from inhibiting other targets such as Aurora Kinase B, Jak2, or SRC.

The centrosome activation effect of MEAP may, by extension, offer insight into the still-unknown mechanistic basis for the synergistic effect between Aurora Kinase A inhibition and antimicrotubule inhibitors in ATC [73] as the increased severity of spindle multipolarity caused by

MEAP/Aurora-A inhibition would, in principle, augment the microtubule-stabilizing effects of paclitaxel in driving ATC cells to mitotic catastrophe.

In conclusion, our findings reveal a novel approach to eliminating tumorigenic ALDH+ thyroid cancer cells [39] [40,41] by targeting their inactivated supernumerary centrosomes. The observation that tumor tissues from ATC patients show a high proportion of cells with supernumerary and poorly nucleated centrosomes supports the targeting of centrosome activation as a strategy with clinical applications. The asymmetrical centrosome behavior in ATC stem-like cells is reminiscent of the asymmetrical stem cell behavior observed in models such as *Drosophila* germline stem cells, as they do share the similarities of having only one of the centrosome pair (or ~half the total centrosomes, in the case of cells with supernumerary centrosomes) accumulating PCM during interphase [17-19]. If this analogy holds in other cancer models, this approach could potentially be broadly extrapolated this approach may be a broadly relevant option for management of advanced malignancies that also frequently exhibit both elevated stemness and CA[4,15,72,74-76].

Figures

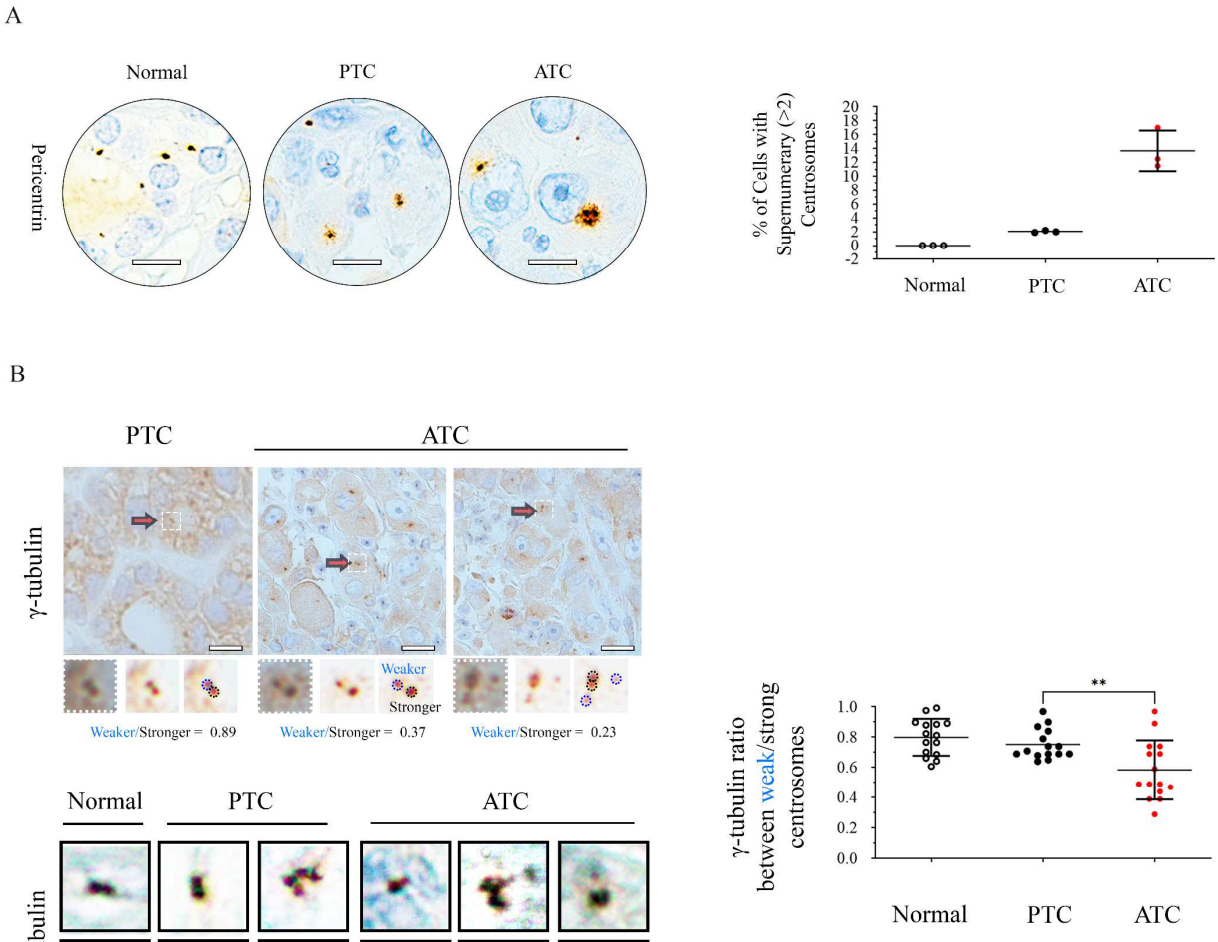
A
Normal
PTC
ATC
Pericentrin
% of Cells with Supernumerary (>2) Centrosomes
20
18
16
14
12
10
8
6
4
2
0
-2
Normal
PTC
ATC
B
PTC
ATC
γ-tubulin
Weaker
Stronger
Weaker/Stronger = 0.89
Weaker/Stronger = 0.37
Weaker/Stronger = 0.23
Normal
PTC
ATC
γ-tubulin
γ-tubulin ratio between weak/strong centrosomes
**
1.0
0.8
0.6
0.4
0.2
0.0
Normal
PTC
ATC

M3-Figure 1: Anaplastic thyroid cancer patient tissues contain γ-tubulin-deficient supernumerary centrosomes

A. Images: Representative image of pericentrin IHC staining in normal, papillary thyroid cancer, and anaplastic thyroid cancer patient samples (original magnification 100x). The arrow depicts centrosome amplification in patient samples (n=3; each data point represents the average quantification from 4 randomly captured image fields of the same sample). **B.** Images: Representative immunohistochemistry images of γ-tubulin staining in papillary (n=5) and anaplastic thyroid cancer patient (n=5) tissues. Graph: Quantification of centrosome nucleation asymmetry measured by the relative intensity of γ-tubulin-positive dots (weak/strong). At least ten centrosome pairs from each patient sample were assessed. The formula used for cells with >2 centrosomes was (sum of weaker 50th percentile/sum of stronger 50th percentile). To ensure cell cycle parity, only centrosomes of equal distance are measured. IHC images were taken using Leica DM LB2 at the noted magnification. ATC: anaplastic thyroid cancer. PTC: papillary thyroid cancer. Statistical significance was determined using two-tailed Student's t tests. **P<0.01

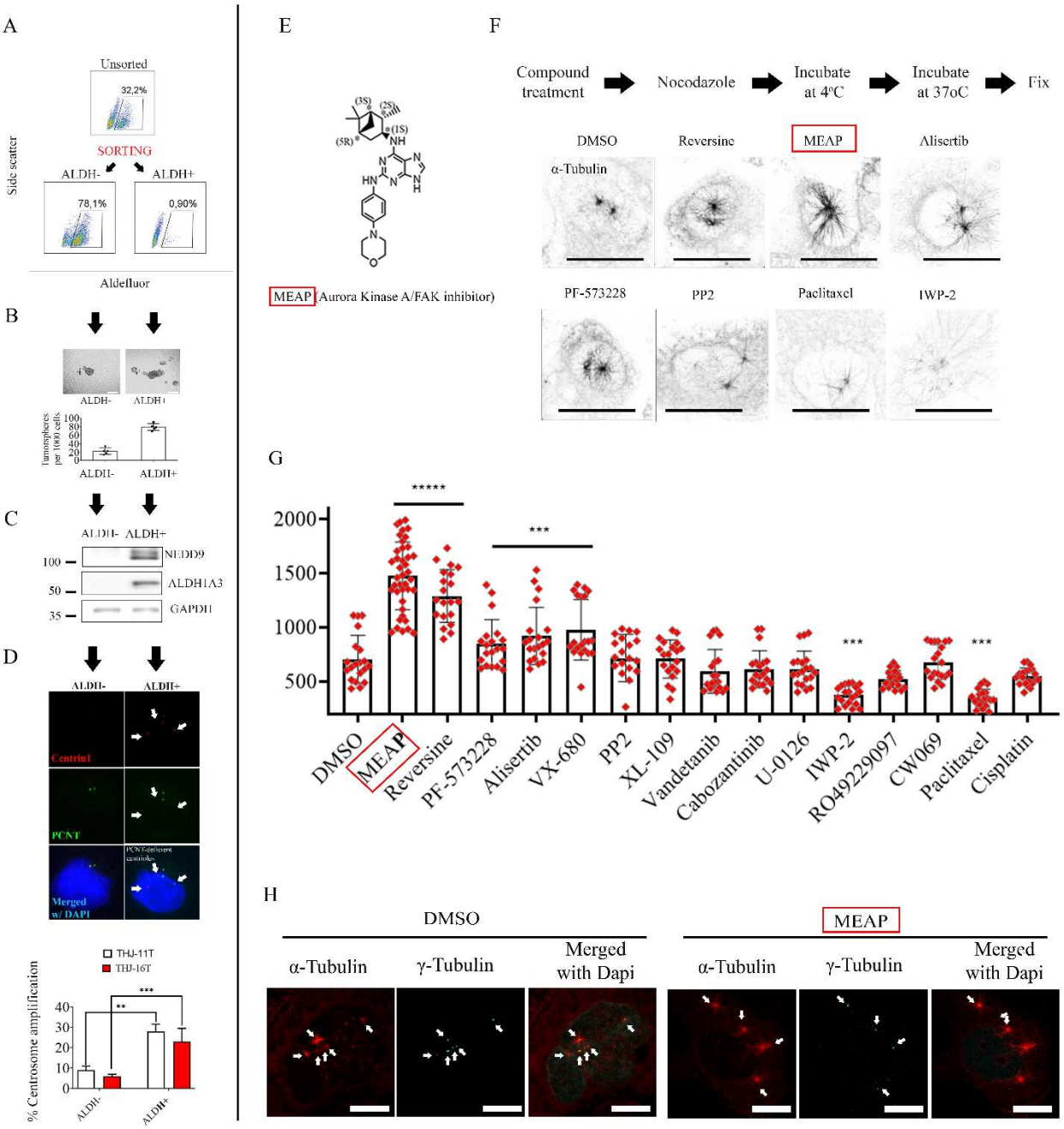
A
Unsorted
32,2%
SORTING
ALDH-
ALDH+
78,1%
0,90%
Side scatter
Aldefluor
B
ALDH-
ALDH+
Tumospheres per 1000 cells
ALDH-
ALDH+
C
ALDH- ALDH+
100
50
35
NEDD9
ALDH1A3
GAPDH
D
ALDH-
ALDH+
Centrin1
PCNT
Merged w/ DAPI
THJ-11T
THJ-16T
% Centrosome amplification
ALDH-
ALDH+
E
MEAP (Aurora Kinase A/FAK inhibitor)
F
Compound treatment
Nocodazole
Incubate at 4°C
Incubate at 37oC
Fix
DMSO
Reversine
MEAP
Alisertib
α-Tubulin
PF-573228
PP2
Paclitaxel
IWP-2
G
DMSO
MEAP
Reversine
PF-573228
Alisertib
VX-680
PP2
XL-109
Vandetanib
Cabozantinib
U-0126
IWP-2
RO49229097
CW069
Paclitaxel
Cisplatin
H
DMSO
MEAP
α-Tubulin
γ-Tubulin
Merged with Dapi

M3-Figure 2: Identification of a small molecule MEAP that can activate γ-tubulin-deficient supernumerary centrosomes found primarily in ALDH+ ATC cells

A. Sorting of THJ-16T ATC cells by ALDH status using aldefluor staining via fluorescence-activated cell sorting panels and immunofluorescent imaging. For post-sorted immunofluorescent images, a single sorted ALDH+ or ALDH- cells was imaged on days 2 and 7 using aldefluor assay showing that once sorted, ALDH+ cells over time recapitulate ALDH+/- heterogeneity while ALDH- cells mainly generate only ALDH- progenies (arrows indicate ALDH- cells generated through divisions of ALDH+ cells). **B.** Relative tumorsphere forming potential of ALDH+ and ALDH- sorted THJ-16T cells. 150 cells were seeded in polyhema-coated plates in tumorsphere growing media (DMEM/F12 +EGF + B27). Images were taken after seven days, using 10x magnification; bright-field microscopy was used to count spheres over 50um C for quantification**.** Western blot of ALDH1A3 and NEDD9 in sorted THJ-16T cells. **D.** Representative image and quantification of centrosome amplification in ALDH- and ALDH+ sorted ATC cells. Centrosome amplification is defined as cells with >4 centrioles; note how in ALDH+ cells, centrioles are frequently devoid of PCNT staining, indicative of inactivated centrosomes. **E.** Chemical structure of MEAP (2-(4-Morpholinoanilino-6-[(2-exo-norbornyl). **F.** Experimental scheme of microtubule regrowth assay and representative images of microtubule regrowth of cells fixed 1-minute following nocodazole washout. Grayscale α-tubulin images were color-inverted for visual clarity. **G.** Quantification of relative centrosome microtubule-nucleation activity in compound-treated cells based on the intensity of tubulin staining. **H.** Representative images of microtubule regrowth in DMSO or MEAP-treated THJ-16T cells possessing supernumerary centrosomes. Note how DMSO-treated cells possess supernumerary centrosomes with poor capacity for microtubule-nucleation, while MEAP-treated supernumerary centrosomes showed strong microtubule-nucleating potential. Error bars represent $\pm$ SD, $^{**}P<0.01$, $^{***}P<0.001$, *****P<0.00001

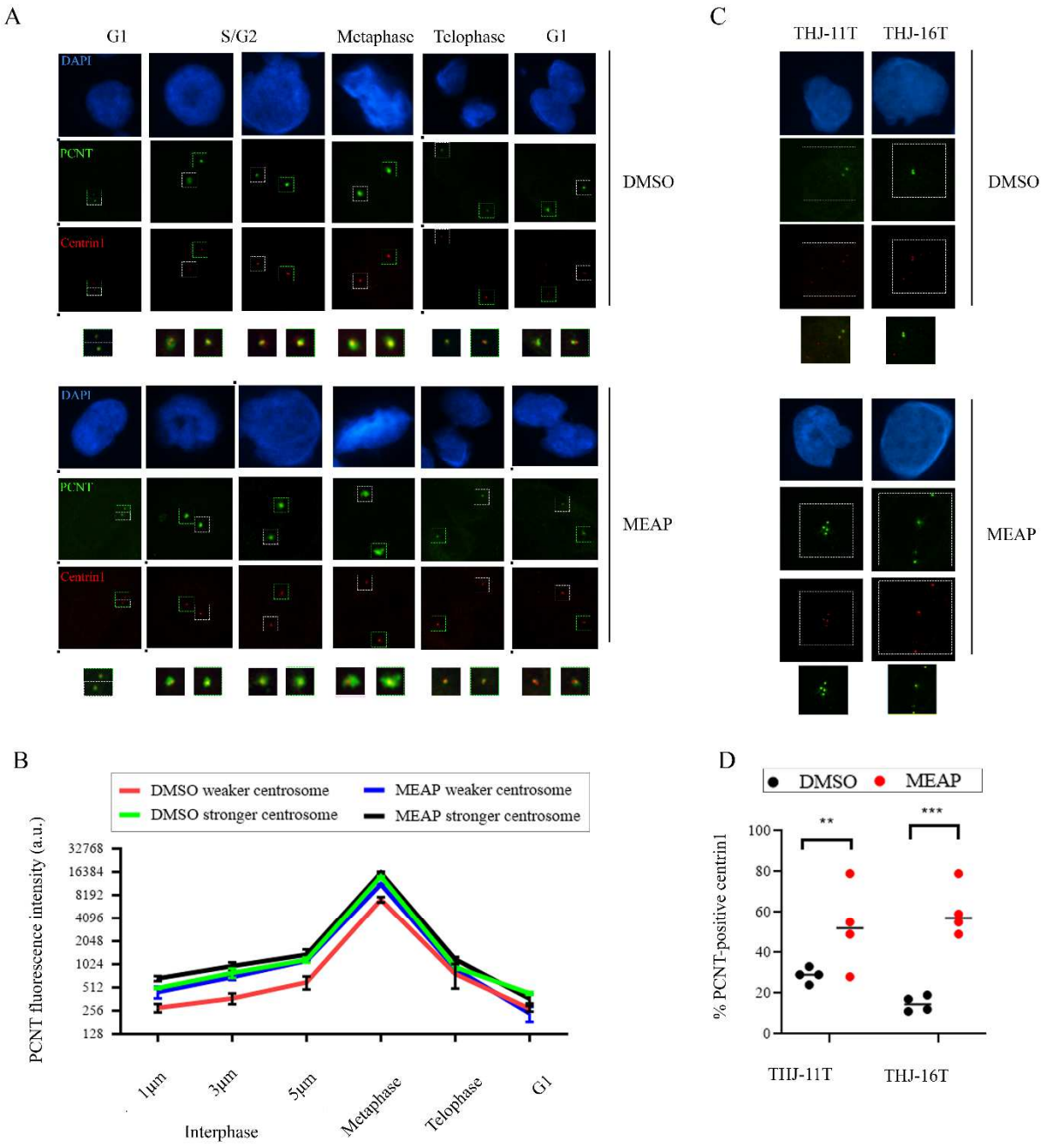
A
G1
S/G2
Metaphase
Telophase
G1
DAPI
PCNT
Centrin1
DMSO
MEAP
C
THJ-11T
THJ-16T
DMSO
MEAP
B
DMSO weaker centrosome
DMSO stronger centrosome
MEAP weaker centrosome
MEAP stronger centrosome
PCNT fluorescence intensity (a.u.)
32768
16384
8192
4096
2048
1024
512
256
128
1μm
3μm
5μm
Metaphase
Telophase
G1
Interphase
D
DMSO
MEAP
% PCNT-positive centrin1
100
80
60
40
20
0
**
***
TIIJ-11T
THJ-16T

M3-Figure 3: MEAP induces pericentriolar material accumulation at inactivated centrosomes during interphase

A. Representative image of centriole (centrin1) and pericentriolar material (pericentrin; PCNT) co-staining in THJ-16T cells with a normal number of centrosomes. Note how one of the two centrosome pairs in DMSO-treated cells is relatively deficient in pericentrin-staining during interphase. In contrast, in MEAP-treated cells, the centrosome pairs are more evenly nucleated. The cell cycle is estimated using the distance between the two centrosome pairs and whether the centriole is duplicated (only the first and last columns shows pre-duplication centrioles) to ensure parity between DMSO and MEAP-treated cells **B**. Quantification of PCNT fluorescence intensity at each of the two centrosomes/centriole to illustrate that MEAP predominantly increased the PCNT levels at the "weaker" of the two centrosomes. The interphase centrosome is quantified based on the distance between the two centrosomes. Quantification was done in ImageJ by drawing a 2.5um line through the center of one or two centrosomes then using the "plot profile" function of Fiji/ImageJ software to measure the integrated area after subtracting the background. For quantification involved three biological replicates in which 25 cells were scored for each condition in each repeat. **C.** Representative image of centriole (centrin1) and pericentriolar material (pericentrin; PCNT) co-staining in THJ-11T and THJ-16T cells with supernumerary centrosomes. Note how DMSO-treated cells exhibit PCNT-free centrioles while MEAP-treated cells show mostly centrioles that acquired PCNT. **D.** Quantification of the impact of MEAP on the % of centrioles that show visible PCNT accumulation. At least 25 cells with centrosome amplification were scored per experiment, n=3 biological replicas. Error bars represent $\pm$ SD, $^{**}P<0.01$, $^{***}P<0.001$

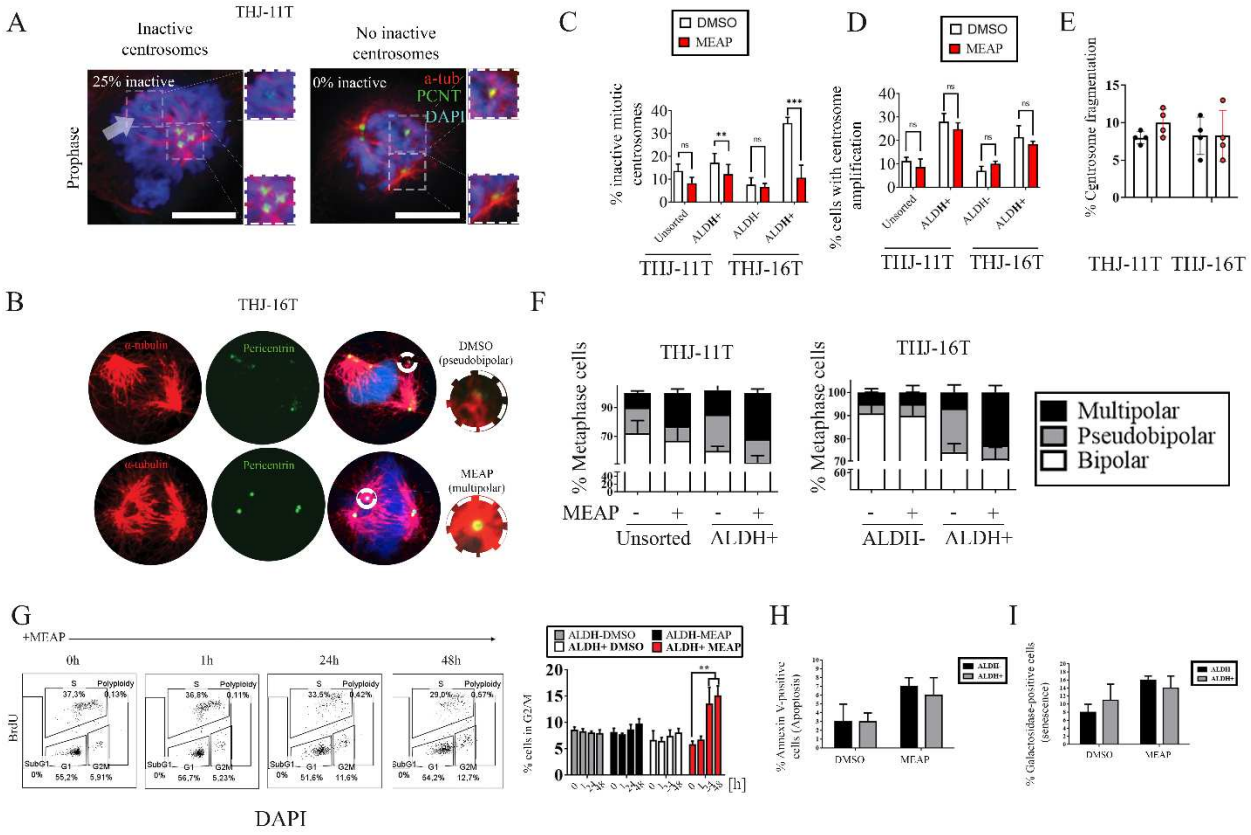
A
THJ-11T
Inactive centrosomes
No inactive centrosomes
25% inactive
0% inactive
a-tub
PCNT
DAPI
Prophase
B
THJ-16T
α-tubulin
Pericentrin
DMSO (pseudobipolar)
MEAP (multipolar)
C
DMSO
MEAP
% inactive mitotic centrosomes
Unsorted
ALDH+
ALDH-
ALDH+
THJ-11T
THJ-16T
D
DMSO
MEAP
% cells with centrosome amplification
Unsorted
ALDH+
ALDH-
ALDH+
THJ-11T
THJ-16T
E
% Centrosome fragmentation
THJ-11T
THJ-16T
F
THJ-11T
THJ-16T
% Metaphase cells
MEAP
Unsorted
ALDH+
ALDH-
ALDH+
Multipolar
Pseudobipolar
Bipolar
G
+MEAP
0h
1h
24h
48h
BrdU
DAPI
H
% Annexin V-positive cells (Apoptosis)
DMSO
MEAP
I
% Galactosidase-positive cells (senescence)
DMSO
MEAP

M3-Figure 4: MEAP preferentially induces multipolar spindles and G2/M arrest in ALDH+ ATC cells

A. Representative image of an "inactive" centrosomes observed in ALDH+ cells at mitosis, defined as centrosomes which are visibly devoid of spindle-forming capacity. Cell model represented is THJ-11T. **B.** Representative images of a pseudobipolar and multipolar spindle in THJ-16T cells with supernumerary centrosomes. **C.** Quantification of the ratio of cells with supernumerary centrosomes (>2 centrosomes). Sorted cells were treated with DMSO or 300nM MEAP for 48h. **D.** Quantification of % inactivated centrosomes during mitosis (represented in panel A). Sorted cells were treated with DMSO or 300nM MEAP for 48h. **E.** Impact of MEAP on centrosome fragmentation (defined as % of pericentrin-positive structures lacking centrin1). **F.** quantification of spindle configuration in ALDH+ cells treated with DMSO or MEAP. Pseudobipolar spindles are defined as >2 centrosomes assembled into two spindle poles, and multipolar spindles were defined as >2 centrosomes assembled into >2 spindle poles(represented in panel B) **G.** Representative flow cytometry panel and quantification of BrDU/DAPI cell cycle compartmentalization assay of sorted THJ-16T cells treated with 300nM MEAP or DMSO. Treated cells were harvested at the indicated timepoints. n=3 biological replicates **H.** Quantification of PI/Annexin V apoptosis assay of sorted THJ-16T cells treated with MEAP. n=3 biological replicates. **I.** Quantification of beta-galactosidase senescence assay of sorted THJ-16T cells treated with MEAP. n=3 biological replicates. Error bars represent $\pm$ SD, $^{**}P<0.01$, $^{***}P<0.001$

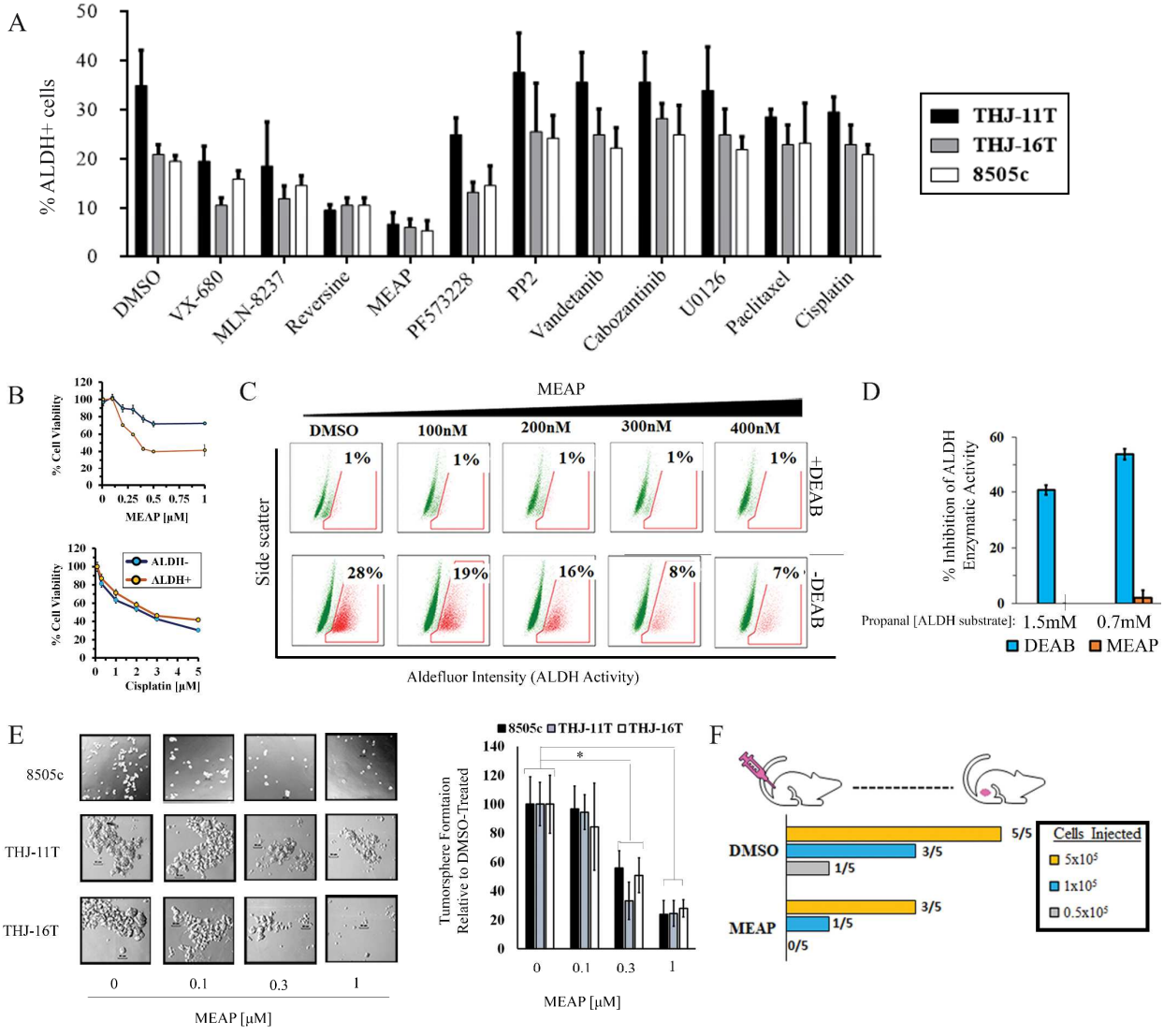
A
% ALDH+ cells
50
40
30
20
10
0
DMSO
VX-680
MLN-8237
Reversine
MEAP
PF573228
PP2
Vandetanib
Cabozantinib
U0126
Paclitaxel
Cisplatin
THJ-11T
THJ-16T
8505c
B
% Cell Viability
MEAP [μM]
ALDH-
ALDH+
Cisplatin [μM]
C
MEAP
DMSO
100nM
200nM
300nM
400nM
1%
28%
19%
16%
8%
7%
+DEAB
-DEAB
Side scatter
Aldefluor Intensity (ALDH Activity)
D
% Inhibition of ALDH Enzymatic Activity
Propanal [ALDH substrate]:
1.5mM
0.7mM
DEAB
MEAP
E
8505c
THJ-11T
THJ-16T
0
0.1
0.3
1
MEAP [μM]
8505c
THJ-11T
THJ-16T
Tumorsphere Formtaion Relative to DMSO-Treated
MEAP [μM]
F
DMSO
MEAP
5/5
3/5
1/5
3/5
1/5
0/5
Cells Injected
5x10⁵
1x10⁵
0.5x10⁵

M3-Figure 5: MEAP selectively eliminates ALDH+ ATC cells and attenuates spherogenic and tumorigenic potential

A. Quantification of the impact of small molecules (300nM) on the ratio (%) of cells expressing the cancer stem-like cell marker ALDH+ in three anaplastic thyroid cancer models **B.** Proliferation assay illustrating that MEAP's selectivity against ALDH+ cells is due to differential effects on ALDH+ versus ALDH- cell growth, where cisplatin is used as control **C.** Dose responsive inhibition of the %ALDH+ cell population in THJ-16T ATC cells after 72h treatment of MEAP, where the addition of the ALDH enzymatic inhibitor "DEAB" is used to establish background levels. **D.** Impact of MEAP on ALDH enzymatic assay. Propanal is added to a cell mixture together with MEAP, DEAB, or DMSO. Reaction inhibition is measured by total NAD+ reduction in MEAP or DEAB (positive control) treated compared to DMSO (negative control); decreasing dose of substrate is for assessing competitive inhibition (n=2). **E.** Representative image and quantification of the impact of MEAP on tumorsphere formation in several ATC cell lines. 1000 cells were seeded in polyhema-coated plates in tumorsphere growing media (DMEM/F12 +EGF + B27). Images were taken after 7 days, using 10x magnification; for quantification, bright-field microscopy was used to count spheres over 50um. Quantification is normalized to DMSO-treated for each cell line. **F.** Limiting dilution transplantation assay to measure the impact of MEAP pre-treatment on ATC cell tumor seeding potential *in vivo*. Cells recovered for 5 days after pre-treatment. Three series dilution of THJ-16T ($5x10^5$, $1x10^5$ and $0.5x10^5$ cells, n=5 for each dilution) was injected into the right flank of NOD-SCID mice. Tumor growth was assessed by palpitation and examined by necropsy after 35 days. Error bars represent $\pm$ SD, $*P<0.05$, $**P<0.01$

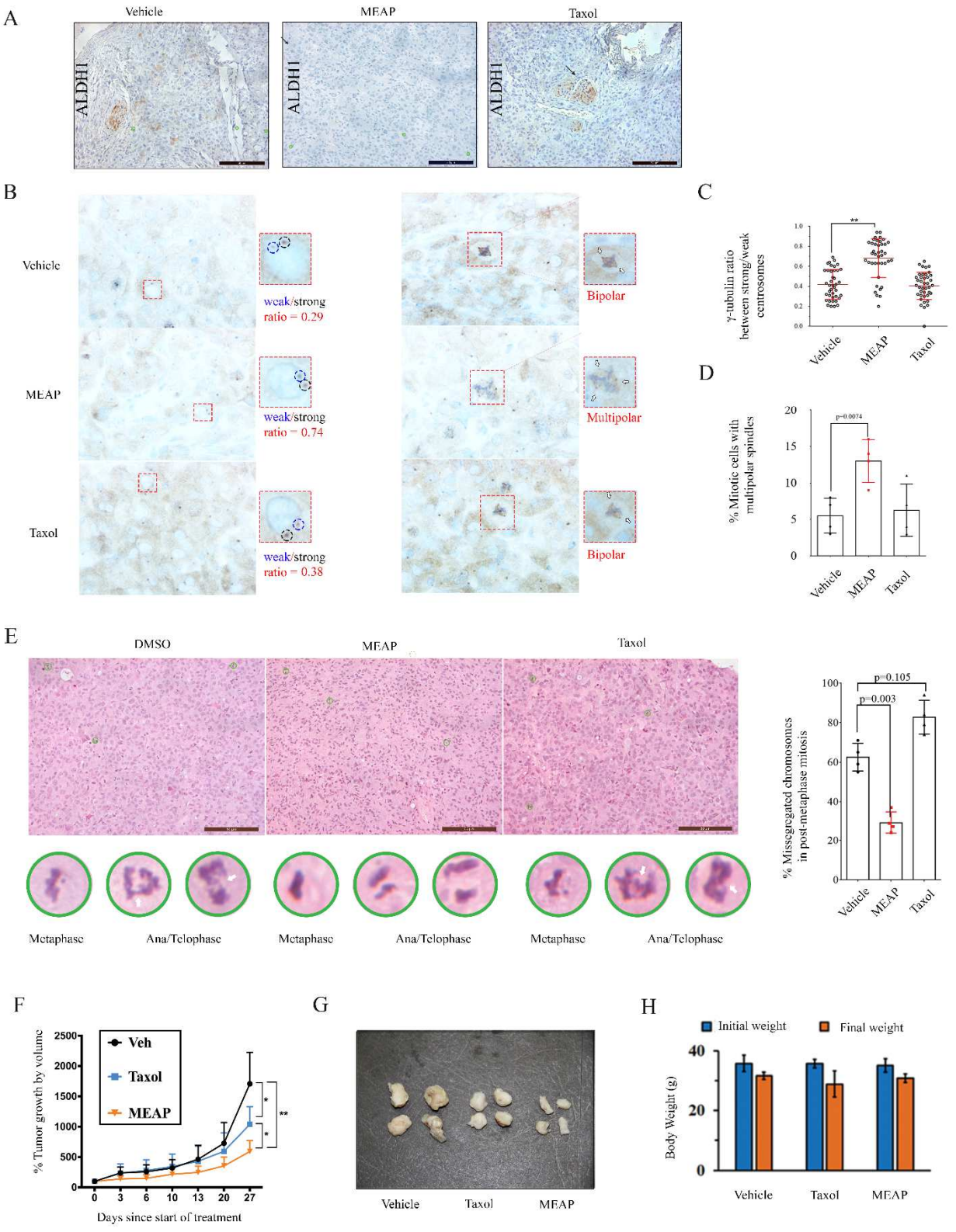
A
Vehicle
MEAP
Taxol
ALDH1
B
Vehicle
MEAP
Taxol
weak/strong ratio = 0.29
weak/strong ratio = 0.74
weak/strong ratio = 0.38
Bipolar
Multipolar
Bipolar
C
γ-tubulin ratio between strong/weak centrosomes
**
Vehicle
MEAP
Taxol
D
% Mitotic cells with multipolar spindles
p=0.0074
Vehicle
MEAP
Taxol
E
DMSO
MEAP
Taxol
Metaphase
Ana/Telophase
Metaphase
Ana/Telophase
Metaphase
Ana/Telophase
% Missegregated chromosomes in post-metaphase mitosis
p=0.105
p=0.003
Vehicle
MEAP
Taxol
F
% Tumor growth by volume
Veh
Taxol
MEAP
Days since start of treatment
G
Vehicle
Taxol
MEAP
H
Initial weight
Final weight
Body Weight (g)
Vehicle
Taxol
MEAP

M3-Figure 6: MEAP eliminates ALDH+ ATC cells, increases PCM levels, induces spindle multipolarity, and reduces chromosomal instability *in vivo*

A-E. Orthotopic model; $5x10^5$ 8505c cells were injected into the right thyroid of NOD-SCID mice on day 0; mice were given 3-dosage of treated DMSO (Vehicle), Taxol (5mg/kg) or MEAP (30mg/kg) (n=3-5) on day 15, 17, and 20 (i.p.); mice were sacrificed, and necropsy was performed on day 30. ALDH1 appeared as localized clusters in DMSO/Taxol-treated tumors which are absent in MEAP-treated tumors. **A.** Bright-field images immunohistochemical (IHC) staining of ALDH1 staining in primary thyroid tumor. IHC images were taken using Leica DM LB2 at the noted magnification. **B.** IHC staining of γ-tubulin in 8505c xenografts treated with DMSO, taxol (5kg/mg) or MEAP (30mg/kg).C**.** symmetry quantification, ten centrosome pairs from each mouse was assessed. Symmetry is measured by comparing the relative intensity of γ-tubulin staining between centrosome pairs (weak/strong). To ensure cell cycle parity, only centrosomes of equal distance are measured. **D.** Spindle multipolarity quantification. For spindle multipolarity, at least 50 mitotic cells from each mouse were evaluated (n=4). **E.** *Images: Representative images representing chromosomal missegregation in 8505c xenografts, observed by H&E staining. Graph.* Missegregated chromosome quantification. Based on H&E images (10 random fields per mice, n=4 for each group), quantification was done for the rate of mitotic cells exhibiting chromosome missegregation (lagging chromosomes or chromosome bridges). At least 50 mitotic cells from each mouse were evaluated (n=4). **F-H**. Subcutaneous model; 1×10^6 8505c cells were implanted subcutaneously into NOD-SCID mice. Treatment started once the tumor reached 40-80mm^3; animals were treated three times a week (i.p.) with DMSO, Taxol (5mg/kg), or MEAP (30mg/kg) (n=8). **F.** Tumor size change curve of subcutaneous growth; **G**: representative images of subcutaneous tumors were taken after necropsy. **H.** Initial and final body weights of animals from the subcutaneous model. Error bars represent ± SD. Statistical significance was determined using two-tailed Student's t-tests (*P<0.05, **P<0.01, ***P<0.001). MEAP: 2-(4-Morpholinoanilino-6-[(2-exo-norbornyl).

Supplemental figures

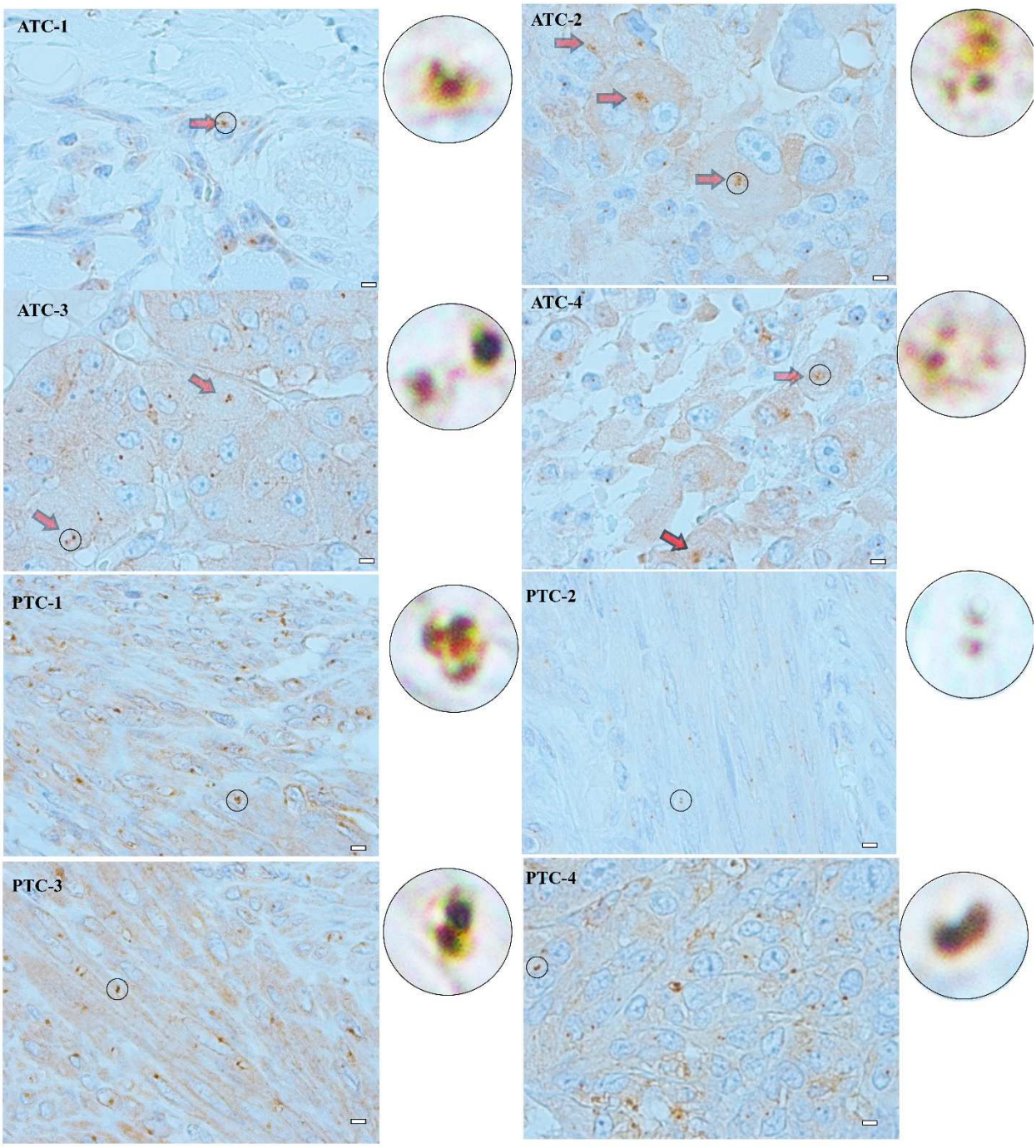

M3-Figure. S1: Additional representative images of γ-tubulin staining in papillary and anaplastic thyroid cancer patient samples. Original magnification: 100x. Scale bar = 10μm. The red arrows indicate the presence of highly asymmetrical centrosomes.

A

SelectScreen kinase profiling results (100nM)

	Reversine	MEAP
AKT1	-	-
Aurora A	+	+++
Aurora B	+	++
Aurora C	+	++
b-RAF	-	-
EEF2K	-	-
EGFR (ErbB1)	-	-
FGFR1	-	-
FLT1 (VEGFR1)	-	-
FRAP1 (mTOR)	-	-
GSK3A	-	-
GSK3B	-	-
IGF1R	-	-
LCK	+	++
cMet	-	-
PDGFR alpha	-	-
PIK3R1	-	-
PKC alpha	-	-
PTK2 (FAK)	+	++
SRC	++	++
SYK	+	++
TGFBR1	-	-
YES1	+	++

B

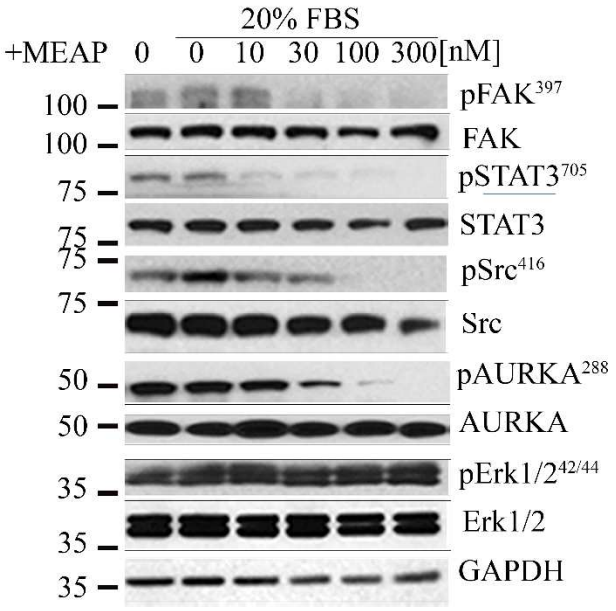

M3-Figure. S2: MEAP is a multikinase inhibitor which inhibits NEDD9-interactors Aurora Kinase A and FAK at a superior potency compared to Reversine:
A. *In vitro* kinase inhibitory profile of MEAP and Reversine, using the SelectScreen service offered by ThermoFisher -: between 0 – 50% inhibition, +: between 51-70% inhibition, ++: between 71-80% inhibition, +++: Between 81 – 100% inhibition **B.** Western blot illustrating the impact of escalating doses of MEAP (treated for 1h) on kinase activation in ALDH+ cells. Note that lower dosage was required to achieved pSTAT3^{705} inhibition under these conditions compared to other kinases.

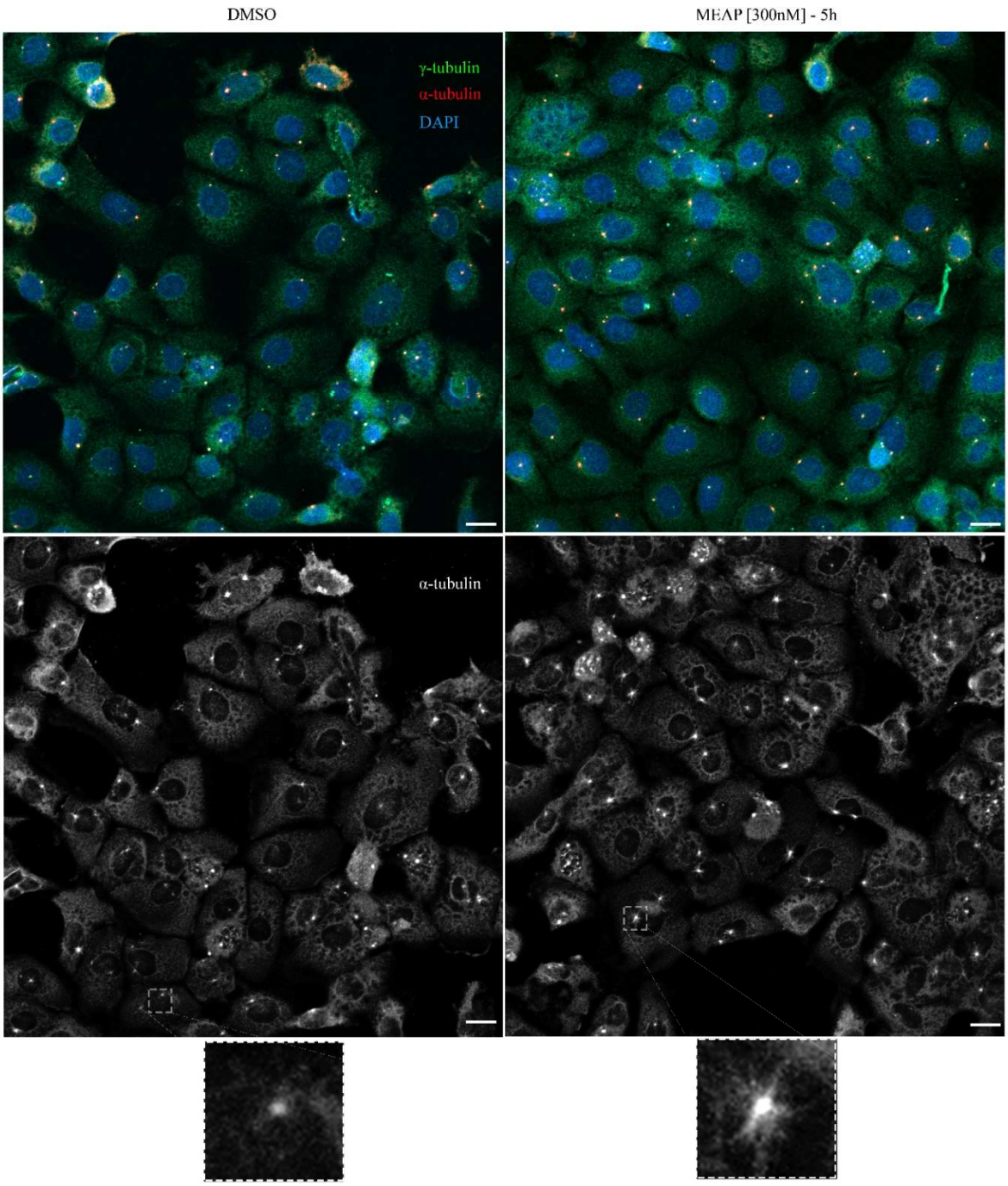

Figure M3-S3: Additional low magnification of MEAP-induced centrosome-microtubule growth. THJ-16T ALDH+ cells were treated with DMSO or MEAP 6 hours before induction of microtubule regrowth and were subsequently fixed and stained for microtubule growth. MT growth was compared between cells where the centrosomes were of similar distances apart and the chromosomes had yet to begin condensing to ensure cell cycle parity.

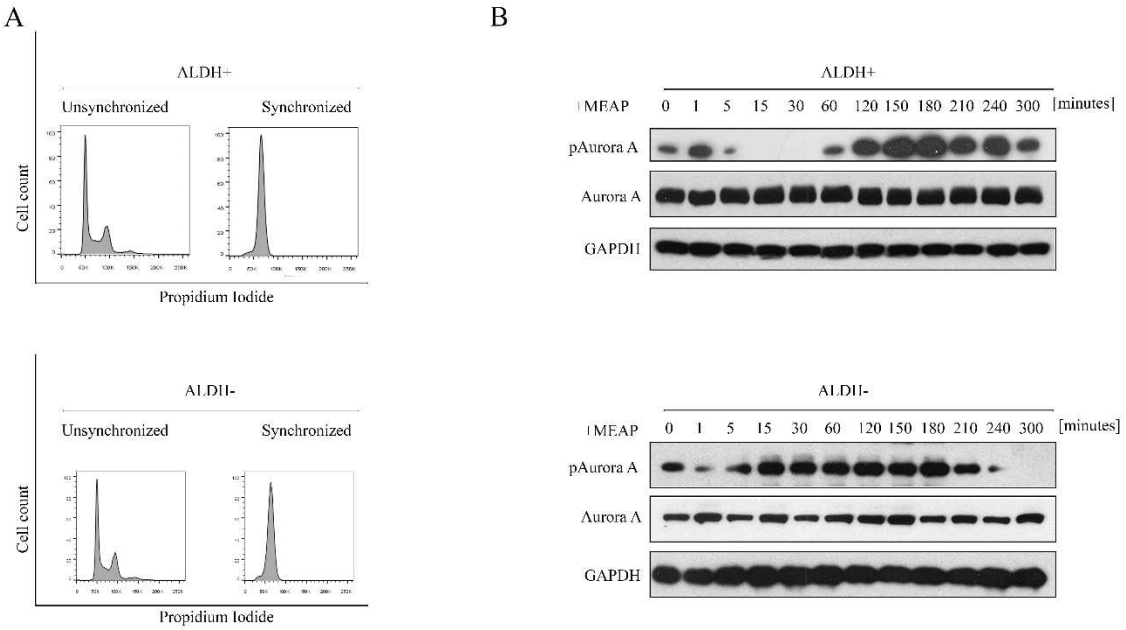

Fig. M3-S4: Impact of MEAP on pAURKA^{288} kinetics in cell cycle synchronized cells. A. Representative flow cytometry panel illustrating the synchronization of sorted THJ-16T cells using double-thymidine block, such that the effect of MEAP on pAURKA levels can be evaluated while minimizing the impact of cell-cycle differences on AURKA levels **B.** Kinetics of pAURKA levels following treatment with 300nM of MEAP. Sorted cells were treated with MEAP for the indicated duration. GAPDH is used as a loading control.

Materials and Methods:

Human study population and tissue microarray: This was a retrospective cohort study approved by the Research Ethics Committee of the Jewish General Hospital – McGill University (Montreal, QC, Canada) through the protocol 13-093. The methods and experimental protocols of the present study were performed in accordance with the approved guidelines and informed consent was obtained from all human participants. Two sets of tissue samples were used: the 8 - patient cohort, with ATC samples, and the 169-patient cohort (Supplementary Table 2, including 13 benign thyroid tumors and 156 papillary thyroid cancer), with surgical samples for immunohistochemistry staining. The inclusion criteria were as follows: (a) (a) location of the tumor in the thyroid; (b) availability of surgical specimens in FFPE blocks; (d) treatment in single Institution; (e) no recurrence or distant metastasis in the moment of the diagnosis. The information collected from the medical records included the following: gender; age; subtype, variant, and laterality. Stained H&E histological slides were evaluated by two pathologists (AS, SDS).

Core biopsies were extracted from previously defined areas using a Tissue Microarrayer (Beecher Instruments, Inc., Sun Prairie, Wis). Tissue cores that measured 1.0 mm from each specimen were punched and arrayed in duplicate on a recipient paraffin block and tissue microarray (TMA) blocks usedfor immunohistochemistry as described earlier[81].

Immunohistochemistry: Immunohistochemistry was carried out as described earlier [82]. Incubations with the primary antibodies diluted in PBS were conducted overnight at 4°C for: anti-NEDD9 (Abcam, 1:100), anti-ALDH1A3 (Novus Biologicals, 1:250), anti-Pericentrin (Abcam, 1:5000), or anti-γ-tubulin (Abcam, 1:5000). The sections were washed and incubated with secondary antibodies (Advanced ™ HRP Link, DakoCytomation, K0690, Denmark) for 30min followed by the polymer detection system (Advanced ™ HRP Link, DakoCytomation) for 30mins at room temperature. Reactions were developed with a solution containing 0.6mg/mL of 3,3'-diaminobenzidine tetrahydrochloride (DAB, Sigma, St Louis) and 0.01% H_2O_2 and then counter-stained with Mayer's hematoxylin, dehydrated and mounted with a glass coverslip. Positive controls (a tissue known to contain the antigen under study) were included in all reactions in accordance with manufacturer's protocols. The negative control consisted in omitting

the primary antibody and incubating slides with PBS and replacing the primary antibody with matching isotype. Quantification of γ-tubulin symmetry is based on ImageJ measurements of the relative DAB intensity of each centrosome pairs, following the same formula as for immunofluorescence measurements.

Cell culture: 8505c, TPC1, and BCPAP cell lines are a courtesy of Dr. M. Trifiro (Department of Endocrinology, Jewish General Hospital, McGill University), which were purchased from DSMZ—and maintained in culture in RPMI medium supplemented with 10% heat-inactivated fetal bovine serum (Wisent) and 1% penicillin-streptomycin . MCF-10A cells were purchased form ATCC and maintained in DMEM/12 supplemented with 5% horse serum, EGF, hydrocortisone, cholera toxin, insulin, and 1% penicillin-streptomycin. THJ-11T and THJ-16T were generously provided by Dr. J. Copland (Mayo Clinic, Jacksonville, Florida). These cell lines are derived from clinic anaplastic thyroid cancer patients and confirmed to match the primary tumor sample via DNA short tandem repeat analysis[83]. They are maintained in RPMI 1640x with 5% FBS, 1x non-essential amino acids, 1mM sodium pyruvate, and 10mM HEPES.

Flow cytometry quantification of ALDH activity and sorting by ALDH-status: ALDH activity was detected using ALDEFLUOR® staining kit (StemCell Technologies). Live cells were harvested after treatment, washed once with PBS, and resuspended in ALDH assay buffer before splitting into 2 tubes, one with DEAB and one without. The cells were incubated in 100µL of assay buffer + 1ul of 300nM aldefluor reagent and 1mL of DEAB reagent for 15-40min (optimized by cell line) at room temperature. The cells were then centrifuged and re-suspended in new assay buffer + 5µL of 7-AAD. 7-AAD staining is used to exclude necrotic cells during FACS analysis. The aldefluor intensity is measured using BD FACScalibur. The samples with DEAB was measured first, followed by the matching sample without DEAB added; positivity is determined by the difference in fluorescence between +DEAB and -DEAB sample. Cell sorting by ALDH-status was conducted using the same protocol in a sterile environment, using the BD-FACSAria machine. To ensure high purification rate, we recovered only the cell population with the 20% highest or lowest Aldefluor staining respectively. Sorted cells were allowed recovery for 3 days before being re-evaluated for ALDH+ positivity.

8505C, THJ-11T, and THJ-16T were sorted based on Aldefluor activity. 8505c had basal 20-30% rate of ALDH+ cells, but intensity-wise showed poor separation of the ALDH- and ALDH+ cells, thus could not be efficiently sorted. THJ-11T had a basal 20-40% rate of ALDH+ cells and exhibited good separation of ALDH+ and ALDH- cell population, but the ALDH- cells post sorting displayed only 20% of the doubling rate compared to ALDH+ cells. THJ-16T had a basal 20-40% rate of ALDH+ cells, exhibited strong separation of ALDH+ and ALDH- cell population, and displayed relatively equal double rating between the ALDH+ and ALDH- population post sorting, which was optimal for fair phenotype studies following genetic or pharmacological perturbations.

Immunofluorescence microscopy

For immunofluorescence microscopy, cells were fixed in 4% paraformaldehyde or 100% methanol and permeabilized using 0.2% triton-X. The centrosome, mitotic spindle, and DNA was visualized using anti-pericentrin (ab4448, Abcam, 1:2000), anti-α-Tubulin (DM1A, Millipore Sigma, 1:1000), anti-γ-tubulin (GTU-88, Abcam, 1:1000), anti-γ-tubulin (EPR16793, 1:1000), and DAPI respectively. Immunofluorescence images were obtained using Quorum wave FX spinning disk (SD) confocal microscope or LSM800 Airyscan (Zeiss) confocal laser scanning microscope and analyzed using Volocity (PerkinElmer) or ImageJ.

To quantify spindle multipolarity in dividing cells, 60 or more random images across 3 biological replicas for each condition was taken at 40x or 63x magnification. At least 80 cells mitotic cells were counted per condition per replica. Representative images were captured at 63x magnification. Mitotic cells are discriminated by three criteria: chromosome condensation as visualized by DAPI, the appearance of the mitotic spindle as visualized by alpha-tubulin, and increased centrosome pericentriolar materials as visualized by pericentrin. Spindle multipolarity were identified based on the presence of >2 spindle poles radiating from distinct pericentrin foci in 1 cell. The number of declustered centrosomes is quantified as a percentage of total mitotic cells.

To quantify centrosome amplification, cells were pericentrin antibodies and visualized at 63x magnification. A cell was defined as centrosome amplified by the presence of >2 pericentrin positive dots. Images were captured using LSM800 Airyscan (Zeiss) confocal laser scanning microscope.

For centrosome proteins intensity assays, images were captured at 63x using focusing on the middle (maximal size and intensity) of an individual centrosome. Quantification was confirmed using two methods. The first is by drawing a circle around an individual centrosome in volocity software, measuring the sum integrated pixel intensity, then subtracting the background fluorescence (measured by placing a circle of the same dimension away from the centrosome). The second way is, in ImageJ, drawing a 2.5um line through the center of one or two centrosomes then using the "plot profile" function of Fiji/ImageJ software to measure the integrated area after subtracting the background. For quantification involved 3 biological replicates in which 15 cells were scored for each condition in each repeat. Cells with 2 or more than 2 centrosomes were scored separately. For cells with 2 centrosomes, only centrosome pairs less than 1μm apart, directly adjacent to the nucleus were included. Centrosome nucleation symmetry is calculated using the formula (peak intensity of weak centrosome / peak intensity of strong centrosome) for cells with 2 centrosomes, or (average peak intensity of weaker 50% of the centrosomes / average peak intensity of the stronger 50% of centrosomes) in the case of centrosome amplification.
For imaging of aldefluor activity, 1:1000 diluted aldefluor reagent in aldefluor buffer was added to cells seeded in 96 well dishes, and images were captured with a fluorescent microscope as described.

Microtubule regrowth assay

The microtubule regrowth assay was performed as previously described [86]. Fluorescence activated cell sorted THJ-16T cells was treated with shCT or shNEDD9 for 36h, then treated with nocodazole for 16h. Cells were then given cold medium and placed on ice for 90 minutes. Thereafter, microtubule regrowth was then induced by pre-warmed media and placing the cells in 37^{o}C for the indicated time (30s – 60s), when they were subsequently fixed with 4% paraformaldehyde and stained for anti-α-tubulin and anti-γ-tubulin. For compound treatments, the dose reported was at the specified time prior to the induction of microtubule regrowth.

Western-blot: Sub-confluent cells were washed 3x with PBS, lysed in RIPA buffer (50 mM Tris-HCl at pH7.5, 150 mM sodium chloride, 1% tritonX-100, 0.1% SDS, 2mM EDTA and 25mM sodium fluoride) with 1mM PMSF and protease inhibitor cocktail (Roche) on ice for 30

minutes and centrifuged at 13,000 rpm for 20 minutes. Cell lysates was mixed with SDS buffer (Tris at pH 6.8, 20% glycerol, 5% SDS, bromophenol blue and β-mercaptoethanol) and boiled for 5 min, then loaded into 8-15% SDS-PAGE gels, transferred to PDVF membranes, and blotted with the primary antibodies. The primary antibodies used were as follows: anti-NEDD9 (Cell Signaling Technology, 4044), anti-Tyr705-STAT3 (Cell Signaling Technology, 9131), anti-STAT3 (Santa Cruz Biotechnology , sc-482), anti-Tyr397-p-FAK (Invitrogen, 44-624G) anti-Tyr416-p-Src (Cell Signaling Technology, 2101), anti-Src (Millipore Sigma, 05-184) and anti-FAK (Millipore Sigma, 05-537), anti-phospho-AURKA(Thr288)/B(Thr232)/C(Thr198) (Cell Signaling Technology, 2914), anti- AURKA (Cell Signaling Technology, 14475), anti-p-S473-AKT (Cell Signaling Technology, 4060), anti-AKT (Cell Signaling Technology, 9272), anti-GAPDH (Sigma Aldrich Corporation, G9545) and anti-FLAG (Sigma Aldrich Corporation, F1804), anti-p-Thr202/Tyr204-MAPK (Cell Signaling Technology, 9101), and anti-p42/44-MAPK (Cell Signaling Technology, 9102). Secondary antibodies for Western-blot assays: anti-mouse IgG-peroxidase-conjugated (Bio-Rad Laboratories, 172-1011), anti-rabbit IgG-peroxiase-conjugated (Bio-Rad Laboratories, 170-6515).

Tumorsphere-forming assays: The tumorsphere medium was prepared with DMEM-F12 (3:1, Invitrogen) containing 2% B27 supplement (Invitrogen), and 20 ng/mL epidermal growth factor (Sigma-Aldrich). Tissue culture dishes were coated with a polyhydroxyethylmethacrylate polymer (polyHEMA, Sigma-Aldrich) to facilitate sphere formation. Briefly, polyHEMA was dissolved in 95% ethanol at 12% (w/v). A working solution was made by further dilution of 1:10 in 95% ethanol and was added to 24-well plates at 0.1mL per well. A hydrophobic surface was formed after the polyHEMA solution dried out at room temperature in a tissue culture hood. Single-cell suspensions were seeded at two dilutions of 300 and 1000 cells per well in 6-replicas. For compound-treatment, drugs were mixed with initial cell-suspension. After ten days, the number of tumorspheres (>50μm) was microscopically counted and statically analyzed. Spheres were quantified using both seeding-dilutions where possible, though dilutions in which too few (<5) or too many (>50) spheres were not used for quantification. Representative images are generated from the same seeding-concentration.

Clonogenic and MTT assay: Wild-type or stable cell lines were harvested from exponential-phase cultures, counted and plated at the described density in 12-well plates for clonogenic assay and 96-well plates for MTT (Corning® Costar®). Four hours after plating, the compounds or vehicle were delivered once at the mentioned concentration. Clonogenic assay: 5 days of incubation in the presence of the compounds, the cells were stained with 0.5% crystal violet and 6% glutaraldehyde, and colonies were counted using GelCount™ Tumor Colony Counter from Oxford Optronix Ltd. Each experiment was done in biological triplicates and each clonogenic graph was constructed from at least two independent experiments. MTT: after 4 days of incubation in the presence of the compounds, 20uL MTT solution (5 mg/ml MTT in PBS, filter sterilized) was added to each well and incubated in 37^{o}C incubator for 4 hours, after which the medium was carefully removed by pipetting and the MTT formazan was resuspended using DMSO. Absorbance was measuring using a spectrophotometric plate-reader at 550nm.

In vivo anticancer activity: Animal experiments were performed in compliance with institutional and federal guidelines after approval from the McGill University Facility Animal Care Committee. (Protocol #5018). NOD-SCID mice were purchased from Charles River Laboratories (St. Zotique, Quebec, Canada). Orthotopic tumor model: 6-8-week-old NOD-SCID female mice were anesthetized (90mg/mL ketamine and 10mg/mL xylazine). A horizontal incision was made to cut the skin and subcutaneous tissues to expose the central component of the neck and the overlying strap muscles were dissected away from the right thyroid. $5x10^5$ 8505c cells in 10uL of serum-free RPMI medium was injected into the right-thyroid gland. Following injection, the incision was closed using 3-0 nylon sutures. Mice were monitored daily for post-surgical complications. Once tumor became palpable on neck examination, mice were treated with three doses of MEAP (30mg/kg) or Taxol (5mg/kg), and then sacrificed a week after the last treatment to evaluate for ALDH1-positive staining by IHC. Subcutaneous tumor model: $1x\ 10^7$ 8505c cells were injected subcutaneously into the right flank of NOD-SCID mice**.** Once tumor volume reached 40-80mm^3, mice were given tri-weekly injection of vehicle, MEAP (30mg/kg) or Taxol (5mg/kg) and tumor size/body weight were recorded every 3 days.

Spectrophotometric Measurement of ALDH enzymatic activity: In vitro measurement of MEAP's impact on ALDH enzymatic activity was carried out as previously described 62. 70%

confluent cells grown in 10cm dishes were lysed using lysis buffer (50 mM Tris (pH 8), 25 mM EDTA, 5 mM β-mercaptoethanol, 1 mM phenylmethylsulfonyl fluoride, and 0.1% sarcosyl). We used cell lysate from SK-BR3, a breast cancer cell line recognized for having high activity of multiple ALDH isoforms 31. Aliquots of 600 µL lysis buffer was incubated at 37 °C with the addition of cell lysate, 5 mM NAD+ and 5 mM propionaldehyde as a substrate. The rate of change in absorbance at 340 nm 1was periodically measured using a spectrophotometer at 5-minute intervals. A control reaction in which the substrate was not added monitored the endogenous rate of NAD+ reduction. Inhibition of ALDH activity by MEAP or DEAB (positive control) is calculated as the ratio of change in absorbance versus DMSO-treated (negative control).

Chemistry: The 2-(4-Morpholinoanilino-6-[(2-exo-norbornyl)amino]-purine (MEAP) and all the other structural analogues of Reversine were synthesized as previously described [87]. Briefly, MEAP as a racemic mixture, was obtained from the reaction of exo-2-Aminonorbornane (racemic, CAS: 7242-92-4, Aldrich cat. #179604) with 6-Chloro-2-fluoropurine (CAS:1651-29-2, Oakwood Chemical cat. #009088) in n-butanol at 100^{o}C for 16h during the first synthetic step of this method. The structure/purity of all analogues was confirmed by ^{1}H NMR, ^{13}C NMR, and HRMS. Other compounds were purchased: XL-019 (MedKoo Biosciences), VX-680 (Cayman Chemical), PF-573228 (Tocris Bioscience), and Reversine (Sigma-Aldrich). Vandetanib (Selleckchem), Cabozantinib (Selleckchem), RO4929097 (Selleckchem). U0126 (Tocris bioscience), PP2 (ADOOQ), IWP-2 (Tocris bioscience).

Cell Cycle analysis: Cells were pulse-labeled with 10uM BrDU for 1 hour, fixed in cold 70% ethanol for 2 hours, then rehydrated in PBS. Cells were thereafter treated with 2N HCl for 10 minutes, followed by 0.1M Na2B4O7 for 5 minutes, then labeled with Alexa 647 anti-Brdu (Biolegends) and DAPI. For flow cytometry acquisition, cells were gated based on FSC-A/SSC-A, FSC-H/FSC-A, and DAPI-H/DAPI-A to discriminate single cells.

Statistical analysis: For discrete variables showing normal distribution, means and standard deviations (SD) are given and comparisons were made using the t-test. In all statistical tests, $P<0.05$ was considered statistically significant

Authors contribution:

HY, KB and MA conceived and designed the experiments and wrote the manuscript. HY performed the ATC cell-based experiments. DW and KB performed design and chemical synthesis of Reversine analogs. GM and JS performed *in vivo* experiments. SDS and AS supervised the immunohistochemistry studies.

Disclosure of potential conflicts of interest

No potential conflict of interest was disclosed by any of the authors.

Data availability statement

All other data are found within the article, supplemental files, or are available from authors upon request.

Acknowledgments

We thank Dr. John Copland for providing the cell lines THJ-11T and THJ-16T, and Dr. Mark Trifiro for providing the cell lines 8505c, TPC, and BCPAP.

References

1. Nigg, E.A. & Stearns, T. The centrosome cycle: centriole biogenesis, duplication and inherent asymmetries. *Nature cell biology* **13**, 1154-1160 (2011).
2. Meraldi, P. & Nigg, E. The centrosome cycle. *FEBS letters* **521**, 9-13 (2002).
3. Bornens, M. Centrosome composition and microtubule anchoring mechanisms. *Current opinion in cell biology* **14**, 25-34 (2002).
4. Chan, J.Y. A clinical overview of centrosome amplification in human cancers. *International journal of biological sciences* **7**, 1122 (2011).
5. Nigg, E.A. Origins and consequences of centrosome aberrations in human cancers. *International journal of cancer* **119**, 2717-2723 (2006).
6. Sluder, G. & Nordberg, J.J. The good, the bad and the ugly: the practical consequences of centrosome amplification. *Current opinion in cell biology* **16**, 49-54 (2004).
7. Kwon, M.*, et al.* Mechanisms to suppress multipolar divisions in cancer cells with extra centrosomes. *Genes & development* **22**, 000-000 (2008).
8. Pannu, V.*, et al.* Centrosome-declustering drugs mediate a two-pronged attack on interphase and mitosis in supercentrosomal cancer cells. *Cell death & disease* **5**, e1538 (2014).
9. Kwon, M.*, et al.* Mechanisms to suppress multipolar divisions in cancer cells with extra centrosomes. *Genes & development* **22**, 2189-2203 (2008).
10. Leber, B.*, et al.* Proteins required for centrosome clustering in cancer cells. *Science translational medicine* **2**, 33ra38-33ra38 (2010).
11. Krämer, A., Maier, B. & Bartek, J. Centrosome clustering and chromosomal (in) stability: a matter of life and death. *Molecular oncology* **5**, 324-335 (2011).
12. Mariappan, A.*, et al.* Inhibition of CPAP–tubulin interaction prevents proliferation of centrosome-amplified cancer cells. *The EMBO journal* **38**, e99876 (2019).
13. Vermeulen, L.*, et al.* Single-cell cloning of colon cancer stem cells reveals a multi-lineage differentiation capacity. *Proceedings of the National Academy of Sciences* **105**, 13427-13432 (2008).
14. Friedmann-Morvinski, D. & Verma, I.M. Dedifferentiation and reprogramming: origins of cancer stem cells. *EMBO reports* **15**, 244-253 (2014).
15. Fukasawa, K. Centrosome amplification, chromosome instability and cancer development. *Cancer letters* **230**, 6-19 (2005).
16. Ganem, N.J., Godinho, S.A. & Pellman, D. A mechanism linking extra centrosomes to chromosomal instability. *Nature* **460**, 278 (2009).
17. Yamashita, Y.M. & Fuller, M.T. Asymmetric centrosome behavior and the mechanisms of stem cell division. *The Journal of cell biology* **180**, 261-266 (2008).
18. Yamashita, Y.M., Mahowald, A.P., Perlin, J.R. & Fuller, M.T. Asymmetric inheritance of mother versus daughter centrosome in stem cell division. *Science (New York, N.Y.)* **315**, 518-521 (2007).
19. Chen, C. & Yamashita, Y.M. Centrosome-centric view of asymmetric stem cell division. *Open Biology* **11**, 200314 (2021).
20. Huang, S. Non-genetic heterogeneity of cells in development: more than just noise. *Development* **136**, 3853-3862 (2009).
21. Clarkson, B. Review of recent studies of cellular proliferation in acute leukemia. *Natl Cancer Inst Monogr* **30**, 81-120 (1969).

22. Clarkson, B., Ohkita, T., Ota, K. & Fried, J. Studies of cellular proliferation in human leukemia. I. Estimation of growth rates of leukemic and normal hematopoietic cells in two adults with acute leukemia given single injections of tritiated thymidine. *The Journal of clinical investigation* **46**, 506-529 (1967).
23. Opyrchal, M.*, et al.* Inhibition of Cdk2 kinase activity selectively targets the CD44+/CD24-/Low stem-like subpopulation and restores chemosensitivity of SUM149PT triple-negative breast cancer cells. *International journal of oncology* **45**, 1193-1199 (2014).
24. Wilkens, L.*, et al.* Induction of aneuploidy by increasing chromosomal instability during dedifferentiation of hepatocellular carcinoma. *Proceedings of the National Academy of Sciences* **101**, 1309-1314 (2004).
25. Smallridge, R.C.*, et al.* American Thyroid Association guidelines for management of patients with anaplastic thyroid cancer. *Thyroid* **22**, 1104-1139 (2012).
26. Perros, P.*, et al.* Guidelines for the management of thyroid cancer. *Clinical endocrinology* **81**, 1-122 (2014).
27. Salvatore, G.*, et al.* A cell proliferation and chromosomal instability signature in anaplastic thyroid carcinoma. *Cancer research* **67**, 10148-10158 (2007).
28. Smallridge, R.C. & Copland, J. Anaplastic thyroid carcinoma: pathogenesis and emerging therapies. *Clinical Oncology* **22**, 486-497 (2010).
29. Cabanillas, M.E., McFadden, D.G. & Durante, C. Thyroid cancer. *The Lancet* **388**, 2783-2795 (2016).
30. Hjelmeland, A.B.*, et al.* Acidic stress promotes a glioma stem cell phenotype. *Cell Death & Differentiation* **18**, 829-840 (2011).
31. Xing, Y., Luo, D.-y., Long, M.-y., Zeng, S.-l. & Li, H.-H. High ALDH1A1 expression correlates with poor survival in papillary thyroid carcinoma. *World journal of surgical oncology* **12**, 29 (2014).
32. Charafe-Jauffret, E.*, et al.* Aldehyde dehydrogenase 1–Positive cancer stem cells mediate metastasis and poor clinical outcome in inflammatory breast cancer. *Clinical Cancer Research* **16**, 45-55 (2010).
33. Li, X., Wan, L., Geng, J., Wu, C.-L. & Bai, X. Aldehyde dehydrogenase 1A1 possesses stem-like properties and predicts lung cancer patient outcome. *Journal of Thoracic Oncology* **7**, 1235-1245 (2012).
34. Cheung, A.*, et al.* Aldehyde dehydrogenase activity in leukemic blasts defines a subgroup of acute myeloid leukemia with adverse prognosis and superior NOD/SCID engrafting potential. *Leukemia* **21**, 1423-1430 (2007).
35. Li, T.*, et al.* ALDH1A1 is a marker for malignant prostate stem cells and predictor of prostate cancer patients' outcome. *Laboratory investigation* **90**, 234-244 (2010).
36. Gao, F.*, et al.* The role of LGR5 and ALDH1A1 in non-small cell lung cancer: Cancer progression and prognosis. *Biochemical and biophysical research communications* **462**, 91-98 (2015).
37. Su, Y.*, et al.* Aldehyde dehydrogenase 1 A1–positive cell population is enriched in tumor-initiating cells and associated with progression of bladder cancer. *Cancer Epidemiology and Prevention Biomarkers* **19**, 327-337 (2010).
38. Yang, L.*, et al.* ALDH1A1 defines invasive cancer stem-like cells and predicts poor prognosis in patients with esophageal squamous cell carcinoma. *Modern Pathology* **27**, 775 (2014).

39. Todaro, M.*, et al.* Tumorigenic and metastatic activity of human thyroid cancer stem cells. *Cancer research* **70**, 8874-8885 (2010).
40. Shiraiwa, K.*, et al.* JAK/STAT3 and NF-κB Signaling Pathways Regulate Cancer Stem-Cell Properties in Anaplastic Thyroid Cancer Cells. *Thyroid* **29**, 674-682 (2019).
41. Nagayama, Y., Shimamura, M. & Mitsutake, N. Cancer stem cells in the thyroid. *Frontiers in endocrinology* **7**, 20 (2016).
42. Knutson, D. & Clagett-Dame, M. atRA Regulation of NEDD9, a gene involved in neurite outgrowth and cell adhesion. *Archives of Biochemistry and Biophysics* **477**, 163-174 (2008).
43. Aquino, J.B.*, et al.* The retinoic acid inducible Cas-family signaling protein Nedd9 regulates neural crest cell migration by modulating adhesion and actin dynamics. *Neuroscience* **162**, 1106-1119 (2009).
44. Singh, M.K., Cowell, L., Seo, S., O'Neill, G.M. & Golemis, E.A. Molecular basis for HEF1/NEDD9/Cas-L action as a multifunctional co-ordinator of invasion, apoptosis and cell cycle. *Cell biochemistry and biophysics* **48**, 54-72 (2007).
45. Izumchenko, E.*, et al.* NEDD9 promotes oncogenic signaling in mammary tumor development. *Cancer research* **69**, 7198-7206 (2009).
46. Wang, Z.*, et al.* NEDD9 may regulate hepatocellular carcinoma cell metastasis by promoting epithelial-mesenchymal-transition and stemness via repressing Smad7. *Oncotarget* **8**, 1714 (2017).
47. Kim, M.*, et al.* Comparative oncogenomics identifies NEDD9 as a melanoma metastasis gene. *Cell* **125**, 1269-1281 (2006).
48. Li, Y.*, et al.* HEF1, a novel target of Wnt signaling, promotes colonic cell migration and cancer progression. *Oncogene* **30**, 2633-2643 (2011).
49. Pugacheva, E.N. & Golemis, E.A. The focal adhesion scaffolding protein HEF1 regulates activation of the Aurora-A and Nek2 kinases at the centrosome. *Nature cell biology* **7**, 937-946 (2005).
50. Pugacheva, E.N., Jablonski, S.A., Hartman, T.R., Henske, E.P. & Golemis, E.A. HEF1-dependent Aurora A activation induces disassembly of the primary cilium. *Cell* **129**, 1351-1363 (2007).
51. Singh, M.K.*, et al.* Enhanced genetic instability and dasatinib sensitivity in mammary tumor cells lacking NEDD9. *Cancer research* **70**, 8907-8916 (2010).
52. O'Neill, G.M., Seo, S., Serebriiskii, I.G., Lessin, S.R. & Golemis, E.A. A new central scaffold for metastasis: parsing HEF1/Cas-L/NEDD9. *Cancer research* **67**, 8975-8979 (2007).
53. Guerrero, M.S., Parsons, J.T. & Bouton, A.H. Cas and NEDD9 contribute to tumor progression through dynamic regulation of the cytoskeleton. *Genes & cancer* **3**, 371-381 (2012).
54. Shagisultanova, E., Gaponova, A.V., Gabbasov, R., Nicolas, E. & Golemis, E.A. Preclinical and clinical studies of the NEDD9 scaffold protein in cancer and other diseases. *Gene* **567**, 1-11 (2015).
56. Wells Jr, S.A.*, et al.* Vandetanib in patients with locally advanced or metastatic medullary thyroid cancer: a randomized, double-blind phase III trial. *Journal of clinical oncology* **30**, 134 (2012).

57. Yakes, F.M.*, et al.* Cabozantinib (XL184), a novel MET and VEGFR2 inhibitor, simultaneously suppresses metastasis, angiogenesis, and tumor growth. *Molecular cancer therapeutics* **10**, 2298-2308 (2011).
58. D'Alise, A.M.*, et al.* Reversine, a novel Aurora kinases inhibitor, inhibits colony formation of human acute myeloid leukemia cells. *Molecular cancer therapeutics* **7**, 1140-1149 (2008).
59. Bijian, K.*, et al.* Targeting focal adhesion turnover in invasive breast cancer cells by the purine derivative reversine. *British journal of cancer* **109**, 2810-2818 (2013).
60. Verstovsek, S.*, et al.* Phase I evaluation of XL019, an oral, potent, and selective JAK2 inhibitor. *Leukemia research* **38**, 316-322 (2014).
61. Hotokezaka, H.*, et al.* U0126 and PD98059, specific inhibitors of MEK, accelerate differentiation of RAW264. 7 cells into osteoclast-like cells. *Journal of Biological Chemistry* **277**, 47366-47372 (2002).
62. Kollman, J.M., Merdes, A., Mourey, L. & Agard, D.A. Microtubule nucleation by γ-tubulin complexes. *Nature reviews Molecular cell biology* **12**, 709-721 (2011).
63. Nigg, E.A. & Holland, A.J. Once and only once: mechanisms of centriole duplication and their deregulation in disease. *Nature reviews Molecular cell biology* **19**, 297 (2018).
64. Tang, N. & Marshall, W.F. Centrosome positioning in vertebrate development. *J Cell Sci* **125**, 4951-4961 (2012).
65. Nigg, E.A. & Raff, J.W. Centrioles, centrosomes, and cilia in health and disease. *Cell* **139**, 663-678 (2009).
66. Dutertre, S., Descamps, S. & Prigent, C. On the role of aurora-A in centrosome function. *Oncogene* **21**, 6175-6183 (2002).
67. Hannak, E., Kirkham, M., Hyman, A.A. & Oegema, K. Aurora-A kinase is required for centrosome maturation in Caenorhabditis elegans. *Journal of Cell Biology* **155**, 1109-1116 (2001).
68. Mori, D.*, et al.* NDEL1 phosphorylation by Aurora-A kinase is essential for centrosomal maturation, separation, and TACC3 recruitment. *Molecular and cellular biology* **27**, 352-367 (2007).
69. Shagisultanova, E., Dunbrack Jr, R.L. & Golemis, E.A. Issues in interpreting the in vivo activity of Aurora-A. *Expert opinion on therapeutic targets* **19**, 187-200 (2015).
70. Quintyne, N.J., Reing, J.E., Hoffelder, D.R., Gollin, S.M. & Saunders, W.S. Spindle multipolarity is prevented by centrosomal clustering. *Science (New York, N.Y.)* **307**, 127-129 (2005).
71. Morrison, J.A.*, et al.* Characterization of thyroid cancer cell lines in murine orthotopic and intracardiac metastasis models. *Hormones and Cancer* **6**, 87-99 (2015).
72. Ganem, N.J., Godinho, S.A. & Pellman, D. A mechanism linking extra centrosomes to chromosomal instability. *Nature* **460**, 278-282 (2009).
73. Isham, C.R.*, et al.* Pazopanib enhances paclitaxel-induced mitotic catastrophe in anaplastic thyroid cancer. *Science translational medicine* **5**, 166ra163-166ra163 (2013).
74. Saygin, C., Matei, D., Majeti, R., Reizes, O. & Lathia, J.D. Targeting cancer stemness in the clinic: from hype to hope. *Cell stem cell* **24**, 25-40 (2019).
75. Godinho, S.A.*, et al.* Oncogene-like induction of cellular invasion from centrosome amplification. *Nature* **510**, 167-171 (2014).
76. Ayob, A.Z. & Ramasamy, T.S. Cancer stem cells as key drivers of tumour progression. *Journal of biomedical science* **25**, 1-18 (2018).

2.7 General discussion

The work presented in the three manuscripts of this thesis investigates the conceptual significance, molecular factors, and application value of a previously unknown NEDD9-interactome that promotes asymmetrical centrosome behavior and CIN within thyroids cancer stem-like cells. We found that NEDD9 upregulation in ALDH+ cells, by impacting downstream effects such as STAT3 and STING, directly links stemness - a trait associated with cancer recurrence, to genomic instability - a trait associates with therapy resistance. As demonstrated by both manuscripts 2 and 3, although NEDD9 is not currently druggable, its expression highly impacts the outcomes of small molecules that inhibit AURKA and FAK. Overall, in addition to the classical hallmarks of cancer that CSCs (outlined in 1.2 of the thesis), our has identified at least one model in which cancer stemness can directly impact CIN-tolerance and thus, genomic stability.

The work in this thesis addresses two of the knowledge gaps that were highlighted in the introductory chapter of this thesis. First, it sheds light on how the processes which govern asymmetrical cell division could impact CSCs. We showed that centrosome asymmetry is a phenotype CSCs could leverage to tolerate centrosome amplification during mitosis better. Presently, asymmetrical centrosome inheritance and behavior are recognized features only in stem cells. Our studies, to our knowledge, are the first to investigate the regulatory and functional significance of this attribute in CSCs.

Secondly, our study also explored the interplay between cancer stemness and CIN, which could help explain why both traits often develop parallel during cancer progression[322]. Based on findings reviewed in the introductory chapters, cancer progression, relapse, and drug resistance can be driven by both phenotypic and genotypic heterogeneity. Although the stem-like state has long been understood as a source of phenotypic variation in cancer, it has never been shown to contribute to genotypic diversity. Our findings demonstrated that, at least in this advanced form of thyroid cancer, stemness could directly impact CIN. One of the most conceptually interesting aspects of these studies is that they expand the functional significance of cancer stem-like cells to act as a source of phenotypic heterogeneity and genotypic heterogeneity, thus elevating their importance as therapeutic targets.

To a large extent, our findings indicate that the effects observed are not due to NEDD9 overexpression itself, but rather that ALDH+ ATC cells depend on this upregulated NEDD9 to

achieve cell signaling homeostasis for maintaining their stemness and CIN properties. Evidence of this is that overexpression of NEDD9 in ALDH- cells did not recapitulate the phenotype of ALDH+ cells, such as increasing CIN or downregulating STING. This interpretation is consistent with previous studies suggesting that although ALDH enzymatic activity is crucial for tumorigenic properties of ALDH+ cells, overexpression of this enzyme in ALDH- cells did not introduce stemness [323]. This interpretation of NEDD9's role as an indirect coordinator of stemness/CIN features rather than their direct drivers has important implications regarding these manuscripts' findings. First, it suggests that the connection between stemness/CIN observed in ALDH+ cells is not necessarily due to NEDD9 upregulation itself and is more likely that those ALDH+ stem-like cells are "addicted" to a high level of NEDD9 to tolerate CIN. Secondly, it implies that NEDD9 is potentially useful as a biomarker to assess the utility of targeting NEDD9's downstream effectors.

Our work also offered new critical insight into the functional role of NEDD9 in cancer. NEDD9 is well-recognized as a pro-invasive factor in several cancer models through metastatic signaling cascades [324-334]. However, its connection with the CSC phenotype, though observed, has remained relatively nebulous until now. In hepatocellular carcinoma, NEDD9 overexpression promoted the expansion of CD133+ or ALDH+ stem-like cells through the repression of the TGFβ pathway. In ovarian cancer, NEDD9 expression was found correlated with a stem cell-like transcriptomic signature [335]. While useful, those studies neither did examine if the endogenous level of NEDD9 differed between stem cell-like and nonstem cell-like cells nor answered how NEDD9 contributes to stem cell-like properties. Our study provides more mechanistic clarity by showing in the ATC model that the endogenous expression of NEDD9 drastically differed between ALDH- and ALDH+ cells and delineated the functional significance of NEDD9 upregulation in ALDH+ cells.

Furthermore, our study also expanded the understanding of how NEDD9 contributes to centrosome regulation. Conventionally, NEDD9 expression should be relatively suppressed during most interphase and is only elevated during late-G2 to promote activation of Aurora Kinase A for driving centrosome maturation [329]. However, our findings suggest that in ALDH+ ATC stem-like cells, NEDD9 does not promote Aurora Kinase A activation in a cell-cycle-dependent manner. The reason is likely because NEDD9 is constitutively expressed in these cells, and its regulation of centrosome is consequently distinct from those observed in MCF-7 cells [329]. These findings

exemplify the importance of molecular context to the functional role of scaffolding proteins such as NEDD9.

Lastly, our work may offer novel clues to new therapy development for ATC, a disease for which effective treatments are urgently needed. Presently, ATC treatment is largely reliant on a combination of surgery, chemotherapy, and radiation therapy, and only in some rarer cases, immune checkpoint inhibitors or Dafratenib/Trametinib are used as targeted therapy [336]. The American Thyroid Association guideline recommends experimental treatments (clinical trials) whenever possible due to the relatively poor efficacy of existing treatment [336]. Among the novel drug candidates being clinically tested for ATC, AURKA inhibitors offer a promising lead. AURKA inhibitors have been shown to act synergistically with paclitaxel to eliminate ATC cells by introducing mitotic catastrophe; however, the underlying mechanism is unclear [337]. An ongoing clinical trial (NCT01236547) might confirm the benefits of adding AURKA inhibitor to paclitaxel regimens. Based on initial results, AURKAi improved the overall survival from 29% to 37.1% after ~4 years and reduced the incidence of local-regional relapse from 33.6% to 28.6%. Concordantly, our results show that AURKAi inhibitors promoted supernumerary centrosome activation in ATC cells. This effect should theoretically synergize with paclitaxel, as the microtubule-stabilizing effect of this chemotherapy drug would be enhanced by the presence of extra MTOCs during mitosis.

While we have not yet formally tested if these findings can directly extend to other cancer models, strong evidence suggests that the concepts can be broadly applicable. Our first manuscript showed that stemness-related centrosome (but not stemness genes or centrosome genes alone) effectively predicts aneuploidy across multiple types of cancer, consistent with our proposal that centrosome-regulatory programs activated in normal stem cells could drive CIN. In manuscript 2, we showed that NEDD9 and STAT3 co-upregulation occurred in thyroid cancer and several other types of cancer, such as glioblastoma, suggesting that the NEDD9-STAT3 axis may manifest in those cancer types. Collectively, there are strong indications that many key findings could be extrapolated to other cancer.

2.8 Conclusions and future perspectives

This work hopes to lay the foundation to further explore centrosomes as a common player in cancer stemness and genomic instability. These findings highlight a presently understudied feature of CSCs in cancer biology - their asymmetrical centrosomal behavior and demonstrate that this centrosome asymmetry is a source of genomic instability and a potential vulnerability of tumorigenic cancer stem-like cells. As the key challenge in treating cancers that have progressed to an advanced stage is finding a way to eliminate a large number of clones with genotypic and functional variations, identifying the mechanisms underlying tumor heterogeneity is an important step to elucidating the core processes that allow cancer to arrive at those untreatable stages.

This study raises several important questions that merit studies in the future. The most obvious question is whether the connection between cancer stemness and CIN is a universal phenomenon across other cancer types. NEDD9 has been implicated in cancer stemness in ovarian and liver cancer, and these are logical models to expand our findings. Conceptually, stemness/CIN are common features of cancer, which offers confidence that our findings could be extrapolated to other cancer models. However, NEDD9 is not necessarily a key player in all cancer cell types, as this protein activity is highly model/context-sensitive. Other candidate genes should be explored as universal regulators of CSC centrosomes. Centrosome genes correlated with aneuploidy across patient genomic datasets, or centrosome proteins are known to be asymmetrically enriched in one of the centrosome pairs (such as Centrobin) are logical candidates to pursue. An unbiased approach using functional RNAi screening would be preferable.

Future studies build based on this work can examine several unresolved questions. First, presuming that the centrosomes in CSCs behave analogously to normal stem cells, is it possible that they are likewise asymmetrically enriched in cell-fate determinant protein/mRNA? Second, the unexpected involvement of STING in the first study raises very interesting questions regarding the importance of DNA sensing pathways in CSCs; this thread merits further investigation as the biological implication of a distinct STING pathway, particularly concerning enabling CSCs to metastasize via cGAS/STING-regulated NF-KB activation. Lastly, CSCs are presently understood to function contextually dependent on the niche of the tumor microenvironment. While studies from stem cells inform us that certain aspects of stem cell behavior are intrinsic to themselves, other features are dependent or amplified by extracellular factors. As such, the impact of

modulating asymmetrical centrosome behavior on stem cell properties, mitosis, and CIN should be re-assessed in the context of CSCs residing within the tumor microenvironment.

Reference list for background and discussion

1. Levan, A. & Hauschka, T.S. Endomitotic reduplication mechanisms in ascites tumors of the mouse. *Journal of the National Cancer Institute* **14**, 1-43 (1953).
2. Makino, S. Further evidence favoring the concept of the stem cell in ascites tumors of rats. *Annals of the New York Academy of Sciences* **63**, 818 (1956).
3. Liu, A.Y., Roudier, M.P. & True, L.D. Heterogeneity in primary and metastatic prostate cancer as defined by cell surface CD profile. *The American journal of pathology* **165**, 1543-1556 (2004).
4. Shackleton, M., Quintana, E., Fearon, E.R. & Morrison, S.J. Heterogeneity in cancer: cancer stem cells versus clonal evolution. *Cell* **138**, 822-829 (2009).
5. Shlush, L.I.*, et al.* Tracing the origins of relapse in acute myeloid leukaemia to stem cells. *Nature* **547**, 104-108 (2017).
6. Vitale, I., Shema, E., Loi, S. & Galluzzi, L. Intratumoral heterogeneity in cancer progression and response to immunotherapy. *Nature medicine* **27**, 212-224 (2021).
7. Strickland, S. & Mahdavi, V. The induction of differentiation in teratocarcinoma stem cells by retinoic acid. *Cell* **15**, 393-403 (1978).
8. Bennett, D.C., Peachey, L.A., Durbin, H. & Rudland, P.S. A possible mammary stem cell line. *Cell* **15**, 283-298 (1978).
9. Clarkson, B., Ohkita, T., Ota, K. & Fried, J. Studies of cellular proliferation in human leukemia. I. Estimation of growth rates of leukemic and normal hematopoietic cells in two adults with acute leukemia given single injections of tritiated thymidine. *The Journal of clinical investigation* **46**, 506-529 (1967).
10. Hope, K.J., Jin, L. & Dick, J.E. Acute myeloid leukemia originates from a hierarchy of leukemic stem cell classes that differ in self-renewal capacity. *Nature immunology* **5**, 738-743 (2004).
11. Clarkson, B. Review of recent studies of cellular proliferation in acute leukemia. *Natl Cancer Inst Monogr* **30**, 81-120 (1969).
12. Jones, P.H. & Watt, F.M. Separation of human epidermal stem cells from transit amplifying cells on the basis of differences in integrin function and expression. *Cell* **73**, 713-724 (1993).
13. Hsu, Y.-C., Li, L. & Fuchs, E. Transit-amplifying cells orchestrate stem cell activity and tissue regeneration. *Cell* **157**, 935-949 (2014).
14. Jessa, S.*, et al.* Stalled developmental programs at the root of pediatric brain tumors. *Nature genetics* **51**, 1702-1713 (2019).
15. Cairns, J. Somatic stem cells and the kinetics of mutagenesis and carcinogenesis. *Proceedings of the National Academy of Sciences* **99**, 10567-10570 (2002).
16. Eppert, K.*, et al.* Stem cell gene expression programs influence clinical outcome in human leukemia. *Nature medicine* **17**, 1086-1093 (2011).
17. Lapidot, T.*, et al.* A cell initiating human acute myeloid leukaemia after transplantation into SCID mice. *Nature* **367**, 645-648 (1994).
18. Al-Hajj, M., Wicha, M.S., Benito-Hernandez, A., Morrison, S.J. & Clarke, M.F. Prospective identification of tumorigenic breast cancer cells. *Proceedings of the National Academy of Sciences* **100**, 3983-3988 (2003).

19. Collins, A.T., Berry, P.A., Hyde, C., Stower, M.J. & Maitland, N.J. Prospective identification of tumorigenic prostate cancer stem cells. *Cancer research* **65**, 10946-10951 (2005).
20. Todaro, M.*, et al.* Tumorigenic and metastatic activity of human thyroid cancer stem cells. *Cancer research* **70**, 8874-8885 (2010).
21. Eramo, A.*, et al.* Identification and expansion of the tumorigenic lung cancer stem cell population. *Cell Death & Differentiation* **15**, 504-514 (2008).
22. Li, C.*, et al.* Identification of pancreatic cancer stem cells. *Cancer research* **67**, 1030-1037 (2007).
23. Ma, S.*, et al.* Identification and characterization of tumorigenic liver cancer stem/progenitor cells. *Gastroenterology* **132**, 2542-2556 (2007).
24. Wang, J.C. & Dick, J.E. Cancer stem cells: lessons from leukemia. *Trends in cell biology* **15**, 494-501 (2005).
25. Lan, X.*, et al.* Fate mapping of human glioblastoma reveals an invariant stem cell hierarchy. *Nature* **549**, 227-232 (2017).
26. Kreso, A. & Dick, J.E. Evolution of the cancer stem cell model. *Cell stem cell* **14**, 275-291 (2014).
27. Wainwright, E.N. & Scaffidi, P. Epigenetics and cancer stem cells: unleashing, hijacking, and restricting cellular plasticity. *Trends in cancer* **3**, 372-386 (2017).
28. Torres, C.M.*, et al.* The linker histone H1. 0 generates epigenetic and functional intratumor heterogeneity. *Science (New York, N.Y.)* **353**(2016).
29. Wong, S.H.*, et al.* The H3K4-methyl epigenome regulates leukemia stem cell oncogenic potential. *Cancer cell* **28**, 198-209 (2015).
30. Kidder, B.L., Palmer, S. & Knott, J.G. SWI/SNF-Brg1 regulates self-renewal and occupies core pluripotency-related genes in embryonic stem cells. *Stem cells* **27**, 317-328 (2009).
31. Khan, A.Q.*, et al.* Role of miRNA-regulated cancer stem cells in the pathogenesis of human malignancies. *Cells* **8**, 840 (2019).
32. Gerlinger, M.*, et al.* Intratumor heterogeneity and branched evolution revealed by multiregion sequencing. *N Engl j Med* **366**, 883-892 (2012).
33. Yachida, S.*, et al.* Distant metastasis occurs late during the genetic evolution of pancreatic cancer. *Nature* **467**, 1114-1117 (2010).
34. Heddleston, J.M., Li, Z., McLendon, R.E., Hjelmeland, A.B. & Rich, J.N. The hypoxic microenvironment maintains glioblastoma stem cells and promotes reprogramming towards a cancer stem cell phenotype. *Cell cycle* **8**, 3274-3284 (2009).
35. Li, Z.*, et al.* Hypoxia-inducible factors regulate tumorigenic capacity of glioma stem cells. *Cancer cell* **15**, 501-513 (2009).
36. Gupta, P.B.*, et al.* Stochastic state transitions give rise to phenotypic equilibrium in populations of cancer cells. *Cell* **146**, 633-644 (2011).
37. Tian, H.*, et al.* A reserve stem cell population in small intestine renders Lgr5-positive cells dispensable. *Nature* **478**, 255-259 (2011).
38. Van Es, J.H.*, et al.* Dll1+ secretory progenitor cells revert to stem cells upon crypt damage. *Nature cell biology* **14**, 1099-1104 (2012).
39. Wang, X. Stem cells in tissues, organoids, and cancers. *Cellular and Molecular Life Sciences* **76**, 4043-4070 (2019).
40. Greaves, M. & Maley, C.C. Clonal evolution in cancer. *Nature* **481**, 306-313 (2012).

41. Burrell, R.A., McGranahan, N., Bartek, J. & Swanton, C. The causes and consequences of genetic heterogeneity in cancer evolution. *Nature* **501**, 338-345 (2013).
42. Gilbertson, R.J. & Rich, J.N. Making a tumour's bed: glioblastoma stem cells and the vascular niche. *Nature Reviews Cancer* **7**, 733-736 (2007).
43. Plaks, V., Kong, N. & Werb, Z. The cancer stem cell niche: how essential is the niche in regulating stemness of tumor cells? *Cell stem cell* **16**, 225-238 (2015).
44. Balic, M.*, et al.* Most early disseminated cancer cells detected in bone marrow of breast cancer patients have a putative breast cancer stem cell phenotype. *Clinical cancer research* **12**, 5615-5621 (2006).
45. Jin, X.*, et al.* Targeting glioma stem cells through combined BMI1 and EZH2 inhibition. *Nature medicine* **23**, 1352-1361 (2017).
46. Zhou, W.*, et al.* Periostin secreted by glioblastoma stem cells recruits M2 tumour-associated macrophages and promotes malignant growth. *Nature cell biology* **17**, 170-182 (2015).
47. Heddleston, J.*, et al.* Hypoxia inducible factors in cancer stem cells. *British journal of cancer* **102**, 789-795 (2010).
48. Lathia, J.D., Heddleston, J.M., Venere, M. & Rich, J.N. Deadly teamwork: neural cancer stem cells and the tumor microenvironment. *Cell stem cell* **8**, 482-485 (2011).
49. Calabrese, C.*, et al.* A perivascular niche for brain tumor stem cells. *Cancer cell* **11**, 69-82 (2007).
50. Krishnamurthy, S.*, et al.* Endothelial cell-initiated signaling promotes the survival and self-renewal of cancer stem cells. *Cancer research* **70**, 9969-9978 (2010).
51. Lu, J.*, et al.* Endothelial cells promote the colorectal cancer stem cell phenotype through a soluble form of Jagged-1. *Cancer cell* **23**, 171-185 (2013).
52. Keith, B. & Simon, M.C. Hypoxia-inducible factors, stem cells, and cancer. *Cell* **129**, 465-472 (2007).
53. Lin, S.*, et al.* Distributed hepatocytes expressing telomerase repopulate the liver in homeostasis and injury. *Nature* **556**, 244-248 (2018).
54. Morrissy, A.S.*, et al.* Spatial heterogeneity in medulloblastoma. *Nature genetics* **49**, 780-788 (2017).
55. Hanahan, D. & Weinberg, R.A. Hallmarks of cancer: the next generation. *Cell* **144**, 646-674 (2011).
56. Shenghui, H., Nakada, D. & Morrison, S.J. Mechanisms of stem cell self-renewal. *Annual Review of Cell and Developmental* **25**, 377-406 (2009).
57. Teng, Y., Wang, X., Wang, Y. & Ma, D. Wnt/β-catenin signaling regulates cancer stem cells in lung cancer A549 cells. *Biochemical and biophysical research communications* **392**, 373-379 (2010).
58. Malanchi, I.*, et al.* Cutaneous cancer stem cell maintenance is dependent on β-catenin signalling. *Nature* **452**, 650-653 (2008).
59. Holland, J.D., Klaus, A., Garratt, A.N. & Birchmeier, W. Wnt signaling in stem and cancer stem cells. *Current opinion in cell biology* **25**, 254-264 (2013).
60. Wang, J., Sullenger, B.A. & Rich, J.N. Notch signaling in cancer stem cells. in *Notch Signaling in Embryology and Cancer* 174-185 (Springer, 2012).
61. Hao, J.*, et al.* Role of Hippo signaling in cancer stem cells. *Journal of cellular physiology* **229**, 266-270 (2014).

62. Das, D.*, et al.* Notch induces cyclin-D1-dependent proliferation during a specific temporal window of neural differentiation in ES cells. *Developmental biology* **348**, 153-166 (2010).
63. Gregory, C.A., Singh, H., Perry, A.S. & Prockop, D.J. The Wnt signaling inhibitor dickkopf-1 is required for reentry into the cell cycle of human adult stem cells from bone marrow. *Journal of Biological Chemistry* **278**, 28067-28078 (2003).
64. Davidson, G. & Niehrs, C. Emerging links between CDK cell cycle regulators and Wnt signaling. *Trends in cell biology* **20**, 453-460 (2010).
65. Huang, J., Wu, S., Barrera, J., Matthews, K. & Pan, D. The Hippo signaling pathway coordinately regulates cell proliferation and apoptosis by inactivating Yorkie, the Drosophila Homolog of YAP. *Cell* **122**, 421-434 (2005).
66. Wang, Q.*, et al.* Tamoxifen enhances stemness and promotes metastasis of ERα36+ breast cancer by upregulating ALDH1A1 in cancer cells. *Cell research* **28**, 336-358 (2018).
67. Pollyea, D.A.*, et al.* Venetoclax with azacitidine disrupts energy metabolism and targets leukemia stem cells in patients with acute myeloid leukemia. *Nature medicine* **24**, 1859-1866 (2018).
68. Dong, C.*, et al.* Loss of FBP1 by Snail-mediated repression provides metabolic advantages in basal-like breast cancer. *Cancer cell* **23**, 316-331 (2013).
69. Lin, C.-H., Hung, P.-H. & Chen, Y.-J. CD44 is associated with the aggressive phenotype of nasopharyngeal carcinoma through redox regulation. *International journal of molecular sciences* **14**, 13266-13281 (2013).
70. Ye, X.Q.*, et al.* Mitochondrial and energy metabolism-related properties as novel indicators of lung cancer stem cells. *International journal of cancer* **129**, 820-831 (2011).
71. Janiszewska, M.*, et al.* Imp2 controls oxidative phosphorylation and is crucial for preserving glioblastoma cancer stem cells. *Genes & development* **26**, 1926-1944 (2012).
72. Sancho, P.*, et al.* MYC/PGC-1α balance determines the metabolic phenotype and plasticity of pancreatic cancer stem cells. *Cell metabolism* **22**, 590-605 (2015).
73. Lagadinou, E.D.*, et al.* BCL-2 inhibition targets oxidative phosphorylation and selectively eradicates quiescent human leukemia stem cells. *Cell stem cell* **12**, 329-341 (2013).
74. Nakada, D., Saunders, T.L. & Morrison, S.J. Lkb1 regulates cell cycle and energy metabolism in haematopoietic stem cells. *Nature* **468**, 653-658 (2010).
75. Luo, M.*, et al.* Targeting breast cancer stem cell state equilibrium through modulation of redox signaling. *Cell metabolism* **28**, 69-86. e66 (2018).
76. Lewis, C.*, et al.* SREBP maintains lipid biosynthesis and viability of cancer cells under lipid-and oxygen-deprived conditions and defines a gene signature associated with poor survival in glioblastoma multiforme. *Oncogene* **34**, 5128-5140 (2015).
77. Pandey, P.*, et al.* Elevated lipogenesis in epithelial stem-like cell confers survival advantage in ductal carcinoma in situ of breast cancer. *Oncogene* **32**, 5111-5122 (2013).
78. Wang, X., Sun, Y., Wong, J. & Conklin, D. PPAR γ maintains ERBB2-positive breast cancer stem cells. *Oncogene* **32**, 5512-5521 (2013).
79. Wang, T.*, et al.* JAK/STAT3-regulated fatty acid β-oxidation is critical for breast cancer stem cell self-renewal and chemoresistance. *Cell metabolism* **27**, 136-150. e135 (2018).
80. Fu, T.*, et al.* FXR regulates intestinal cancer stem cell proliferation. *Cell* **176**, 1098-1112. e1018 (2019).

81. Silva, J.*, et al.* Nanog is the gateway to the pluripotent ground state. *Cell* **138**, 722-737 (2009).
82. Chen, C.-L.*, et al.* NANOG metabolically reprograms tumor-initiating stem-like cells through tumorigenic changes in oxidative phosphorylation and fatty acid metabolism. *Cell metabolism* **23**, 206-219 (2016).
83. Noto, A.*, et al.* Stearoyl-CoA desaturase-1 is a key factor for lung cancer-initiating cells. *Cell death & disease* **4**, e947-e947 (2013).
84. Noto, A.*, et al.* Stearoyl-CoA-desaturase 1 regulates lung cancer stemness via stabilization and nuclear localization of YAP/TAZ. *Oncogene* **36**, 4573-4584 (2017).
85. Ma, X.-L.*, et al.* Sphere-forming culture enriches liver cancer stem cells and reveals Stearoyl-CoA desaturase 1 as a potential therapeutic target. *BMC cancer* **19**, 1-12 (2019).
86. M'barek, K.B.*, et al.* ER membrane phospholipids and surface tension control cellular lipid droplet formation. *Developmental cell* **41**, 591-604. e597 (2017).
87. Sheetz, M.P. & Dai, J. Modulation of membrane dynamics and cell motility by membrane tension. *Trends in cell biology* **6**, 85-89 (1996).
88. Lv, J.*, et al.* Cell softness regulates tumorigenicity and stemness of cancer cells. *The EMBO journal* **40**, e106123 (2021).
89. Bringold, F. & Serrano, M. Tumor suppressors and oncogenes in cellular senescence☆. *Experimental gerontology* **35**, 317-329 (2000).
90. Nevins, J.R. E2F: a link between the Rb tumor suppressor protein and viral oncoproteins. *Science (New York, N.Y.)*, 424-429 (1992).
91. Calo, E.*, et al.* Rb regulates fate choice and lineage commitment in vivo. *Nature* **466**, 1110-1114 (2010).
92. Korenjak, M. & Brehm, A. E2F–Rb complexes regulating transcription of genes important for differentiation and development. *Current opinion in genetics & development* **15**, 520-527 (2005).
93. Kareta, M.S.*, et al.* Inhibition of pluripotency networks by the Rb tumor suppressor restricts reprogramming and tumorigenesis. *Cell stem cell* **16**, 39-50 (2015).
94. Zilfou, J.T. & Lowe, S.W. Tumor suppressive functions of p53. *Cold Spring Harbor perspectives in biology* **1**, a001883 (2009).
95. Attardi, L.D. & Donehower, L.A. Probing p53 biological functions through the use of genetically engineered mouse models. *Mutation Research/Fundamental and Molecular Mechanisms of Mutagenesis* **576**, 4-21 (2005).
96. Krizhanovsky, V. & Lowe, S.W. The promises and perils of p53. *Nature* **460**, 1085-1086 (2009).
97. Liu, Y.*, et al.* p53 regulates hematopoietic stem cell quiescence. *Cell stem cell* **4**, 37-48 (2009).
98. Cicalese, A.*, et al.* The tumor suppressor p53 regulates polarity of self-renewing divisions in mammary stem cells. *Cell* **138**, 1083-1095 (2009).
99. Godar, S.*, et al.* Growth-inhibitory and tumor-suppressive functions of p53 depend on its repression of CD44 expression. *Cell* **134**, 62-73 (2008).
100. Dobashi, Y.*, et al.* Stepwise participation of p53 gene mutation during dedifferentiation of human thyroid carcinomas. *Diagnostic Molecular Pathology* **3**, 9-14 (1994).
101. Jerry, D.J., Tao, L. & Yan, H. Regulation of cancer stem cells by p53. *Breast Cancer Research* **10**, 304 (2008).

102. Woo, H.G., *et al.* Association of TP53 mutations with stem cell-like gene expression and survival of patients with hepatocellular carcinoma. *Gastroenterology* **140**, 1063-1070. e1068 (2011).
103. Rahman, S. & Islam, R. Mammalian Sirt1: insights on its biological functions. *Cell Communication and Signaling* **9**, 11 (2011).
104. Elmore, S. Apoptosis: a review of programmed cell death. *Toxicologic pathology* **35**, 495-516 (2007).
105. Lowe, S.W., Cepero, E. & Evan, G. Intrinsic tumour suppression. *Nature* **432**, 307-315 (2004).
106. Ryoo, H.D. & Bergmann, A. The role of apoptosis-induced proliferation for regeneration and cancer. *Cold Spring Harbor perspectives in biology* **4**, a008797 (2012).
107. Fogarty, C.E. & Bergmann, A. Killers creating new life: caspases drive apoptosis-induced proliferation in tissue repair and disease. *Cell Death & Differentiation* **24**, 1390-1400 (2017).
108. Chera, S., *et al.* Apoptotic cells provide an unexpected source of Wnt3 signaling to drive hydra head regeneration. *Developmental cell* **17**, 279-289 (2009).
109. Zhang, Z., Dong, Z., Lauxen, I.S., Sant'Ana Filho, M. & Nör, J.E. Endothelial cell-secreted EGF induces epithelial to mesenchymal transition and endows head and neck cancer cells with stem-like phenotype. *Cancer research* **74**, 2869-2881 (2014).
110. Knüpfer, H. & Preiß, R. Significance of interleukin-6 (IL-6) in breast cancer. *Breast cancer research and treatment* **102**, 129-135 (2007).
111. Dhanasekaran, D.N. & Reddy, E.P. JNK signaling in apoptosis. *Oncogene* **27**, 6245-6251 (2008).
112. Chen, F. JNK-induced apoptosis, compensatory growth, and cancer stem cells. *Cancer research* **72**, 379-386 (2012).
113. Matsuda, K.-i., *et al.* Targeting JNK for therapeutic depletion of stem-like glioblastoma cells. *Scientific reports* **2**, 516 (2012).
114. Li, Q.V., *et al.* Genome-scale screens identify JNK–JUN signaling as a barrier for pluripotency exit and endoderm differentiation. *Nature genetics* **51**, 999-1010 (2019).
115. Rosso, S.B., Sussman, D., Wynshaw-Boris, A. & Salinas, P.C. Wnt signaling through Dishevelled, Rac and JNK regulates dendritic development. *Nature neuroscience* **8**, 34-42 (2005).
116. Todaro, M., *et al.* Colon cancer stem cells dictate tumor growth and resist cell death by production of interleukin-4. *Cell stem cell* **1**, 389-402 (2007).
117. Zobalova, R., *et al.* CD133-positive cells are resistant to TRAIL due to up-regulation of FLIP. *Biochemical and biophysical research communications* **373**, 567-571 (2008).
118. Piggott, L., Omidvar, N., Pérez, S.M., Eberl, M. & Clarkson, R.W. Suppression of apoptosis inhibitor c-FLIP selectively eliminates breast cancer stem cell activity in response to the anti-cancer agent, TRAIL. *Breast Cancer Research* **13**, 1-16 (2011).
119. Kim, S.Y., *et al.* Cancer stem cells protect non-stem cells from anoikis: bystander effects. *Journal of cellular biochemistry* **117**, 2289-2301 (2016).
120. Smit, M.A., Geiger, T.R., Song, J.-Y., Gitelman, I. & Peeper, D.S. A Twist-Snail axis critical for TrkB-induced epithelial-mesenchymal transition-like transformation, anoikis resistance, and metastasis. *Molecular and cellular biology* **29**, 3722-3737 (2009).

121. Gates, K.S. An overview of chemical processes that damage cellular DNA: spontaneous hydrolysis, alkylation, and reactions with radicals. *Chemical research in toxicology* **22**, 1747-1760 (2009).
122. Diehn, M.*, et al.* Association of reactive oxygen species levels and radioresistance in cancer stem cells. *nature* **458**, 780-783 (2009).
123. Bao, S.*, et al.* Glioma stem cells promote radioresistance by preferential activation of the DNA damage response. *nature* **444**, 756-760 (2006).
124. Debnath, J., Baehrecke, E.H. & Kroemer, G. Does autophagy contribute to cell death? *Autophagy* **1**, 66-74 (2005).
125. Baehrecke, E.H. Autophagy: dual roles in life and death? *Nature reviews Molecular cell biology* **6**, 505-510 (2005).
126. Yu, S.W.*, et al.* Autophagic death of adult hippocampal neural stem cells following insulin withdrawal. *Stem cells* **26**, 2602-2610 (2008).
127. Warr, M.R.*, et al.* FOXO3A directs a protective autophagy program in haematopoietic stem cells. *Nature* **494**, 323-327 (2013).
128. Ho, T.T.*, et al.* Autophagy maintains the metabolism and function of young and old stem cells. *Nature* **543**, 205-210 (2017).
129. Oliver, L., Hue, E., Priault, M. & Vallette, F.M. Basal autophagy decreased during the differentiation of human adult mesenchymal stem cells. *Stem cells and development* **21**, 2779-2788 (2012).
130. Hou, J.*, et al.* Autophagy prevents irradiation injury and maintains stemness through decreasing ROS generation in mesenchymal stem cells. *Cell death & disease* **4**, e844-e844 (2013).
131. Song, Y.-j.*, et al.* Autophagy contributes to the survival of CD133+ liver cancer stem cells in the hypoxic and nutrient-deprived tumor microenvironment. *Cancer letters* **339**, 70-81 (2013).
132. Yang, H.-Z.*, et al.* Autophagy contributes to the enrichment and survival of colorectal cancer stem cells under oxaliplatin treatment. *Cancer letters* **361**, 128-136 (2015).
133. Balic, A.*, et al.* Chloroquine targets pancreatic cancer stem cells via inhibition of CXCR4 and hedgehog signaling. *Molecular cancer therapeutics* **13**, 1758-1771 (2014).
134. Choi, D.S.*, et al.* Chloroquine eliminates cancer stem cells through deregulation of Jak2 and DNMT1. *STEM CELLS* (2014).
135. van Galen, P.*, et al.* The unfolded protein response governs integrity of the haematopoietic stem-cell pool during stress. *Nature* **510**, 268-272 (2014).
136. Wielenga, M.C.*, et al.* ER-stress-induced differentiation sensitizes colon cancer stem cells to chemotherapy. *Cell reports* **13**, 489-494 (2015).
137. Heijmans, J.*, et al.* ER stress causes rapid loss of intestinal epithelial stemness through activation of the unfolded protein response. *Cell reports* **3**, 1128-1139 (2013).
138. Hayflick, L. & Moorhead, P.S. The serial cultivation of human diploid cell strains. *Experimental cell research* **25**, 585-621 (1961).
139. Plentz, R.*, et al.* Telomere shortening of epithelial cells characterises the adenoma-carcinoma transition of human colorectal cancer. *Gut* **52**, 1304-1307 (2003).
140. Plentz, R.R.*, et al.* Hepatocellular telomere shortening correlates with chromosomal instability and the development of human hepatoma. *Hepatology* **40**, 80-86 (2004).

141. Serrano, D.*, et al.* Inhibition of telomerase activity preferentially targets aldehyde dehydrogenase-positive cancer stem-like cells in lung cancer. *Molecular cancer* **10**, 1-15 (2011).
142. Joseph, I.*, et al.* The telomerase inhibitor imetelstat depletes cancer stem cells in breast and pancreatic cancer cell lines. *Cancer research* **70**, 9494-9504 (2010).
143. Miyazaki, T.*, et al.* Telomestatin impairs glioma stem cell survival and growth through the disruption of telomeric G-quadruplex and inhibition of the proto-oncogene, c-Myb. *Clinical Cancer Research* **18**, 1268-1280 (2012).
144. Park, J.-I.*, et al.* Telomerase modulates Wnt signalling by association with target gene chromatin. *Nature* **460**, 66-72 (2009).
145. Beck, S.*, et al.* Telomerase activity-independent function of TERT allows glioma cells to attain cancer stem cell characteristics by inducing EGFR expression. *Molecules and cells* **31**, 9-15 (2011).
146. Liu, Z.*, et al.* Telomerase reverse transcriptase promotes epithelial–mesenchymal transition and stem cell-like traits in cancer cells. *Oncogene* **32**, 4203-4213 (2013).
147. Risau, W.*, et al.* Vasculogenesis and angiogenesis in embryonic-stem-cell-derived embryoid bodies. *Development* **102**, 471-478 (1988).
148. Weidner, N., Semple, J.P., Welch, W.R. & Folkman, J. Tumor angiogenesis and metastasis—correlation in invasive breast carcinoma. *New England Journal of Medicine* **324**, 1-8 (1991).
149. Weidner, N., Carroll, P., Flax, J., Blumenfeld, W. & Folkman, J. Tumor angiogenesis correlates with metastasis in invasive prostate carcinoma. *The American journal of pathology* **143**, 401 (1993).
150. Roskoski Jr, R. Vascular endothelial growth factor (VEGF) signaling in tumor progression. *Critical reviews in oncology/hematology* **62**, 179-213 (2007).
151. Carmeliet, P. & Jain, R.K. Principles and mechanisms of vessel normalization for cancer and other angiogenic diseases. *Nature reviews Drug discovery* **10**, 417-427 (2011).
152. Rios, M. & Williams, D.A. Systematic analysis of the ability of stromal cell lines derived from different murine adult tissues to support maintenance of hematopoietic stem cells in vitro. *Journal of cellular physiology* **145**, 434-443 (1990).
153. Seton-Rogers, S. VEGF promotes stemness. *Nature Reviews Cancer* **11**, 831-831 (2011).
154. Beck, B.*, et al.* A vascular niche and a VEGF–Nrp1 loop regulate the initiation and stemness of skin tumours. *Nature* **478**, 399-403 (2011).
155. Liu, K., Hao, M., Ouyang, Y., Zheng, J. & Chen, D. CD133+ cancer stem cells promoted by VEGF accelerate the recurrence of hepatocellular carcinoma. *Scientific reports* **7**, 1-10 (2017).
156. Charles, N.*, et al.* Perivascular nitric oxide activates notch signaling and promotes stem-like character in PDGF-induced glioma cells. *Cell stem cell* **6**, 141-152 (2010).
157. Varnat, F.*, et al.* Human colon cancer epithelial cells harbour active HEDGEHOG-GLI signalling that is essential for tumour growth, recurrence, metastasis and stem cell survival and expansion. *EMBO molecular medicine* **1**, 338-351 (2009).
158. Zhao, D.*, et al.* VEGF drives cancer-initiating stem cells through VEGFR-2/Stat3 signaling to upregulate Myc and Sox2. *Oncogene* **34**, 3107-3119 (2015).
159. Bao, S.*, et al.* Stem cell–like glioma cells promote tumor angiogenesis through vascular endothelial growth factor. *Cancer research* **66**, 7843-7848 (2006).

160. Ricci-Vitiani, L.*, et al.* Tumour vascularization via endothelial differentiation of glioblastoma stem-like cells. *Nature* **468**, 824-828 (2010).
161. Maniotis, A.J.*, et al.* Vascular channel formation by human melanoma cells in vivo and in vitro: vasculogenic mimicry. *The American journal of pathology* **155**, 739-752 (1999).
162. Fan, J.*, et al.* Glutamine-driven oxidative phosphorylation is a major ATP source in transformed mammalian cells in both normoxia and hypoxia. *Molecular systems biology* **9**, 712 (2013).
163. Shangguan, W.*, et al.* Endothelium originated from colorectal cancer stem cells constitute cancer blood vessels. *Cancer Science* **108**, 1357-1367 (2017).
164. Caplan, A.I. All MSCs are pericytes? *Cell stem cell* **3**, 229-230 (2008).
165. Ochs, K.*, et al.* Immature mesenchymal stem cell-like pericytes as mediators of immunosuppression in human malignant glioma. *Journal of neuroimmunology* **265**, 106-116 (2013).
166. Cheng, L.*, et al.* Glioblastoma stem cells generate vascular pericytes to support vessel function and tumor growth. *Cell* **153**, 139-152 (2013).
167. Zhou, W.*, et al.* Targeting glioma stem cell-derived pericytes disrupts the blood-tumor barrier and improves chemotherapeutic efficacy. *Cell stem cell* **21**, 591-603. e594 (2017).
168. Flavahan, W.A.*, et al.* Brain tumor initiating cells adapt to restricted nutrition through preferential glucose uptake. *Nature neuroscience* **16**, 1373-1382 (2013).
169. Hjelmeland, A.B.*, et al.* Acidic stress promotes a glioma stem cell phenotype. *Cell Death & Differentiation* **18**, 829-840 (2011).
170. Sutherland, H.J., Lansdorp, P.M., Henkelman, D.H., Eaves, A.C. & Eaves, C.J. Functional characterization of individual human hematopoietic stem cells cultured at limiting dilution on supportive marrow stromal layers. *Proceedings of the National Academy of Sciences* **87**, 3584-3588 (1990).
171. Shibue, T. & Weinberg, R.A. EMT, CSCs, and drug resistance: the mechanistic link and clinical implications. *Nature reviews Clinical oncology* **14**, 611 (2017).
172. Frixen, U.H.*, et al.* E-cadherin-mediated cell-cell adhesion prevents invasiveness of human carcinoma cells. *The Journal of cell biology* **113**, 173-185 (1991).
173. Becker, K.-F.*, et al.* E-cadherin gene mutations provide clues to diffuse type gastric carcinomas. *Cancer research* **54**, 3845-3852 (1994).
174. Mani, S.A.*, et al.* The epithelial-mesenchymal transition generates cells with properties of stem cells. *Cell* **133**, 704-715 (2008).
175. Guo, W.*, et al.* Slug and Sox9 cooperatively determine the mammary stem cell state. *Cell* **148**, 1015-1028 (2012).
176. Williams, E.D., Gao, D., Redfern, A. & Thompson, E.W. Controversies around epithelial–mesenchymal plasticity in cancer metastasis. *Nature reviews Cancer*, 1-17 (2019).
177. Beck, B.*, et al.* Different levels of Twist1 regulate skin tumor initiation, stemness, and progression. *Cell stem cell* **16**, 67-79 (2015).
178. Wellner, U.*, et al.* The EMT-activator ZEB1 promotes tumorigenicity by repressing stemness-inhibiting microRNAs. *Nature cell biology* **11**, 1487-1495 (2009).
179. Yang, M.-H.*, et al.* Bmi1 is essential in Twist1-induced epithelial–mesenchymal transition. *Nature cell biology* **12**, 982-992 (2010).

180. Díaz-López, A., Moreno-Bueno, G. & Cano, A. Role of microRNA in epithelial to mesenchymal transition and metastasis and clinical perspectives. *Cancer management and research* **6**, 205 (2014).
181. Li, R.*, et al.* A mesenchymal-to-epithelial transition initiates and is required for the nuclear reprogramming of mouse fibroblasts. *Cell stem cell* **7**, 51-63 (2010).
182. Liu, S.*, et al.* Breast cancer stem cells transition between epithelial and mesenchymal states reflective of their normal counterparts. *Stem cell reports* **2**, 78-91 (2014).
183. Pastushenko, I.*, et al.* Identification of the tumour transition states occurring during EMT. *Nature* **556**, 463-468 (2018).
184. Jolly, M.K.*, et al.* Implications of the hybrid epithelial/mesenchymal phenotype in metastasis. *Frontiers in oncology* **5**, 155 (2015).
185. Pastushenko, I. & Blanpain, C. EMT transition states during tumor progression and metastasis. *Trends in cell biology* **29**, 212-226 (2019).
186. Aiello, N.M.*, et al.* EMT subtype influences epithelial plasticity and mode of cell migration. *Developmental cell* **45**, 681-695. e684 (2018).
187. Schliekelman, M.J.*, et al.* Molecular portraits of epithelial, mesenchymal, and hybrid States in lung adenocarcinoma and their relevance to survival. *Cancer research* **75**, 1789-1800 (2015).
188. Bocci, F.*, et al.* Numb prevents a complete epithelial–mesenchymal transition by modulating Notch signalling. *Journal of the Royal Society Interface* **14**, 20170512 (2017).
189. Gupta, P.B., Pastushenko, I., Skibinski, A., Blanpain, C. & Kuperwasser, C. Phenotypic Plasticity: Driver of Cancer Initiation, Progression, and Therapy Resistance. *Cell stem cell* **24**, 65-78 (2019).
190. Ruscetti, M., Quach, B., Dadashian, E.L., Mulholland, D.J. & Wu, H. Tracking and functional characterization of epithelial–mesenchymal transition and mesenchymal tumor cells during prostate cancer metastasis. *Cancer research* **75**, 2749-2759 (2015).
191. Strauss, R.*, et al.* Analysis of epithelial and mesenchymal markers in ovarian cancer reveals phenotypic heterogeneity and plasticity. *PloS one* **6**, e16186 (2011).
192. Grosse-Wilde, A.*, et al.* Stemness of the hybrid epithelial/mesenchymal state in breast cancer and its association with poor survival. *PloS one* **10**, e0126522 (2015).
193. Yamashita, N.*, et al.* Epithelial paradox: clinical significance of coexpression of E-cadherin and vimentin with regard to invasion and metastasis of breast cancer. *Clinical Breast Cancer* **18**, e1003-e1009 (2018).
194. Kahlert, U.D., Joseph, J.V. & Kruyt, F.A. EMT-and MET-related processes in nonepithelial tumors: importance for disease progression, prognosis, and therapeutic opportunities. *Molecular oncology* **11**, 860-877 (2017).
195. Yu, J.*, et al.* Induced pluripotent stem cell lines derived from human somatic cells. *Science (New York, N.Y.)* **318**, 1917-1920 (2007).
196. Liu, S.*, et al.* Breast cancer stem cells are regulated by mesenchymal stem cells through cytokine networks. *Cancer research* **71**, 614-624 (2011).
197. Fiori, M.E.*, et al.* Cancer-associated fibroblasts as abettors of tumor progression at the crossroads of EMT and therapy resistance. *Molecular cancer* **18**, 70 (2019).
198. Puram, S.V.*, et al.* Single-Cell Transcriptomic Analysis of Primary and Metastatic Tumor Ecosystems in Head and Neck Cancer. *Cell* **171**, 1611-1624.e1624 (2017).

199. Dunn, G.P., Bruce, A.T., Ikeda, H., Old, L.J. & Schreiber, R.D. Cancer immunoediting: from immunosurveillance to tumor escape. *Nat Immunol* **3**, 991-998 (2002).
200. Miranda, A.*, et al.* Cancer stemness, intratumoral heterogeneity, and immune response across cancers. *Proceedings of the National Academy of Sciences* **116**, 9020-9029 (2019).
201. Agudo, J.*, et al.* Quiescent tissue stem cells evade immune surveillance. *Immunity* **48**, 271-285. e275 (2018).
202. Chen, W., Dong, J., Haiech, J., Kilhoffer, M.-C. & Zeniou, M. Cancer stem cell quiescence and plasticity as major challenges in cancer therapy. *Stem cells international* **2016**(2016).
203. Di Tomaso, T.*, et al.* Immunobiological characterization of cancer stem cells isolated from glioblastoma patients. *Clinical Cancer Research* **16**, 800-813 (2010).
204. Lee, Y.*, et al.* CD44+ Cells in Head and Neck Squamous Cell Carcinoma Suppress T-Cell-Mediated Immunity by Selective Constitutive and Inducible Expression of PD-L1. *Clinical cancer research : an official journal of the American Association for Cancer Research* **22**, 3571-3581 (2016).
205. Kong, T.*, et al.* CD44 Promotes PD-L1 Expression and Its Tumor-Intrinsic Function in Breast and Lung Cancers. *Cancer research* **80**, 444-457 (2020).
206. Castagnoli, L.*, et al.* WNT signaling modulates PD-L1 expression in the stem cell compartment of triple-negative breast cancer. *Oncogene* **38**, 4047-4060 (2019).
207. Chen, L.*, et al.* Metastasis is regulated via microRNA-200/ZEB1 axis control of tumour cell PD-L1 expression and intratumoral immunosuppression. *Nature communications* **5**, 5241 (2014).
208. Wei, F.*, et al.* PD-L1 promotes colorectal cancer stem cell expansion by activating HMGA1-dependent signaling pathways. *Cancer Lett* **450**, 1-13 (2019).
209. Almozyan, S.*, et al.* PD-L1 promotes OCT4 and Nanog expression in breast cancer stem cells by sustaining PI3K/AKT pathway activation. *Int J Cancer* **141**, 1402-1412 (2017).
210. Miao, Y.*, et al.* Adaptive immune resistance emerges from tumor-initiating stem cells. *Cell* **177**, 1172-1186. e1114 (2019).
211. Zhou, S.L.*, et al.* A Positive Feedback Loop Between Cancer Stem-Like Cells and Tumor-Associated Neutrophils Controls Hepatocellular Carcinoma Progression. *Hepatology* **70**, 1214-1230 (2019).
212. Panni, R.Z.*, et al.* Tumor-induced STAT3 activation in monocytic myeloid-derived suppressor cells enhances stemness and mesenchymal properties in human pancreatic cancer. *Cancer immunology, immunotherapy : CII* **63**, 513-528 (2014).
213. Lu, H.*, et al.* A breast cancer stem cell niche supported by juxtacrine signalling from monocytes and macrophages. *Nature cell biology* **16**, 1105-1117 (2014).
214. Korkaya, H.*, et al.* Activation of an IL6 inflammatory loop mediates trastuzumab resistance in HER2+ breast cancer by expanding the cancer stem cell population. *Mol Cell* **47**, 570-584 (2012).
215. Tilg, H., Dinarello, C.A. & Mier, J.W. IL-6 and APPs: anti-inflammatory and immunosuppressive mediators. *Immunology today* **18**, 428-432 (1997).
216. Pöllänen, P.*, et al.* Role of transforming growth factor beta in testicular immunosuppression. *Journal of reproductive immunology* **24**, 123-137 (1993).
217. Bayik, D. & Lathia, J.D. Cancer stem cell–immune cell crosstalk in tumour progression. *Nature Reviews Cancer*, 1-11 (2021).

218. Kaiser, J. The cancer stem cell gamble. (American Association for the Advancement of Science, 2015).
219. Garber, K. Cancer stem cell pipeline flounders. *Nature Reviews Drug Discovery* **17**, 771-774 (2018).
220. Gerber, D.E.*, et al.* Phase 2 study of the focal adhesion kinase inhibitor defactinib (VS-6063) in previously treated advanced KRAS mutant non-small cell lung cancer. *Lung Cancer* **139**, 60-67 (2020).
221. Venkei, Z.G. & Yamashita, Y.M. Emerging mechanisms of asymmetric stem cell division. *Journal of Cell Biology* **217**, 3785-3795 (2018).
222. Morrison, S.J. & Kimble, J. Asymmetric and symmetric stem-cell divisions in development and cancer. *nature* **441**, 1068-1074 (2006).
223. Inaba, M. & Yamashita, Y.M. Asymmetric stem cell division: precision for robustness. *Cell stem cell* **11**, 461-469 (2012).
224. Knoblich, J.A. Mechanisms of asymmetric stem cell division. *Cell* **132**, 583-597 (2008).
225. Clevers, H. Stem cells, asymmetric division and cancer. *Nature genetics* **37**, 1027-1028 (2005).
226. Nakagawa, T., Nabeshima, Y.-i. & Yoshida, S. Functional identification of the actual and potential stem cell compartments in mouse spermatogenesis. *Developmental cell* **12**, 195-206 (2007).
227. Snippert, H.J. & Clevers, H. Tracking adult stem cells. *EMBO reports* **12**, 113-122 (2011).
228. Simons, B.D. & Clevers, H. Strategies for homeostatic stem cell self-renewal in adult tissues. *Cell* **145**, 851-862 (2011).
229. Satir, P. Chirality of the cytoskeleton in the origins of cellular asymmetry. *Philosophical Transactions of the Royal Society B: Biological Sciences* **371**, 20150408 (2016).
230. Samatey, F.A.*, et al.* Structure of the bacterial flagellar protofilament and implications for a switch for supercoiling. *Nature* **410**, 331-337 (2001).
231. Novak, M.*, et al.* The mitotic spindle is chiral due to torques within microtubule bundles. *Nature communications* **9**, 1-10 (2018).
232. Chin, A.S.*, et al.* Epithelial cell chirality revealed by three-dimensional spontaneous rotation. *Proceedings of the National Academy of Sciences* **115**, 12188-12193 (2018).
233. Ray, P.*, et al.* Intrinsic cellular chirality regulates left–right symmetry breaking during cardiac looping. *Proceedings of the National Academy of Sciences* **115**, E11568-E11577 (2018).
234. Xu, J.*, et al.* Polarity reveals intrinsic cell chirality. *Proceedings of the National Academy of Sciences* **104**, 9296-9300 (2007).
235. Kiger, A.A., Jones, D.L., Schulz, C., Rogers, M.B. & Fuller, M.T. Stem cell self-renewal specified by JAK-STAT activation in response to a support cell cue. *Science (New York, N.Y.)* **294**, 2542-2545 (2001).
236. Tulina, N. & Matunis, E. Control of stem cell self-renewal in Drosophila spermatogenesis by JAK-STAT signaling. *Science (New York, N.Y.)* **294**, 2546-2549 (2001).
237. Shivdasani, A.A. & Ingham, P.W. Regulation of stem cell maintenance and transit amplifying cell proliferation by TGF-β signaling in Drosophila spermatogenesis. *Current Biology* **13**, 2065-2072 (2003).
238. Lechler, T. & Fuchs, E. Asymmetric cell divisions promote stratification and differentiation of mammalian skin. *Nature* **437**, 275-280 (2005).

239. Shin, J.-W.*, et al.* Contractile forces sustain and polarize hematopoiesis from stem and progenitor cells. *Cell stem cell* **14**, 81-93 (2014).
240. Pereira, G., Tanaka, T.U., Nasmyth, K. & Schiebel, E. Modes of spindle pole body inheritance and segregation of the Bfa1p–Bub2p checkpoint protein complex. *The EMBO journal* **20**, 6359-6370 (2001).
241. Caydasi, A.K. & Pereira, G. SPOC alert—when chromosomes get the wrong direction. *Experimental cell research* **318**, 1421-1427 (2012).
242. Reichert, H. Drosophila neural stem cells: cell cycle control of self-renewal, differentiation, and termination in brain development. in *Cell Cycle in Development* 529-546 (Springer, 2011).
243. Sousa-Nunes, R. & Somers, W.G. Mechanisms of asymmetric progenitor divisions in the Drosophila central nervous system. in *Transcriptional and translational regulation of stem cells* 79-102 (Springer, 2013).
244. Goldstein, B. & Hird, S.N. Specification of the anteroposterior axis in Caenorhabditis elegans. *Development* **122**, 1467-1474 (1996).
245. Aguilaniu, H., Gustafsson, L., Rigoulet, M. & Nyström, T. Asymmetric inheritance of oxidatively damaged proteins during cytokinesis. *Science (New York, N.Y.)* **299**, 1751-1753 (2003).
246. Ackermann, M., Stearns, S.C. & Jenal, U. Senescence in a bacterium with asymmetric division. *Science (New York, N.Y.)* **300**, 1920-1920 (2003).
247. Ackermann, M., Chao, L., Bergstrom, C.T. & Doebeli, M. On the evolutionary origin of aging. *Aging cell* **6**, 235-244 (2007).
248. Macara, I.G. & Mili, S. Polarity and differential inheritance—universal attributes of life? *Cell* **135**, 801-812 (2008).
249. Caviston, J.P. & Holzbaur, E.L. Microtubule motors at the intersection of trafficking and transport. *Trends in cell biology* **16**, 530-537 (2006).
250. Martin-Belmonte, F. & Mostov, K. Regulation of cell polarity during epithelial morphogenesis. *Current opinion in cell biology* **20**, 227-234 (2008).
251. Lee, M. & Vasioukhin, V. Cell polarity and cancer–cell and tissue polarity as a non-canonical tumor suppressor. *Journal of cell science* **121**, 1141-1150 (2008).
252. Martin-Belmonte, F. & Perez-Moreno, M. Epithelial cell polarity, stem cells and cancer. *Nature Reviews Cancer* **12**, 23-38 (2012).
253. Cao, X., Surma, M.A. & Simons, K. Polarized sorting and trafficking in epithelial cells. *Cell research* **22**, 793-805 (2012).
254. Martin-Belmonte, F.*, et al.* PTEN-mediated apical segregation of phosphoinositides controls epithelial morphogenesis through Cdc42. *Cell* **128**, 383-397 (2007).
255. Ang, A.L.*, et al.* Recycling endosomes can serve as intermediates during transport from the Golgi to the plasma membrane of MDCK cells. *The Journal of cell biology* **167**, 531-543 (2004).
256. Cresawn, K.O.*, et al.* Differential involvement of endocytic compartments in the biosynthetic traffic of apical proteins. *The EMBO journal* **26**, 3737-3748 (2007).
257. Weisz, O.A. & Rodriguez-Boulan, E. Apical trafficking in epithelial cells: signals, clusters and motors. *Journal of cell science* **122**, 4253-4266 (2009).
258. Royer, C. & Lu, X. Epithelial cell polarity: a major gatekeeper against cancer? *Cell Death & Differentiation* **18**, 1470-1477 (2011).

259. Tsukita, S., Yamazaki, Y., Katsuno, T. & Tamura, A. Tight junction-based epithelial microenvironment and cell proliferation. *Oncogene* **27**, 6930-6938 (2008).
260. Zen, K.*, et al.* Defective expression of polarity protein PAR-3 gene (PARD3) in esophageal squamous cell carcinoma. *Oncogene* **28**, 2910-2918 (2009).
261. Xue, B., Krishnamurthy, K., Allred, D.C. & Muthuswamy, S.K. Loss of Par3 promotes breast cancer metastasis by compromising cell–cell cohesion. *Nature cell biology* **15**, 189-200 (2013).
262. Jung, H.-Y.*, et al.* Apical–basal polarity inhibits epithelial–mesenchymal transition and tumour metastasis by PAR-complex-mediated SNAI1 degradation. *Nature cell biology* **21**, 359-371 (2019).
263. Willott, E.*, et al.* The tight junction protein ZO-1 is homologous to the Drosophila discs-large tumor suppressor protein of septate junctions. *Proceedings of the National Academy of Sciences* **90**, 7834-7838 (1993).
264. Harten, S.K.*, et al.* Regulation of renal epithelial tight junctions by the von Hippel-Lindau tumor suppressor gene involves occludin and claudin 1 and is independent of E-cadherin. *Molecular biology of the cell* **20**, 1089-1101 (2009).
265. Schneeberger, E.E. & Lynch, R.D. The tight junction: a multifunctional complex. *American Journal of Physiology-Cell Physiology* **286**, C1213-C1228 (2004).
266. Pine, S.R., Ryan, B.M., Varticovski, L., Robles, A.I. & Harris, C.C. Microenvironmental modulation of asymmetric cell division in human lung cancer cells. *Proceedings of the National Academy of Sciences* **107**, 2195-2200 (2010).
267. Wang, J.*, et al.* Symmetrical and asymmetrical division analysis provides evidence for a hierarchy of prostate epithelial cell lineages. *Nature communications* **5**, 1-13 (2014).
268. Ma, R., Minsky, N., Morshed, S.A. & Davies, T.F. Stemness in human thyroid cancers and derived cell lines: the role of asymmetrically dividing cancer stem cells resistant to chemotherapy. *The Journal of clinical endocrinology and metabolism* **99**, E400 (2014).
269. Chen, G.*, et al.* Human Brat ortholog TRIM3 is a tumor suppressor that regulates asymmetric cell division in glioblastoma. *Cancer research* **74**, 4536-4548 (2014).
270. Patel, S.A.*, et al.* Delineation of breast cancer cell hierarchy identifies the subset responsible for dormancy. *Scientific reports* **2**, 906 (2012).
271. Kwong, L.N. & Dove, W.F. APC and its modifiers in colon cancer. in *Apc Proteins* 85-106 (Springer, 2009).
272. Bu, P.*, et al.* A microRNA miR-34a-regulated bimodal switch targets Notch in colon cancer stem cells. *Cell stem cell* **12**, 602-615 (2013).
273. Wang, L.*, et al.* A long non-coding RNA targets microRNA miR-34a to regulate colon cancer stem cell asymmetric division. *Elife* **5**, e14620 (2016).
274. Nigg, E.A. & Stearns, T. The centrosome cycle: centriole biogenesis, duplication and inherent asymmetries. *Nature cell biology* **13**, 1154-1160 (2011).
275. Bettencourt-Dias, M. & Glover, D.M. Centrosome biogenesis and function: centrosomics brings new understanding. *Nature reviews Molecular cell biology* **8**, 451-463 (2007).
276. Meraldi, P. & Nigg, E. The centrosome cycle. *FEBS letters* **521**, 9-13 (2002).
277. Jakobsen, L.*, et al.* Novel asymmetrically localizing components of human centrosomes identified by complementary proteomics methods. *The EMBO journal* **30**, 1520-1535 (2011).
278. Lattao, R., Kovács, L. & Glover, D.M. The centrioles, centrosomes, basal bodies, and cilia of Drosophila melanogaster. *Genetics* **206**, 33-53 (2017).

279. Carvalho-Santos, Z., Azimzadeh, J., Pereira-Leal, J.B. & Bettencourt-Dias, M. Evolution: Tracing the origins of centrioles, cilia, and flagella. *The Journal of cell biology* **194**, 165 (2011).
280. Wang, W.-J.*, et al.* De novo centriole formation in human cells is error-prone and does not require SAS-6 self-assembly. *Elife* **4**, e10586 (2015).
281. Uetake, Y.*, et al.* Cell cycle progression and de novo centriole assembly after centrosomal removal in untransformed human cells. *The Journal of cell biology* **176**, 173-182 (2007).
282. Kleylein-Sohn, J.*, et al.* Plk4-induced centriole biogenesis in human cells. *Developmental cell* **13**, 190-202 (2007).
283. Strnad, P. & Gönczy, P. Mechanisms of procentriole formation. *Trends in cell biology* **18**, 389-396 (2008).
284. Tsou, M.-F.B. & Stearns, T. Mechanism limiting centrosome duplication to once per cell cycle. *Nature* **442**, 947-951 (2006).
285. Pelletier, L. & Yamashita, Y.M. Centrosome asymmetry and inheritance during animal development. *Current opinion in cell biology* **24**, 541-546 (2012).
286. Rusan, N.M. & Peifer, M. A role for a novel centrosome cycle in asymmetric cell division. *Journal of Cell Biology* **177**, 13-20 (2007).
287. Yamashita, Y.M. & Fuller, M.T. Asymmetric centrosome behavior and the mechanisms of stem cell division. *The Journal of cell biology* **180**, 261-266 (2008).
288. Wang, G., Jiang, Q. & Zhang, C. The role of mitotic kinases in coupling the centrosome cycle with the assembly of the mitotic spindle. *Journal of cell science* **127**, 4111-4122 (2014).
289. Yamashita, Y.M., Mahowald, A.P., Perlin, J.R. & Fuller, M.T. Asymmetric inheritance of mother versus daughter centrosome in stem cell division. *Science (New York, N.Y.)* **315**, 518-521 (2007).
290. Ranjan, R., Snedeker, J. & Chen, X. Asymmetric centromeres differentially coordinate with mitotic machinery to ensure biased sister chromatid segregation in germline stem cells. *Cell stem cell* **25**, 666-681. e665 (2019).
291. Graser, S.*, et al.* Cep164, a novel centriole appendage protein required for primary cilium formation. *The Journal of cell biology* **179**, 321-330 (2007).
292. Lange, B.M. & Gull, K. A molecular marker for centriole maturation in the mammalian cell cycle. *The Journal of cell biology* **130**, 919-927 (1995).
293. Nakagawa, Y., Yamane, Y., Okanoue, T., Tsukita, S. & Tsukita, S. Outer dense fiber 2 is a widespread centrosome scaffold component preferentially associated with mother centrioles: its identification from isolated centrosomes. *Molecular biology of the cell* **12**, 1687-1697 (2001).
294. Ou, Y.Y., Mack, G.J., Zhang, M. & Rattner, J.B. CEP110 and ninein are located in a specific domain of the centrosome associated with centrosome maturation. *Journal of cell science* **115**, 1825-1835 (2002).
295. Zou, C.*, et al.* Centrobin a novel daughter centriole–associated protein that is required for centriole duplication. *The Journal of cell biology* **171**, 437-445 (2005).
296. Tozer, S., Baek, C., Fischer, E., Goiame, R. & Morin, X. Differential routing of mindbomb1 via centriolar satellites regulates asymmetric divisions of neural progenitors. *Neuron* **93**, 542-551. e544 (2017).

297. Lambert, J.D. & Nagy, L.M. Asymmetric inheritance of centrosomally localized mRNAs during embryonic cleavages. *Nature* **420**, 682-686 (2002).
298. Tsankova, A., Pham, T.T., Garcia, D.S., Otte, F. & Cabernard, C. Cell polarity regulates biased myosin activity and dynamics during asymmetric cell division via Drosophila rho kinase and protein kinase N. *Developmental Cell* **42**, 143-155. e145 (2017).
299. Cabernard, C., Prehoda, K.E. & Doe, C.Q. A spindle-independent cleavage furrow positioning pathway. *Nature* **467**, 91-94 (2010).
300. Li, R. The art of choreographing asymmetric cell division. *Developmental cell* **25**, 439-450 (2013).
301. Siller, K.H. & Doe, C.Q. Spindle orientation during asymmetric cell division. *Nature cell biology* **11**, 365-374 (2009).
302. Morin, X. & Bellaïche, Y. Mitotic spindle orientation in asymmetric and symmetric cell divisions during animal development. *Developmental cell* **21**, 102-119 (2011).
303. Siegrist, S.E. & Doe, C.Q. Microtubule-induced Pins/Gαi cortical polarity in Drosophila neuroblasts. *Cell* **123**, 1323-1335 (2005).
304. Cai, Y., Chia, W. & Yang, X. A family of snail-related zinc finger proteins regulates two distinct and parallel mechanisms that mediate Drosophila neuroblast asymmetric divisions. *The EMBO journal* **20**, 1704-1714 (2001).
305. Wang, H., Cai, Y., Chia, W. & Yang, X. Drosophila homologs of mammalian TNF/TNFR-related molecules regulate segregation of Miranda/Prospero in neuroblasts. *The EMBO journal* **25**, 5783-5793 (2006).
306. Siller, K.H. & Doe, C.Q. Lis1/dynactin regulates metaphase spindle orientation in Drosophila neuroblasts. *Developmental biology* **319**, 1-9 (2008).
307. Chan, J.Y. A clinical overview of centrosome amplification in human cancers. *International journal of biological sciences* **7**, 1122 (2011).
308. Fukasawa, K. Centrosome amplification, chromosome instability and cancer development. *Cancer letters* **230**, 6-19 (2005).
309. Castellanos, E., Dominguez, P. & Gonzalez, C. Centrosome dysfunction in Drosophila neural stem cells causes tumors that are not due to genome instability. *Current Biology* **18**, 1209-1214 (2008).
310. Vitre, B.*, et al.* Chronic centrosome amplification without tumorigenesis. *Proceedings of the National Academy of Sciences* **112**, E6321-E6330 (2015).
311. Basto, R.*, et al.* Centrosome amplification can initiate tumorigenesis in flies. *Cell* **133**, 1032-1042 (2008).
312. Levine, M.S.*, et al.* Centrosome amplification is sufficient to promote spontaneous tumorigenesis in mammals. *Developmental cell* **40**, 313-322. e315 (2017).
313. Salmon, E., Cimini, D., Cameron, L. & DeLuca, J. Merotelic kinetochores in mammalian tissue cells. *Philosophical Transactions of the Royal Society B: Biological Sciences* **360**, 553-568 (2005).
314. Cimini, D. Merotelic kinetochore orientation, aneuploidy, and cancer. *Biochimica et Biophysica Acta (BBA)-Reviews on Cancer* **1786**, 32-40 (2008).
315. Dzafic, E., Strzyz, P.J., Wilsch-Bräuninger, M. & Norden, C. Centriole amplification in zebrafish affects proliferation and survival but not differentiation of neural progenitor cells. *Cell reports* **13**, 168-182 (2015).
316. Ganem, N.J., Godinho, S.A. & Pellman, D. A mechanism linking extra centrosomes to chromosomal instability. *Nature* **460**, 278-282 (2009).

317. Quintyne, N.J., Reing, J.E., Hoffelder, D.R., Gollin, S.M. & Saunders, W.S. Spindle multipolarity is prevented by centrosomal clustering. *Science (New York, N.Y.)* **307**, 127-129 (2005).
318. Kwon, M.*, et al.* Mechanisms to suppress multipolar divisions in cancer cells with extra centrosomes. *Genes & development* **22**, 2189-2203 (2008).
319. Bradshaw, R.A. & Stahl, P.D. *Encyclopedia of cell biology*, (Academic Press, 2015).
320. Leber, B.*, et al.* Proteins required for centrosome clustering in cancer cells. *Science translational medicine* **2**, 33ra38-33ra38 (2010).
321. Mariappan, A.*, et al.* Inhibition of CPAP–tubulin interaction prevents proliferation of centrosome-amplified cancer cells. *The EMBO journal* **38**, e99876 (2019).
322. Wilkens, L.*, et al.* Induction of aneuploidy by increasing chromosomal instability during dedifferentiation of hepatocellular carcinoma. *Proceedings of the National Academy of Sciences* **101**, 1309-1314 (2004).
323. Shao, C.*, et al.* Essential role of aldehyde dehydrogenase 1A3 for the maintenance of non–small cell lung cancer stem cells is associated with the STAT3 pathway. *Clinical cancer research* **20**, 4154-4166 (2014).
324. Singh, M.K., Cowell, L., Seo, S., O'Neill, G.M. & Golemis, E.A. Molecular basis for HEF1/NEDD9/Cas-L action as a multifunctional co-ordinator of invasion, apoptosis and cell cycle. *Cell biochemistry and biophysics* **48**, 54-72 (2007).
325. Izumchenko, E.*, et al.* NEDD9 promotes oncogenic signaling in mammary tumor development. *Cancer research* **69**, 7198-7206 (2009).
326. Wang, Z.*, et al.* NEDD9 may regulate hepatocellular carcinoma cell metastasis by promoting epithelial-mesenchymal-transition and stemness via repressing Smad7. *Oncotarget* **8**, 1714 (2017).
327. Kim, M.*, et al.* Comparative oncogenomics identifies NEDD9 as a melanoma metastasis gene. *Cell* **125**, 1269-1281 (2006).
328. Li, Y.*, et al.* HEF1, a novel target of Wnt signaling, promotes colonic cell migration and cancer progression. *Oncogene* **30**, 2633-2643 (2011).
329. Pugacheva, E.N. & Golemis, E.A. The focal adhesion scaffolding protein HEF1 regulates activation of the Aurora-A and Nek2 kinases at the centrosome. *Nature cell biology* **7**, 937-946 (2005).
330. Pugacheva, E.N., Jablonski, S.A., Hartman, T.R., Henske, E.P. & Golemis, E.A. HEF1-dependent Aurora A activation induces disassembly of the primary cilium. *Cell* **129**, 1351-1363 (2007).
331. Singh, M.K.*, et al.* Enhanced genetic instability and dasatinib sensitivity in mammary tumor cells lacking NEDD9. *Cancer research* **70**, 8907-8916 (2010).
332. O'Neill, G.M., Seo, S., Serebriiskii, I.G., Lessin, S.R. & Golemis, E.A. A new central scaffold for metastasis: parsing HEF1/Cas-L/NEDD9. *Cancer research* **67**, 8975-8979 (2007).
333. Guerrero, M.S., Parsons, J.T. & Bouton, A.H. Cas and NEDD9 contribute to tumor progression through dynamic regulation of the cytoskeleton. *Genes & cancer* **3**, 371-381 (2012).
334. Shagisultanova, E., Gaponova, A.V., Gabbasov, R., Nicolas, E. & Golemis, E.A. Preclinical and clinical studies of the NEDD9 scaffold protein in cancer and other diseases. *Gene* **567**, 1-11 (2015).

335. Gabbasov, R.*, et al.* NEDD9 promotes oncogenic signaling, a stem/mesenchymal gene signature, and aggressive ovarian cancer growth in mice. *Oncogene* **37**, 4854-4870 (2018).
336. Bible, K.C.*, et al.* 2021 American Thyroid Association Guidelines for Management of Patients with Anaplastic Thyroid Cancer: American Thyroid Association Anaplastic Thyroid Cancer Guidelines Task Force. *Thyroid* **31**, 337-386 (2021).
337. Isham, C.R.*, et al.* Pazopanib enhances paclitaxel-induced mitotic catastrophe in anaplastic thyroid cancer. *Science translational medicine* **5**, 166ra163-166ra163 (2013).

Appendix: Rights to Reprint

Figure 2
ELSEVIER LICENSE
TERMS AND CONDITIONS

Jul 26, 2021

This Agreement between Mr. Henry Yu ("You") and Elsevier ("Elsevier") consists of your license details and the terms and conditions provided by Elsevier and Copyright Clearance Center.

License Number	5116310928629
License date	Jul 26, 2021
Licensed Content Publisher	Elsevier
Licensed Content Publication	Cell
Licensed Content Title	Hallmarks of Cancer: The Next Generation
Licensed Content Author	Douglas Hanahan,Robert A. Weinberg
Licensed Content Date	Mar 4, 2011
Licensed Content Volume	144
Licensed Content Issue	5
Licensed Content Pages	29
Start Page	646

End Page	674
Type of Use	reuse in a thesis/dissertation
Portion	figures/tables/illustrations
Number of figures/tables/illustrations	1
Format	both print and electronic
Are you the author of this Elsevier article?	No
Will you be translating?	No
Title	Investigation of centrosome-dependent signaling axis driving stemness and chromosomal instability of ALDH-positive cancer stem-like cells
Institution name	McGill University
Expected presentation date	Aug 2021
Portions	Figure 4
Publisher Tax ID	GB 494 6272 12

Figure 4

This is a License Agreement between Henry G. Yu ("User") and Copyright Clearance Center, Inc. ("CCC") on behalf of the Rightsholder identified in the order details below. The license consists of the order details, the CCC Terms and Conditions below, and any Rightsholder Terms and Conditions which are included below.

All payments must be made in full to CCC in accordance with the CCC Terms and Conditions below.

Order Date	26-Jul-2021	**Type of Use**	Republish in a thesis/dissertation
Order License ID	1135810-1		
ISSN	1540-8140	**Publisher**	ROCKEFELLER UNIVERSITY PRESS
		Portion	Image/photo/illustration

LICENSED CONTENT

Publication Title	The journal of cell biology	**Rightsholder**	Rockefeller University Press
Date	01/01/1962		
Language	English	**Publication Type**	e-Journal
Country	United States of America	**URL**	http://www.jcb.org/

REQUEST DETAILS

Portion Type	Image/photo/illustration	**Distribution**	Canada
Number of images / photos / illustrations	1	**Translation**	Original language of publication
Format (select all that apply)	Print, Electronic	**Copies for the disabled?**	No
		Minor editing privileges?	No
Who will republish the content?	Academic institution	**Incidental promotional use?**	No
Duration of Use	Life of current edition	**Currency**	USD
Lifetime Unit Quantity	Up to 99,999		
Rights Requested	Main product		

NEW WORK DETAILS

Title	Investigation of centrosome-dependent signaling axis driving stemness and chromosomal instability of ALDH-positive cancer stem-like cells	**Institution name**	McGill University
		Expected presentation date	2021-08-15
Instructor name	Moulay Alaoui-Jamali		

ADDITIONAL DETAILS

Order reference number	N/A	**The requesting person / organization to appear on the license**	Henry G. Yu

Figure 5

This is a License Agreement between Henry G Yu, McGill University ("User") and Copyright Clearance Center, Inc. ("CCC") on behalf of the Rightsholder identified in the order details below. The license consists of the order details, the CCC Terms and Conditions below, and any Rightsholder Terms and Conditions which are included below.

All payments must be made in full to CCC in accordance with the CCC Terms and Conditions below.

Order Date	24-Jul-2021	**Type of Use**	Republish in a thesis/dissertation
Order License ID	1135657-1		
ISSN	1477-9137	**Publisher**	COMPANY OF BIOLOGISTS LTD.
		Portion	Image/photo/illustration

LICENSED CONTENT

Publication Title	Journal of cell science	**Publication Type**	e-Journal
Article Title	The role of mitotic kinases in coupling the centrosome cycle with the assembly of the mitotic spindle.	**Start Page**	4111
		End Page	4122
		Issue	Pt 19
		Volume	127
Author/Editor	Company of Biologists.	**URL**	http://jcs.biologists.org/
Date	01/01/1966		
Language	English		
Country	United Kingdom of Great Britain and Northern Ireland		
Rightsholder	The Company of Biologists Ltd.		

Figure 6

ELSEVIER LICENSE
TERMS AND CONDITIONS
Jul 24, 2021

This Agreement between Mr. Henry Yu ("You") and Elsevier ("Elsevier") consists of your license details and the terms and conditions provided by Elsevier and Copyright Clearance Center.

License Number	5115640254640
License date	Jul 24, 2021
Licensed Content Publisher	Elsevier
Licensed Content Publication	Cell Stem Cell
Licensed Content Title	Asymmetric Centromeres Differentially Coordinate with Mitotic Machinery to Ensure Biased Sister Chromatid Segregation in Germline Stem Cells
Licensed Content Author	Rajesh Ranjan,Jonathan Snedeker,Xin Chen
Licensed Content Date	Nov 7, 2019
Licensed Content Volume	25
Licensed Content Issue	5
Licensed Content Pages	21
Start Page	666
End Page	681.e5
Type of Use	reuse in a thesis/dissertation
Portion	figures/tables/illustrations
Number of figures/tables/illustrations	1
Format	both print and electronic
Are you the author of this Elsevier article?	No
Will you be translating?	No
Title	Investigation of centrosome-dependent signaling axis driving stemness and chromosomal instability of ALDH-positive cancer stem-like cells
Institution name	McGill University
Expected presentation date	Aug 2021
Portions	Graphical Abstract
Attn: Mr. Henry Yu	
Publisher Tax ID	GB 494 6272 12
Total	0.00 USD
Terms and Conditions	

Figure 7

ELSEVIER LICENSE
TERMS AND CONDITIONS
Aug 15, 2021

This Agreement between Mr. Henry Yu ("You") and Elsevier ("Elsevier") consists of your license details and the terms and conditions provided by Elsevier and Copyright Clearance Center.

License Number	5130560909201
License date	Aug 15, 2021
Licensed Content Publisher	Elsevier
Licensed Content Publication	Elsevier Books
Licensed Content Title	Encyclopedia of Cell Biology
Licensed Content Author	J. Sillibourne,M. Bornens
Licensed Content Date	Jan 1, 2016
Licensed Content Pages	11
Start Page	649
End Page	659
Type of Use	reuse in a thesis/dissertation
Portion	
Number of	figures/tables/illustrations
1	
figures/tables/illustrations	
Format	both print and electronic
Are you the author of this	
No	
Elsevier chapter?	
Will you be translating?	No
Title	Investigation of centrosome-dependent signaling axis driving stemness and chromosomal instability of ALDH-positive cancer stem-like cells
Institution name	McGill University
Expected presentation date	Aug 2021
Portions	Figure 5. Centrosome amplification.
Attn: Mr. Henry Yu	
Publisher Tax ID	GB 494 6272 12
Total	
Terms and Conditions	0.00 USD